Draft:Wednesday 15th August, 2018-11:19

IHEP-CEPC-DR-2018-XX

IHEP-EP-2018-XX

IHEP-TH-2018-XX

CEPC

Conceptual Design Report

Volume II - Physics & Detector

The CEPC Study Group

Fall 2018

ACKNOWLEDGMENTS

The CEPC Physics and Detector Conceptual Design Report (CDR) was prepared and written by the CEPC Study Group. The study was organised and led by scientists from the Institute of High Energy Physics (IHEP) of the Chinese Academy of Sciences (CAS), and from many universities and other institutes in China and abroad. The study was partially supported ...

...

CONTENTS

CHAPTER 1

EXECUTIVE SUMMARY – INTRODUCTION

The discovery of the Higgs boson in 2012 by the ATLAS and CMS collaborations [1, 2] at CERN's Large Hadron Collider (LHC) opened a new era in particle physics and raised new opportunities for a large-scale accelerator. Due to the low mass of the Higgs, it is possible to produce it in the relatively clean environment of a circular electron-positron collider with reasonable luminosity, technology, cost and power consumption. The Higgs boson is a crucial cornerstone of the Standard Model (SM). It is at the center of the biggest mysteries of modern particle physics, such as the large hierarchy between the weak scale and the Planck scale, the nature of the electroweak phase transition, and many other related questions. Precise measurements of the properties of the Higgs boson, together with precise measurements of the W and Z bosons, serve as excellent tests of the underlying fundamental physics principles of the SM, and they are instrumental in explorations beyond the SM. Such physics program will be a critical component of any roadmap for high energy physics in the coming decades.

The Circular Electron Positron Collider (CEPC) is a large international scientific project initiated and hosted by China. It was first presented to the international community at the ICFA Workshop "Accelerators for a Higgs Factory: Linear vs. Circular" (HF2012) in November 2012 at Fermilab. A Preliminary Conceptual Design Report (Pre-CDR) [3] was published in March 2015. This document is the second volume of the Conceptual Design Report (CDR). It summarizes the physics potential of the CEPC, possible detector concepts and the corresponding R&D program. The first volume [**?**], released in July 2018, describes the CEPC accelerator complex design, associated civil engineering and strategic alternative scenarios.

The main purpose of this document is to address the physics potential of such future circular electron positron collider. The CEPC operation will be staged in a few steps

of center-of-mass energy to maximize its physics potential. It is expected the CEPC to start operations at 240 GeV, giving raise to a wealth of Higgs physics, and then move to lower center-of-mass energies and collect large samples of W and Z bosons. This complete program of precision standard-model physics will place stringent constraints on new physics, and it has the potential for direct observation of new physics.

This CDR volume presents the essential features of the detectors that are required to extract the full physics potential of the CEPC. The experimental conditions at high-luminosity high-energy circular electron positron colliders are *more challenging than those considered previously for electron-positron linear colliders due to the higher levels of beam-induced backgrounds, and the 25 ns bunch-spacing required to collect extremely large samples of Z boson events.* A main goal of this report is to demonstrate that a wide range of high-precision physics measurements can be made at CEPC with detectors that are feasible to complete in the next 12-15 years, expanding on an on-going realistic R&D program.

Consequently, part of this report is devoted to understanding the impact of the machine environment on the detector with the aim of demonstrating, with the example of a few realistic detector concepts, that high-precision physics measurements can be made at the CEPC. This document concentrates on the detector requirements and physics measurements at the highest CEPC center-of-mass energy of 240 GeV, when the beam induced backgrounds are higher, but consideration is also given to the high-rate operation at the Z-boson mass energy.

A preliminary version of this Physics and Detector CDR was reviewed by an international review committee in September 2018. The comments from the reviewers have been taken into account in this final document, and details about it can be found in Appendix [**?**].

This volume of the CEPC CDR consists of 11 chapters. The next chapter presents an overview of the phyiscs case for the CEPC, where we highlight the physics potential for both SM precison measurement and searches beyond the SM. Chapter 3 introduces the CEPC accelerator and the experimental environment and lists the detector requirements that must be met to achieve the CEPC physics goals. This chapter ends with the introduction of the CEPC detector concepts proposed to satisfy these physics requirements. The detector subsystems are then described together in more detailed in the subsequent chapters. Chapter 4 describes the tracking systems of all detector concepts, including the vertex detectors. Chapter 5 presents the calorimeter options, while Chapter 7 describes the muon system concepts. Results from detailed full simulation and test beam studies are presented when available. The challenges referring to the design of the interaction region are described in Chapter 9, together with the beam backgrounds and details about the plans for the luminosity measurement. The design of the detector solenoid is addressed in Chapter 6, while a summary plan for the readout electronics and data acquisition system is presented in Chapter 8. The overall performance of the CEPC baseline detector concept is presented in Chapters 10 and 11. Chapters 10 introduces the detector software used in the studies and details the physics object performance, taking into account full detector simulation and reconstruction. Chapter 11 demonstrates the full physics potential of the CEPC by emphasizing selected benchmark physics results. Finally, Chapter 12 ends this report with an overview of future plans on detector R&D and physics studies towards the Technical Design Report.

Operation mode	$\sqrt{s}$ (GeV)	L per IP (10^{34} cm^{-2}s^{-1})	Years	Total $\int L$ (ab^{-1}, 2 IPs)	Event yields
H	240	3	7	5.6	1×10^6
Z	91.2	32 (*)	2	16	7×10^{11}
W^+W^-	158-172	10	1	2.6	2×10^7

Table 1.1: CEPC operation plan at different center-of-mass energies ($\sqrt{s}$), and corresponding anticipated instantaneous luminosity (L), total integrated luminosity ($\int L$) and event yields. (*) The maximum instaneous luminosity achievable at the Z pole operation is dependent on the detector solenoid magnet field. The value reported here assumes a 2 Tesla solenoid. For a 3 Tesla magnet, the luminosity will be 50% lower.

This section is just a placeholder for now. It will be a short introduction 2-4 pages with a very short motivation for the CEPC project [4] and the workings of the CDR. We will define here the goals of the CDR and will already mention the connection between the different detector concepts. We will mention quickly some of the challenges and the future R&D program. We can also provide the short descriptions to the chapters in the CDR. There will be no subsections sections in this text. Each part below will be a short executive summary of the corresponding sections in the text.

Physics Potential Short summary paragraphs from LianTao's chapter

Collider and the Experimental Environment The CEPC is a double-ring e^+e^-collider with 100 km circumference and two interaction points (IP). It will operate in three different modes, corresponding to three different center-of-mass energies ($\sqrt{s}$): Higgs factory ($e^+e- \to ZH$) at $\sqrt{s} = 240$ GeV, Z boson factory ($e^+e- \to Z$) at $\sqrt{s} = 91.2$ GeV and W threshold ($e^+e- \to W^+W^-$) at $\sqrt{s} =\sim 160$ GeV. The instantaneous luminosities are expected to reach 3×10^{34}, 32×10^{34} and 10×10^{34} cm^{-2}s^{-1}, respectively, as shown in Table 1.1. The current tentative operation plan will allow the CEPC to collect one million Higgs particles or more, close to one trillion Z boson events, and ten million W^+W^- event pairs.

The detectors will record collisions in beam conditions presented in Figure 3.1. Several of these parameters impose important constraints on the detectors. The bunch spacing of the colliding beams differ greatly in the three operational modes (25 ns, 210 ns, and 680 ns, respectively) as do the background levels and event rates. The three most important sources of radiation backgrounds are (1) synchrotron radiation photons from the last bending dipole magnet, (2) e^+e^- pair production following the beamstrahlung process, and (3) off-energy beam particles lost in the interaction region. These backgrounds generate a hit density in the first vertex detector layer ($r = 1.6$ cm) of about 2.4 hits/cm^2 per bunch crossing when running at $\sqrt{s} = 240$ GeV and tolerable levels of the total ionizing energy (TID) and non-ionizing energy loss (NIEL). The event rate reaches ~32 kHz for Z factory operation from Z boson decays and Bhabha events.

Detector Concepts Include summary of main physics requirements needed to take into consideration, then briefly describe the solutions with the detector concepts. Follow chapter 3.

Include brief summaries of highlights from the detector chapters

The CEPC detector concepts are based on the stringent performance requirements needed to deliver a precision phyiscs program that tests the Standard Model and searches for new physics over a wide range of center-of-mass energies and at high beam luminosities. These specifications include large and precisely defined solid angle coverage, precise track momentum resolution, high efficiency vertex reconstruction, precise photon energy reconstruction, excellent particle identification, excellent jet reconstruction and flavor tagging.

Performance and Physics Benchmarks Brief summary of the findings in the performance and physics benchmark chapters

Future Plans The CEPC construction is expected to start in 2022 and be completed in 2030, followed by the commissioning of the accelerator and detectors. A tentative operational plan covers 10 years of physics data: 7 years for Higgs physics, followed by 2 years operation in Z mode and 1 year operation in W mode. Prior to the construction there will be a five-year R&D period (2018-2022). During this period, two international collaborations will be formed to produce Technical Design Reports, build and operate two large experiments. Prototypes of key-technical detector components will be built, and worldwide infrastructure established for industrialization and manufacturing of the required components.

The CEPC is an important part of the world plan for high-energy particle physics research. It will support a comprehensive research program by scientists from all over the world and provide premiere educational opportunities for universities and research institutes in China and around the world. Physicists from many countries will work together to explore the science and technology frontiers, and to bring a new level of understanding of the fundamental nature of matter, energy and the universe.

Add more comment about internationalization and how to move from here?

References

[1] The ATLAS Collaboration, G. Aad et al., *Observation of a new particle in the search for the Standard Model Higgs boson with the ATLAS detector at the LHC*, Phys. Lett. B **716** (2012) 1–29, arXiv:1207.7214 [hep-ex].

[2] The CMS Collaboration, S. Chatrchyan et al., *Observation of a new boson at a mass of 125 GeV with the CMS experiment at the LHC*, Phys. Lett. **B716** (2012) 30–61, arXiv:1207.7235 [hep-ex].

[3] The CEPC-SPPC Study Group, *CEPC-SPPC Preliminary Conceptual Design Report, Volume II - Accelerator*, 2015. IHEP-CEPC-DR-2015-01, IHEP-AC-2015-01.

[4] CEPC project website. http://cepc.ihep.ac.cn.

CHAPTER 2

OVERVIEW OF THE PHYSICS CASE FOR CEPC

Lorem ipsum dolor sit amet, consectetuer adipiscing elit. Ut purus elit, vestibulum ut, placerat ac, adipiscing vitae, felis. Curabitur dictum gravida mauris. Nam arcu libero, nonummy eget, consectetuer id, vulputate a, magna. Donec vehicula augue eu neque. Pellentesque habitant morbi tristique senectus et netus et malesuada fames ac turpis egestas. Mauris ut leo. Cras viverra metus rhoncus sem. Nulla et lectus vestibulum urna fringilla ultrices. Phasellus eu tellus sit amet tortor gravida placerat. Integer sapien est, iaculis in, pretium quis, viverra ac, nunc. Praesent eget sem vel leo ultrices bibendum. Aenean faucibus. Morbi dolor nulla, malesuada eu, pulvinar at, mollis ac, nulla. Curabitur auctor semper nulla. Donec varius orci eget risus. Duis nibh mi, congue eu, accumsan eleifend, sagittis quis, diam. Duis eget orci sit amet orci dignissim rutrum.

Nam dui ligula, fringilla a, euismod sodales, sollicitudin vel, wisi. Morbi auctor lorem non justo. Nam lacus libero, pretium at, lobortis vitae, ultricies et, tellus. Donec aliquet, tortor sed accumsan bibendum, erat ligula aliquet magna, vitae ornare odio metus a mi. Morbi ac orci et nisl hendrerit mollis. Suspendisse ut massa. Cras nec ante. Pellentesque a nulla. Cum sociis natoque penatibus et magnis dis parturient montes, nascetur ridiculus mus. Aliquam tincidunt urna. Nulla ullamcorper vestibulum turpis. Pellentesque cursus luctus mauris.

This [1] is an example with plots, please edit ...

2.1 First theory subsection

Lorem ipsum dolor sit amet, consectetuer adipiscing elit. Ut purus elit, vestibulum ut, placerat ac, adipiscing vitae, felis. Curabitur dictum gravida mauris. Nam arcu libero, nonummy eget, consectetuer id, vulputate a, magna. Donec vehicula augue eu neque.

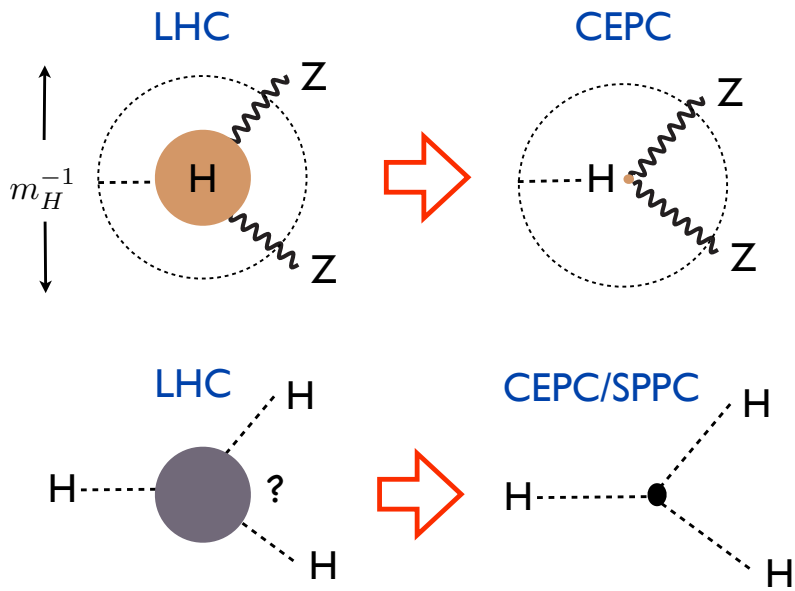

Figure 2.1: A sketch of two of the central goals of the CEPC and SPPC. The CEPC will probe whether the Higgs is truly "elementary", with a resolution up to a hundred times more powerful than the LHC. The SPPC will see, for the first time, a fundamentally new dynamical process — the self-interaction of an elementary particle — uniquely associated with the Higgs.

Pellentesque habitant morbi tristique senectus et netus et malesuada fames ac turpis egestas. Mauris ut leo. Cras viverra metus rhoncus sem. Nulla et lectus vestibulum urna fringilla ultrices. Phasellus eu tellus sit amet tortor gravida placerat. Integer sapien est, iaculis in, pretium quis, viverra ac, nunc. Praesent eget sem vel leo ultrices bibendum. Aenean faucibus. Morbi dolor nulla, malesuada eu, pulvinar at, mollis ac, nulla. Curabitur auctor semper nulla. Donec varius orci eget risus. Duis nibh mi, congue eu, accumsan eleifend, sagittis quis, diam. Duis eget orci sit amet orci dignissim rutrum.

Nam dui ligula, fringilla a, euismod sodales, sollicitudin vel, wisi. Morbi auctor lorem non justo. Nam lacus libero, pretium at, lobortis vitae, ultricies et, tellus. Donec aliquet, tortor sed accumsan bibendum, erat ligula aliquet magna, vitae ornare odio metus a mi. Morbi ac orci et nisl hendrerit mollis. Suspendisse ut massa. Cras nec ante. Pellentesque a nulla. Cum sociis natoque penatibus et magnis dis parturient montes, nascetur ridiculus mus. Aliquam tincidunt urna. Nulla ullamcorper vestibulum turpis. Pellentesque cursus luctus mauris.

References

[1] CEPC project website. http://cepc.ihep.ac.cn.

CHAPTER 3

CEPC EXPERIMENTAL CONDITIONS, PHYSICS REQUIREMENTS AND DETECTOR CONCEPTS

The CEPC physics program spans a wide range of center-of-mass energies and beam luminosities to achieve the highest yields of Z, W and Higgs bosons produced in the exceptionally clean environment of an $\mathrm{e^+e^-}$ collider. As described in Chapter 2, the CEPC data will provide new levels of high precision tests of the Standard Model and in the search for new physics. This chapter describes the design requirements for the CEPC detectors to achieve these physics goals, taking into account the CEPC collision environment and the related backgrounds. The CEPC precision physics program places stringent requirements on the detector performance. These include large and precisely defined solid angle coverage, precise track momentum resolution, high efficiency vertex reconstruction, precise photon energy reconstruction, excellent particle identification, excellent jet reconstruction and flavor tagging.

Three preliminary CEPC detector concepts are introduced in this chapter. They derive from detector concepts introduced for the International Linear Collider project, benefiting from a long period of prior development, and incorporate modifications motivated by the circular collider experimental environment and by the higher luminosity. Although the overall design and main building blocks of the three concepts are similar, the particular technology choices are different. The CEPC baseline detector is based on a 3 Tesla solenoid magnetic field and follows closely the International Large Detector (ILD) design. It is guided by particle flow principles and it includes an ultra high granularity calorimeter system and a Time Projection Chamber (TPC). An alternative proposal substitutes the TPC with a full-silicon tracker (FST). A third design based on a lower magnetic field of 2 Tesla, a drift chamber, and dual readout calorimetry is also presented. While the baseline concept detector is used for the physics performance studies in this Conceptual Design Report, the other two designs are considered fully valid alternatives. The final two CEPC

detectors are likely to be composed of the detector technologies included in any of these three concepts.

3.1 CEPC Experimental Conditions

The CEPC is an electron-positron collider with 100 km circumference and two interaction points (IP). The details of the full CEPC accelerator complex are described in the CDR Volume I [1]. The final stage of the CEPC complex is a double-ring collider. Electron and positron beams circulate in opposite directions in separate beam pipes. They collide at two interaction points (IPs) where are located large detectors, the specifications of which are presented in this volume.

The detectors must operate in three primary sets of conditions, corresponding to three different center-of-mass energies ($\sqrt{s}$): Higgs factory ($e^+e- \rightarrow ZH$) at $\sqrt{s} = 240$ GeV, Z boson factory ($e^+e- \rightarrow Z$) at $\sqrt{s} = 91.2$ GeV and W threshold scan ($e^+e- \rightarrow W^+W^-$) at $\sqrt{s} =\sim 160$ GeV. The instantaneous luminosities are expected to reach 3×10^{34}, 32×10^{34} and 10×10^{34} cm^{-2}s^{-1}, respectively, as shown in Table 3.1, and will remain relatively constant throughout operation through a process of full-energy top-up injection by the CEPC accelerator complex. The current tentative operation plan will allow the detectors to collect one million Higgs particles or more, close to one trillion Z boson events, and ten million W^+W^- event pairs.

The detector designs must comprehensively meet the requirements imposed by the CEPC experimental conditions and the physics program. Each of the beam conditions and corresponding detector implications are presented below.

3.1.1 The CEPC beam

The detectors will record collisions in beam conditions presented in Figure 3.1. Several of these parameters impose important constraints on the detectors. The bunch spacing of the colliding beams differ greatly in the three operational modes (25 ns, 210 ns, and 680 ns, respectively) as does the power dissipated into synchrotron radiation (16.5 MW for Z factory and 30 MW for W threshold scan and Higgs factory). Other important differences are also present in the expected beam backgrounds, described in more detail below, and, most importantly, in the event rates and types of events to be recorded, according to the cross sections shown in Figure 3.2 for different center-of-mass energies.

3.1.2 Beam backgrounds

Three most important sources of radiation backgrounds are evaluated for the CEPC:

1. synchrotron radiation photons from the last bending dipole magnet
2. e^+e^- pair production following the beamstrahlung process
3. off-energy beam particles lost in the interaction region

3.1.2.1 Synchrotron radiation

Synchrotron radiation (SR) photons are critical at circular machines. A large flux SR photons are generated in the last bending dipole magnets. They are then transported to the interaction region with the BDSim software [2]. They can hit the central beam pipe, either

	Higgs	*W*	*Z (3T)*	*Z (2T)*
Number of IPs	2			
Beam energy (GeV)	120	80	45.5	
Circumference (km)	100			
Synchrotron radiation loss/turn (GeV)	1.73	0.34	0.036	
Crossing angle at IP (mrad)	16.5×2			
Piwinski angle	2.58	7.0	23.8	
Number of particles/bunch N_e (10^{10})	15.0	12.0	8.0	
Bunch number	242	1524	12000 (10% gap)	
Bunch spacing (ns)	680	210	25	
Beam current (mA)	17.4	87.9	461.0	
Synchrotron radiation power (MW)	30	30	16.5	
Bending radius (km)	10.7			
Momentum compaction (10^{-5})	1.11			
β function at IP β_x^* / β_y^* (m)	0.36/0.0015	0.36/0.0015	0.2/0.0015	0.2/0.001
Emittance x/y (nm)	1.21/0.0031	0.54/0.0016	0.18/0.004	0.18/0.0016
Beam size at IP σ_x/σ_y (μm)	20.9/0.068	13.9/0.049	6.0/0.078	6.0/0.04
Beam-beam parameters ξ_x/ξ_y	0.031/0.109	0.013/0.106	0.004/0.056	0.004/0.072
RF voltage V_{RF} (GV)	2.17	0.47	0.10	
RF frequency f_{RF} (MHz)	650			
Harmonic number	216816			
Natural bunch length σ_z (mm)	2.72	2.98	2.42	
Bunch length σ_z (mm)	3.26	5.9	8.5	
Damping time $\tau_x/\tau_y/\tau_E$ (ms)	46.5/46.5/23.5	156.4/156.4/74.5	849.5/849.5/425.0	
Natural Chromaticity	-493/-1544	-493/-1544	-520/-1544	-520/-3067
Betatron tune ν_x/ν_y	363.10 / 365.22			
Synchrotron tune ν_s	0.065	0.0395	0.028	
HOM power/cavity(2cell) (kw)	0.54	0.75	1.94	
Natural energy spread (%)	0.1	0.066	0.038	
Energy acceptance requirement (%)	1.35	0.40	0.23	
Energy acceptance by RF (%)	2.06	1.47	1.70	
Photon number due to beamstrahlung	0.29	0.35	0.55	
Lifetime _simulation (min)	100			
Lifetime (hour)	0.67	1.4	4.0	2.1
F (hour glass)	0.89	0.94	0.99	
Luminosity/IP L (10^{34}cm^{-2}s^{-1})	3	10	17	32

Figure 3.1: Main beam parameters for the CEPC operation.

Operation mode	Z factory	W threshold scan	Higgs factory
$\sqrt{s}$/GeV	91.2	158 - 172	240
L/$10^{34}\mathrm{cm}^{-2}\mathrm{s}^{-1}$	16-32	10	3
Running time/year	2	1	7
Integrated Luminosity/ab^{-1}	8 - 16	2.5	5
Higgs yield	-	-	10^6
W yield	-	10^7	10^8
Z yield	10^{11-12}	10^9	10^9

Table 3.1: Instantaneous luminosities at different $\sqrt{s}$ and anticipated boson yields at the CEPC.

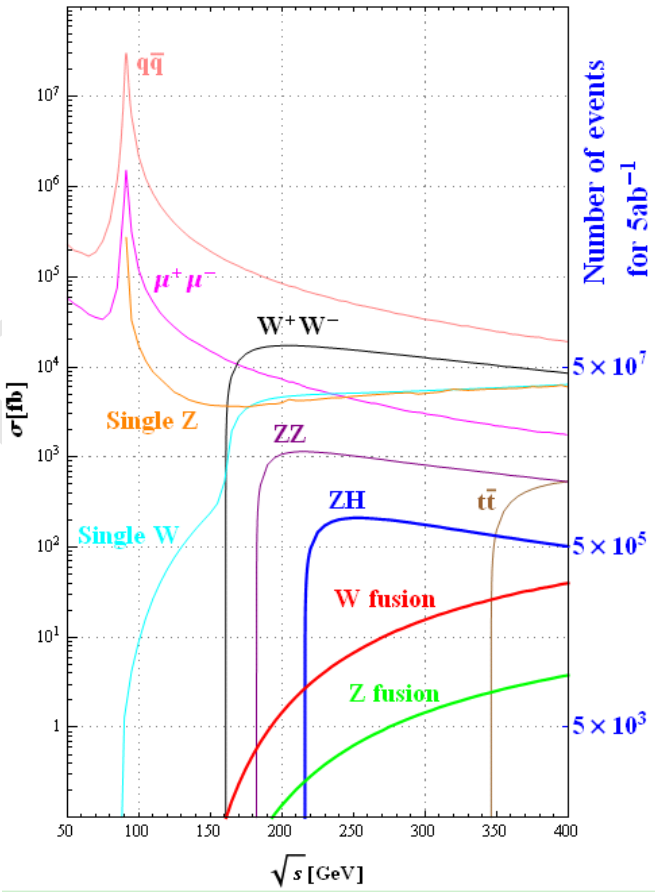

Figure 3.2: Cross sections of the leading Standard Model processes for unpolarized electron-positron collisions.

directly or after scattered by the beam pipe in the forward region. SR photons can also be generated in the final focusing magnets but contribute little to the detector backgrounds because they are produced with extremely small polar angles and can leave the interaction region without interacting in the beam pipe. To suppress the SR photons, three sets of mask tips made with high-Z material are introduced at $|z| = 1.51$, 1.93 and 4.2 m away from the interaction point. The studies prove that the masks can reduce effectively the number of SR photons hitting the central beam pipe, from almost 40,000 to below 80 from one of the two beams per bunch crossing. Further optimization may suppress SR photons even more and make this particular background well controlled.

3.1.2.2 Pair production

Electron-positron pairs are produced via the interaction of beamstrahlung photons with the strong electromagnetic fields of the colliding bunches. Pair production, in particular the incoherent pair production, represents the most important detector background at CEPC. The process is simulated with GUINEAPIG [3] and interfaced to GEANT4 [4–6] for detector simulation. Despite of the magnitude of beam squeezing being different in x and y directions, the hit distribution is almost uniform in the azimuthal (ϕ) direction. The resulting hit density at the first vertex detector layer ($r = 1.6$ cm) is about 2.2 hits/cm^2 per bunch crossing when running at $\sqrt{s} = 240$ GeV. The total ionizing energy (TID) and non-ionizing energy loss (NIEL) are 620 kRad/year and 1.2×10^{12} 1 MeV n_{eq}/cm$^2 \cdot$ year, respectively. For the background estimation, safety factors of ten are applied to cope with the uncertainties on the event generation and the detector simulation.

3.1.2.3 Off-energy beam particles

Beam particles after loosing a certain amount of energy, *i.e.* 1.5% of the nominal beam energy, can be kicked off their orbit. Such off-energy beam particles may hit machine and/or detector elements close to the interaction region and give rise to important backgrounds. The three main scattering process are radiative Bhabha scattering, beamstrahlung and beam-gas interaction. After the introduction of two sets of collimators upstream of the IPs, backgrounds due to beamstrahlung and beam-gas interaction become negligible. The residual backgrounds due to radiative Bhabha scattering yields hit densities of about 0.22 hits/cm^2 per bunch crossing when operating at $\sqrt{s} = 240$ GeV. The corresponding TID and NIEL are 310 kRad/year and 9.3×10^{11} 1 MeV n_{eq}/cm$^2 \cdot$ year, respectively.

3.1.2.4 Backgrounds at different energies

When operating the machine at the center-of-mass energy of $\sqrt{s} = 240$ GeV, the main detector backgrounds come from the pair-production and off-energy beam particles. At lower operational energies, *i.e.* $\sqrt{s} = 160$ GeV for W and $\sqrt{s} = 91$ GeV for Z, the background particles are usually produced with lower energies but with higher rates given the higher machine luminosities. The pair-production becomes dominant, while contributions from other sources tend to be negligible.

3.1.3 Beam polarization

Short statement about the beam polarization possibilities. Refer to accelerator CDR for more details. Clarify if this is longitudinal polarization or the LEP method of g-2 resonant depolarization of a transverse polarization for purposes of beam energy measurement.

3.2 Physics Requirements

As a tremendous Higgs, Z, and W boson factory, the CEPC should be equipped with detectors that can identify all the corresponding physics objects with high efficiency, high purity and measure them with high precision. In addition, the CEPC physics program requires a precise determination of the instant luminosity, a precise control and monitoring of the beam energy. Generally, the CEPC detector is required to:

1. Operate reliably at high efficiency in the CEPC collision environment. The detector should be fast enough to record all the physics events with excellent efficiency and meet the performance requirements throughout the CEPC operation, including being robust against beam backgrounds.

2. Provide highly hermetic coverage for physics events. The detector should provide a solid angle coverage of $|cos(\theta)| < 0.99$.

3. Accurately record the integrated luminosity. The luminosity should be measured to a relative accuracy of 0.1% for the Higgs factory operation, and 10^{-4} for the Z line shape scan.

4. The beam energy should be measured to an accuracy of the order of 1 MeV for the Higgs factory operation, and 100 keV for the Z pole and W mass threshold scan.

The requirements on the physics objects reconstruction are briefly quantified with benchmark physics analyses, see discussion below.

3.2.1 Multiplicity

In each physics event, the visible final state particles include the electrons, muons, charged hadrons, photons, and neutral hadrons. The multiplicities of these three basic ingredients, with the charged particles collectively described as tracks, are shown in Figure 3.3 for the WW, ZZ, and ZH processes (the leading SM processes) at the CEPC Higgs factory operation.

The charged tracks and the photons carry most of the visible energies and are much numerous than the neutral hadrons. They follow a similar distribution of multiplicity, which can be as high as $\mathcal{O}(10^2)$. These final state particles can have extremely small angles in between, especially for those generated in high energy jets. An efficient separation of these final state particles provides a solid basis for the reconstruction of all the physics objects, which is addressed explicitly by the Particle Flow Principle.

3.2.2 Tracking

The CEPC detector should have excellent track finding efficiency and track momentum resolution. Corresponding to the WW, ZZ and the ZH processes at the CEPC Higgs factory operation, the energy and polar angle distributions of the charged particles are shown in Figure 3.4.

In the polar angle distribution, the ZH process is almost flat in the polar angle direction, while the other two processes are more forward region dominated. A large solid angle

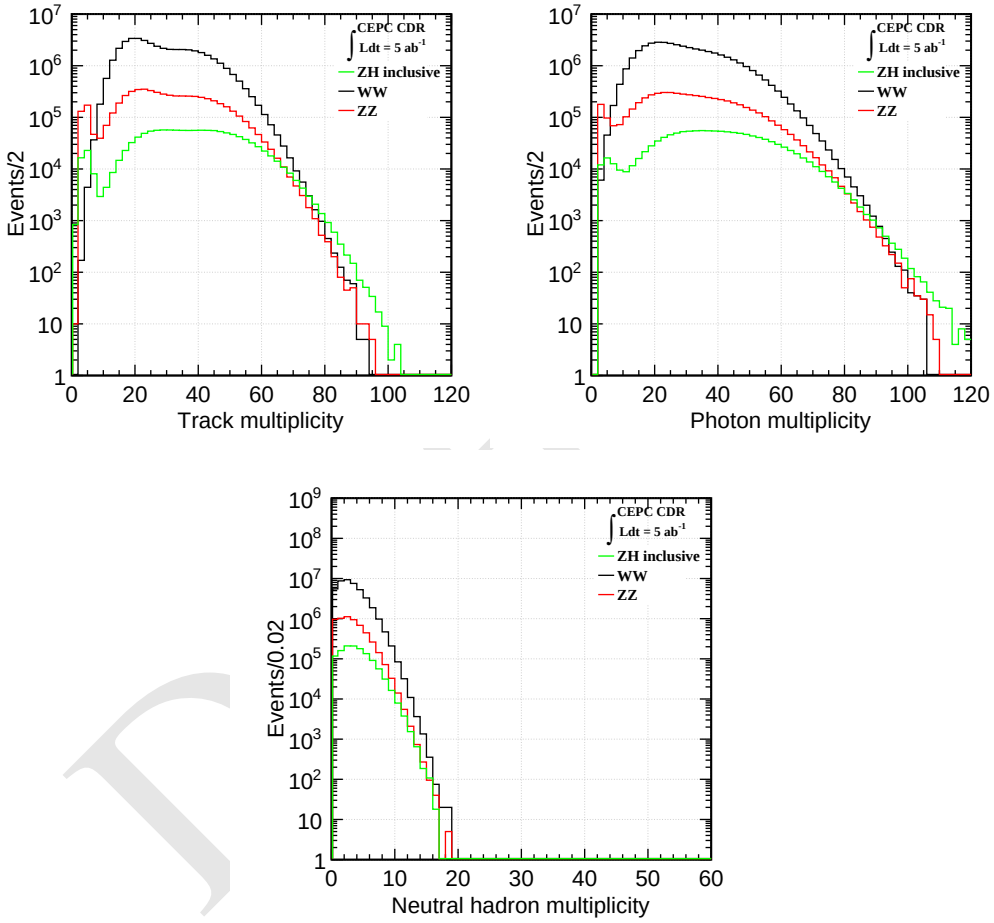

Figure 3.3: The multiplicities of charged particles, photons, and neutral hadrons from the leading physics processes at the CEPC Higgs factory operation, normalized to 5 ab^{-1} nominal integrated luminosity.

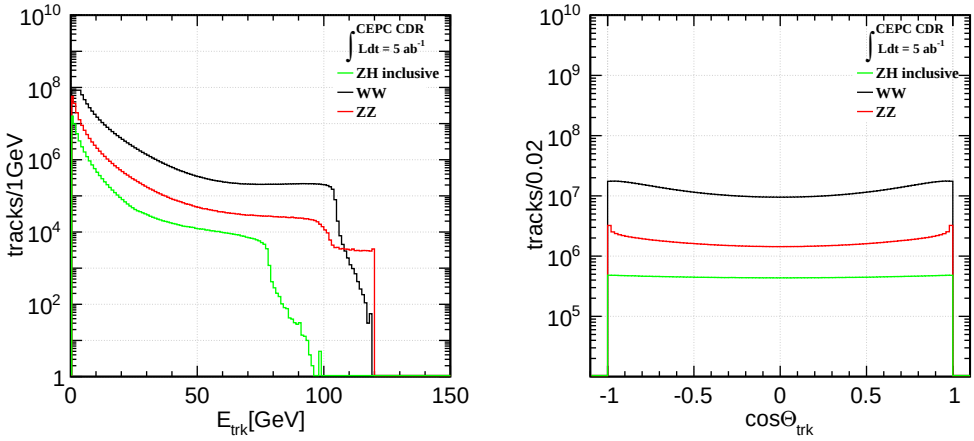

Figure 3.4: Energy and polar angle distributions of charged particles from the leading physics processes at the CEPC Higgs factory operation, normalized to 5 ab^{-1} nominal integrated luminosity.

coverage is essential to characterize and to distinguish different physics processes, and a coverage of $|cos(\theta)| = 0.99$ is benchmarked. In the energy distribution, these three processes share the same pattern. For energies below 20 GeV, these distributions follow an exponential distribution, while in the high energy side there is a flat plateau with a steep cliff. Therefore, the CEPC detector should have a high efficiency track reconstruction, especially for these low energy tracks. Meanwhile, it should have an excellent momentum resolution and linearity for a wide energy range (0.1 - 120 GeV).

For any tracks within the detector acceptance and a transverse momentum larger than 1 GeV, we request an track finding efficiency better than 99%. In order to measure the $H \to \mu^+\mu^-$ signal and to reconstruct precisely the Higgs boson mass from the recoil mass distribution at l^+l^-H events, the momentum resolution is required to achieve a per mille level relative accuracy.

3.2.3 Charged Leptons

The charged lepton is one of the most important physics signatures and it plays a crucial role in the classification of different physics events. A high efficiency and high purity charged lepton identification is fundamental for the CEPC physics program.

At the CEPC Higgs factory operation, roughly 7% of the Higgs bosons are generated with a pair of charged leptons. These l^+l^-H samples are the golden signal for the Higgs recoil mass analyses. Figure 3.5 shows the energy distribution of the prompt leptons and these generated in Higgs decay cascade. The prompt muons in $\mu^+\mu^-H$ events have a flat energy distribution within the kinematic range (20 - 100 GeV) and a low energy tail induced by the Z boson width and final state radiation (FSR). The prompt electron-positron pair in e^+e^-H events follows a similar pattern, except the population increases at energy smaller than 10 GeV.

The Higgs decay also generates leptons, which is mostly concentrated in the low energy side, but can have energies as high as 70 GeV. These high energy leptons are mainly generated from $H \to \tau^+\tau^-, ZZ^*, WW^*$ decay cascades.

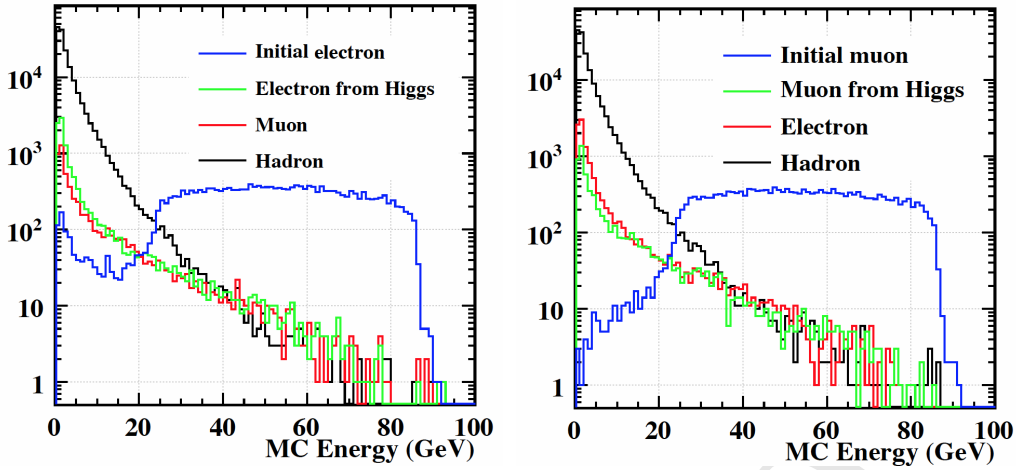

Figure 3.5: Energy spectrum of the leptons and the charged hadrons in the e^+e^-H events (left) and the $\mu^+\mu^-H$ events (right).

The basic requirements on the lepton identification for the CEPC detector is, to identify the prompt charged leptons with high efficiency and high purity. Therefore, we require a lepton identification with efficiency higher than 99% and misidentification rate smaller than 2% for energetic isolated leptons (energetic means energy higher than 5 GeV). These requirements are also essential for the identification of $H \to \tau^+\tau^-$ events and the semi-leptonic/leptonic decays modes of $H \to ZZ^*, WW^*$ events.

The charged leptons produced in the numerous jets generated in the Higgs decay cascades can be crucial for the jet flavor tagging and jet charge reconstruction. Therefore, a good identification of leptons in jets is highly advantageous. More detailed study is needed to quantify the requirements on the lepton-in-jet identification.

3.2.4 Charged hadron identification

The particle identification, especially the identification of charged kaons, is crucial for the flavor physics. Similar to the jet leptons, the identification of charged kaon is highly appreciated for the jet flavor tagging and jet charge reconstruction. Typically, we request the efficiency and purity of the kaon identification at the inclusive Z pole sample to be better than 90%.

3.2.5 Photons

The photons are crucial for the jet energy resolution, the $H \to \gamma\gamma$ branching ratio measurements, radiative processes and the physics with τ final states. Figure 3.6 shows the energy and polar angle distributions for the inclusive photons, and the ISR photons in Figure 3.7, from these benchmark physics processes at the CEPC Higgs factory operation.

As for the photon reconstruction, we request a photon identification efficiency higher than 99% and a misidentification rate smaller than 5%, for unconverted, isolated photons with energy higher than 1 GeV. To observe at least 50% of di-photon resonances with a pair of unconverted photons, the material budget in front of the calorimeter should be less than 0.35 X_0 averaged over all solid angle. To identify the τ leptons with different decay modes, the photons should be identified from the π^0 with an efficiency and purity

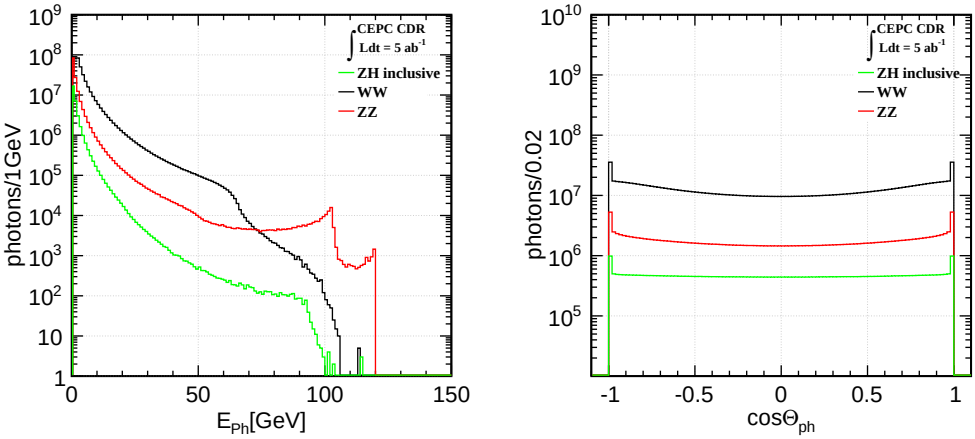

Figure 3.6: Energy and polar angle distributions of all photons from the leading physics processes at the CEPC Higgs factory operation.

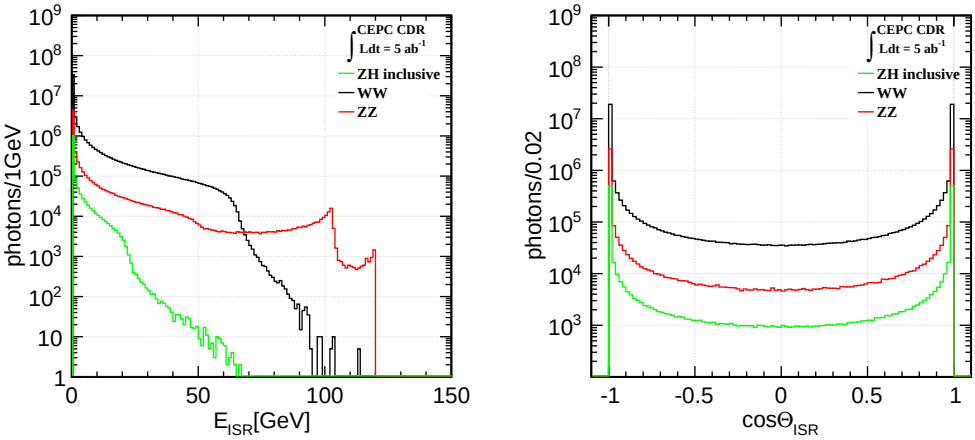

Figure 3.7: Energy and polar angle distributions of ISR photons from the leading physics processes at the CEPC Higgs factory operation.

higher than 95% from the $Z \rightarrow \tau^+\tau^-$ event sample at CEPC Z factory operation. To fully exploit the hadronic decays of the Z, W, and Higgs bosons, the requirements on the jet energy resolution, described in the next section, impose a photon energy resolution requirement of better than $20\%/\sqrt{E} \oplus 1\%$. This photon energy resolution requirement for jets is sufficient to meet the needs of the $g(H\gamma\gamma)$ measurement at CEPC due to the low background environment for the di-photon final state. Further evaluation of photon energy resolution requirements for radiative processes need to be carefully studied.

3.2.6 Jets and Missing energy

The reconstruction of jets is essential for the CEPC physics program, since the majority of W, Z, and Higgs bosons decay into hadronic final states. Jets are measured with particles that interact with the full range of sub-detector systems. The Particle Flow principle and corresponding particle flow algorithms (PFA), based upon it, are an overarching approach to reconstructing and interpreting measurements into a form that identifies and optimally measures the properties and kinematic quantities of all individual final state particles produced in the high-energy collision. For Particle Flow oriented detectors, the jet is constructed from a list of final state particles produced by the PFA. Therefore, the jet reconstruction is determined by the reconstruction of final state particles and the jet clustering algorithm. Consequently, the jet reconstruction performance should be evaluated at two stages.

The first is the Boson Mass Resolution (BMR) for massive SM bosons. The boson mass resolution represents the jet energy resolution with perfect jet clustering, or more accurately, a perfect identification of the color singlet. The BMR is defined as the relative resolution of the visible mass on the $v\bar{v}H, H \rightarrow gluons$ events with a standard cleaning procedure. The cleaning procedure has a typical efficiency of 65%, it vetos the events with energetic visible ISR photon(s), energetic neutrinos generated in the Higgs decay, and jets pointing to the very forward regions. Since the width of the SM Higgs boson (4 MeV) is negligible comparing to the jet energy resolution (GeV), BMR is equivalently the Higgs mass resolution with cleaned $v\bar{v}H, H \rightarrow gluons$ event sample.

Figure 3.8 shows the reconstructed H, W, Z boson masses with different BMR. In order to distinguish the W, Z, and the Higgs boson from their hadronic decay final state, a boson mass resolution better than 4% is required. It should be remarked that an efficient separation of individual W, Z, and Higgs boson is a prerequisite for a clear separation of WW, ZZ, and ZH events in the 4-jet final states, since the latter strongly depends on the jet clustering performance.

The missing energy measurement with jet final states can also be characterized by the BMR. The physics benchmark for the missing energy-momentum measurement is the $Br(H \rightarrow invisible)$ measurement with $q\bar{q}H$ final states. The signal has a Higgs mass peak in the missing mass spectrum. The dominant SM background, the $ZZ \rightarrow v\bar{v}q\bar{q}$ process, exhibits a peak at the Z boson mass. Meanwhile, because the initial state radiation and the heavy flavor component of the $Z \rightarrow q\bar{q}$ decay, both missing mass distributions exhibit a high mass tail. The missing mass distributions at different BMR are displayed in Figure 3.9. At a BMS worse than 4%, the Z recoil mass peak of the background becomes so wide that it starts to overlap with the Higgs mass peak. Therefore, for this benchmark, a boson mass resolution better than 4% is certainly advantageous.

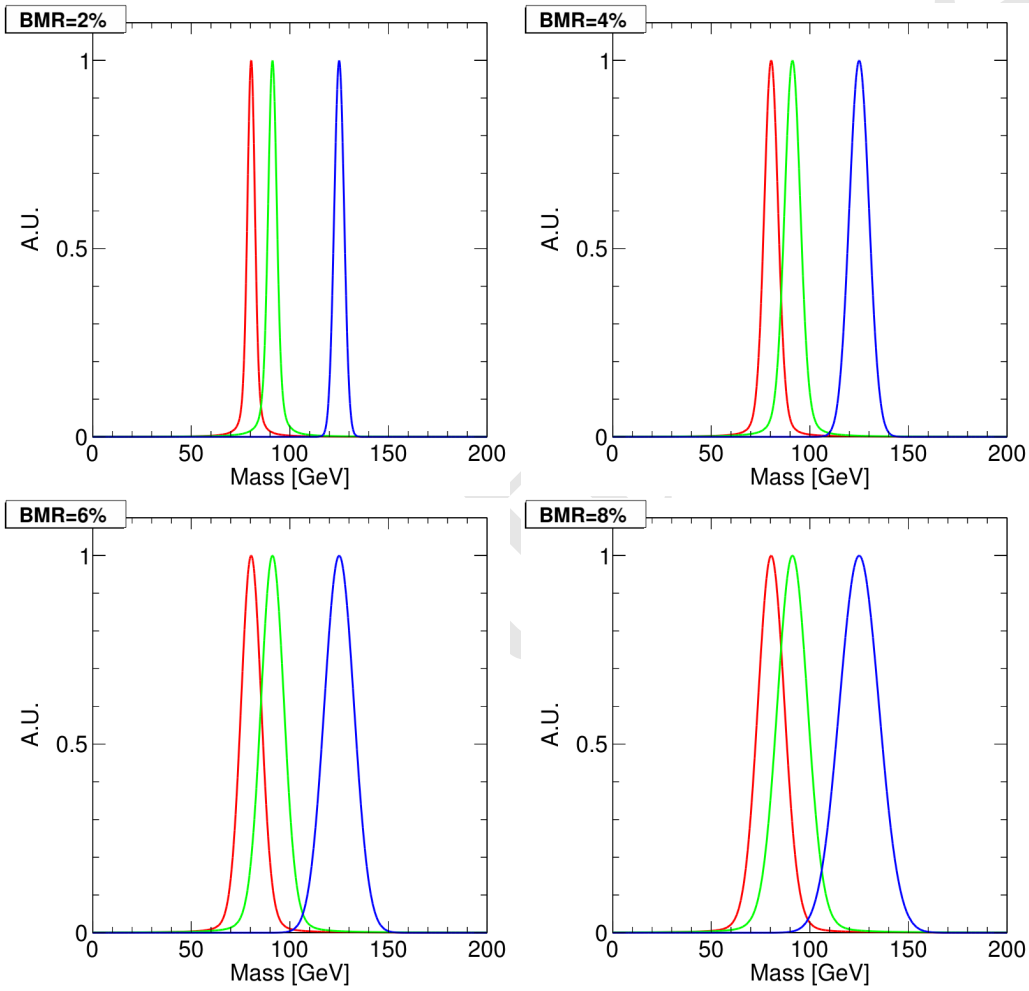

Figure 3.8: Invariant mass distributions of H, W, and Z bosons for different boson mass resolutions. Normalized to unit height.

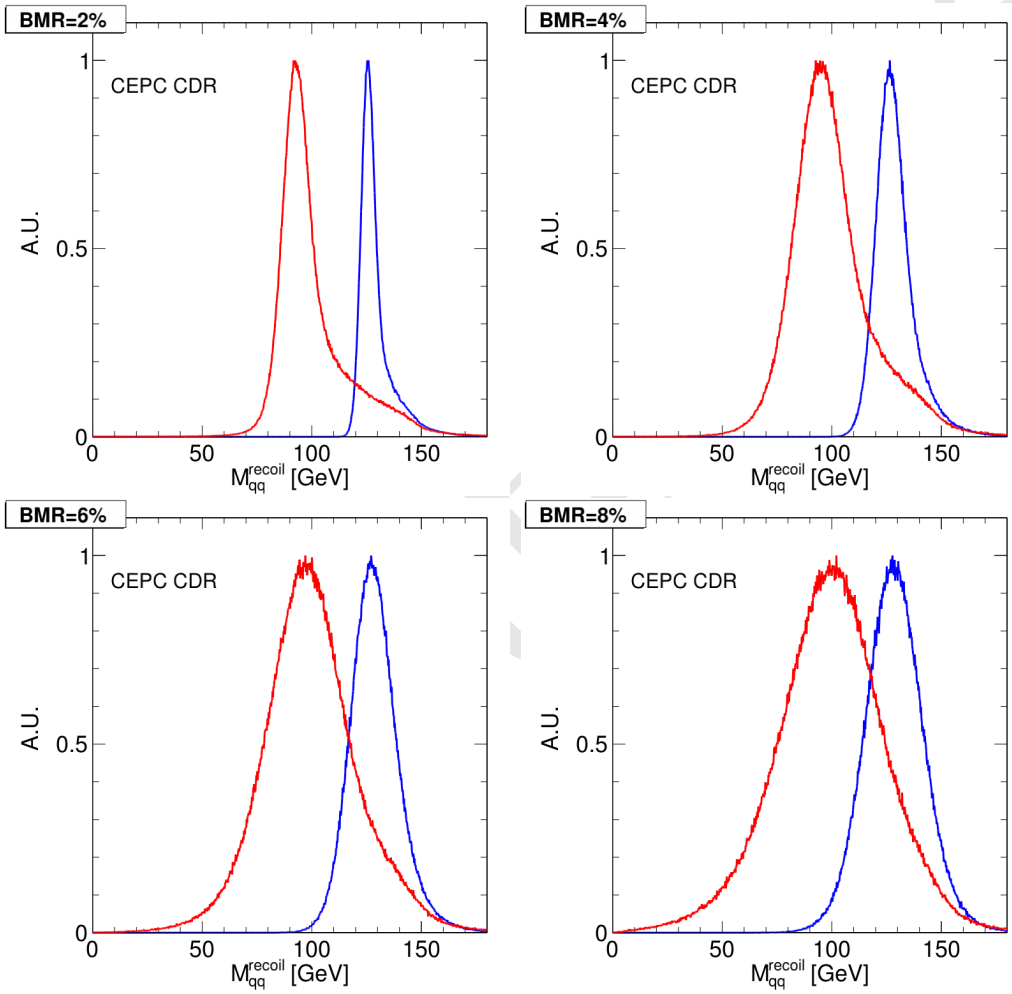

Figure 3.9: Recoil mass distribution of $ZZ \to \nu\bar{\nu}q\bar{q}$ events and ZH events with Z decays into a pair of quarks and the Higgs decaying invisibly.

The identification of individual jets, and its energy-momentum reconstruction is crucial for the CEPC physics measurements. The individual jet energy response is highly depending on the event topology and the jet clustering algorithms. Detailed analyses are required to disentangle the actual physics requirement, which need to be analyzed carefully.

3.2.7 Flavor Tagging

One of the key physics objectives of the CEPC Higgs program is to measure the $g(Hcc)$ coupling. The CEPC detector is therefore required to efficiently distinguish the b-jets, the c-jets, and the light jets from each other. High performance flavor tagging is also highly advantageous in EW precision measurements.

Benchmarked with the $Z \rightarrow q\bar{q}$ sample at 91.2 GeV c.m.s, we require the b-jets to be identified with a efficiency and purity higher than 80%, and a c-jet identification efficiency/purity better than 60%.

The classification of different kinds of jets depends strongly on the reconstruction of secondary vertex, where the performance of the vertex system is crucial. The clean collision environment of the CEPC allows much aggressive vertex system design, a detailed vertex optimization study can be found in Section 4.1.3.

3.2.8 Requirements on the physics objects: summary

The discussion above quantifies the physics requirements on the physics object reconstruction. It can be summarized as:

1. Tracking performance: For tracks with transverse momentum greater than 1 GeV that are within the detector acceptance, a reconstruction efficiency of better than 99% is required. The relative resolution of the track momentum should achieve per mille level accuracy, required by the measurements of $g(H\mu^+\mu^-)$ and the Higgs recoil mass analyses with l^+l^-H events.

2. Excellent lepton identification. For isolated leptons with a momentum larger than 5 GeV, we request an identification efficiency of 99% and accumulated misidentification rate smaller than 2%. The leptons inside the jets also need to be identified well, as they provide information on the jet flavor and jet charge.

3. Capability to identify charged kaons, which enhances the rich flavor physics program at CEPC Z factory operation. For the inclusive $Z \rightarrow q\bar{q}$ sample at 91.2 GeV c.m.s, we request a charged kaon identification with efficiency and purity to be both higher than 90%.

4. Precise reconstruction of photons. Required by the $g(H\gamma\gamma)$ measurement and the jet energy reconstruction, the photon energy should be measured to a precision better than $20\%/\sqrt{E}\oplus 1\%$. Meanwhile, to identify the τ leptons with different decay modes, the photons should be identified from the π^0 with an efficiency and purity higher than 95% in the $Z \rightarrow \tau^+\tau^-$ event sample at CEPC Z factory operation.

5. Excellent Jet/Missing Energy reconstruction. The jet/missing energy reconstruction is essential for the CEPC since most of the physics events are generated with

one or more of these physics objects. To avoid the complication from jet clustering performance, we characterize the jet and missing energy reconstruction with Boson Mass Resolution. Benchmarked with the separation of massive SM bosons (W, Z, and Higgs boson) and the $Br(H \rightarrow invisible)$ measurements, a BMR better than 4% is identified.

6. Capability to separate b-jets, c-jets and light jets (uds and gluon jets): required by the $g(Hb\bar{b})$, the $g(Hc\bar{c})$, the $g(Hgg)$, and the EW measurements. Benchmarked with the $Z \rightarrow q\bar{q}$ sample at 91.2 GeV c.m.s, we require the b-jets to be identified with an efficiency and purity higher than 80%, and a c-jet identification efficiency/purity better than 60%.

Most of the above-mentioned requirements are driven by the precision Higgs measurements. However, it also applies to the precise EW measurements as the W and Z bosons decay into similar physics objects.

3.3 Detector concepts

To address the physics requirements at the CEPC, two(three) different detector concepts are proposed.

The first (two) detector concept(s) is (are) guided by the Particle Flow Principle. The Particle Flow principle interprets all the detector signals as originataing from final state particles. For each physics event, all the physics objects are reconstructed from an unique list of final state particles. The single particle level physics objects, for example the leptons, the photons, and the kaons, are identified directly from the final state particle list. The composite physics objects, for example the converted photons, the K_s^0, the τ lepton and the jets, are identified using dedicated finding algorithms such as the τ finder and jet clustering algorithms. Subtracting the total visible four-momentum of all the final state particles from the initial four momentum determines the missing four-momentum. This global interpretation of the final state particles leads to high efficiency and high purity reconstruction of all the physics objects. In addition, the Particle Flow algorithm in principle associates the detector hits to each individual particle, therefore, the final state particle could be measured in the most-suited sub-detector system. For the charged particles, the relative accuracy of track momentum resolution from the tracking system is usually much better than the energy resolution from the calorimeter system. Therefore, the Particle Flow algorithm also significantly improves the accuracies on the energy reconstruction of composite objects, especially for the τ lepton and the jets.

The baseline detector geometry is named APODIS, which stands for A Particle Flow Oriented Detector for the HIggS factory. It was initially developed from the concept of International Large Detector (ILD, the baseline detector for the linear colliders). It is optimized for the CEPC collision environments, and enhances the particle identification performance which is essential for flavor physics. The APODIS uses an ultra high granularity calorimeter system to efficiently separate the final state particle showers, low material tracking system to limit the probability of interaction of final state particles in the tracking material, and a large volume solenoid that hosts the entire ECAL and HCAL inside. There are two options for its tracking system, the time-projection chamber (TPC) and the full silicon tracking (FST).

Concept	ILD	APODIS	IDEA
Tracker	TPC/Silicon	TPC/Silicon	Drift Chamber/Silicon
Solenoid B-Field (T)	3.5	3	2
Solenoid Inner Radius (m)	3.4	3.2	2.1
Solenoid Length (m)	8.0	7.8	6.0
L* (m)	3.5	2.2	2.2
VTX Inner Radius (mm)	16	16	16
Tracker Outer Radius (m)	1.81	1.81	2.05
Pairs of forward tracking disks	7	5	5
Calorimeter	PFA	PFA	Dual readout
Calorimeter λ_I	6.6	5.6	7.5
ECAL Cell Size (mm)	5	10	-
ECAL Time resolution (ns)	-	200 ps/hit	-
ECAL X_0	24	24	-
HCAL Layer Number	48	40	-
HCAL Absorber	Fe	Fe	-
HCAL λ_I	. 5.9	4.9	-
DRCAL Cell Size (mm)	-	-	6.0
DRCAL Time resolution (ns)	-	-	100 ps/hit
DRCAL Absorber	-	-	Pb or Cu or Fe
Overall Height (m)	14.0	11.4	11.0
Overall Length (m)	13.2	11.1	13.0

Table 3.2: Comparison of detector parameters. Do we need the number of forward tracking disks? We would need to mention the barrel silicon as well. The tracker outer radius needs to include the last silicon layer. Check absorbers.

An alternative detector geometry, IDEA, is also proposed. IDEA uses a dual readout calorimeter to achieve excellent energy resolution for both electromagnetic and hadronic showers. Comparing to APODIS, IDEA uses a lower field solenoid but compensates with a large tracking volume. The IDEA is also used as a reference detector for FCC-ee studies.

The main detector parameters of both concepts are summarized in Table 3.2.

3.3.1 The baseline detector concept

From inner to outer, as shown in Figure 3.10, the baseline geometry is composed of a silicon pixel vertex system, a silicon internal tracker, a TPC main tracker, a Silicon-tungsten sampling ECAL, an Iron-Glass Resistive Plate Chamber HCAL, a solenoid, and a return yoke.

The baseline geometry has a dedicated design in the forward region and machine-detector interface (MDI). The L* of the baseline geometry has a length of 2.2 meters,

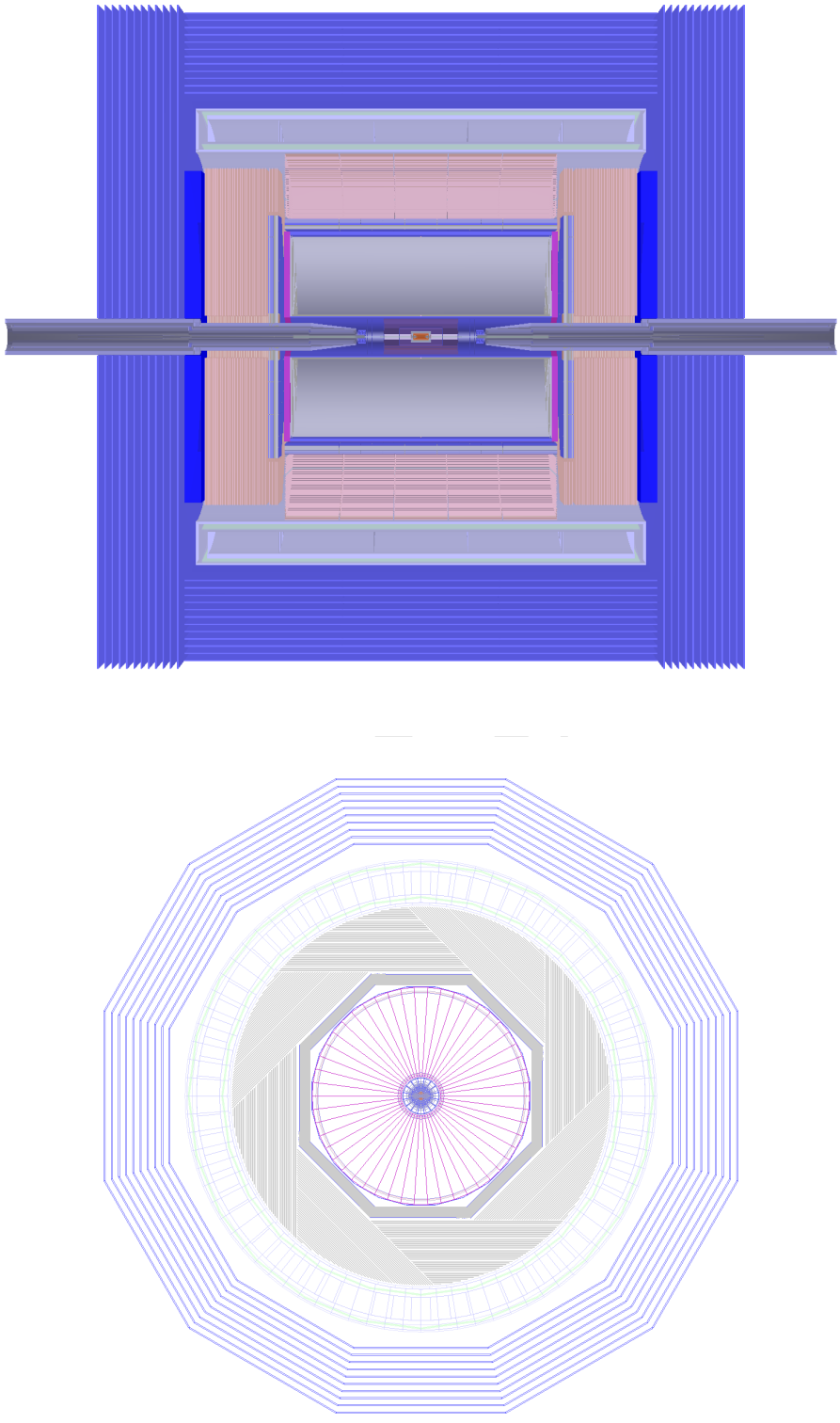

Figure 3.10: The RZ and R-ϕ view of the baseline detector geometry. The baseline geometry uses a double beam with 33 mrad crossing angle, and has a short L* of 2.2 meter. In the central Barrel, from inner to outer, the baseline geometry is composed of a Vertex system, a Silicon Inner Tracker, a TPC, a Silicon External Tracker, an ECAL, an HCAL, a Solenoid of 3 Tesla and a Return Yoke. In the forward region, 5 pairs of tracking disks are installed to enlarge the detector acceptance.

and a compensation solenoid system is installed at a z position of 1100 - 6000 mm. A luminosity calorimeter (LumiCal) is installed at the end of this nose structure. A compact, forward tracking system composed of 5 pairs of tracking disks is installed in between a z position of 200 - 1000 mm.

The solenoid B-Field of the baseline is 3 Tesla. The CEPC uses a double ring configuration, with a crossing angle of 33 mrad at the interaction point. Each time the bunch passing through the detector, the beam emittance increases via the coupling to the detector solenoid B-Field (especially the vertical emittance). In order to achieve a high luminosity, this solenoid B-Field needs to be compensated locally. Therefore, a compensating solenoid is installed in the forward region of the CEPC detector. Considering the technology challenge of the compensating solenoid and the physics requirements at the CEPC, the baseline geometry uses a solenoid of 3 Tesla for CEPC Higgs factory operation, and the central solenoid may be ramped down to 2 Tesla for CEPC Z factory operation.

The baseline geometry uses the Time Projection Chamber (TPC) as its main tracker. The TPC provides good energy resolution, excellent track reconstruction efficiency, low material budgets, and its $\mathrm{dE/dx}$ measurement is important for particle identification, see Section 10.2.7. On the other hand, compared to the silicon tracking, the TPC is a slow technology: the drift time of ions is of the order of one second in the APODIS TPC. In the TPC, both primary ionization of charged tracks and ion backflow from the amplification procedure generates ions, which accumulate in the gas volume. These ions will distort the drift electric field and eventually limit the precision of track momentum measurement. The physics event rate at the CEPC Z factory operation is of the order of 10^{3-4} Hz. Therefore, ions generated from thousands of events pile up in the gas volume. The control of backflow ion is then essential for the TPC operation.

Iterated with the hardware R&D, dedicated simulation studies are performed in the CEPC TPC study. Using a double amplification layer, the ion backflow could be controlled to per mille level without gating [7]. On the other hand, the simulation analysis shows that at this level of ion backflow control, the degrading of spatial point resolution is smaller than the intrinsic TPC spatial resolution. The TPC occupancy is also analyzed at the CEPC Z factory. Those studies lead to the conclusion that the TPC is a feasible technology option for the CEPC [8].

The TPC in the baseline has an inner radius of 0.3 meters, an outer radius of 1.8 meters, and a length of 4.7 meters. It is divided into 220 radial layers, each has a thickness of 6 mm. Along the ϕ direction, each layer is segmented into 1 mm wide cells. In total, the TPC has 1 million readout channels in each endcap. Operating in 3 Tesla solenoid B-Field, the TPC provides a spatial resolution of 100 μm in the $R-\phi$ plane and 500 μm resolution in the Z direction for each tracker hit. The TPC reaches a standalone momentum resolution of $\delta(1/P_t) \sim 10^{-4}\mathrm{GeV}^{-1}$.

The baseline is equipped with large-area silicon tracking devices, including the pixel vertex system, the forward tracking system, and the silicon inner/external tracking layers located at the boundary of the TPC. Combining the measurements from the silicon tracking system and the TPC, the track momentum resolution could be improved to $\delta(1/P_t) \sim 2 \times 10^{-5}\mathrm{GeV}^{-1}$. In fact, the TPC is mainly responsible for the pattern recognition and track finding, while the silicon tracking devices dominate the momentum measurement. The silicon pixel vertex system also provides precise impact parameter resolution ($\sim 5\mu\mathrm{m}$), which is highly advantageous for the τ lepton reconstruction and the jet flavor tagging.

The baseline geometry uses a high granular sampling Electromagnetic Calorimeter (ECAL) and Hadronic Calorimeter (HCAL). The calorimeter is responsible for separating final state particle showers, measuring the neutral particle energy, and providing information for the lepton identification [9][10]. The entire ECAL and HCAL are installed inside the solenoid, providing 3-dimensional spatial position and the energy information. The ECAL geometry parameter is determined by a dedicated optimization study [11]. The ECAL is composed of 30 layers of alternating silicon sensors and tungsten absorber. It has a total absorber thickness of 84 mm. Transversely, each sensor layer is segmented into 10 mm by 10 mm cells. The HCAL uses Resistive Plate Chamber sensor and Iron absorber. It has 40 longitudinal layers, each consists of a 25 mm Iron absorber. Transversely, it is segmented into 10 mm by 10 mm cells.

This calorimeter system provides good energy measurement for the neutral particles (i.e. roughly $16\%/\sqrt{E/\mathrm{GeV}}$ for the photons and $60\%/\sqrt{E/\mathrm{GeV}}$ for the neutral hadrons). More importantly, it records enormous information of the shower spatial development, ensuring efficient separation between nearby showers and providing essential information for the lepton identification, see Section 10.2.1. In addition, the silicon-tungsten ECAL could provide precise time measurements. Requesting a cluster level time resolution of 50 ps, the ECAL Time-of-Flight (ToF) measurement plays a complementary role to the TPC $\mathrm{dE/dx}$ measurement, leading to good charged Kaon identification performance, see Section 10.2.7.

As will be introduced in the following chapter, the baseline geometry maintains the same performance for the CEPC Higgs measurements comparing to the ILD. Meanwhile, the total cost, the total weight, and the calorimeter thickness have been significantly optimized (by 25%, 50% and 20% respectively). In addition, the baseline geometry has good performance for charged kaon identification, which is highly advantageous for flavor physics and in the jet flavor/charge reconstruction.

3.3.2 Full silicon detector concept

Silicon detectors provide at present the most precise tracking for charged particles in high energy physics experiments. They have an excellent space point resolution and granularity to cope track separation in dense jets and hits from the high luminosity beam related background. A full-silicon tracker (FST) would offer a competitive choice of detector concepts for CEPC that provides excellent tracking efficiency, momenta resolution, and vertexing capability for charged particles from the interaction point as well as from the decay of secondary particles. The challenge is to build it with minimal material to preserve the momentum resolution and being covered hermetically down to the dip angle of $|cos\theta| < 0.992$ from the beam pipe.

Here we will demonstrate that the full-silicon tracking concept is a viable option for CEPC by replacing the TPC with additional silicon stereo-strip layers while keeping the rest of detector unchanged under the same detector boundary conditions used by the CEPC baseline concept described above. We so far have not changed the detector boundary conditions such as the B field and the track volume in order to provide a cost-optimized detector since the performance may not matter. However, within these boundary conditions, we have optimized the layout with the number of silicon layers, single- versus double-sided layers, and support materials using a toy simulation. This concept option is described below in Section 4.3.

Two approaches are considered for the design: the first is to keep the silicon detectors (VXD, SIT, FTD) in the CEPC baseline detector and replacing TPC with additional silicon detectors , as shown in Figure 3.11 for 3D view of a full and zoomed detector; the second is to optimize the ILC-SID tracker to fulfil the CEPC tracking volume in order to achive the excellent momentum resolution using 3 Tesla B field. The new detector geometry has been implemented in the simulation and the track reconstruction has also been adoped for the full silicon tracker. The initial study of the tracking performance looks promising. There are still many improvements needed in the simulation and reconstruction in order to explore the full potential of the full-silicon tracker.

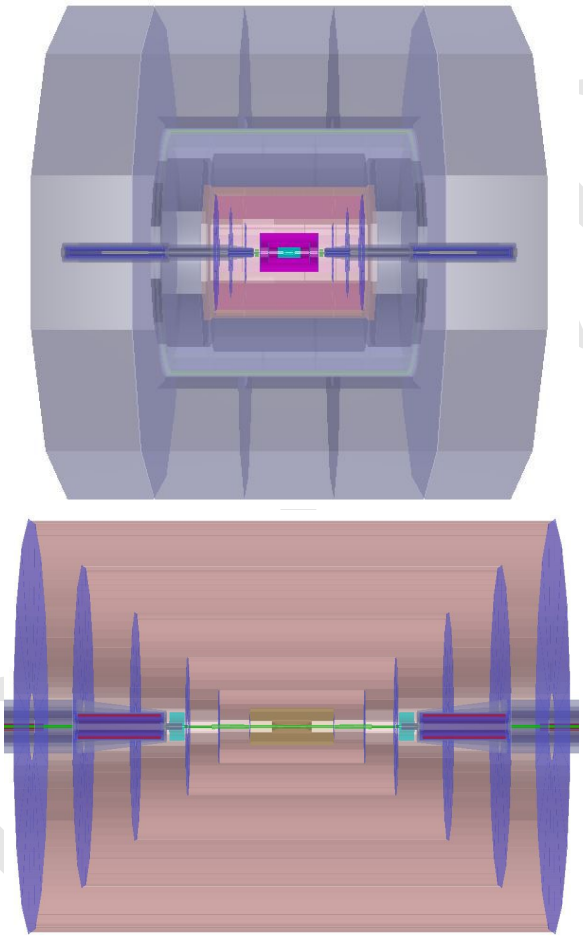

Figure 3.11: Schematic 3-D view of the FST detector and the zoomed full-silicon tracker.

3.3.3 An alternative low magnetic field detector concept

The baseline detector described in this CDR is a very straightforward evolution of the ILD detector originally conceived for the International Linear Collider (ILC) [12]. We propose here a new detector concept, IDEA (Innovative Detector for Electron-positron Accelerator), that is specifically designed for a circular electron-positron collider and also attempts to economize on the overall cost of the detector.

While most detector requirements needed for detectors at ILC are very similar to those for CEPC [13], there are however some notable differences. First of all the typical lumi-

nosity expected both at the Z pole ($\sqrt{s} = 90\,\mathrm{GeV}$) and above the ZH threshold ($\sqrt{s} = 240\,\mathrm{GeV}$) is expected to be one or two orders of magnitude larger, with a much shorter bunch spacing and no large time gaps in the beam structure. This places severe constraints on the tracking system. In particular one would prefer an intrinsically fast main tracker to fully exploit the cleanliness of the e^+e^- environment while integrating as little background as possible, and a very low-power vertex detector, since power pulsing is not allowed by the bunch spacing. Additional issues of emittance preservation, typical of circular machines, set limits on the maximum magnetic field usable for the tracker solenoid, especially when running at lower center-of-mass energies. This could be a problem for a large volume TPC, due to the resolution degradation, and also for a silicon tracker, since it would require more layers at a large radius, thus significantly increasing the cost.

Additional specific requirements on a detector for CEPC come from precision physics at the Z pole, where the statistical accuracy on various electroweak parameters is expected to be over an order of magnitude better than at the ILC. This calls for a very tight control of the systematic error on the acceptance, with a definition of the acceptance boundaries at the level of a few μm, and a very good $e - \gamma - \pi_0$ discrimination to identify τ leptons efficiently and measure their polarization. A layer of silicon microstrip detectors around the main tracker can provide the needed acceptance control for charged tracks, while also improving the tracking resolution. Similarly, the acceptance accuracy and improved identification efficiency of γ's can be obtained with a pre-shower based on micro-pattern gas detectors (MPGD) located just outside the detector magnet, which serves as a radiator.

The particle flow calorimeters, currently proposed for both ILC and CLIC, feature an extremely large number of readout channels and require significant data processing to obtain the optimal performance. A less expensive and more effective calorimeter can be made using the dual readout technique [14], which has been extensively studied and demonstrated in over ten years of R&D by the DREAM/RD52 collaboration [15, 16]. With this technology the electromagnetic and hadronic calorimeters come in a single package that plays both functions and allows an excellent discrimination between hadronic and electromagnetic showers [17]. Since all the readout electronics is located in the back of the calorimeter, its cooling is greatly simplified relative to the case of particle flow calorimeters.

Finally recent developments in micro-pattern gas detector technology, such as μRwell [18], can significantly reduce the cost of large area tracking chambers to be used for tracking muons outside the calorimeter volume.

The IDEA detector The structure of the IDEA detector is outlined in Figure 3.12, which also shows its overall dimensions.

A key element of IDEA is a thin, ∼30 cm, and low mass, $\sim 0.8\,X_0$, solenoid with a magnetic field of 2 Tesla. This field is optimal, according to studies done for FCC-ee, as it minimizes the impact on emittance growth and allows for manageable fields in the compensating solenoids [19], but it is certainly not optimal for a large TPC or a silicon tracker of reasonable size. The low mass and thickness of the solenoid allows it to be located between the calorimeter and the tracking volume without a significant performance loss.

The innermost detector, surrounding the 1.5 cm radius beam pipe, is a silicon pixel detector for the precise determination of the impact parameter of charged particle tracks. Recent test beam results on the detectors planned for the ALICE inner tracker system

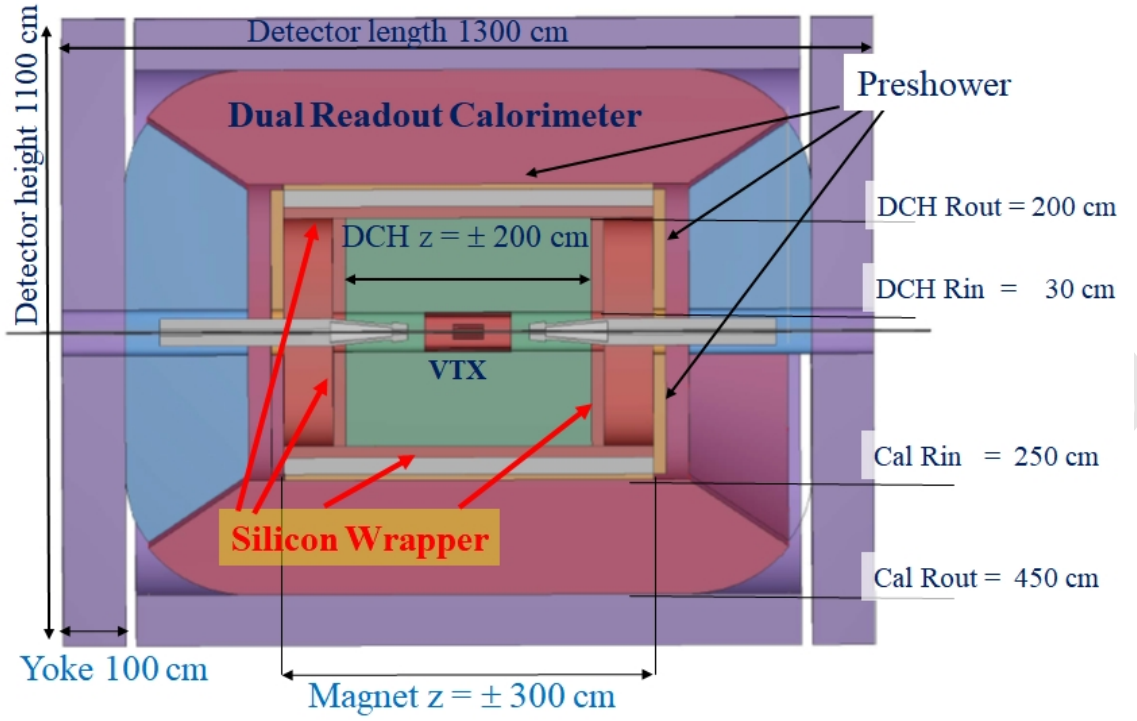

Figure 3.12: Schematic layout of the IDEA detector.

(ITS) upgrade, based on the ALPIDE readout chip [20], indicate an excellent resolution, $\sim$5 μm, and high efficiency at low power and dark noise rate [21]. This looks like a good starting point for the IDEA vertex detector and a similar approach is proposed for the CEPC baseline detector (see Section4.1). The two detector concepts could then share the same pixel technology as well as profit from the electronic and mechanical work of the ALICE ITS.

Outside the vertex detector we have a 4 m long cylindrical drift chamber starting from a radius of $\sim$35 cm and extending until 2 m. The chamber can be made extremely light, with low mass wires and operation using 90% helium gas; less than 1% X_0 is considered feasible for 90° tracks. Additional features of this chamber, which is described in detail in Section 4.4, are a good spatial resolution, $<$100 μm, dE/dx resolution at the 2% level and a maximum drift time of only 400 ns. A layer of silicon microstrip detectors surrounds the drift chamber in both barrel and forward/backward regions. Track momentum resolution of less then 0.5% for 100 GeV tracks is expected when vertex detector and silicon wrapper information is included in the track fit. It is worth noting that the design of this chamber is the evolution of work done over many years on two existing chambers, that of the KLOE detector [22] and that of the recent MEG experiment upgrade [23]; major R&D work was done also for the 4th concept detector at ILC [24] and then for the Mu2E tracker [25].

A pre-shower is located between the solenoid magnet and the calorimeter in the barrel region and between the drift chamber and the end-cap calorimeter in the forward region. This detector consists of two passive material radiators each followed by a layer of MPGD detectors. In the barrel region the solenoidal magnet plays the role of the first radiator, while in all other cases the radiators are made of lead. The actual thickness of the radiators are still being optimized based on test beams currently in progress. In the extreme case

of using a total of two radiation lengths about 75% of the π^0's can be tagged by having both γ's from their decay identified by the pre-shower. Additional π^0 identification power comes from the high granularity of the calorimeter.

A solenoidal magnet surrounds the tracking system and the first pre-shower layer. Presently planned dimensions are 6 m of length and 4.2 m inner diameter. The relatively low two Tesla field and the small dimensions have important implications on the overall magnet package thickness, that can be kept at the 30-40 cm level, and on the size of the flux return yoke, which scales linearly with the field and the square of the coil diameter. With the given dimensions a yoke thickness of less than 100 cm of iron is sufficient to completely contain the magnetic flux and provide adequate shielding and support for the muon chambers.

A dual readout fiber calorimeter (see Section 5.5) is located behind the second pre-shower layer. We assume a total calorimeter depth of 2 m, corresponding to approximately seven pion interaction lengths. The detector resolution is expected to be about $10.5\%/\sqrt{E}$ for electrons and $35\%/\sqrt{E}$ for isolated pions with negligible constant terms, as obtained from extrapolations from test beam data using GEANT4 without including the pre-shower. This detector has very good intrinsic discrimination between muons, electrons/photons and hadrons for isolated particles [17]. This discrimination power is further enhanced when the information of the pre-shower and the muon chambers is added, extending the separation power also into hadronic jets and making it suitable for the application of particle flow algorithms. The intrinsic high transverse granularity provides a good matching of showers to tracks and pre-shower signals.

The muon system consists of layers of muon chambers embedded in the magnet yoke. The area to be covered is substantial, several hundreds of square meters, requiring an inexpensive chamber technology. Recent developments in the industrialization of μRwell based large area chambers, as planned for the CMS Phase II upgrade, are very promising (see Section 7.3).

Conclusions A different concept for a detector at CEPC has been proposed. This detector is designed specifically for CEPC and its specific running conditions and physics goals. In particular it is safe with respect to interaction between the detector solenoid field and the beam. Although additional R&D to optimize performance, reduce costs and come to a detailed engineered design of the detector is still necessary, this detector is based on technologies which are established after many years of R&D and whose feasibility has by large been established. Furthermore several choices are made to simplify the detector structure and reduce the cost, which in the end should be smaller than for an ILD-like detector.

References

[1] The CEPC-SPPC Study Group, *CEPC-SPPC Conceptual Design Report, Volume I - Accelerator*, IHEP, Beijing, China, Rep. IHEP-CEPC-DR-2018-01 (2018) .

[2] I. Agapov, G. A. Blair, S. Malton, and L. Deacon, *BDSIM: A particle tracking code for accelerator beam-line simulations including particle-matter interactions*, Nucl. Instrum. Meth. **A606** (2009) 708–712.

[3] D. Schulte, *Beam-beam simulation with GUINEA-PIG*, In 5th International Computational Accelerator Physics Conference (1998) . CLIC-NOTE 387.

[4] GEANT4 Collaboration, S. Agostinelli et al., *GEANT4: A Simulation toolkit*, Nucl. Instrum. Meth. **A506** (2003) 250–303.

[5] J. Allison et al., *Geant4 developments and applications*, IEEE Trans. Nucl. Sci. **53** (2006) 270.

[6] Geant4 Collaboration, M. Asai et al., *Recent developments in Geant4*, Annals Nucl. Energy **82** (2015) 19–28.

[7] H. Qi, *Status and progress of TPC module and prototype R&D for CEPC*, 2017.

[8] M. Zhao, M. Ruan, H. Qi, and Y. Gao, *Feasibility study of TPC at electron positron colliders at Z pole operation*, Journal of Instrumentation **12** (2017) no. 07, P07005. http://stacks.iop.org/1748-0221/12/i=07/a=P07005.

[9] M. Ruan, D. Jeans, V. Boudry, J.-C. Brient, and H. Videau, *Fractal dimension of particle showers measured in a highly granular calorimeter*, Physical review letters **112** (2014) no. 1, 012001.

[10] D. Yu, M. Ruan, V. Boudry, and H. Videau, *Lepton identification at Particle Flow oriented detector for the future e^+e^- Higgs factories*, The European Physical Journal C **77** (2017) no. 9, 591.

[11] H. Zhao, M. Ruan, et al., *PFA Oriented ECAL Optimization for the CEPC*, JINST (2018) .

[12] H. Abramowicz et al., *The International Linear Collider Technical Design Report - Volume 4: Detectors*, arXiv:1306.6329 [physics.ins-det].

[13] C.-S. S. Group, *CEPC-SPPC Preliminary Conceptual Design Report. 1. Physics and Detector*, IHEP, Beijing, China, Rep. IHEP-CEPC-DR-2015-01, IHEP-TH-2015-01, IHEP-EP-2015-01 (2015) .

[14] DREAM Collaboration, R. Wigmans, *The DREAM project: Towards the ultimate in calorimetry*, Nucl. Instrum. Meth. **A617** (2010) 129–133.

[15] N. Akchurin et al., *The electromagnetic performance of the RD52 fiber calorimeter*, Nucl. Instrum. Meth. **A735** (2014) 130–144.

[16] RD52 (DREAM) Collaboration, R. Wigmans, *New results from the RD52 project*, Nucl. Instrum. Meth. **A824** (2016) 721–725.

[17] N. Akchurin et al., *Particle identification in the longitudinally unsegmented RD52 calorimeter*, Nucl. Instrum. Meth. **A735** (2014) 120–129.

[18] M. Poli Lener, G. Bencivenni, R. de Olivera, G. Felici, S. Franchino, M. Gatta, M. Maggi, G. Morello, and A. Sharma, *The μ-RWELL: A compact, spark protected, single amplification-stage MPGD*, Nucl. Instrum. Meth. **A824** (2016) 565–568.

[19] M. Koratzinos et al., *Progress in the FCC-ee Interaction Region Magnet Design*, http://inspirehep.net/record/126211/files/wepik034.pdf (2017) , IPAC2017.

[20] ALICE Collaboration, M. Mager, *ALPIDE, the Monolithic Active Pixel Sensor for the ALICE ITS upgrade*, Nucl. Instrum. Meth. **A824** (2016) 434–438.

[21] ALICE Collaboration, G. Aglieri Rinella, *The ALPIDE pixel sensor chip for the upgrade of the ALICE Inner Tracking System*, Nucl. Instrum. Meth. **A845** (2017) 583–587.

[22] KLOE Collaboration, A. Calcaterra, *The KLOE drift chamber*, Nucl. Instrum. Meth. **A367** (1995) 104–107.

[23] MEG Collaboration, Y. Uchiyama, *Upgrade of MEG experiment*, PoS **EPS-HEP2013** (2013) 380.

[24] A. Mazzacane, *The 4th concept detector for the ILC*, Nucl. Instrum. Meth. **A617** (2010) 173–176.

[25] L. De Lorenzis, F. Grancagnolo, A. L'Erario, A. Maffezzoli, A. Miccoli, S. Rella, M. Spedicato, and G. Zavarise, *Analysis and Characterization of the Mechanical Structure for the I-Tracker of the Mu2e Experiment*, Nucl. Phys. Proc. Suppl. **248-250** (2014) 134–136.

CHAPTER 4

TRACKING SYSTEM

The CEPC physics program demands a robust and highly performant charged particle tracking system. Charged particles are used directly in physics analyses; they are input to determine primary and secondary vertices; and they are crucial input to particle flow calorimetry.

The tracking system has two major components. The vertex tracker has excellent spatial resolution and is optimized for vertex reconstruction. The main tracker is optimized for tracking efficiency and resolution required for the CEPC physics program.

Section 4.1 describes the CEPC vertex tracker, which can be paired with one of the main tracker options discussed in Section 4.2 (the Time Projection Chamber), Section 4.3 (the All Silicon Tracker) and Section 4.4 (the Drift Chamber Tracker).

4.1 Vertex tracker detector

The identification of heavy-flavor (b- and c-) quarks and τ leptons is essential for the CEPC physics program. It requires precise determination of the track parameters of charged particles in the vicinity of the interaction point (IP), permitting reconstruction of the displaced decay vertices of short-lived particles. This drives the need for a vertex detector with low material budget and high spatial resolution. The baseline design of the CEPC vertex detector is a cylindrical barrel with six silicon pixel layers and optimized for the energy regime and utilizes modern sensors.

4.1.1 Performance Requirements and Detector Challenges

As required for the precision physics program, the CEPC vertex detector is designed to achieve excellent impact parameter resolution, which in the $r\phi$ plane can be parameterized

by:

$$\sigma_{r\phi} = a \oplus \frac{b}{p(GeV)sin^{3/2}\theta} \tag{4.1}$$

where $\sigma_{r\phi}$ denotes the impact parameter resolution, p the track momentum, and θ the polar track angle. The first term describes the intrinsic resolution of the vertex detector in the absence of multiple scattering and is independent of the track parameters, while the second term reflects the effects of multiple scattering. The parameters a=5 μm and b=10 $\mu\mathrm{m} \cdot \mathrm{GeV}$ are taken as the design values for the CEPC vertex detector. The main physics performance goals can be achieved with a three concentric cylinders of double-layer pixellated vertex detector with the following characteristics:

- Single-point resolution of the first layer better than 3 μm;
- Material budget below 0.15% X_0/layer;
- First layer located close to the beam pipe at a radius of 16 mm, with a material budget of 0.15% X_0 for the beam pipe;
- Detector occupancy not exceeding 1%.

The power consumption of the sensors and readout electronics should be kept below 50 $\mathrm{mW/cm^2}$, if the detector is air cooled. The readout time of the pixel sensor needs to be shorter than 10 μs, to minimize event accumulation from consecutive bunch crossings. The radiation tolerance requirements, which are critical for the innermost detector layer, are driven by the beam-related backgrounds as described in Chapter 9.

4.1.2 Baseline design

The baseline layout of the CEPC vertex detector consists of six concentric cylindrical layers of high spatial resolution silicon pixel sensor located between 16 and 60 mm from the beam line, providing six precise space-points for charged particles traversing the detector. The main mechanical structure is called a ladder. Each ladder supports sensors on both sides; thus, there are three sets of ladders for the vextex detector. The material budget of each detector layer amounts to ∼0.15% X_0. Extensive simulation studies (see Section 4.1.3) show that this configuration with the single-point resolutions listed in Table 4.1 achieves the required impact parameter resolution.

	$R(mm)$	$\|z\|(mm)$	$\|cos\theta\|$	pixel size ($\mu m \times \mu m$)	$\sigma(\mu m)$
Layer 1	16	62.5	0.97	16×16	2.8
Layer 2	18	62.5	0.96	25×25	6
Layer 3	37	125.0	0.96	25×25	4
Layer 4	39	125.0	0.95	25×25	4
Layer 5	58	125.0	0.91	25×25	4
Layer 6	60	125.0	0.90	25×25	4

Table 4.1: Vertex detector parameters.

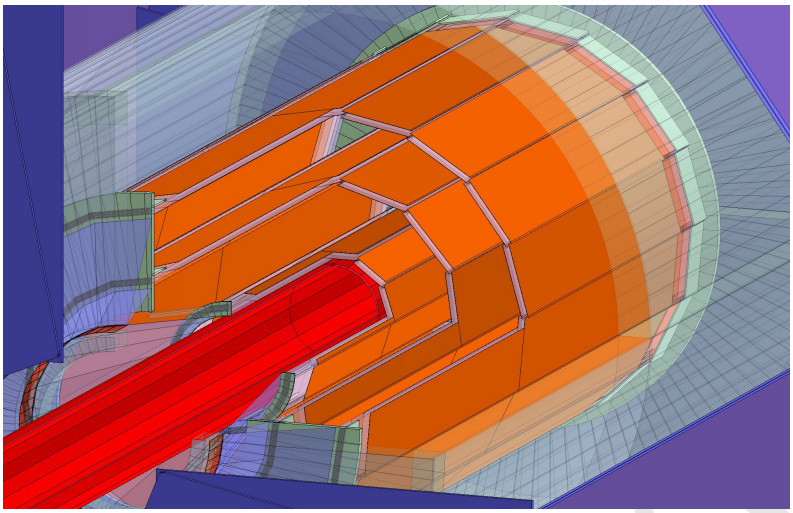

Figure 4.1: Schematic view of pixel detector. Two layers of silicon pixel sensors (in oragnge) are mounted on both sides of each of three ladders to provide six space points. The vertex detector surrounds the beam pipe (red).

4.1.3 Detector performance studies

The identification of b/c-quark jets (called "flavor-tagging") is essential in physics analysis where signal events with b/c-quark jets in the final state have to be separated from one another and from light-quark jets. Flavor tagging requires the precise determination of the trajectory of charged tracks embedded in the jets. For CEPC operation at the center-of mass energy of 240 GeV, those tracks are often of low momentum, for which the multiple scattering effect dominates the tracking performance as illustrated by Eq. 4.1.

The CEPC vertex detector layout has been fully implemented in the GEANT4-based simulations framework MOKKA [1]. In addition, the LiC Detector TOY fast simulation and reconstruction framework (LDT) [2] have been used for detector performance evaluation and layout optimization. The preliminary studies for optimization to evaluate the sensitivity of the results on the chosen parameters have been done, for the purpose of assessing the impact of the detector geometries and material budgets on required flavor-tagging performance. However, beam-induced background was not included at the moment.

4.1.3.1 Performance of the Baseline Configurations

The impact parameter resolution following from the single-point resolutions provided in the Table 4.1 is displayed in Figure 4.2 as a function of the particle momentum, showing that the ambitious impact parameter resolution is achievable.

4.1.3.2 Material Budget

The baseline design includes very small material budget for the beam pipe as well as for the sensor layers and their support. To assess the sensitivity of the performance on the amount of material, the material budget of the beam pipe and the vertex detector layers has been varied. The resulting transverse impact-parameter resolutions for low-momentum tracks are shown in Figure 4.3. When increasing the material of the detector layers by a factor of two, the resolution degrades by approximately 20%.

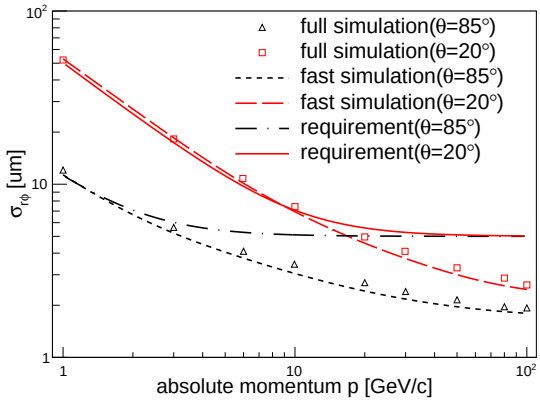

Figure 4.2: Transverse impact-parameter resolutions for single muon events as a function of momentum for two polar angles 20° and 85°.

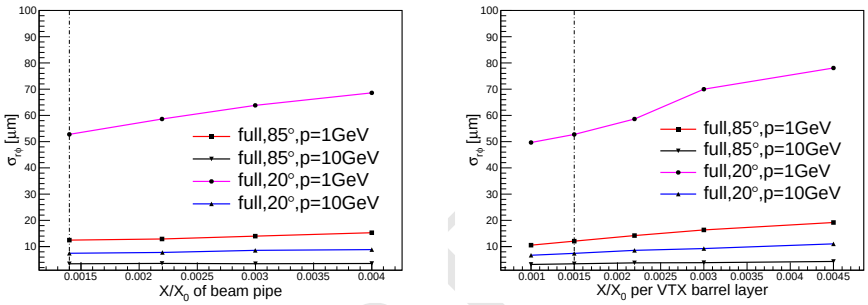

Figure 4.3: Transverse impact-parameter resolution as function of the amount of material in beam pipe (left) and in each vertex detector barrel layer (right), as obtained from the simulation. The results are shown for 1 GeV and 10 GeV muon tracks and for polar angles of θ=20 degrees and of θ=85 degrees. The material budget corresponding to the baseline configuration is indicated by dashed lines.

4.1.3.3 Dependence on Single-Point Resolution

The dependence of the transverse impact-parameter resolution on the pixel size was studied by worsening the single-point resolution of the vertex layers by 50% w.r.t. the baseline values. The resulting impact parameter resolution for high and low momentum tracks as function of the polar angle θ is shown in Figure 4.4. The resolution for track momenta of 100 GeV is found to change by approximately 50% in the barrel region, which is expected. Here they are better than the target value for the high-momentum limit of a≈5 μm in both cases, as expected from the corresponding single-point resolutions. The previous sentence is about MOMENTUM resolution. Why is it here in between impact parameter resolution for high and low momentum particles? If we want to talk about momentum resolution, let's start a new paragraph and then discuss it in more detail, e.g. for both low and high momentum particles. For 1 GeV, where multiple-scattering effects dominate, the corresponding variation of the transverse impact-parameter resolution is only 10% larger. The target value for the multiple-scattering term of b≈10 $\mu\mathrm{m} \cdot \mathrm{GeV}$ is approximately reached in both cases. It should be noted, however, that the pixel size is also constrained by the background occupancies (see Section 4.1.4) and the ability to separate adjacent tracks in very dense jets in the presence of such backgrounds.

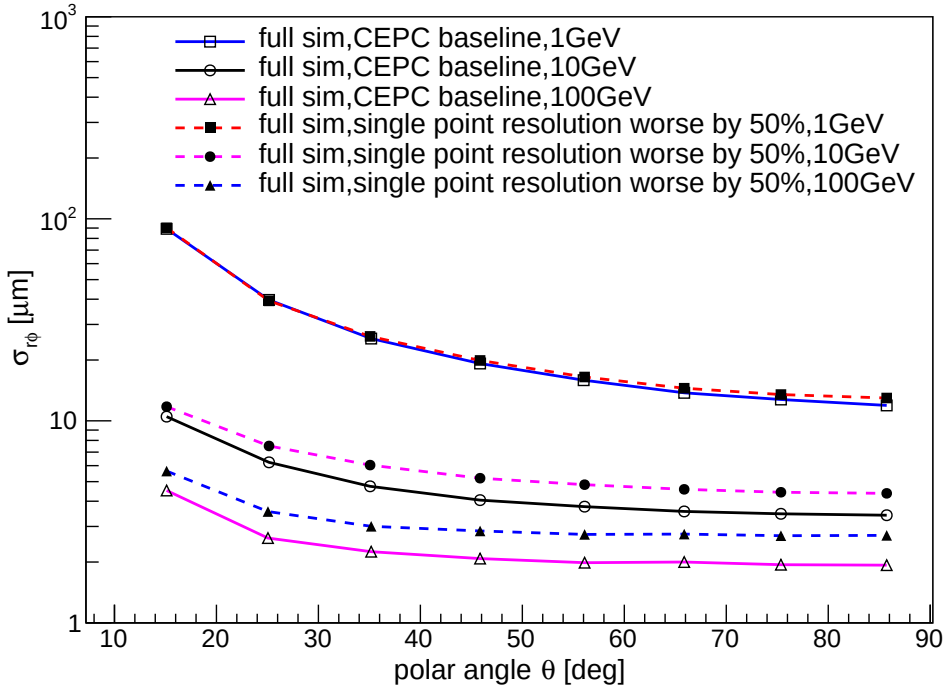

Figure 4.4: Transverse impact-parameter resolutions as function of the polar angle θ for different values of the single-point resolution of the CEPC vertex detector. Shown are the resolutions for 1 GeV, 10 GeV and 100 GeV tracks.

4.1.3.4 Distance to Beam Line

The distance of the first two vertex layers, which are supported by a single ladder, from the interaction point (IP) was varied by $\pm$4 mm relative to baseline geometry of the CEPC vertex detector. When we move the first layer from 16 to 12 mm, does it still clear the beam pipe? In any case, what do we do with beam pipe radius in this study? It is the last scattering surface when extrapolating back and has impact on the answer. I think we need to clarify what has been studied. Figure 4.5 shows the resulting transverse impact parameter resolution at θ=85 degrees as function of the momentum and for different radial distances of the innermost barrel vertex layer from the IP. For low momentum tracks, the transverse impact-parameter resolution is proportional to the inner radius, as expected from the parameter formula.

4.1.4 Beam-induced Background in the Vertex Detector

Pair-production and off-energy beam sparticles are expected to be the dominating source of detector backgrounds originating from the interaction region. These processes have been studied with detailed Monte Carlo simulation in Chapter 9. For the first vertex detector layer, the maximum annual values of the Total Ionising Dose (TID) and Non-Ionising Energy Loss (NIEL) are estimated to be 3.4 MRad and 6.2×10^{12} 1 MeV $\mathrm{n_{eq}/cm^2}$ per year, respectively, with a safety factor of 10 included (see Table 9.4 in Chapter 9). This happens when the machine is operating at the Z-pole energy, and imposes radiation tolerance requirements on the silicon pixel sensor and associated readout electronics.

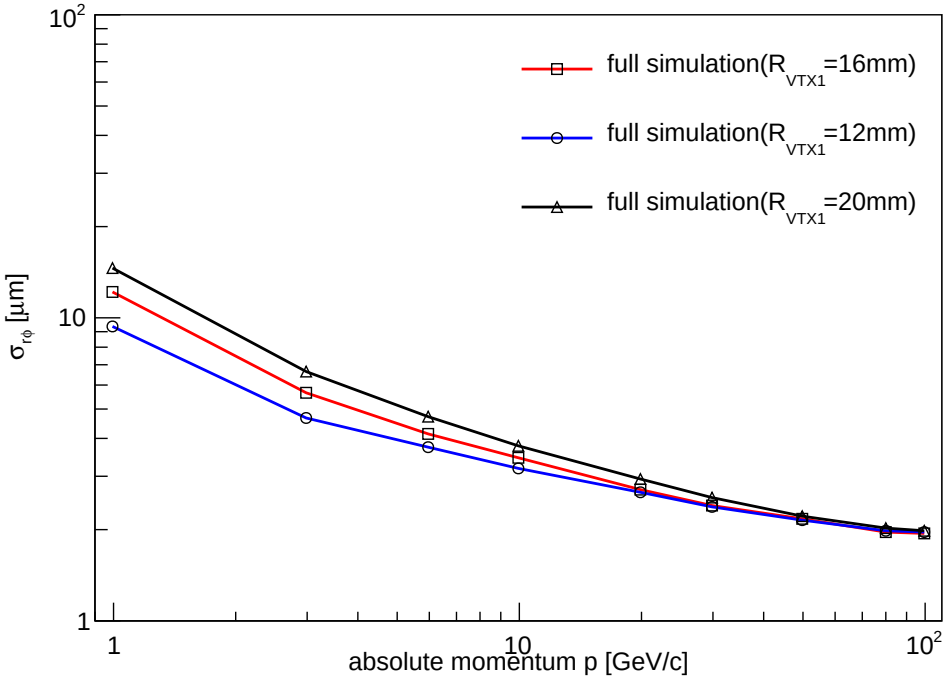

Figure 4.5: Transverse impact-parameter resolution at θ=85 degrees as function of the momentum for different values of inner most layer radius R_{VTX1}. The red curve indicates the baseline configuration of R_{VTX1}=16 mm.

	H(240)	W(160)	Z(91)
Hit density ($\mathrm{hits \cdot cm^{-2} \cdot BX^{-1}}$)	2.4	2.3	0.25
Bunching spacing (μs)	0.68	0.21	0.025
Occupancy (%)	0.08	0.25	0.23

Table 4.2: Occupancies of the first vertex detector layer at different machine operation energies: 240 GeV for ZH production, 160 GeV near W-pair threshold and 91 GeV for Z-pole.

The beam-induced background will have impacts on vertex detector occupancy, which is critical for the innermost detector layer. Table 4.2 shows the expected hit density and occupancies of the first vertex detector layer at different machine operation energies. The result of occupancies depends on assumptions of detector readout time and average cluster size. Here we assume 10 μs of readout time for the silicon pixel sensor and an average cluster size of 9 pixels per hit, where a pixel is taken to be 16×16 $\mu\mathrm{m}^2$. The resulting maximal occupancy at each machine operation mode is below 1%.

4.1.5 Sensor Technology Options

Significant progress has been made since the first silicon pixel detector was first used in high-energy physics experiments, and considerable R&D efforts have taken place to develop pixel sensors for vertex tracking at future particle physics experiments [3], driven by track density, single-point resolution and radiation level.

As outlined in Section 4.1.1, the detector challenges for the CEPC include high impact-parameter resolution, low material budget, low occupancy and sufficient radiation tolerance (mild comparing to LHC but not necessarily easy to achieve). To fulfill these requirements at system level, sensor technologies which achieve fine pitch, low power and fast readout must be selected. These considerations present unique challenges to the CEPC vertex detector. CEPC has a bunch spacing of 0.68 μs, and power pulsing cannot be utilized to reduce average power as is planned at the ILC. Experiments such as the STAR[4], BELLEII[5] and ALICE upgrade[6] readout continuously as the CEPC. However, they have less stringent requirements in terms of impact-parameter resolution and material budget.

The monolithic pixel sensor has the potential to satisfy the low-material and high-resolution requirements of the CEPC vertex detector. This technology has been developing fast. The 1^{st} generation MAPS-based vertex detector for the STAR HFT upgrade [4, 7] just completed 3-year physics run successfully, while the new generation HR CMOS Pixel Sensor for ALICE-ITS upgrade [6] is in mass production. In the previous 0.35 μm double-well process, only N-MOS transistors can be used in the pixel design. This constraint is removed in the new 0.18 μm quadruple-well process. Both N- and P-MOS transistors could be used in the pixel design. Combining with the smaller feature size, it becomes a very appealing technology. A good start point for the CEPC vertex would be the ALPIDE design [8], which is developed for the aforementioned ALICE-ITS upgrade and has achieved performances very close to the requirements of the CEPC. Further R&Ds are needed to shrink the pixel pitch to 16 μm (binary readout) in order to accomplish the required 2.8 μm single-point resolution. Another monolithic option is the Silicon On Insulator (SOI) pixel sensor. After more than 10 years of evolution, SOI has entered a new stage of maturity. Fundamental issues, including the transistor shielding [9] and the TID tolerance [10], have been addressed and wafer thinning [11] has been demonstrated. In the meanwhile, R&Ds for the ILC and CLIC [12, 13] are exploring time stamping and analog readout schemes. The SOI has a unique feature of a fully-depleted substrate as the active silicon. And its 0.2 μm CMOS process provides the necessary density of transistors as the 0.18 μm CMOS in HR CMOS does. Therefore it is envisaged that the readout design for the CEPC vertex may be adapted for both processes and to exploit each ones potentials.

Depleted P-channel Field Effect Transistor (DEPFET) is referred to as semi-monolithic because the first amplification stage can be integrated into the pixel combined with subsequent processing circuit in separate readout ASICs. The BELLE II is anticipating its full detector operation with a DEPFET-based vertex detector [5] installed at the end of 2018. It is very helpful to have the readout ASICs, as the major heat sources, located outside the detector acceptance area, while keeping the sensors exceptionally low power and low material. The challenge is to periodically sample the modulated current over a large pixel array within required intervals, 20 μs/frame or even less.

Hybrid pixel has been used at hadron colliders for the past decades, and now CLIC R&D is pushing for 50 μm thinned sensors, bump-bonded on 25 μm pitch to 50 μm thinned ASICs [14]. The hybrid approach evolves constantly and profits from industrial technology developments. Apart from the Very Deep Sub-Micron (VDSM) ASIC technology that enables complex functionalities and superior performances, a close watch on industrial developments of the vertical and lateral inter-connection technologies will also be very helpful to meet the material budget.

4.1.6 Mechanics and Integration

The design of the vertex detector is conceived as a barrel structure with three concentric cylinders of double-sided layers. Each double-sided layer is equipped with pixel sensors on both sides, and has a common support frame. In the azimuthal direction, each layer is segmented in elements called ladders. The ladder, which extends over the whole length of the layer, is the basic building block of the detector. It contains all structural and functional components, such as chips, flex cable, support frame and cold plate if it is necessary. Pixel chips in a row are connected to flex cable by wire bonding or other bonding techniques, and then glued to the support frame, which is composed of low Z materials, such as carbon fiber and silicon carbide, providing stable mechanical support. The other side of the support frame is equipped with another layer of pixel sensors.

The design of the ladders should take into account the specifications of the vertex detector. In order to reduce a small multiple Coulomb scattering contribution to the charged-track vertex resolution and control deformations from gravity and cooling forces for the sensor position stability, the ladder mechanical support must fulfill stringent requirements in terms of minimum material budget and highest stiffness. Ladder designs similar to the STAR pixel detector, the ALICE ITS, the BELLE II PXD, and the ILD double-sided ladder are under consideration.

The ladder mechanical support is inherently linked to the layout of the cooling system that will be adopted to remove the heat dissipated by the pixel sensors since the cooling system is integrated in the mechanical structure. The cooling system of the CEPC vertex detector must balance the conflicting demands of efficient heat dissipation with a minimal material budget. Therefore a suitable, high thermal conductivity and low material budget, cold plate coupled with pixel sensors should be implemented in the ladder design. There are two main types of cooling methods in particle physics experiments, air cooling and active cooling. Table 4.3 gives a list of cooling methods and the corresponding material of each layer of the aforementioned experiments. The upgrade of ALICE ITS [6] adopts water cooling with respect to a chips power dissipation value of 300 $\mathrm{mW/cm^2}$. Polyimide cooling pipes fully filled with water are embedded in the cold plate. STAR-PXL [15] uses air cooling according to its chips power consumption of 170 $\mathrm{mW/cm^2}$. For ILD [16] vertex system, two different cooling options are considered, depending on the sensor technology. The sensors and SWITCHER chips of BELLE II PXD [17] require air cooling, while active cooling will be used for readout chips on each end of the detector, which is out of the sensitive region of the detector. So for CEPC vertex detector, the suitable cooling method will be determined according to the sensor option and the power consumption.

Simulation and module prototype studies should be carried out to find suitable designs that can meet requirements of stability, cooling and the performance of the vertex detector.

For the design of the whole mechanical structure of the vertex detector, some criteria must be taken into account. Firstly, minimum material has to be used in the sensitive region to reduce multiple Coulomb scattering. Secondly, to ensure high accuracy in the relative position of the detector sensors and provide an accurate position of the detector with respect to the central tracker of TPC and the beam pipe, a mechanical connector or locating pin at each end of the ladder should be considered to allow the fixation and alignment of the ladder itself on the end rings. Thirdly, the cooling system should be arranged

Vertex detector	Power dissipation	Cooling method	Material budget requirement/layer
Alice ITS	300 mW/cm^2	water	0.3%
STAR PXL	170 mW/cm^2	air	0.39%
ILD vertex	<120mW/cm^2 (CPS and DEPFET)	air or N_2	0.15%
	35W inside cryostat (FPCCD)	two-phase CO_2	
BELLE-II PXD	20W for sensor and SWITCHER	Air	0.2%
	180W on each end	CO_2	

Table 4.3: Cooling method of the vertex detector in each experiment.

reasonably to ensure stable heat dissipation. Lastly, to reduce the dead region caused by the boundary of each ladder, neighboring ladders should be partially superimposed.

In addition, the main mechanical support structures of the vertex should also meet the requirements of the integration with the other detectors, such as time-projection chamber (TPC) and forward tracking disks.

4.1.7 Critical R&D

The inner most layers have to fulfill the most demanding requirements imposed by the physics program. In addition, the system is bounded by stringent running constraints. The technology options in Section 4.1.5 are able to meet each individual requirement, including single-point resolution, low material budget, fast readout, low power consumption and radiation tolerance, but R&D is needed to select the specific design which can achieve the combination of all these criteria. Due to the limited manpower and availability of process, presently R&D efforts have been put into CMOS and SOI pixel sensor development to address the challenges concerning single-point resolution and low power consumption. Further developments are foreseen to follow in the future, including enhancement of density, radiation hardness and ultra-light module assembly.

The current R&D activities have access to two advanced processes. The TowerJazz 0.18 μm quadruple-well process enables the full CMOS pixel circuit, while Lapis 0.2 μm double-SOI process has properly solved the crosstalk between sensor and digital part, and improved TID tolerance significantly.

In order to exploit the potential of these new developments, two design teams have started chip designs using HR CMOS and SOI technologies, respectively. Two designs have been submitted to the TowerJazz foundry. The first one uses simple three transistor (3T) analog amplification circuit to carry out the optimization of sensing diode and evaluate the influence of radiation damage [18]. The second one implements a well-proved rolling shutter readout as well as an innovative data-driven readout [19, 20]. Another two designs that adopt the SOI technology have also been submitted [21]. With the amplifier and discriminator integrated into each pixel, the pixel size has been shrunk to 16μm pitch.

The chip has been thinned to 75 μm successfully and an infrared laser test has shown that a single-point resolution of 2.8 μm is achievable with that pitch [11]. All the designs for current R&D are in line with the same principle of in-pixel discrimination even though each one has its own implementation. An in-pixel discriminator can reduce analog current therefore lead to reduced power consumption.

Enhancements of the TowerJazz 0.18 μm process or Lapis 0.2 μm process are possible by migrating to a smaller feature size, 0.13 μm for example, or combining with a micro-bump 3D integration process. The latter is able to attach a second layer of pixel circuit on top of the existing layer of the sensing diode and front-end circuit. The upper tier can be the fully digital part that implements data-driven readout architecture, while the lower tier can be HR CMOS or SOI pixel matrix. A promising result has been demonstrated by the successful formation of 2.5 μm Au cone bump with NpD (Nano-particle deposition) technique [22]. However, the throughput needs further improvement and the thinning of sensors has to be compatible with micro-bump 3D integration.

The TowerJazz process is expected to be sufficiently radiation hard for the expected TID. An N-type plain implant has recently been added to improve the charge collection efficiency [23], which therefore will benefit the non-ionization radiation damage. In terms of the SOI process, the weak point is the BOX layer of SiO_2. Although the TID tolerance of the SOI process has been improved dramatically by the introduction of Double-SOI and the optimization of transistor doping recipe (LDD, lightly doped drain) [10], SOI needs carefully study on the irradiation of large scale chips and of low power designs.

Sensor thinning and ultra-low material construction of modules are subject to the constraint of 0.15% X_0/layer. HR CMOS wafer thinned to 50 μm is routine in semiconductor industry nowadays. SOI wafers thinned to 75 μm with backside implant have also been demonstrated by current R&D. However, low material detector modules need to integrate mechanical support, power and signal connections, and have sufficient stiffness to avoid vibration.

4.1.8 Summary

The basic concepts of the CEPC Vertex detector, including the pixel sensors specifications required by the impact parameter resolution and radiation tolerance, the low-mass mechanical design, and the detector layout, are implemented in the baseline design. Do we mean implementation in SIMULATION? If we have really implemented it already, then I don't understand the next sentences about developing pixel sensors, designing mechanical support and other R&D. It will be crucial to develop pixel sensors with lower power consumption and fast readout electronics because of continuous colliding mode and strong beam-related background. Detailed designs for mechanical supports and cooling, cabling, and power conversion are also necessary. Most of these issues will be addressed by R&D for the CEPC and by exploring synergies with experiments which have similar requirements.

4.2 Time Projection Chamber and Silicon main tracker

The Time Projection Chambre (TPC) is one of the options being considered for the CEPC main tracker. The high density of space points provides unparrelleled pattern recognition capability. The TPC is complemented by an envelope of solicon detectors to improve its

momentum resolution. The silicon detectors are also useful for monitoring possible field distortions in the TPC and for alignment purposes.

4.2.1 Time Projection Chamber

Time Projection Chambers have been extensively studied and used in many fields, especially in particle physics experiments such as STAR [24] and ALICE [25]. The technology directly provides three-dimensionl space points; the gaseous detector volume gives a low material budget; and the high density of such space points enables excellent pattern recognition capability. However, care must be taken to address space charge distortion resulting from the accumulation of positive ions in the drift volume [26]. This issue is especially important in high rate conditions.

There have been extensive R&D on readout modules to optimize position resolution and to control ion feedback. These studeis will continue for the next few years in order to understand and resolve several critical technology challenges.

4.2.1.1 CEPC Time Projection Chamber

The CEPC TPC consists of a cylindrical drift volume with an inner radius of 0.3 m and an outer radius of 1.8 m, and it has a full length of 6 m. check. The central cathode plane is held at a potential of 50 KV, and the two anodes at the two endplates are at ground potential. The cylindrical walls of the volume form the field cage, which ensures a highly homogeneous electrical field between the electrodes of 300 V/cm. The drift volume is filled with Ar/CF4/C4H10 in the ratio of 95/3/2 is this this intended gas?. Ionization electrons released by charged particle tracks drift along the electric field to the anodes where they are amplified in an electron avanlanche and readout using a micro-pattern gaseous detector (MPGD).

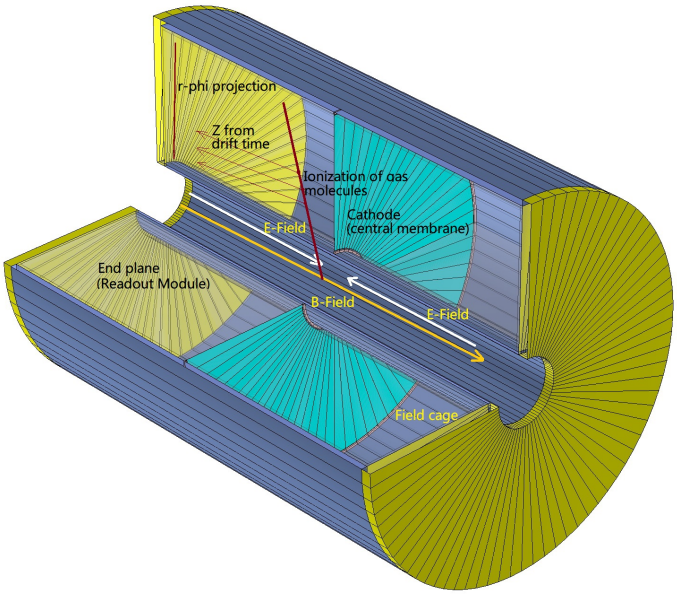

Figure 4.6: Sketch of the TPC structure. Is this a sketch of the CEPC TPC? The vertex detector looks suspiciously not CEPC-like.

The CEPC TPC is operated at atmosheric pressure resulting in a material budget of less than $1\% X_0$ in the central region. The 3-Tesla solenoidal magnetic field suppresses

tranverse diffusion and improves position resolution. It also curls up low-momentum tracks resulting in higher occupancy near the beam line. I have no idea what the next two sentences are saying. They also sound like a detail that can be deferred to later, though I wouldn't know where it belongs. The chambers are attached to the end-plate from the inside to minimise the dead area between adjacent chambers. Thus, a particular mounting technique is required to enable rotation and tilting of the chambers.

The chamber's cylindrical inner and outer walls serve multiple functions. They hold the field forming strips, which are attached to a divider chain of non-magnetic resistors. Since the central cathode will be held at approximately 50 kV, the walls must withstand this enormous potential. What are mirror strips inthe next sentence? They have not been mentioned before.The narrow mirror strips will be arranged between the inner and outer walls to maintain the electron field uniform in over the whole active TPC volume. Carbon fiber composite material will be used for the cylindrical walls because of its low mass.

The MPGD detector on each endplate is divided into many independent readout modules to facilitate construction and maintenance. The modules are mounted closely together on the endplate to provide nearly full coverage. Power cables, electronic connectors, cooling pipes, PCB boards and support brackets wall are also mounted on the end-plate. The end-plate needs to constructed from a lightweight material in order not to compromise the jet energy resolution in the forward region but also should be still sufficiently rigid to maintain stable positioning of the detector modules with a position accuracy better than 50 μm. The mechanical structure has a thickness of $8\%X_0$. Additional material for the readout planes, front-end electronics and cooling is estimated to be $7\%X_0$, and power cables and the connector up to $10\%X_0$. Are these numbers to be added together? Or does the last 10% already includes the earlier 7%? Reword as appropriate to clarify.

The CEPC TPC provides 220 space points per track with a single-point resolution in $r-\phi$ of $100\mu m$. In addition to position information, the TPC measures the energy loss on each readout pads. This can be combined with the measurement of momentum in the magnetic field to provide particle identification.

4.2.1.2 Baseline design and technology challenges

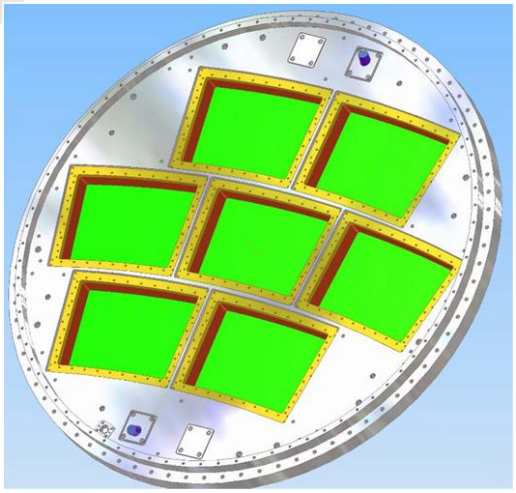

Figure 4.7: The diagram of large prototype module design.

The readout structure is designed to be modular to facilitate construction and maintainence. Each module will consist of gas amplification system, readout pad plane and the associated front-end electronics. An MPGD-based gas amplification system will be necessary to achieve the required performance, and the charge from the amplification system will be collected on a pad board. The readout module will also have to provide all necessary power and cooling. Each module will be approximately 170 mm in width and 200 mm in height.

Figure 4.7 shows the design of a large prototype module in LC-TPC international collaboration group $R\&D$. We need to say more here. For example, are module dimensions similar to CEPC, are modules close to one another as we need it here, etc. Otherwise, we should delete this paragraph as it has no relevance to CEPC.

Gas amplification detector module

The required physics performance can be achieved with any amplification technology with gain in the range of $10^3 - 10^4$ combined with pad readout. Gas Electron Multiplier (GEM) [27] and Micro-Mesh Gaseous Structure detector (MicroMEGAS) [28] of the (MPGDs) detectors [29] are both viable technologies for the large-area application in the CEPC TPC readout module, generating the very high fields necessary for gas amplification with modest voltages (300-400V) across $50 - 100\mu m$ structures. In the case of GEM, two or three will be stacked together to achieve sufficient charge amplification while MicroMEGAS have enough amplification in a single stage.

Micro-pattern gaseous devices such as GEM and MicroMEGAS provide:

1. Higher rate capability: MPGDs provide a rate capability over $10^5 Hz/mm^2$ without discharges that can damage electronics.
2. Intrinsic ion feedback suppression: The ions produced in the ampligication region do not go back to the drift volume, and most of them will be neutralised on the mesh or GEM foil.
3. A direct electron signal, which gives a better time resolution($-100\mu m$). I think we mean time, right? Is it supposed to be 100 pico-second?
4. A larger gain, by the specific operation high voltage. Not sure what it is larger than. Or the intent of the phrase about operating HV. Do e just mean it provides enough gain?
5. Much smaller $E \times B$ effects than wires chamber for which the spacing of the wires is about a few mm. Not sure what we have in mind here for wire chambers geometry to read out TPC. The comment about several mm certainly implies higher voltage but not necessarily higher field. That would not increase the value of ExB though it increases the distance over which it acts. Isn't the angle between B and E an important factor? The two are nearly parallel in the case of MPGD.

Optimization readout pad size

Readout pad size is a vital parameter for the TPC detector module whether using GEM or MicroMEGAS as the readout detector because accurate position information requires to process the adjacent pad's signal with the Center-of-Gravity Method (CGM).

We need to clarify the next paragraph. First of all, are we doing PADs or STRIPs? The last sentence says each strip is connected to one electronis chanel. Sounds like we do

NOT use pads. There are detailed dimension numbers and strip counts. Why are there more y strips than x strips by almost a factor of two? I thought we have not made a final design for CEPC TPC. Do these numbers refer to some prototype? The design of the two-dimensional readout strips has been developed with the triple GEMs of $100mm^2$ in IHEP. The readout strips in the X direction are $193\mu m$ wide at $752\mu m$ intervals. There are pads with a size of 356 $\mu m \times 356\mu m$ connected with each other in the Y direction, and their strip pitch is $457\mu m$. The difference in strip widths is to improve signal sharing between X-axis and Y-axis strips, to ensure a homogeneous charge distribution between adjacent strips. The total number of strips in X and Y directions are 267 channels and 437 channels respectively. Each strip is connected to one electronic channel to process the signal.

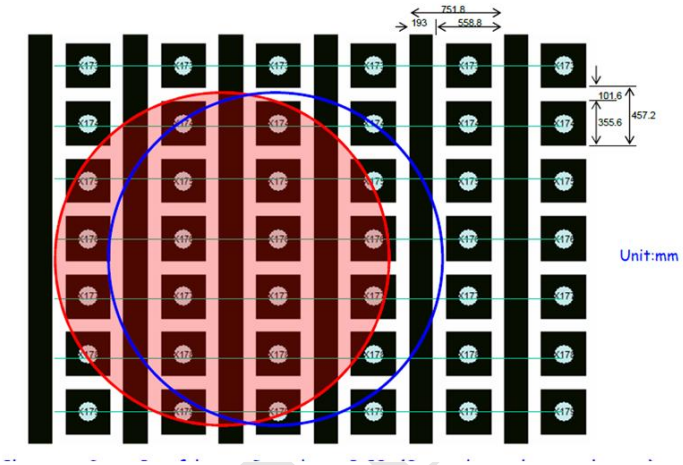

Figure 4.8: The profile of the electrons cluster in Triple GEMs.

The next paragraph also needs clarification. I don't understand what is being discussed to propose edits. Other readers may not understand the intent either. In the figure4.8 of the typical profile of the electrons cluster in readout strips, the pink circle could be move to the blue circle and the profile is the Gaussian distribution. If there is a enough number pads to use Center-of-Gravity Method, the pad width should be designed to 1.0mm and the length of pad should be designed to 6.0mm to obtain the sufficient charge information when the amplifier gain is 10mV/fC.

Operation gas for the long drift

The choice of chamber gas strongly affects the properties and eventually the performance of a TPC. Desirable characteristics are:

1. High drift velocity (to avoid accumulation of too many events inside the chamber)
2. Low electron capture probability (to preserve signal size)
3. Low transverse and longitudinal diffu0sion coefficients (to prevent deterioration of the spatial resolution)
4. Large specific energy loss dE/dx (to improve particle identification)
5. Stability against electrical breakthroughs (to allow reliable operation of the amplification device)

6. Nonhazardous chemical properties (to address safety concerns like inflammability and damages to the hardware)

Ion distortion is of course a valid concern. However, the comment about avoiding ions escape into the gas volume is not part of gas properties but of design of gas amplification section. I propose to replace the following sentences with a change to the first bullet above: and to reduce the effect of ions distorting drift field. Due to the long drift distance of the several meters(3.0m), and the fact that ions are more massive and much slower than electrons, ions can accumulate in the chamber. This effect can lead to electric field distortions and should be avoided. To decrease this effect, the structure of the readout chambers is generally designed to avoid ions from escaping into the gas volume. A gas with a large drift velocity is also chosen in experiments with large interaction rate.

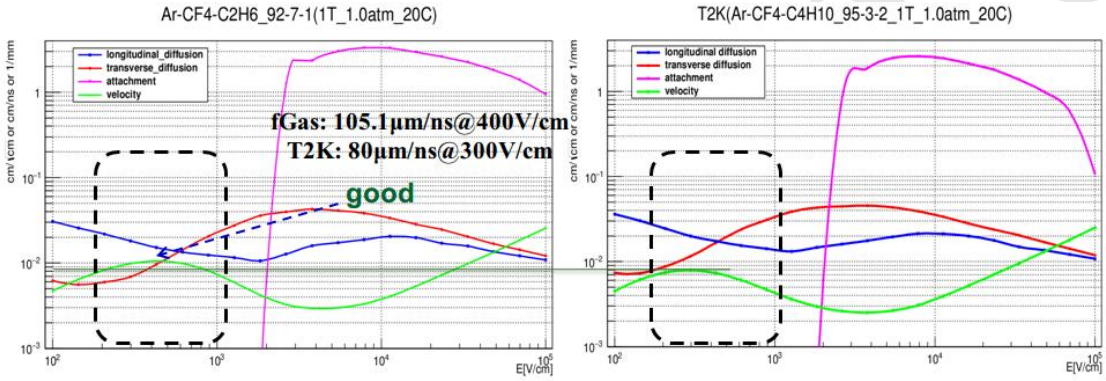

Figure 4.9: The drift velocity in different gas mixture. Expnad caption to explain the plot. What is dashed rectangle? Should we have an arrow around 300 V/cm instead since that is the expected operating point? Why do we show two gases? The embedded comments in the left figure seem to be off topic.

In a given working gas, the drift velocity of electron is a function of E/P where E denotes the electric field and P the gas pressure. The drift velocity varies slowly near the maximum around few hundred V per cm-atm, Fig. 4.9 shows the drift velocity obtained in different mixture gases. The mixture of Ar/CF_4/iC_4H_{10} (95%/3%/2%) has a saturated drift velocity of approximately 8 cm/μs in a drift field of 300 V/cm. In addition, the gas has a large parameter of $\omega\tau$ and transverse diffusion coefficient of 30 μm/$\sqrt{\text{cm}}$ in the drift field of 300 V/cm.

The bunch spacing at the CEPC is ~ 3.6 μs(the preliminary example beam structure parameter). A working gas with a higher saturated drift velocity should be considered. I am confused. Is the 95/3/2 mix the default or not? If it is, this should be rephrased to something like other mixes are being investigated to further improve performance. Besides, the gas amplification requires to achieve approximately 6000 and the signal attenuation of the electron attachment should be kept below $1\%/m$. Why is electron attachment coming up here? Let's understand what we want to say and then edit some more.

Low power consumption electronics readout

Small readout pads of a few square millimeters (e.g. $1mm \times 6mm$) We talked earlier about 356 micron x 356 micron pads. These are massive in comparison, no? are needed to achieve high spatial and momentum resolution in TPC, demanding about 1 million channels of readout electronics per endcap. The total power consumption of the

Total number of channels		1 million per endcap
APE or AFE?	ENC	500e @ 10pF input capacitance
	Gain	$10mV/fC$
	Shaper	CR-RC
	Peaking time	100ns
ADC	Sampling rate	$\geq 20MSPS$
	Resolution	10 bit
Power consumption		$\leq 5mW$ per channel
Output data bandwidth		300MB-500MB
Channel number		32
Process		TSMC 65nm LP

Table 4.4: TPC readout electronics. I don't understand th output badwidth number. Is it 300 - 500 MBps? There must be a time associated with the unit. 20 MSPS and 10 bits per sample is roughly 300 Mbps (not MBps) We have 32 channels. There is zero suppression going on. Are we convinced that all these numbers work out?

front-end electronics is limited by the cooling system to be several kilo-watts in practice. The architecture of the TPC readout electronics is shown in Fig.1 Figure 1 is a hardwired number. Which figure are we referring to really? , selected from a broad range of survey on current electronics installed or under development during past decades, including ALTRO/S-ALTRO and more recently SAMPA for ALICE, AFTER/GET for T2K and Timepix for ILC. It consists of the front-end electronics on the detector panel and the data acquisition system several meters away from the detector.

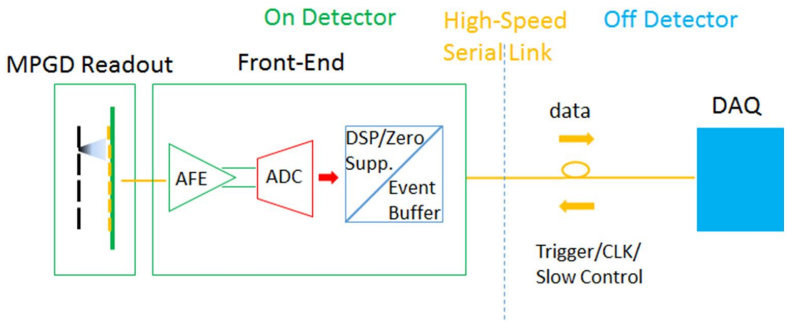

Figure 4.10: The architecture of the TPC readout electronics.

The waveform sampling front end is preferable, including a preamplifier and a shaper as the analog front-end (AFE), a waveform sampling ADC operating at 10MSPS, Huh? Table 4.4 says greater than 20 MSPS. a dedicated digital signal processing (DSP) and zero-suppression unit and a de-randomize event buffer for each channel. To satisfy the stringent requirements on the integration and the power consumption, a front-end ASIC will be developed in advanced 65nm CMOS process. The key specifications of the front-end ASIC are summarized in Table 4.4 as follow.

CMOS scales down in favor of digital circuits regarding power and density. The power consumption of the DSP circuits reported in $Ref.[3]$ was $4mW/ch$ in a 130nm process

and could be reduced by a factor of at least two by migrating the same design to 65nm. However, this is not the equivalent of the analog circuits. The design strategy for the front-end ASIC is to keep the analog part as simple as possible. The block diagram of the analog front-end and the successive approximation (SAR) ADCare shown in Fig.2 and Fig.3 respectively. The CR-RC shaper and the SAR ADC instead of pipeline ADC will be used for their simplicity in analog circuits and hence the higher power efficiency, hence the development of the low power front-end ASIC is essential.

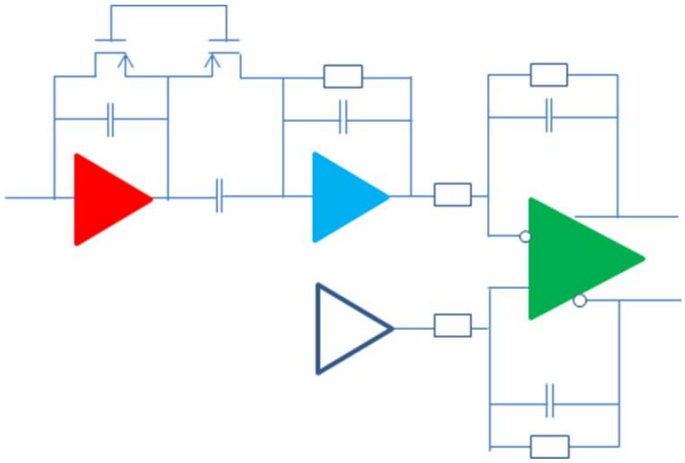

Figure 4.11: The block diagram of the analog front-end. This figure needs work. Either, we can provide more information or we should just delete it. Give a hint of what each block is doing. What are the two inputs to the green triangle?

Dedicated digital filters will be applied to the continuously digitized input signals to suppress the pedestal perturbations caused by the non-ideal effects such as temperature variation and environmental disturbance. Then the data will be compressed by only storing the data packets above a programmable threshold with a specified number of pre- and post-samples. A data head will be added to each packet with its timestamp and other information for reconstruction afterward. The buffered data are readout through high-speed serial links to the DAQ system. The front-end electronics can support both external trigger and self-trigger mode.

Even with the state of the art technology, the TPC front-end electronics on the endplate needs cooling system to keep the temperature stable. Two-phase CO_2 cooling[7] is a well-developed technology and can be used as a baseline solution to bring out the heat generated by the front-end electronics and to keep the temperature of the TPC chamber stable at 20°C. Micro-channel CO_2 cooling has lower mass and may be studied further and can be an alternative technique to copper pipes [8].

The TPC readout electronics are meters away from the collision point, and the radiation dose is rather low ($< 1krad$) at CEPC, which allows us to use standard, radiation soft technologies. On the other hand, energetic particles can always produce instantaneous failure (SEU or SEL) from time to time. Hence radiation sophisticated design needs to be considered that the overall system performance will not be affected or even irreversibly damaged by the rare events.

Critical technology challenges of TPC detector

The mechanical support for the TPC is a challenging issue. The mechanical structure of

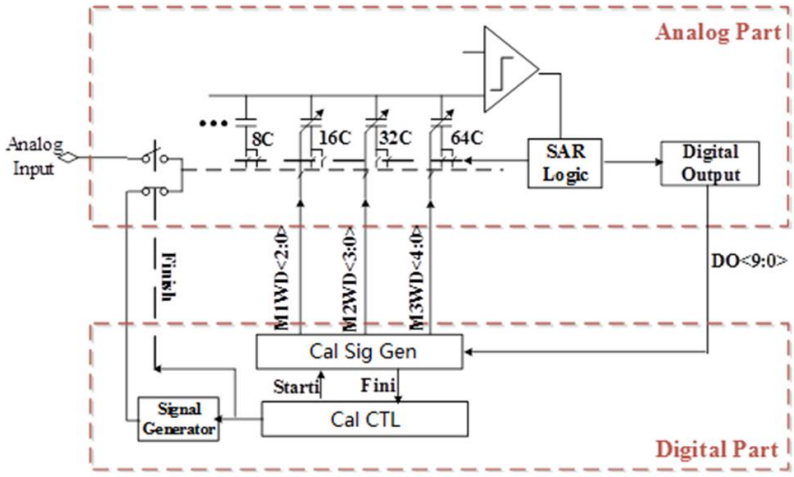

Figure 4.12: The block diagram of the SAR-ADC.

the TPC consists of a field cage, which is made with advanced composite materials, and two readout end-plates that are self-contained including the gas amplification, readout electronics, supply voltage, and cooling. It will be challenging to design and manufacture the TPC support structure with a relatively light material, and at the same time very rigid. Yes, the support structure should be light. However, it is not clear to me that it should be rigid. It appears that some comments here refer to the TPC while others refer to the support structure. I think the issue here is with SUPPORT. Please remove content to do with TPC; it will make it cleaner. It is required to maintain accuracy, robustness in all directions, and stability over long time periods. As the field cage is not strong enough due to the limited material budget, the end-plates become the only choice, where the support structure connects to. In the current stage of design, how the TPC end-plate should be supported is not fixed yet. A promising solution is to suspend from the solenoid, in which a number of spokes run radically along the faces of the calorimeter to the TPC end-plates. A bearing is not the most challenging issue.

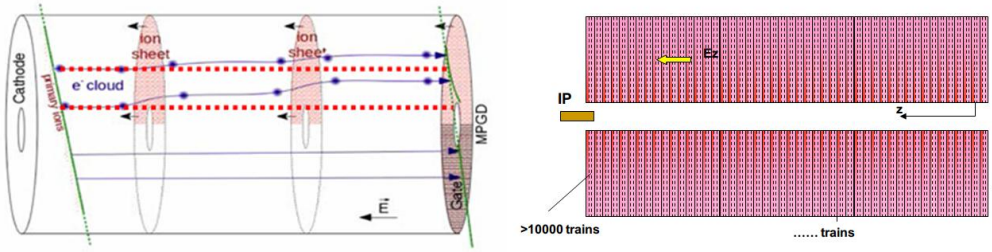

Figure 4.13: The diagram of distortion and ion disks in CEPC.

Ions in the drift volume of the TPC move towards the cathode at a much lower velocity than electrons, and they can accumulate in this volume to build up a significant space charge in the form os 'ion discs' that distort the trajectory of electrons moving towards the anodes. In the CEPC TPC, the majority of ions inside the drift volume are created in the

amplification region and backflow to the drift region. It is therefore important to suppress this ion backflow in order to minimize the deteriorating influence on spatial resolution.

An often used method of backflow suppression is a so-called gating grid; however, it is not applicable here because the bunch spacing of $3.6\mu s$ is short compared with the maximum electron drift time. What is the purpose of the next sentence? It seems to disrupt the flow of thught here. Move it to earlier? It indicates in the figure4.13 of the diagram of distortion and ion disks in CEPC. Another promising option is to exploit the 'built-in' ion backflow suppression of GEMs or MicroMEGAS. In next section, the $R\&D$ study of the hybrid detector module has been promoted to control ions continuously, and the updated results will be described.

4.2.1.3 Simulation and estimation for the key issues

Occupancy requirement of Higgs and Z pole run

Occupancy at 240 GeV center-of-mass energy for Higgs production has been estimated based on the signal cross-section of $200fb$ and the CEPC accelerator design instantaneous luminosity of $2\times10^{34}cm^2s^{-1}$. Occupancy when operting at the Z-pole has been estimated based on a cross-section of $300nbforZ \rightarrow q\bar{q}$) and a luminosity of $2 \times 10^{34}cm^2s^{-1}$. Are the two luminosities meant to be the same?

Using an sample of 9 thousand fully simulated $Z \rightarrow q\bar{q}$ events at center of mass energy of 91.2 GeV[30], we studied the voxel occupancy and the local charge density of the CEPC TPC at Z pole operation for future circular electron positron colliders, with the value of an instant luminosity from $2 \times 10^{34}cm^2s^{-1}$ to $2 \times 10^{36}cm^2s^{-1}$.

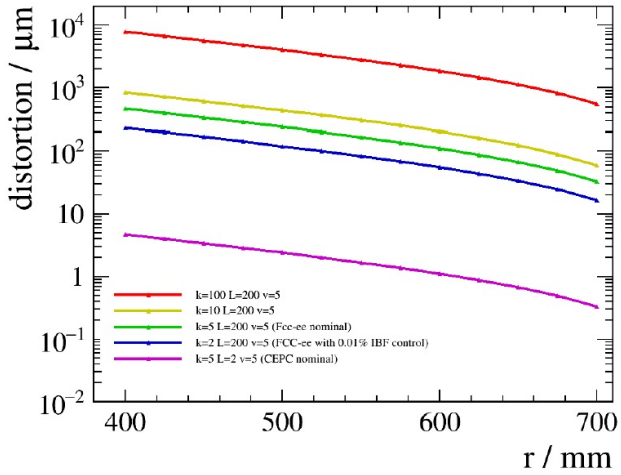

Figure 4.14: Distortion as a function of electron initial r position with different parameters.

Given the fact that the beam bunch is evenly distributed along the accelerator circumference, the voxel occupancy is extremely low ($1.4 \times 10^{-5}/1.4 \times 10^{-7}$ for the innermost layer and $3.4 \times 10^{-6}/3.4 \times 10^{-8}$ for average) and poses no pressure for the TPC usage. The distortion on TPC hit positions induced by the ion charges is estimated with dedicated program and calculation. At instant luminosity of 1×10^{36} and an ion backflow control of percent level, the distortion can be as significant as 10 mm at the innermost TPC layer at the CEPC conceptual detector geometry, which is two orders of magnitude larger than the intrinsic TPC spatial resolution.

A few approaches are proposed to reduce the effects caused by distortion:

1. Ion backflow control technology; the ion backflow should be controlled to per mille level, in other words, only $1 - 10$ backflow ions are allowed for each primary ionization.

2. Dedicated distortion correction algorithm, for the innermost layers, which should result in a mitigation of the hit position distortion by one order of magnitude.

3. Adequate track finding algorithm that could link the TPC track fragments to vertex tracks at high efficiency and purity.

Taking all of these approaches account, the distortion can be mitigated by approximately the safe factors of magnitude. To conclude, the pad occupancy and distortion stress no pressure to CEPC and if the above items can be achieved.

Distortion of Ions backflow in drift length

Early TPCs were equipped with multi-wire positional chambers (MWPCs) as gas amplification devices. The IBF ratio in a standard MWPC is $30 - 40\%$, so a gating grid is essential to prevent ions from reaching the drift volume. In the presence of a trigger, the gating grid switches to the open state to allow ionization electrons to travel into the gas amplification region. After a maximum drift time of about 100 μs (depending on the drift length, electric field and gas mixture), It should not depend on drift length - the maximum drift time should be computed for the maximum drift length. Am I missing something? We should also use the nominal field and mixure. In that case, the entire parenthetic comment can be removed.the gating grid is closed to prevent positive ions from drifting back into the drift volume. Since it must remain closed until the ions have been collected on the grid wires, the ionization electrons are also blocked during this time and the dead time consequently increases.

Triggered operation of a gating grid will, therefore, lead to loss of data. Thus, the TPC at the proposed circular collider will have to be operated continuously, and the backflow of ions must be minimized without the use of a gating grid.

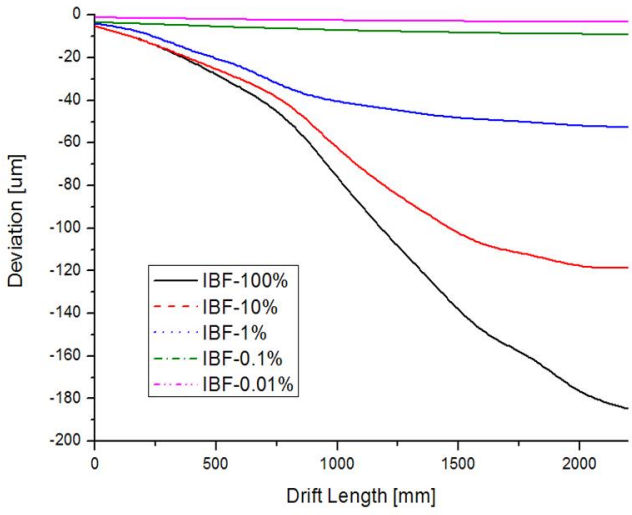

Figure 4.15: Evaluation of track distortions due to space charge effects of positive ions. Lines in legend do not agree with lines in plot

The ions generated from the ionisation in the drift volume or from the avalanche multiplication and have found their way into the drift region will not only introduce field distortion, but also reduce the TPC counting rate capability. This effect is called ion backflow, and should be fully suppressed in the TPC drift volume. With an averaged 300 eV required by per ion-electron ionisation and 2 keV energy loss per mili-meter, there will be roughly $12,000$ primary electrons generated by a track with a typical length of 1.8 m in the TPC and there will be in total 240 k electrons in one event. We must assume a mltiplicty to get to the event-level number. What is it? Also, we worried about curled-up tracks and said they are a concern. In that case, we need to mention it here. At least whether we included their efect or not. With the electron drift velocity of 5 cm/μs, it takes $\sim$ 40 μs for all the electrons to drift 2 m to reach the end-plate. With the expected bunch spacing of 3.6 μs at the CEPC, there will be about 11 events overlapping in the TPC volume. Therefore there will be 240k$\times 11/2 = 1.32$ M electrons continuously drifting toward the end-plate. On the other hand, ions drift much slower than electrons, with a velocity of only 500 cm/s in an electric field of 500 V/cm. This leads to ions from 110,000 events overlapping in the TPC volume. All of the ions should be reduce continuously.

4.2.1.4 Feasibility study of TPC detector module and future work

Hybrid structure TPC detector module

TPC readout with micro-pattern gaseous detectors (MPGDs), especially Gas Electron Multipliers (GEM)and micro-mesh gaseous structures (Micromegas), is very attractive, because the IBF of those detectors is intrinsically low, usually around a few percents. GEM detectors have been extensively proved in the last decade to be the prime candidate, as they offer excellent results for spatial resolution and low IBF. Numerous GEM foils can be cascaded, allowing multilayer GEM detectors to be operated at an overall gas gain above 10^4 in the presence of highly ionized particles. Micromegas is another kind of MPGD that is likely to be used as endcap detectors for the TPC readout. It is a parallel plate device, composed of a very thin metallic micromesh which separates the detector region into a drift and amplification volumes. The IBF of this detector is equal to the inverse of the field ratio between the amplification and the drift electric fields. Low IBF, therefore, favors high gain. However, the high gain will make it particularly vulnerable to sparking. The idea of combining GEM with Micromegas was first proposed with the goal of reducing the spark rate of Micromegas detectors. Pre-amplification using GEMs also extends the maximum achievable gain, so there have also been studies on gaseous photomultipliers with this hybrid configuration.

The TPC detector at the proposed circular collider will have to be operated continuously and the IBF of ions must be minimized without the open/close time of a gating device technology. The gain of the selection detector module can be achieved up to about 5000 without any obvious discharge behaviour. The currents on the anode and drift cathode were measured precisely with an electrometer. The experimental results showed that IBF can be reduced to -0.1% at the gain of about 5000.

To accomplish the physics purposes of the future circular collider, a TPC with superior performance is required. MPGDs with outstanding single-point accuracy and excellent multi-track resolution are needed. We have proposed and investigated the performance of a novel configuration detector module: a combination of GEM and a Micromegas. The detector will be called GEM-MM for short throughout this paper. This study aims to

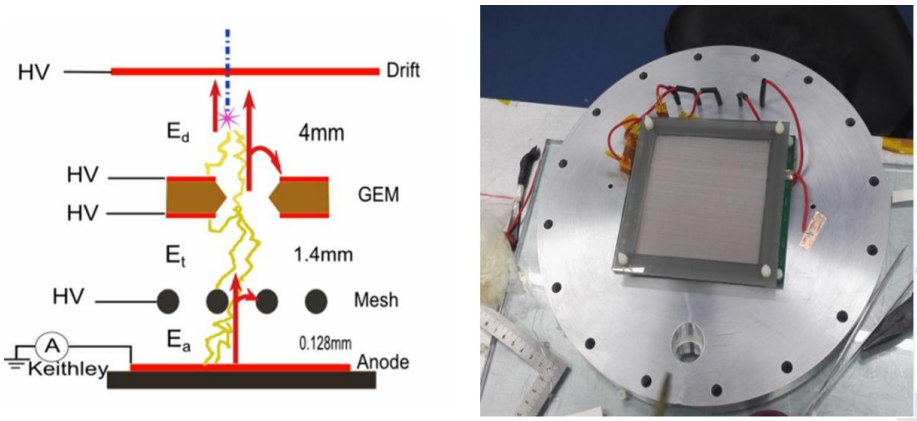

Figure 4.16: Schematic diagram of the detector module.

suppress IBF continually by eliminating the gating grid. The design concept and some preliminary results of the detector module are described as following.

^{55}Fe X-ray source with a characteristic energy of 5.9 keV was used in the test. In the argon-based working gas mixture, a typically pulse height spectrum for a GEM or Micromegas detector contains one major peak corresponding to the 5.9 keV X-rays and an escape peak at lower pulse heights corresponds to the ionization energy of an electron from the argon K-shell.

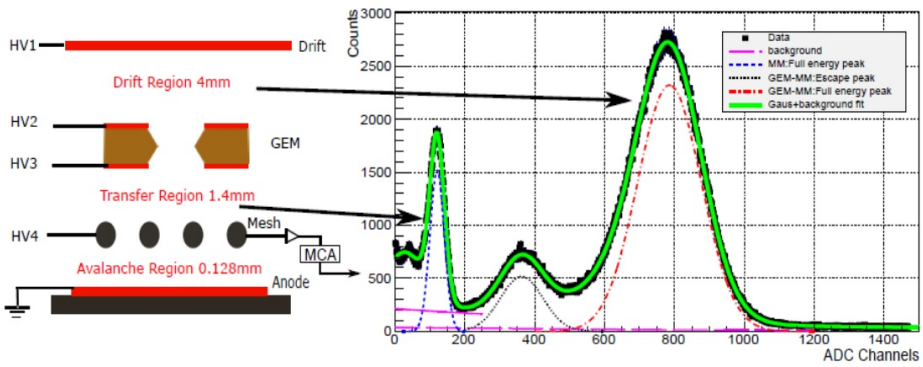

Figure 4.17: Result of the IBF TPC detector module.

In the GEM-MM detector, the situation is different. There are two amplification stages inside this detector. The primary ionization created by photon absorption can be in the drift region or in the transfer region (Figure4.17). Photoelectrons starting from the drift region get amplified by both the GEM detector and the Micromegas detector before they are collected on the anode. If the photons are absorbed in the transfer region, the primary electrons will be amplified only once (by Micromegas).

Figure4.17 depicts a typical ^{55}Fe pulse height spectrum obtained by the GEM-MM detector. Four peaks are seen in the pulse height spectrum. From left, the first peak and the second peak are the escape peak and the full energy peak of the stand alone Micromegas. The last two peaks are created by photons with their energy deposited in the drift region.

These primary electrons show combination amplification. The principle of the GEM-MM detector is fully verified.

Another issue should be considered that is the spacee charge effect to reduce the IBF value. To quantify the effect of IBF in terms of resulting space-charge distortions one can study the gas-dependent parameters as a function of the space-charge density. We make the experiment to confirm the IBF value according to the different X-ray's voltage and current.

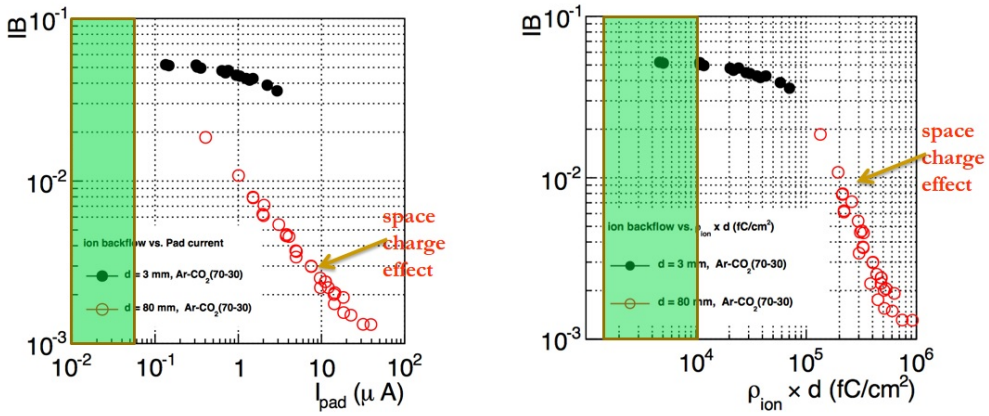

Figure 4.18: Comparison of the IBF with the different X-ray's voltage and current.

Our IBF results just obtained in the green rectangle area, there is no any obvious discharge or spark, and there is no high electrons to led the high space charge to reduce the value of IBF.

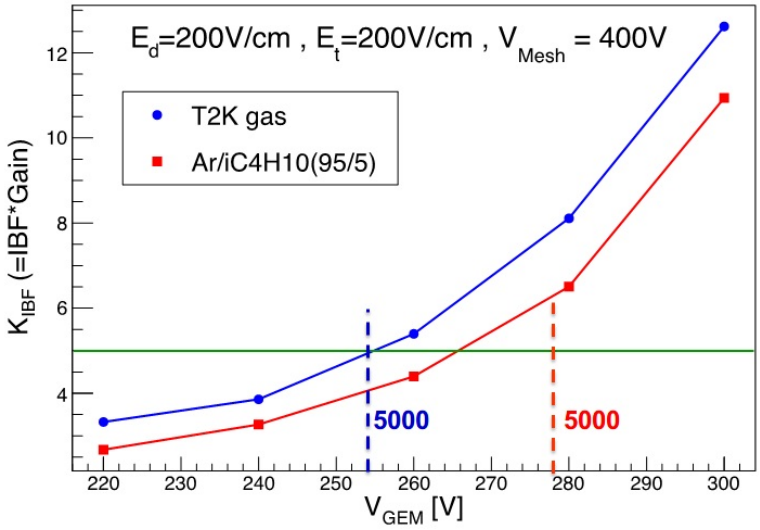

Figure 4.19: Result of the IBF TPC detector module.

A new concept in IBF reduction uses a hybrid structure with one GEM foil above a MicroMega detector. A prototype has been built, and tests have been carried out in Ar/CO_2 (90/10) gas mixture with a 55Fe X-ray source. The pre-amplification effect of GEM foil has been demonstrated in the energy spectrum measurement. With the novel hybrid structure, the effective gain of the GEM can be measured even when it is relatively

low. The energy resolution of this hybrid structure gaseous detector is measured to be 27%(FWHM). The gain properties of this device were measured. A gain up to about 5000 can be achieved without any apparent discharge behavior. The currents on the anode and drift cathode were measured precisely with an electrometer. Out experimental measurements show that IBF can be reduced down to 0.19% at a gain of about 5000.

In 2018, the parameters of the electric field of drift, transfer, GEM detector and Micromegas detector have been optimized testing. The key factor of the gas gain times IBF obtained at the mixtures gases of T2K and Ar/iC_4H_{10} separately. The new results has been shown in the Figure4.19.

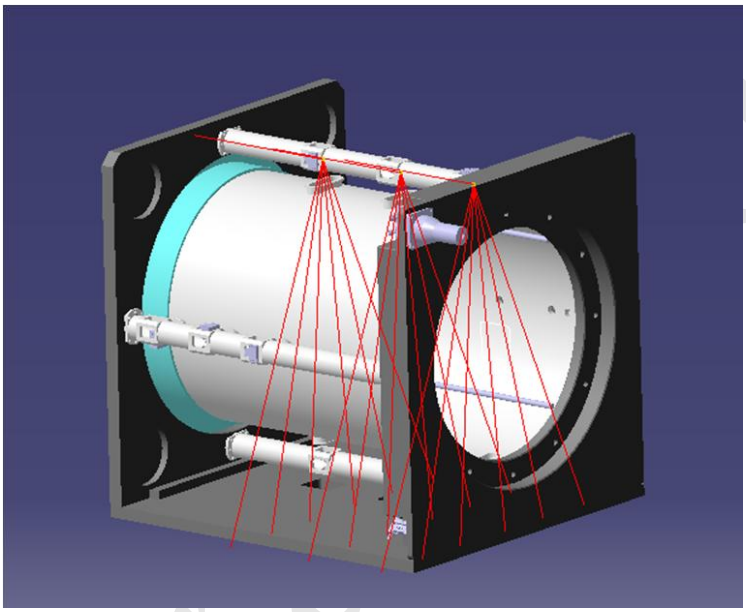

Figure 4.20: Schematic diagram of the detector module with the laser system.

Laser calibration and alignment system

Alaser calibratio system with narrow laser beams inside the drift volume to simulate ionizing tracks at predefined locations will be used for calibration and distortion measurements. The goal is to obtain a uniformity of the TPC drift field within a reasonable relative error corresponding to a spacial resolution of $\sigma_{r\phi} = 100\mu m$. The system can be used for tests and calibration either outside or during normal data taking with the aim of understanding the chamber performance. Of particular interest is the testing of electronics, alignment of the read-out chambers, and measurements of variations of the drift velocity due to mechanical imperfections and non-uniformities in the gas, temperature and the electric and magnetic fields.

The laser system would be used for calibration and distortion measurement in the prototype with one module as a readout or large, A Nd:YAG laser with a wavelength of 266nm shall be used to study the track distortions. An additional UV-lamp could generate additional ions. The complete optical path and the laser power will be split into $6-7$ laser tracks. The laser map coupling into the chamber and the planned laser tracks could be designed. The UV laser beam for calibration and alignment purposes to monitor the drift velocity, operation gas, gain uniformity and electric field. Nd:YAG laser device with 266nm wavelength could make the ionization in the gas volume along the laser path

occurs via two-photon absorption by organic impurities. The laser power should reach $\sim 10\mu J/mm^2$ to equal $10MIP$.

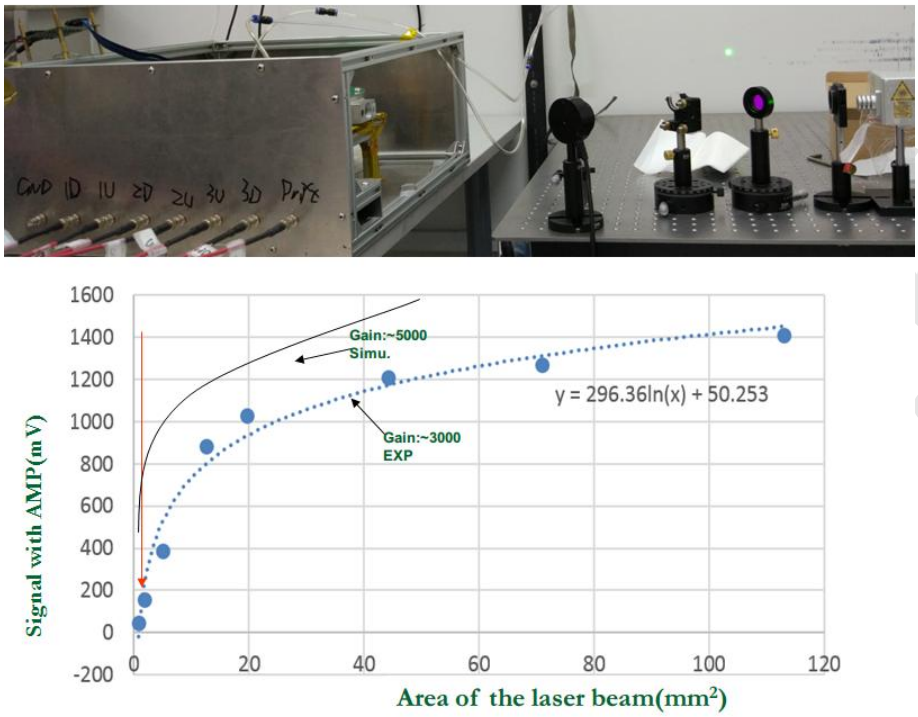

Figure 4.21: Signal with the different size of laser beam.

- Photoelectric laser source with UV light source: Enlights the cathode with UVs could produce photoelectrons to study and monitor distortions, the cathode with UVs to produce photoelectrons to study and monitor distortions, Deuterium lamp with $160nm - 400nm$ of the wavelength as UV light source and smooth Aluminum film as a cathode. To mimic the bunch structure and the ions distortion with UV light lamp by the specific time structure shine controller, UV could create more than about 10000 $electrons/s.mm^2$.

- Calibration laser beam size: The shine and entrance window could use the fused silica as of $99\%\ trans.@266nm$. Provides a UV laser beam for calibration and alignment purposes to monitor the drift velocity, operation gas, gain uniformity and electric field. The ionization in the gas volume along the laser path occurs via two-photon absorption by organic impurities. The study has been done using Nd:YAG laser device has the 266nm of wavelength(4.68eV). The optimization laser beam area of the laser device will be the range from $0.8mm^2$ to $1.0mm^2$ in the figure4.21.

To solve the critical technology problems in CEPC, the hybrid structure MPGD detector module has been developed, and some preliminary results have been obtained and analyzed, the further study will be done from this combination detector module. Another small TPC prototype with 266nm laser calibration system and UV photoelectric function has been designed and would be assembled, and the calibration experiment would be further studied for CEPC.

4.2.1.5 Conclusion

The TPC designed following the CEPC CDR concept provides an excellent starting point for the CEPC TPC R&D, but numerous modifications are foreseen due to the different performance requirements and experimental conditions. Several critical R&D issues have been identified in pre-studies. Possible solutions to those issues have been suggested and will have to be verified with a prototype TPC in future.

Aiming for the CDR and next steps of the CEPC project, two-phase funding scheme is proposed by the funding agency, the Ministry of Science and Technology (MOST) of China. To launch the project, the MOST funded the CEPC accelerator and detector R&D project for phase-I period of $2016-2021$. Among sub-detectors, the feasibility study of the TPC tracker detector was initiated for the purpose to identify feasible technology options and to gain expertise to build the detector units which meet the basic requirements of the CEPC detector design.

4.2.2 Silicon tracker

As described in the PreCDR [31], the silicon tracker, together with the vertex detector and the TPC (Time Projection Chamber, see Section 4.2.1), forms the complete tracking system of CEPC. With sufficiently low material budget to minimize the multi-scattering effect, the silicon tracker provides additional high-precision hit points along trajectories of charged particles, improving tracking efficiency and precision significantly. In addition to complementary tracking, it also provides the following functionalities:

- monitoring possible field distortion in the TPC,
- contributing detector alignment,
- separating events between bunch crossings with relative time-stamping,
- potentially dE/dx measurement.

The transverse momentum resolution can be parameterized as [32]

$$\sigma_{1/p_{\mathrm{T}}} = a \oplus \frac{b}{p \sin^{3/2}\theta} \quad [\,\mathrm{GeV}^{-1}] \tag{4.2}$$

with p and p_{T} in GeV, θ the polar angle, a in GeV^{-1} and b a dimensionless number. The two terms characterize tracking resolution and multiple scattering effect separately. If a track is measured at N points equally distributed along the trajectory, we have

$$a = \frac{\sigma_{\mathrm{SP}}}{0.3BL'^2}\sqrt{\frac{720}{N+4}}$$

where B is in tesla, σ_{SP} in meter is the measurement resolution of each point and L' in meter is the projected length of the track onto the transverse plane. For multiple scattering and for relativistic particles, namely $\beta = 1$, there is

$$b = 0.053\frac{1}{BL'}\sqrt{\frac{L'}{X_0}}$$

where X_0 is radiation length in units of length.

The CEPC physics requirements put required performance on a tracker as

$$a \sim 2 \times 10^{-5}\,\mathrm{GeV}^{-1} \quad \text{and} \quad b \sim 1 \times 10^{-3}. \tag{4.3}$$

At low momenta, less than $50\,\mathrm{GeV}$ for perpendicular tracks, the resolution is dominant with the multiple scattering effect, and at high momenta, the resolution approaches to the tracking resolution, in turn determined by the single-point resolution. Hence, stringent constrain has to be put on material budget.

4.2.2.1 Baseline design

The main characteristic of the baseline design for the CEPC silicon tracker is a silicon envelope [33] around the TPC. It consists of four components: the Silicon Inner Tracker (SIT), the Silicon External Tracker (SET), the End-cap Tracking Detector (ETD) and the Forward Tracking Detector (FTD). The overall layout is shown in Figure 4.22, and the main parameters are summarized in Table 4.5.

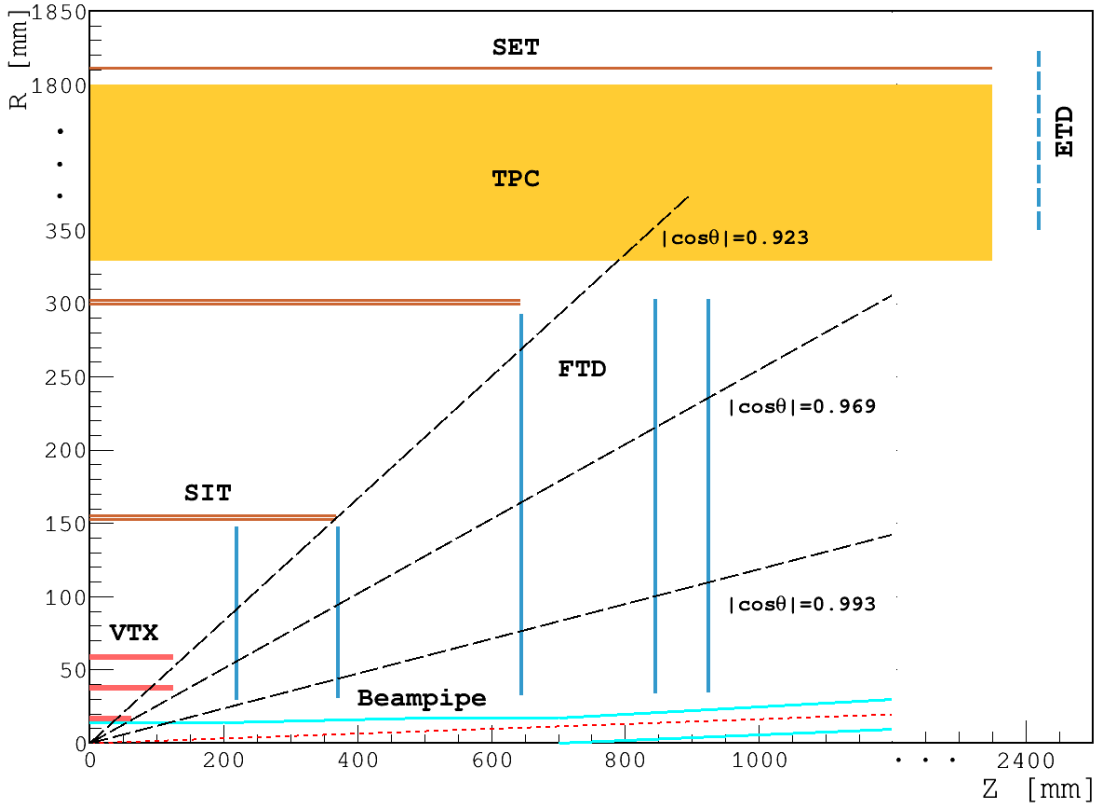

Figure 4.22: Preliminary layout of the CEPC silicon tracker.

The barrel components SIT and SET provide precise hit points before and after the TPC, improving the overall tracking performance in the central region. The SIT helps the link between the vertex detector and the TPC, enhancing the reconstruction efficiency, particularly for low-momentum charged particles. The SET sits between the TPC and the calorimeter and helps in extrapolating from the TPC to the calorimeter. In addition, the good timing resolution of silicon sensors provides time-stamping for bunch separation.

The ETD is positioned in the gap between the endplate of the TPC and the end-cap calorimeter. It helps to reconstruct charged particles with a reduced path in the TPC. The

Detector		Geometric dimensions			Material budget $[X/X_0]$
SIT	Layer 1:	$r = 153$ mm,		$z = 371.3$ mm	0.65%
	Layer 2:	$r = 300$ mm,		$z = 664.9$ mm	0.65%
SET	Layer 3:	$r = 1811$ mm,		$z = 2350$ mm	0.65%
FTD	Disk 1:	$r_{in} = 39$ mm,	$r_{out} = 151.9$ mm,	$z = 220$ mm	0.50%
	Disk 2:	$r_{in} = 49.6$ mm,	$r_{out} = 151.9$ mm,	$z = 371.3$ mm	0.50%
	Disk 3:	$r_{in} = 70.1$ mm,	$r_{out} = 298.9$ mm,	$z = 644.9$ mm	0.65%
	Disk 4:	$r_{in} = 79.3$ mm,	$r_{out} = 309$ mm,	$z = 846$ mm	0.65%
	Disk 5:	$r_{in} = 92.7$ mm,	$r_{out} = 309$ mm,	$z = 1057.5$ mm	0.65%
ETD	Disk:	$r_{in} = 419.3$ mm,	$r_{out} = 1822.7$ mm,	$z = 2420$ mm	0.65%

Table 4.5: Main parameters of the CEPC silicon tracker.

SIT, SET and ETD covers the central tracking region. They form the complete silicon envelope and help in calibrating the tracking system.

The FTD is installed between the beam pipe and the inner cage of the TPC, covering the very forward region. It consists of five silicon disks on each side. The FTD is essential for precise and efficient tracking down to very small (or large) solid angles, where a number of challenges exist: the magnetic field approaching zero along the beam pipe, significantly larger occupancies due to forward going jets and high backgrounds from the interaction region. To achieve the best tracking performance, the FTD needs precise space points, a large lever arm, but low material budget. The baseline design would be a compromise among the constraints. Using highly granular pixel sensors for the first two disks can be foreseen to lower the occupancy and improve the $r\phi$ resolution.

4.2.2.2 Sensor technologies

The basic sensor technology is silicon microstrips for all tracker components except the two innermost FTD disks where silicon pixels are foreseen. Requirements of the single point resolution vary with positions of tracker components, but a general condition of $\sigma_{\mathrm{SP}} < 7\,\mu\mathrm{m}$ is required for high precision tracking. The microstrip sensors have proven to be capable of the resolution, taking into account material budget and power consumption. The baseline features of microstrip sensors will be a large detection area of $10 \times 10\ \mathrm{cm}^2$, a fine pitch of $50\,\mu\mathrm{m}$ and the thickness $< 200\,\mu\mathrm{m}$ to minimize the multi-scattering effect.

The alternative is a fully, or at least for inner components, pixelated silicon tracker. Although the choice of pixel technologies is open, the CMOS pixel sensors (CPS) have gained particular interest. The main advantages of the CPS comparing to the microstrip sensors are two folds:

- Granularity. The CPS provides better single-point spatial resolution and significantly reduces the ambiguity caused by multiple hits in a single strip.
- Material budget. The CPS can be thinned to less than $50\,\mu\mathrm{m}$, whereas the strip sensor is usually a few hundred microns.

As for the cost, because the CPS is based on the standard CMOS procedure in industry, production cost could be significantly reduced for fabricating large area sensors. In addi-

tion, the size of pixels used for the tracker can be comparatively large, hence it's possible to embed complicated circuits in the pixel to simplify the tracker readout circuitry. Initial R&D on large area CPS has been carried out.

Table 4.6 estimates the pixel occupancy of SIT-L1 and FTD-D1. There are a few assumptions in the estimation.

1. The pixel dimension is assumed to be $50\,\mu\mathrm{m} \times 350\,\mu\mathrm{m}$, with which at least in one dimension spatial resolution can reach $7\,\mu\mathrm{m}$ by implementing in-pixel ADC with multiple bits.
2. The track multiplicities in different operation modes are inferred from hit densities in Table 9.4.
3. Readout time of pixel sensors is set as $20\,\mu\mathrm{s}$, the same as that of VTX.
4. Cluster size is set as 9 hits per track.

Table 4.6: Pixel occupancy of SIT-L1 and FTD-D1. See context for explanations.

operation mode	H (240)	W (160)	Z (91)
track multiplicity (BX^{-1})	310	300	32
bunching spacing (ns)	680	210	25
SIT-L1 occupancy (%)	0.19	0.58	0.52
FTD-D1 occupancy (%)	0.17	0.54	0.48

4.2.2.3 Front-End electronics

The Front-End (FE) electronics will depend on the choice of sensor, namely microstrips or pixels.

For the microstrips, custom designed ASICs with deep sub-micron CMOS technology will be used. The chips will provide functions of the analogue to digital conversion (ADC), zero suppression, sparcification and possibly time stamping, together with necessary control circuitry. The high degree digitization is for relaxing the data processing pressure on downstream electronics.

As for the pixels, all FE functions can be realized in a pixel chip, even with some functions, e.g., ADC on pixels themselves. Particular concerns are readout time and electronic channels.

Commonly, the FE chip will be developed in mind with low noise, low power consumption and high radiation tolerance. New developments, such as in the SiLC collaboration and the LHC experiment upgrades, will be good references.

4.2.2.4 Powering and cooling

Powering and cooling are a challenge for the CEPC silicon tracker. It is important to investigate the novel powering scheme based on DC-DC converters, which has been already actively pursued by the ATLAS and CMS experiments for silicon detector upgrades [34–36]. It allows significant reduction in material budget for the low-voltage power cables and gives less power dissipation in the delivery system. Cooling is another critical issue.

Although cooling based on forced cooled gas flow might be still feasible to efficiently conduct away the heat generated by the sensors, ASICs and other electronics, it is important to look into other cooling techniques, such as silicon micro-channel cooling [37], which are being investigated by several other experiments. The technique chosen will have to provide sufficient cooling without compromising the detector performance.

4.2.2.5 Mechanics and integration

There will always be additional challenging aspects of the mechanical design for a large area silicon tracker. A lightweight but stiff support structure can be built based on Carbon fibre Reinforced Plastic material [38]. The support structure, cable routing and electronics common to other sub-detectors need to be carefully designed to minimize the overall quantity of material and make easy construction and integration possible. Precise and quick system alignment might be achieved with dedicated laser monitoring systems, while the final alignment will be accomplished using tracks from well-understood physics events [39].

4.2.2.6 Silicon tracker performance

The performance study described in the section is based on the vertex detector and the silicon tracker.

While the tracking performance in the central region has been extensively studied, the performance in the forward region, which has been designed to cope with the rather short L^*, requires additional careful evaluation. Figure 4.23 shows the estimated transverse momentum resolution for single muon tracks for two polar angles $\theta = 20^\circ$ and 85°, and the analytical results from Eq. (4.2) and Eq. (4.3). Due the reduced lever arm of the tracks and fewer FTD disks in the forward region ($\theta = 20^\circ$), the resolution is worse than the required performance.

Tracking performance of the alternative pixelated silicon tracker has been studied with fast simulation, in which the microstrips are replaced with double-sided pixels with certain single point resolution and material budget reduced to $0.3\%X_0$, the same as VTX. Figure 4.24 shows the transverse momentum resolution for single muons with fixed momentum as a function of polar angle, comparing the pixelated tracker with various single point resolutions to the baseline microstrip tracker. Significant improvement can be observed when the polar angle is below about 20°, in the tracking region of FTD. There is no, however, obvious difference for chosen pixel resolutions, all less than $10\,\mu\mathrm{m}$.

Given the importance for heavy-flavor tagging, the impact parameter resolution, both transverse and longitudinal, is assessed, as shown in Figure 4.25 with muon momentum of $10\,\mathrm{GeV}$. Similar improvements can be observed, even in the high momentum range for the longitudinal impact parameter.

Further comparison is made for tracks at a fixed forward polar angle, 10°, which pass all five FTD disks, as shown in Figure 4.26. Significant improvements can be observed in the whole momentum range for resolutions of transverse momentum and transverse impact parameter. As for longitudinal impact parameter, there is only slight improvement for high momenta, that is understandable because the z-resolution mainly depends on disk positions.

The studies are quite preliminary. There are spaces to optimize the performance of the pixelated tracker, particularly the pixel layout of FTD disks. Some other preliminary studies on the resolution of transverse impact parameter can be found in PreCDR [31].

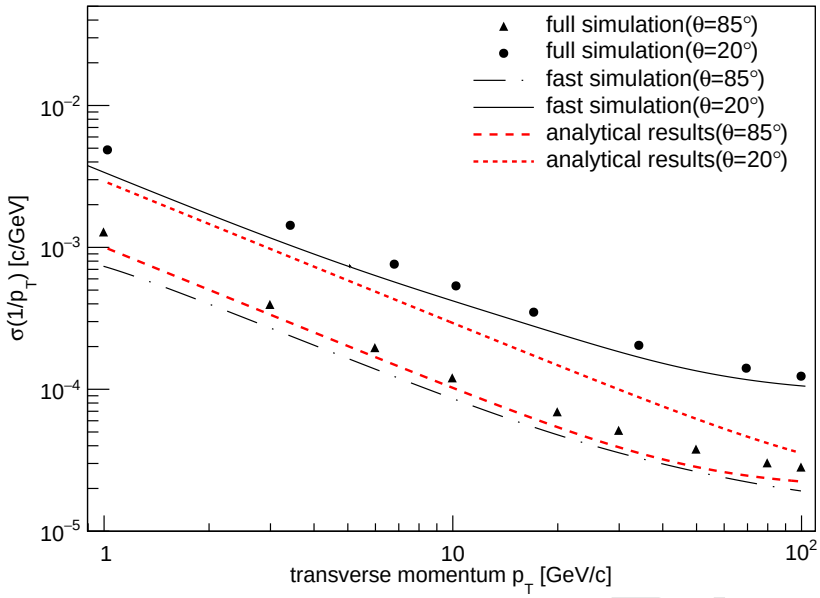

Figure 4.23: Transverse momentum resolution for single muon tracks as a function of the track momentum estimated for the CEPC baseline design with full simulation (dots) and fast simulation (black lines) compared to the analytical results obtained with Eq. 4.2 (red lines).

4.2.2.7 Critical R&D

Silicon technology for large-area tracking detectors will continue to evolve over the next few years [40]. There are ongoing R&D activities conducted by the ATLAS and CMS experiments to develop advanced silicon detectors for the High Luminosity LHC as well as several pioneering R&D projects by the SiLC (Silicon tracking for the Linear Collider) collaboration. Despite the rather different operation conditions and requirements, it is always important to exploit synergies with existing R&D from other experiments to share expertise. During the preliminary studies, several critical R&D items have been identified for the CEPC silicon tracker. All of them, as listed below, will be pursued in the R&D phase of the CEPC project and made available for engineering construction.

- Alternative pixelated strip sensors with CMOS technologies;
- p^+-on-n silicon microstrip sensors with slim-edge structure;
- Front-end electronics with low power consumption and low noise, fabricated with CMOS technologies of small feature size;
- Efficient powering with low material budget and CO_2 cooling techniques;
- Lightweight but robust support structure and related mechanics;
- Detector layout optimization, in particular in the forward region.

It will be vital to develop necessary instrumentation for the module assembly and to verify the detector module performance with beam tests. Prototypes of support structures, including cooling solutions, shall be also built for mechanical and thermal tests.

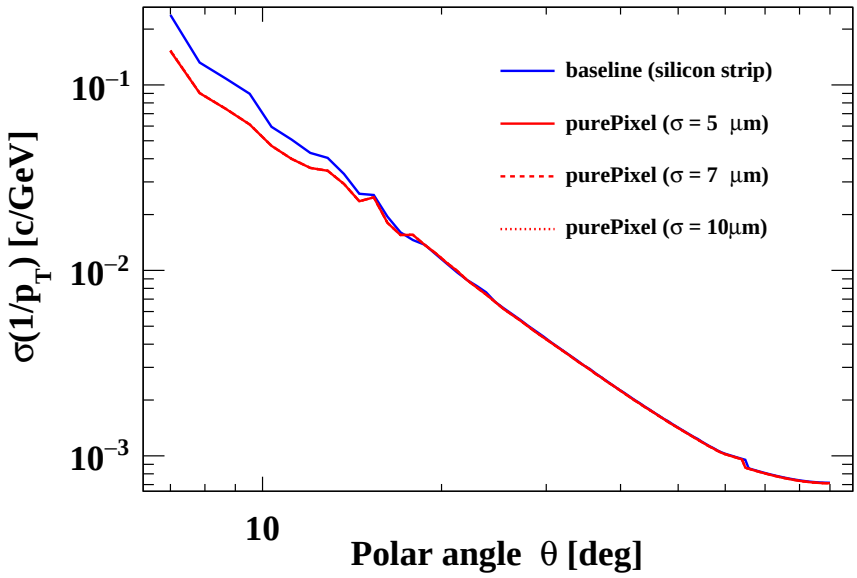

(a) $p = 1\,\mathrm{GeV}$

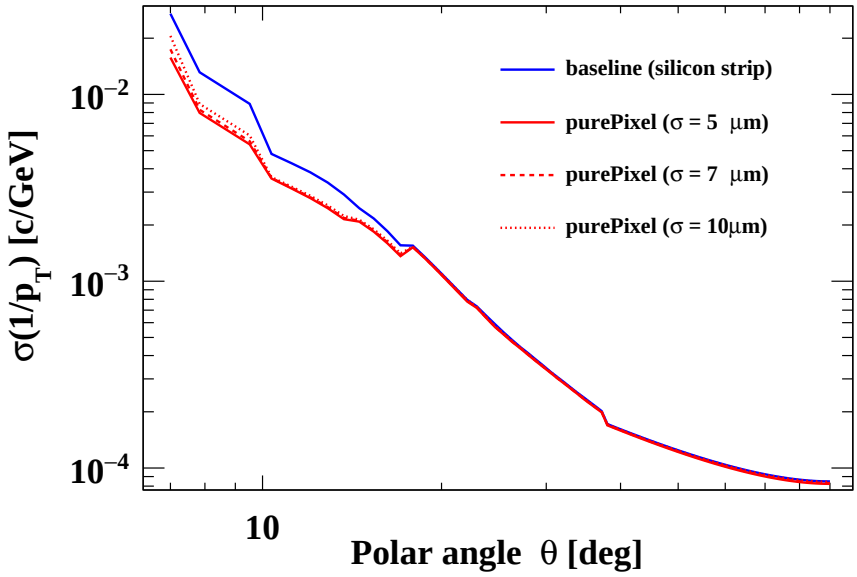

(b) $p = 10\,\mathrm{GeV}$

Figure 4.24: Transverse momentum resolution for single muons with momentum of $p = 1\,\mathrm{GeV}$ (a) and $p = 10\,\mathrm{GeV}$ (b) as a function of polar angle, obtained for the baseline CEPC silicon tracker with microstrips (in blue) and for pixelated tracker (purePixel) with various single point resolutions (in red).

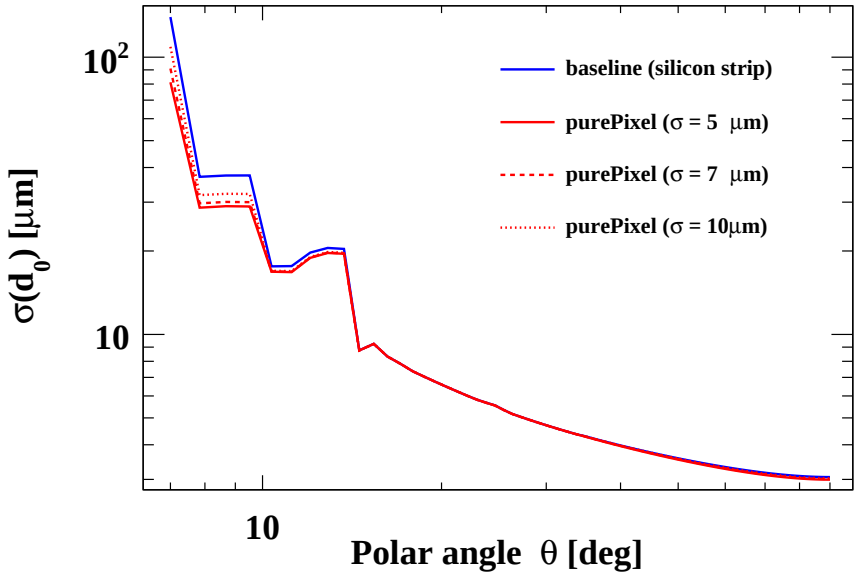

(a) σ_{d_0}

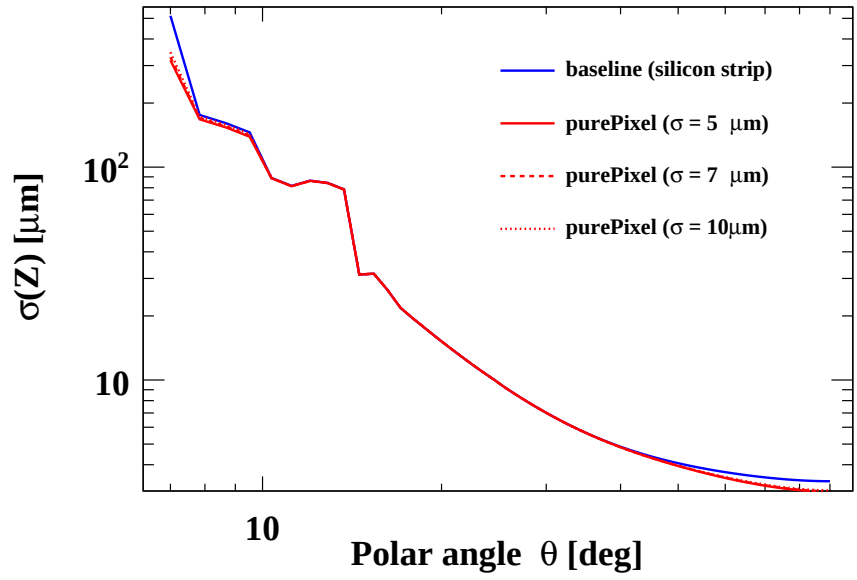

(b) σ_z

Figure 4.25: Transverse (a) and longitudinal (b) impact-parameter resolution for single muons with momentum of $p = 10\,\mathrm{GeV}$ as a function of polar angle, obtained for the baseline CEPC silicon tracker with microstrips (in blue) and for pixelated tracker (purePixel) with various single point resolutions (in red).

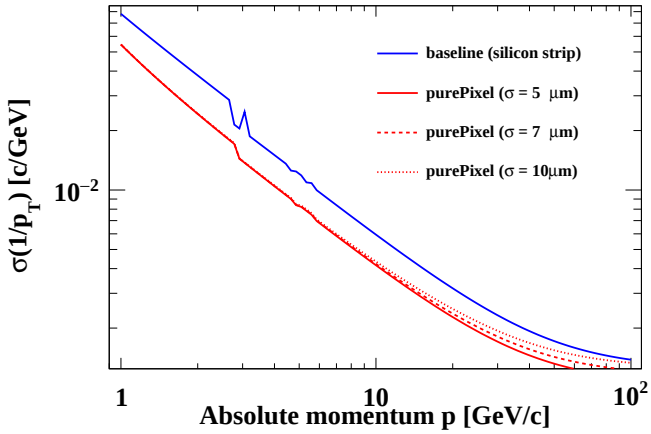

(a) σ_{1/p_T}

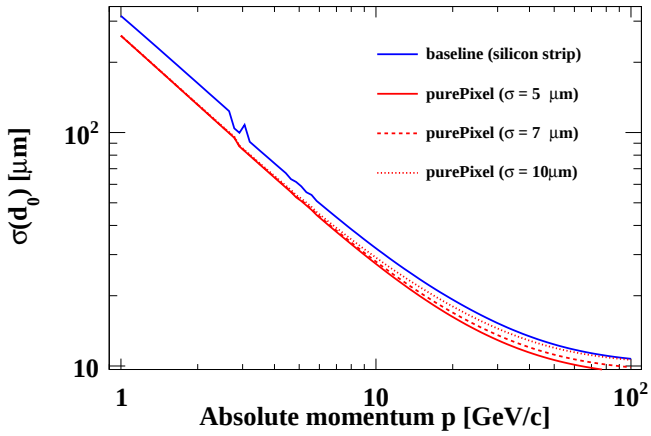

(b) σ_{d_0}

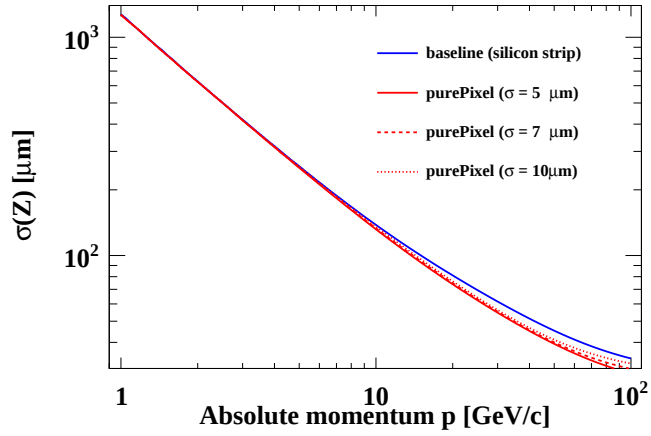

(c) σ_z

Figure 4.26: Transverse momentum (a) and transverse (b) and longitudinal (c) impact-parameter resolution for single muons with the polar angle of 10° as a function of the track momentum, obtained for the baseline CEPC silicon tracker with microstrips (in blue) and for pixelated tracker (purePixel) with various single point resolutions (in red).

4.3 Full-silicon tracker detector

A full-silicon tracker is also an option for the CEPC Main Tracker. It offers a well known technology that provides excellent space point resolution and granularity to cope track separation in dense jets and hits from the high luminosity beam related background. Potential drawbacks include the relatively high materia density within the tracking system, less redundancy, and limited dE/dx measurements. This Section will demonstrate that the full-silicon tracking concept is a viable option for CEPC within the main tracker detector envelope as used in the CEPC baseline layout of TPC and silicon tracker in the previous subsection. While the boundary conditions are held fixed in this study, we have optimzied the layout with the number of silicon layers, single vs double sided, and support maerial using a toy simluation below. The parameters used in this study are summaried in the following:

- the solenoid B field is set to 3 Tesla,
- the tracking envolope consists of a cylinder with a radius of 1.83 m and a length of 4.6 m,
- the tracker covers down to 7.25 degree from the beam pipe,
- the Be beam pipe has a radius of 1.45 cm and 14 cm long.

4.3.1 Full silicon tracker layout

The CEPC baseline detector relies on a mixture of Time Projection Chamber (TPC) and silicon tracking system. However, the tracker could be converted using full silicon if the TPC is replaced with additional silicon stereo-strip layers (SIT) in the central region with disks of silicon stereo-strip detectors (FTD) on each side. In this design, the outer tracking system consists of a full-silicon tracker arranged as a set of six nested SIT layers in the central region with five FTD strip endcap disks on each side as shown in Figure 4.27. Details for design of SIT and FTD detectors can be found in the discussion of the silicon tracker of the CEPC baseline design in Section 4.2 and we will use the similar module design to build a full silicon detector as CEPC-FST. The modification is to change the thickness of layers and the stucture of the support. The pixel vertex detector (VXD) is kept the same as in the CEPC baseline detector.

This new proposed tracking system provides at least 11 precisely measured points for all tracks down to a polar angle of about 15 degree and at least 7 measured points down to a polar angle of about 7.25 degree, as shown in Figure 4.28. With three double pixel layers and forward disks covering a wide of polar angle, they are capable of providing excellent tracking on their own. The outer tracker adds additional track-finding constrains at large radii where hit density is low while improving the momentum measurement over a large level arm with excellent hit resolution in the transverse plane.

Alternatively, we start with the design of ILC-SID detector for CEPC by enlarging the outer silicon strip layers to fill the space up to a radius of 1.83 m and z at $\pm$ 2.3 m in order to achieve comparable momentum resolution using a lower solenoid B filed of 3 Tesla as shown in Figure4.27. The pixel detectors again are kept the same as in the ILC-SID design. We will label this option as CEPC-FST2, which provides an independent cross check on the tracking performance for a full-silicon tracker. The number of expected hits on the track from CEPC-FST2 is also shown in Figure 4.28.

Table 4.7 summarizes the geometry parameters of the proposed outer strip silicon trackers for CEPC for the two variants of the layer and disk configurations that were investigated.

I think we should present ONE and not TWO layouts here. There are already three options for Main Tracker; having sub-options within each option is overkill that will just confuse the reader. All the figures seem to say FST rather than FST2. If indeed most/all of the work has been done with FST, that would be the one to keep.

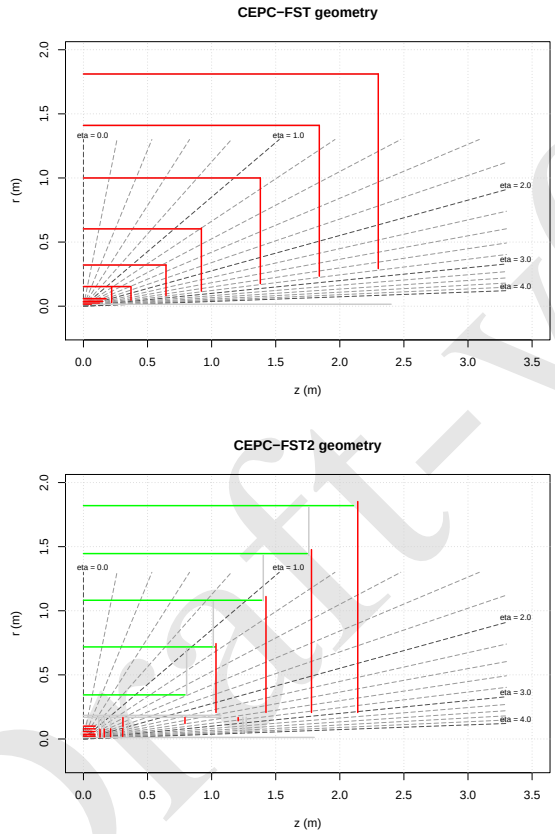

Figure 4.27: The R-Z view of the full silicon tracker proposed for CEPC-FST (top) and CEPC-FST2 (bottom). Both layout positions and layout type are different for CEPC-FST and CEPC-FST2.

4.3.2 Toy simulation

For each layout, we use a toy simulation (Idres) to calculate the expected tracking resolution as function of track momentum for a given incident angle θ, in which the effect of multiple scattering due to the materia are taken into account correctly. Idres was developed by the ATLAS experiment [41]. The results are also cross checked using LDT program [42], which gives a consistent result.

The coverage of the full-silicon tracking system is shown in Figure 4.28 as function of track pesudo-rapidity. At least 7 hits are measured for all tracks with a polar angle down to about 7.25 degree. The total radiation length for all-silicon tracking systems, including dead material such as readout, cables and supports, is about 5-7% for CEPC-FST and 7-10% for CEPC-FST2, respectively.

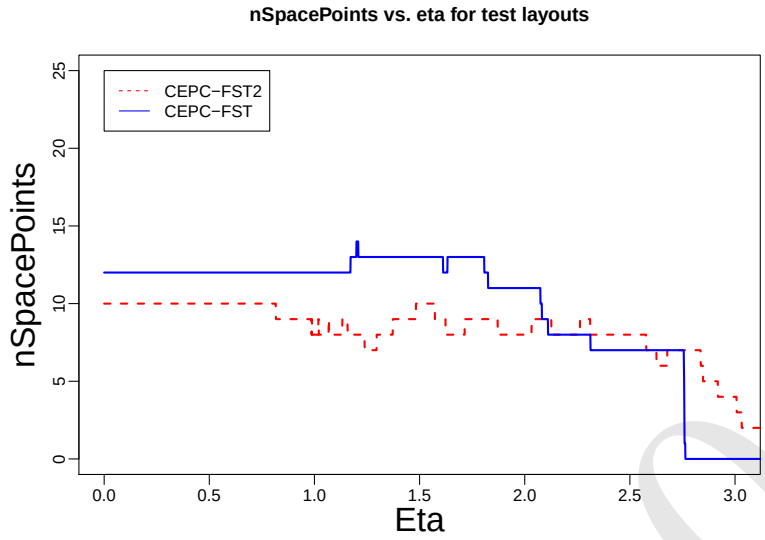

Figure 4.28: The number of expected hits are shown as function of track pesuro-rapadity.

The expected momentum (p_T) and impact parameters (d0, and z0) resolutions are compared as function of track p_T in GeV/c for tracks with $\theta = 85$ and 20 degree, respectively, as shown in Figure 4.29. The z0 resolution is better for CEPC-FST than for CEPC-FST2 due to extra stereo-strip layers while the p_T and d0 resolutions are similar.

4.3.3 Detector simulation and reconstruction

In order to optimize the full silicon tracker detector for CEPC, we generate several benchmark processes that include single muon events, $e^+e^- \rightarrow ZH \rightarrow \nu\nu\mu\mu$, and $e^+e^- \rightarrow ZH \rightarrow \nu\nu GG$ (two gluon jets). The events are then simulated and reconstructed using different detector geometries, which are then used for the tracking performance studies.

4.3.3.1 CEPC-FST detector

The implement of geometry for the CEPC-FST detector is based on a simulation tool Mokka[43]. The CEPC baseline detector is based on a version of database cepc_v4 as summary in Table 3.2, in which the tracker is composed of VXD, SIT, TPC, SET and FTD. In order to implement a full-silicon-tracker, the TPC and SET are considered to be replaced with a new silicon-based strip tracker based on the design of SIT layers and disks while keeping the rest of detectors same as in cepc_v4.

In order to improve the flexibility of design, a new package of SiTracker is implemented in Mokka which represents the silicon tracker by planar structure, which consists of a thin layer of silicon with 150 μm thickness and 50 μm pitch size. For VXD and SIT, they are composed by several layers, and each layer is composed by several ladders, and each ladder is divided to several sensors. The SIT layer consist of double silicon layers mounted back to back with a stereo-angle of 7 degree. For FTD, it is composed by several pixel disks FTD_PIXEL and several double-side strip disks FTD_STRIP that are composed by petals. The strip FTD disk has two sensitive silicon sub-layers on each side with a stereo-angle of 5 degree. The number of ladders/petals, the size and position of layers, and the

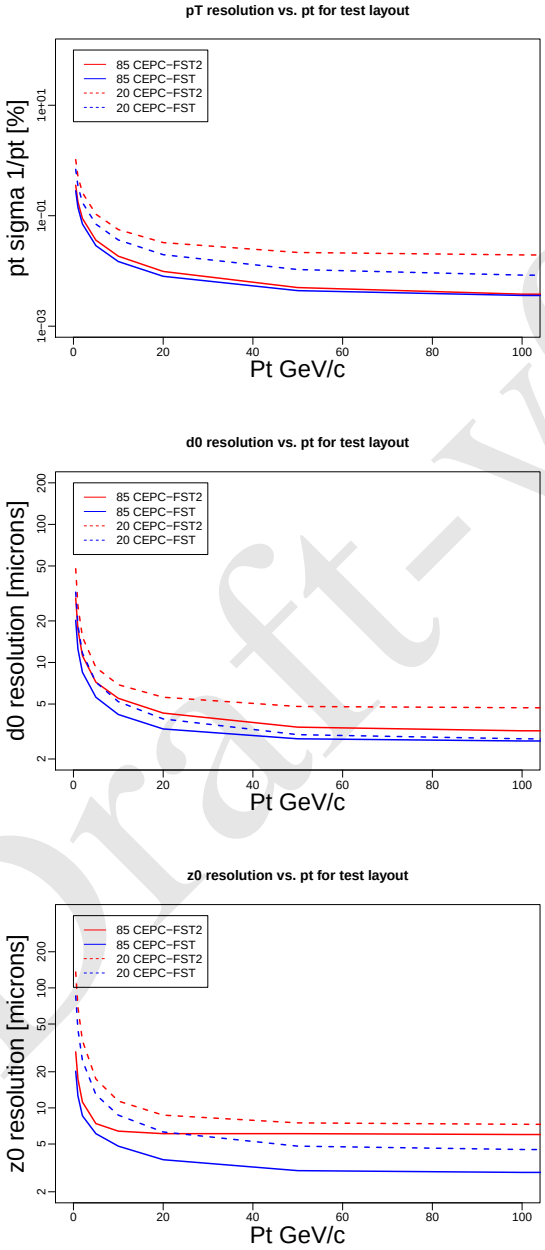

Figure 4.29: The expected p_T, d0, and z0 resolutions from the toy simulation (Idres) are compared as function of track p_T in GeV/c for tracks with $\theta = 85$ and 20 degree, respectively.

Table 4.7: The proposed geometry parameters for the outer strip barrel layers and disks, where D and S stand for double and single-strip layer.

	CEPC-FST				CEPC-FST2			
Barrel	R (m)		±z (m)	Type	R (m)		±z (m)	Type
layer 0	0.153		0.368	D	0.344		0.793	S
layer 1	0.321		0.644	D	0.718		1.029	S
layer 2	0.603		0.920	D	1.082		1.391	S
layer 3	1.000		1.380	D	1.446		1.746	S
layer 4	1.410		1.840	D	1.820		2.107	S
layer 5	1.811		2.300	D				
Endcap	R_{in} (m)	R_{out} (m)	±z (m)	Type	R_{in} (m)	R_{out} (m)	±z (m)	Type
Disk 0	0.082	0.321	0.644	D	0.207	0.744	1.034	D
Disk 1	0.117	0.610	0.920	D	0.207	1.111	1.424	D
Disk 2	0.176	1.000	1.380	D	0.207	1.477	1.779	D
Disk 3	0.234	1.410	1.840	D	0.207	1.852	2.140	D
Disk 4	0.293	1.811	2.300	D				

sub-structure of layers can be modified easily in input file as globalModelParameter. In future, a XML structure is considered as the method to input parameters. Based on these layouts of CEPC-FST, the material budget of the whole tracker is about 5% in the barrel region and about 8% in the endcap region as shown in Figure 4.30, which also shows the material budget of each part of the tracker. In the endcap region, the zigzags are caused by the alternation and overlap of layers. The radiation lengths of support layers of SIT and FTD are larger than what in the baseline detector, because the support struture like what in SiD is used. Therefore, the material budget is reduced obviously.

The lcio format is used to output the simulated signals from the full-silicon-tracker, same as other sub-detector system [44]. The digitization and clustering are done in reconstruction process. In the default version, a smearing technology based on truth information is used as a simple digitization and clustering, which is used for this study. Recently, a new digitization for silicon-based detector has been developed. It first finds out the pixel which the hit is located, and uses the center of the pixel or strip as the new position for the hit. And then those hits in same pixel or neighnoring will be merged into single hit.

A new conformal tracking algorithm has been adapted for the full silicon tracker, which is developed as the main track pattern recognition algorithm at CLIC [44] at FCC-ee. Through the conformal transform $u = \frac{x}{x^2+y^2}$ and $v = \frac{y}{x^2+y^2}$, where x and y are the positions of the track hits in the detector space, the positions of the track hits in the conformal space lie at a straight line for the track in a magnetic field. Therefor, track finding becomes straight line searching in the pattern recognition. Currently, a cellular automaton is used as pattern recognition for the straight line searching.

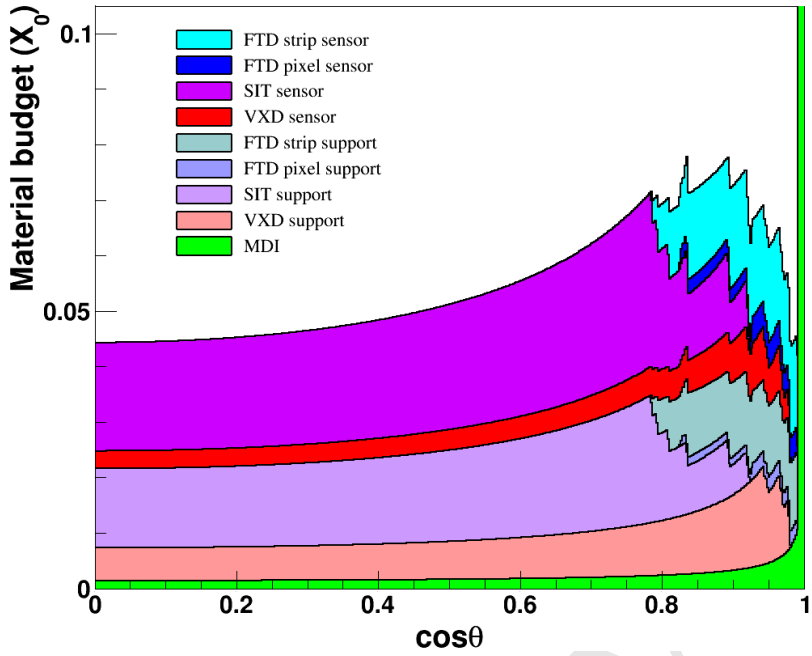

Figure 4.30: The material budget for the CEPC-FST. Comparing to the baseline detector, some differences on the thickness of silicon layers cause the difference for VXD, FTD and SIT.

4.3.3.2 CEPC-FST2 detector

For CEPC-FST2, events were simulated and reconstructed using a software developed for the International Linear Collider (ILC) [45, 46], but re-worked for the HepSim project [47, 48]. The response of the CEPC-FST2 detector to physics events is simulated using the "Simulator for the Linear Collider" (SLIC) 5.0 software [49] interfaced with the GEANT4 10.3p1 program [50]. The track reconstruction was performed with the LCSIM 4.0 package [44] using the "seed tracker" algorithm as for the SiD detector simulation. Track candidates with at least six hits in the silicon pixel and microstrip layers were considered. Only tracks with a minimum transverse momentum (p_T) of 100 MeV were accepted. The track-fitting was performed with the following requirements; maximum distance of closest approach (DCA) is $|DCA| < 6$ mm, $|z_0| < 10$ mm, and fit $\chi^2 < 10$. The reconstruction includes particle-flow algorithms (PFA) which enable identification and reconstruction of individual particles. The PFA objects can be reconstructed using the software algorithms implemented in the PANDORA package [51, 52].

The geometry of CEPC-FST2 detector is implemented using the compact XML geometry description, which can load and built at runtime. The main changes over the ILC-SID detector include the reduced B-field from 5 Tesla to 3 Tesla. The outer tracker is scaled up by a factor of about 1.44 to the radius of 1.83 m and z of $\pm$ 2.3 m. The silicon module sizes were appropriately scaled. The first inner layer of the barrel vertex detector was positioned at 15 mm, just outside of the beam pipe. The outer barrel layer of the silicon vertex detector was moved to 100.3 mm (vs 59 mm for the SiD detector), while other barrel layers are equally spaced. The forward disks, together with the support structures, were appropriately scaled in z by a factor 1.37.

As for the SiD detector, the barrel tracker consists of five layers of silicon sensors with 50 μm pitch. The forward tracker has four disks of silicon sensors. The silicon pixel

detector had 20 μm pitch, consisting of five layers in the barrel and six disks in the forward region. The hadronic and electromagnetic calorimeters, as well as the muon detector, were optimized for CEPC physics as described in [53].

4.3.4 Tracking performance

After the detector simulation and reconstruction, the tracking performances are measured in terms of efficiencies, fake rates, momentum resolution, and the impact parameter resolutions using single muons or $e^+e^- \rightarrow ZH$ events. The tracking efficiency is defined as a fraction of stable charged particles that can be matched to well reconstructed tracks. The stable particles are defined as those charged particles with p_T >1 GeV/c in the detector fiducial region ($9 < \theta < 170$ degree), originated from the interaction point, and lived long enough to reach the calorimeter. A well reconstructed track is defined as sharing more than 50% of its assigned silicon hits originating from a single particle (truth hits). We define a truth hit fraction as ratio of truth hits over total assigned hits of the track using silicon hits only. A poorly reconstructed track is defined to have the truth hit fraction less than 50%. The fake rate is defined as the fraction of poorly reconstructed tracks out of total reconstructed tracks, but this requires a realistic detector simulation, which we are not there yet. Since the CEPC baseline and the CEPC-FST detectors are sharing the common software and design, we will focus on their tracking performance comparisons to demonstrate that the full-silicon tracking concept is a viable option for CEPC.

4.3.4.1 Single muon particle

Figure 4.31 shows the tracking efficiency for single muons in CEPC-FST as function of p_T. The tracking efficiency is close to 100% at high p_T and slightly lower at small p_T. The trend is the same for CEPC baseline (v_4) , which indicate both trackers are capable of finding tracks efficiently in the detector fiducial region.

Since the track resolution depends on the track angle θ, we divide the tracks in the barrel region with $40 < \theta < 140$ degree and in the endcap region with $7.25 < \theta < 40$ degree or $140 < \theta < 172.75$ degree. Figure 4.32 shows the track resolutions of p_T, d0, and z0 as function of track p_T in the barrel and endcap region. The resolutions seem comparable to each other, but they seem slightly better for the low momentum tracks in the CEPC v4 detector (TPC+Silicon) than CEPC-FST due to extra materia in the detector while they are compatible at the high p_T.

4.3.4.2 Di-muon mass resolution

Figure 4.33 shows the di-muon invariant mass distributions from $ZH \rightarrow \nu\nu\mu\mu$ decay between different detector configurations. The higgs mass used in the simulation is 125 GeV/c^2. The di-mass from CEPC baseline detector seems shifted by 0.2 GeV from the input Higgs mass while the mass from CEPC-FST agrees with the expectation. The di-muon mass resolution from CEPC-FST has $\sigma = 0.21$ GeV/c^2 and seems 14% better than ones obtained from CEPC baseline detector.

4.3.4.3 Tracking inside the jets

In order to study the tracking performance inside the jets, we generated and simulated some Higgs decaying into two gluon jets (GG) in $zH \rightarrow \nu\nu GG$ events. Figure 4.34 shows the tracking efficiency inside the jets as function of track momentum. The efficiency of

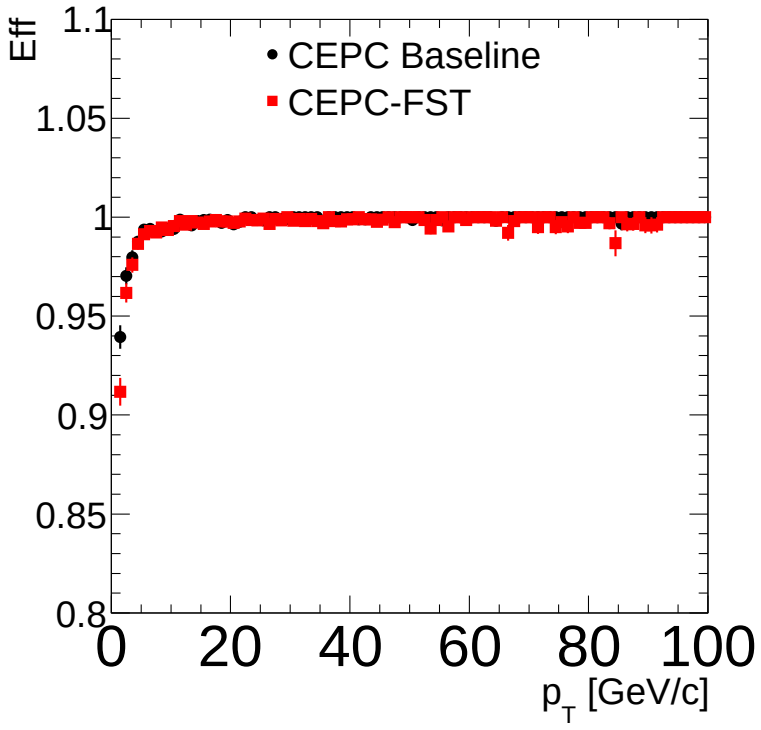

Figure 4.31: The tracking efficiencies are measured as function of p_T for single muons using CEPC baseline (v4) and CEPC-FST detetcors.

finding tracks inside the jets is very similar between the CEPC baseline and the CEPC-FST detectors, which is close to 97%.

4.3.5 Conclusion

We present a preliminary study of full silicon tracker option as an alternative design for CEPC tracker. Two approaches are considered for the design: the first is to keep the silicon detectors (VXD, SIT, FTD) in the CEPC baseline detector and replacing TPC with additional silicon detectors, the second is to optimize the ILC-SID tracker to fulfil the CEPC tracking volume in order to achive the excellent momentum resolution using 3 Tesla B field. The new detector geometry has been implemented in the simulation and the track reconstruction has also been adoped for the full silicon tracker. The initial study of the tracking performance looks promising. There are still many improvements needed in the simulation and reconstruction in order to explore the full potential of the full-silicon tracker.

4.4 Drift chamber tracker detector

4.4.1 Introduction

The drift chamber (DCH) is another option for the CEPC Main Tracker. It is designed to provide good tracking, high precision momentum measurement and excellent particle identification by cluster counting.

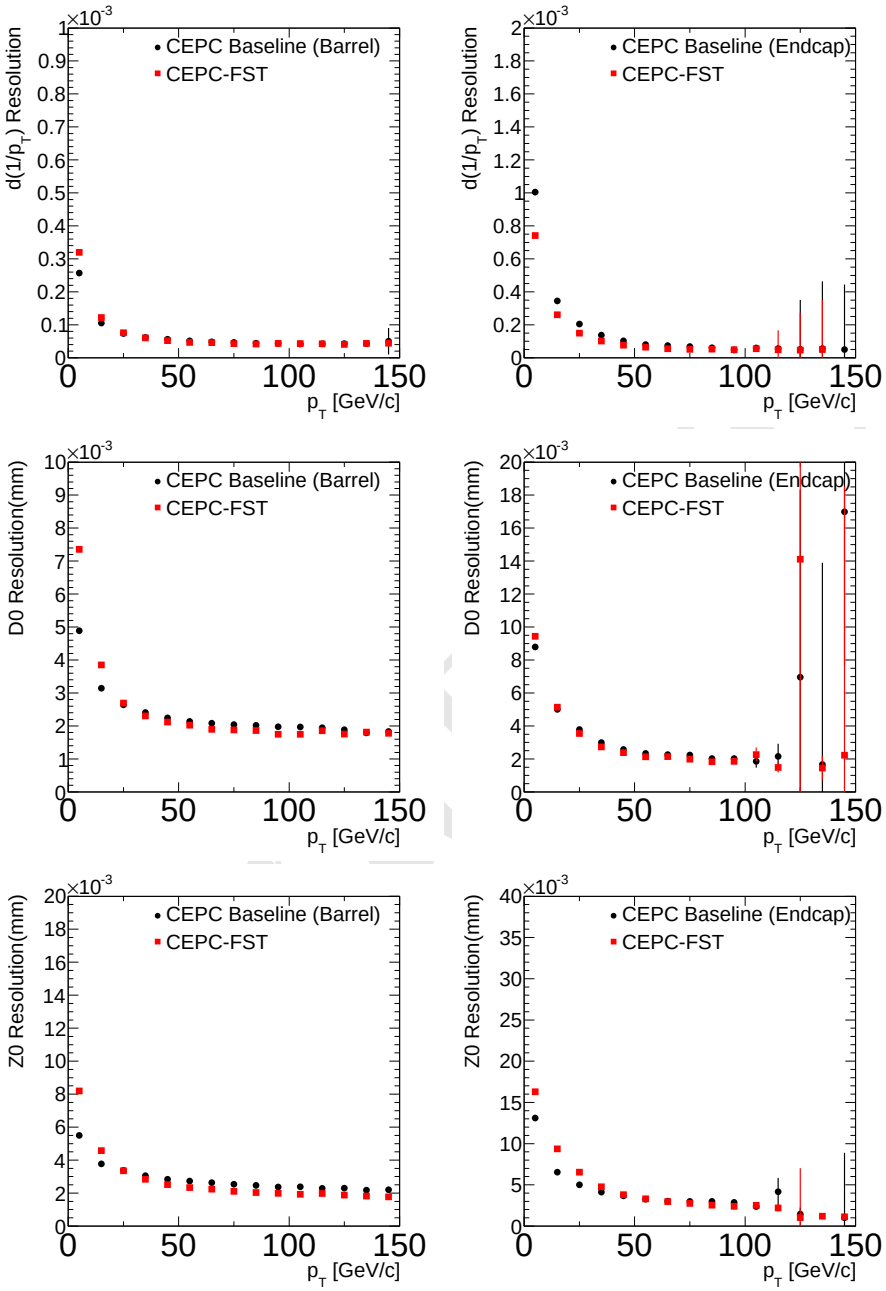

Figure 4.32: The tracking p_T, d0, and z0 resolutions are measured as function of p_T using single muons, left in the barrel region and right in the endcap region. They are compared between CEPC v_4 and CEPC-FST detectors. The resolutions for the low momentum tracks in the CEPC baseline detector seems slightly better than CEPC-FST, due to extra materia in the detector.

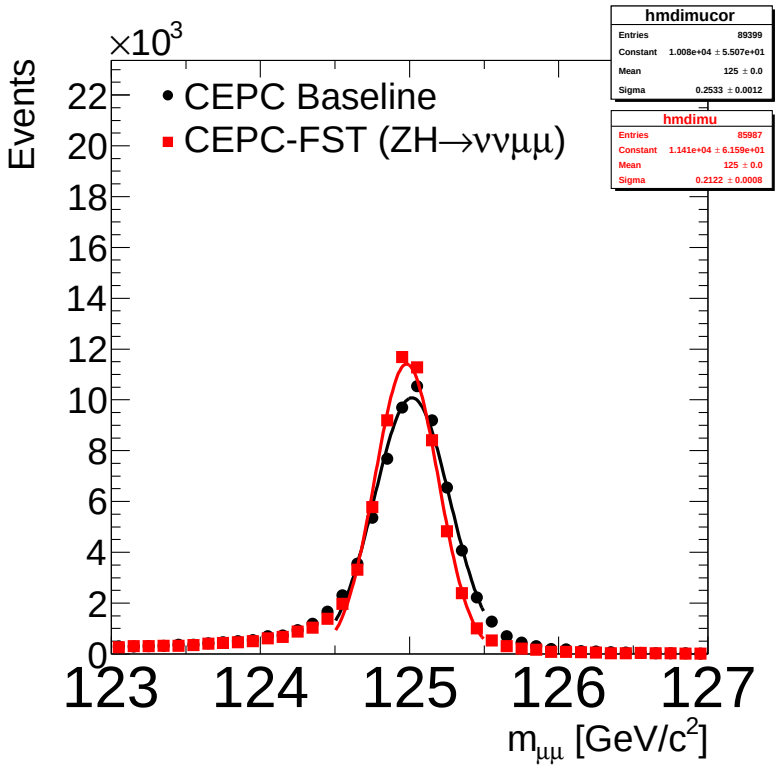

Figure 4.33: The di-muon mass distribution is compared from CEPC baseline and CEPC-FST detectors.

Main peculiarity of this drift chamber is its high transparency, in terms of radiation lengths, obtained thanks to the novel approach adopted for the wiring and assembly procedures. The total amount of material in radial direction, towards the barrel calorimeter, is of the order of $1.6\%\ X_0$, whereas, in the forward and backward directions, this is equivalent to about $5.0\%\ X_0$, including the endplates instrumented with front end electronics. The high transparency is particularly relevant for precision electroweak physics at the Z pole and for flavour physics, where the average charged particles momenta are in a range over which the multiple scattering contribution to the momentum measurement is significant.

Original ancestor of the DCH design is the drift chamber of the KLOE experiment[54], more recently culminated in the realisation of the MEG2[55] drift chamber.

4.4.2 Overview

The DCH is a unique volume, high granularity, all stereo, low mass cylindrical drift chamber, co-axial to the 2 T solenoid field. It extends from an inner radius R_{in} = 0.35 m to an outer radius R_{out} = 2 m, for a length L = 4 m and consists of 112 co-axial layers, at alternating sign stereo angles (in the range from $50\,mrad$ to $250\,mrad$), arranged in 24 identical azimuthal sectors. The square cell size (5 field wires per sense wire) varies between 12.0 and 14.5 mm for a total of 56,448 drift cells. Thanks to the peculiar design of the wiring procedures, successfully applied to the recent construction of the MEG2 drift chamber, such a large number of wires poses no particular concern.

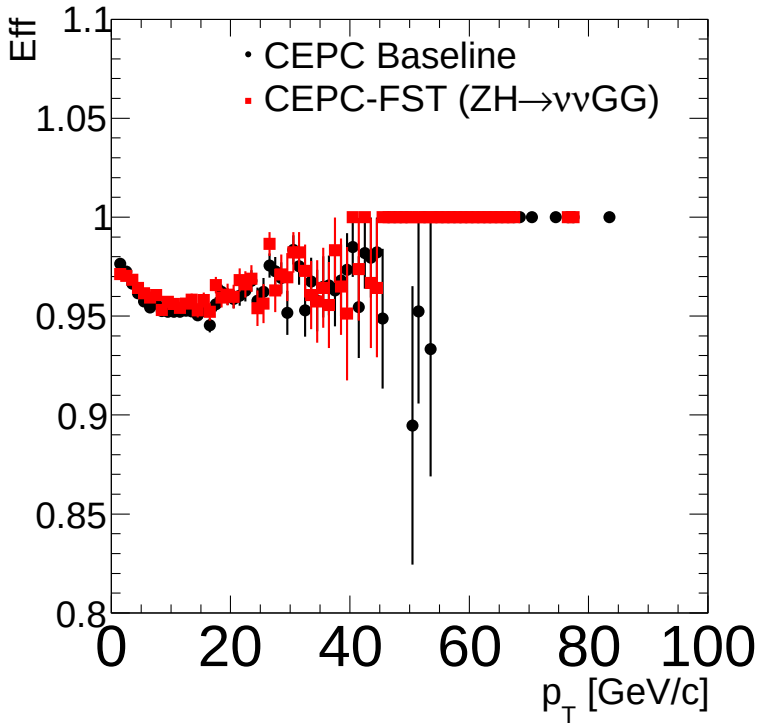

Figure 4.34: The tracking efficiencies for the stable particles inside the gluon jets as function of track p_T with CEPC_v4 and CEPC-FST.

A system of tie-rods directs the wire tension stress to the outer endplate rim, where a cylindrical carbon fibre support structure bearing the total load is attached. Two thin carbon fibre domes, suitably shaped to minimise the stress on the inner cylinder and free to deform under the gas pressure without affecting the wire tension, enclose the gas volume.

The angular coverage, for infinite momentum tracks originated at the interaction point and efficiently reconstructed in space, extends down to approximately $13°$.

In order to facilitate track finding, the sense wires are read out from both ends to allow for charge division and time propagation difference measurements.

The chamber is operated with a very light gas mixture, $90\%He - 10\%iC_4H_{10}$, corresponding to about $400\,ns$ maximum drift time for the largest cell size. The number of ionisation clusters generated by a $m.i.p.$ in this gas mixture is about $12.5\,cm^{-1}$, allowing for the exploitation of the cluster counting/timing techniques for improving both spatial resolution ($\sigma_x < 100\,\mu m$) and particle identification ($\sigma(dN_{cluster}/dx)/(dN_{cluster}/dx) \approx 2\%$).

4.4.3 Expected performance

Figure 4.35 indicates a $100\,\mu m$ drift distance resolution, averaged over all drift times, measured in a MEG2 drift chamber prototype[56] ($7\,mm$ cell size), with very similar electrostatic configuration and gas mixture. A better resolution is expected for DCH, because of the longer drift distances. Cluster timing technique may further improve it. Analytical calculations for the expected transverse momentum and angular resolutions are plotted in Figure 4.36.

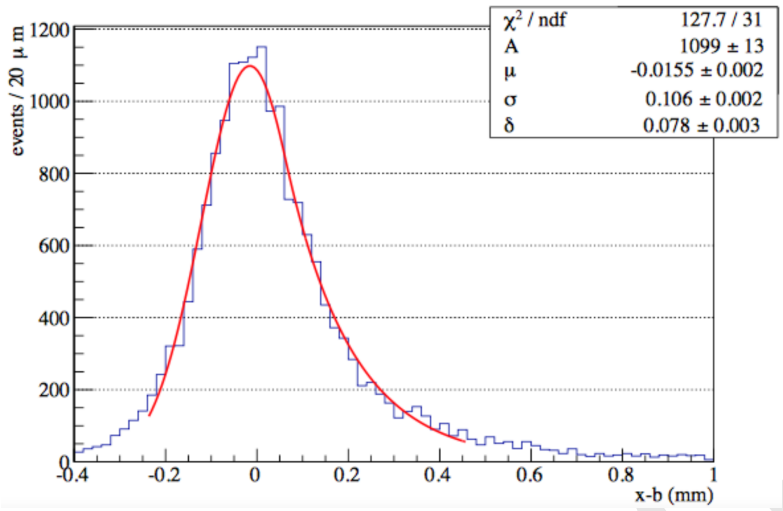

Figure 4.35: Measured drift distance residue distribution in the MEG2 drift chamber prototype under cosmic rays, indicating a resolution of less than 110μm, averaged over all drift times and in a wide range of track angles. $85\%\, He - 15\%\, iC_4H_{10}$ gas mixture.

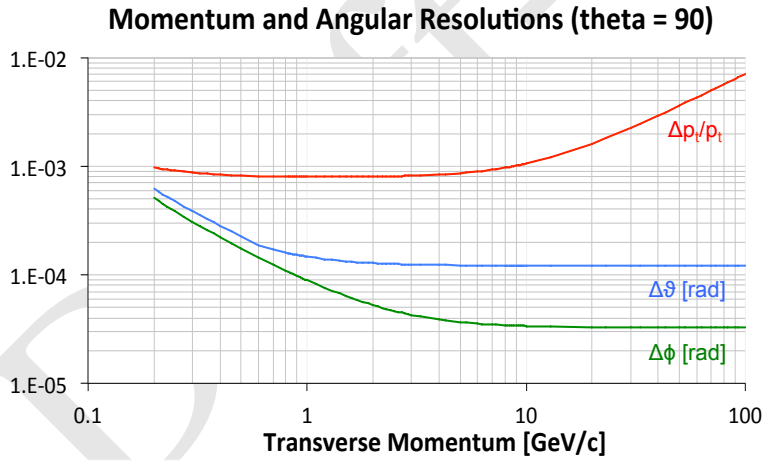

Figure 4.36: Momenta and angular resolutions as a function of the particle momentum for $\theta = 90°$ (left) and of the polar angle for $p = 10\, GeV/c$ (right)

Based on the assumption that one can, in principle, reach a relative resolution on the measurement of the number of primary ionisation clusters, N_{cl}, equal to $1/\sqrt{N_{cl}}$, the expected performance relative to particle separation in number of units of standard deviations is presented in Figure 4.37 as a function of the particle momentum. Solid curves refer to cluster counting technique applied to a $2\, m$ track length with 80% cluster identification efficiency and negligible (a few percent) fake clusters contamination. Dashed curves refer to the best theoretical prediction attainable with the dE/dx technique for the same track length and same number of samples. For the whole range of momenta, particle separation with cluster counting outperforms dE/dx technique by more than a factor of two, estimating an expected pion/kaon separation better than three standard deviations for all momenta below $850\, MeV/c$ and slightly above $1.0\, GeV/c$.

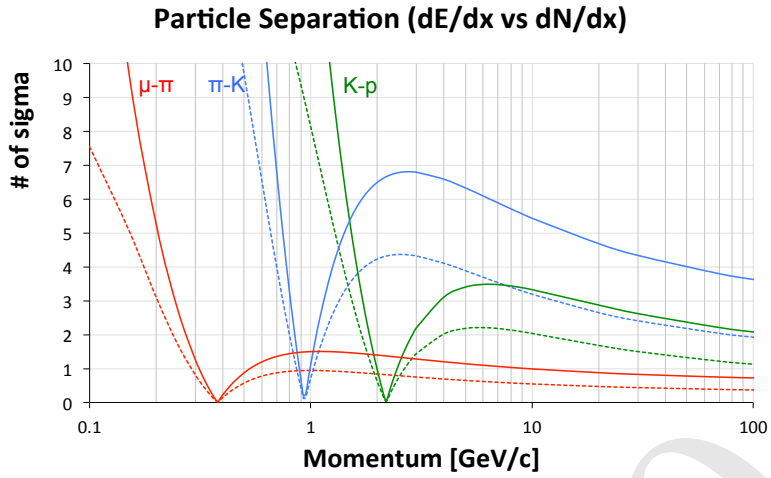

Figure 4.37: Particle type separation in units of standard deviations, with cluster counting (solid lines) and with dE/dx (broken lines) as a function of the particle momentum. A cluster counting efficiency of 80% and a dE/dx resolution of 4.2% have been assumed.

4.4.4 Tracking system simulation results

For the purpose of optimising the track reconstruction performance, a vertex detector (different from the baseline choice) made of seven cylindrical layers, inside the drift chamber inner radius, and of five forward disks, has been simulated together with a layer of silicon microstrip detectors surrounding the drift chamber both in the barrel and in the forward regions, followed by a pre-shower detector system within a homogeneous $2\,T$ longitudinal magnetic field. Details of ionisation clustering for cluster counting/timing analysis have not been included in the simulations, limiting the drift chamber performance both in spatial resolution (a $100\,\mu m$ gaussian smeared point resolution has been assumed) and in particle separation (no dN_{cl}/dx analysis has been simulated). A simplified track finding algorithm at its preliminary stage of development has been used to feed the space points to the GenFit2 interface for the ultimate track fit. Figure 4.38 shows the momentum, angle and impact parameter resolutions obtained by the tracking system simulation. No optimisation has been tried yet. Momentum resolutions $\Delta p/p = 4 \times 10^{-3}$ at $p = 100\,GeV/c$, for $\theta = 65°$, and angular resolutions $\leq 0.1\,mrad$ for $p \geq 10\,GeV/c$, are within reach. Lastly, a fit to the bottom right plot in Figure 4.38 gives a d_0 impact parameter resolution:

$$\sigma_{d_0} = a \oplus \frac{b}{p \sin^{3/2}\theta}$$

with $a = 3\mu m$ and $b = 15\mu m \cdot GeV/c$.

4.4.5 Backgrounds in the tracking system

Of the main sources of backgrounds in the tracking system: incoherent pair production (IPC), synchrotron radiation and $\gamma\gamma$ to hadrons, IPC is the dominant one. However, only very few of the primary $e^{\pm}$ particles will have a transverse momentum large enough to reach the inner radius of the drift chamber and the majority of the hits will be generated by secondary particles (mainly photons of energy below 1 MeV) produced by scattering off the material at low radii. Based on experience from the very similar MEG2 drift

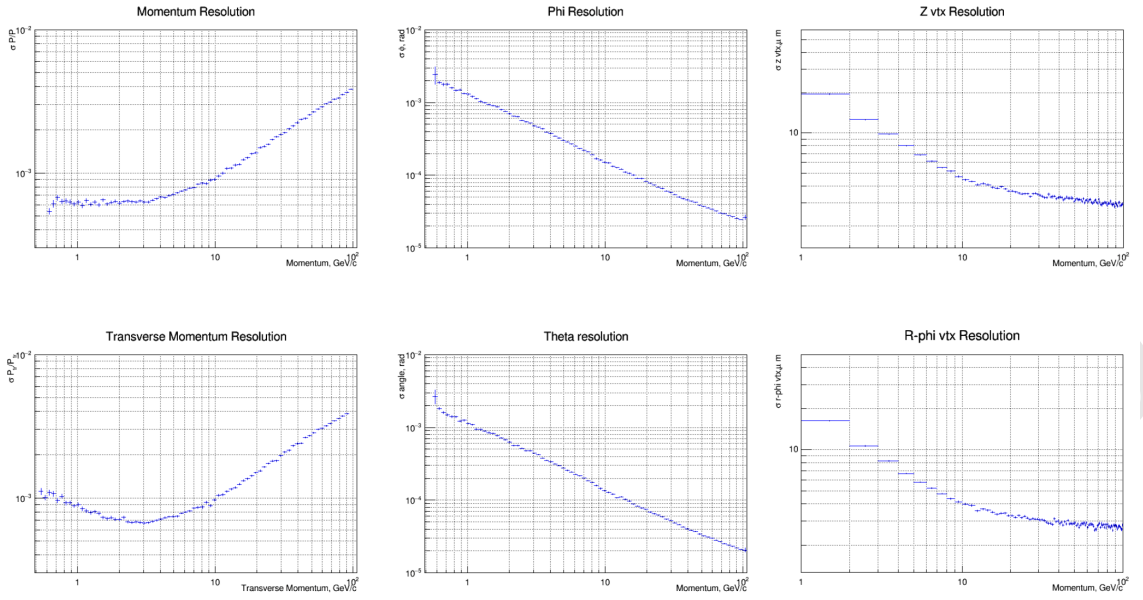

Figure 4.38: Momentum resolutions (top and bottom left), angle resolutions (top and bottom center) and impact parameter resolutions (top and bottom right) from simulation of isolated tracks.

chamber, which has a smaller number of hits per track and a much more complicated event topology, occupancies of up to several percent will not affect tracking efficiency and single track momentum resolution. The level of occupancy here is expected to be even smaller with the use of the drift chamber timing measurement. As opposed to charged particles, indeed, that leave a string of ionisation in the drift cells they traverse, photons are characterised by a localised energy deposition. Signals from photons can therefore be effectively suppressed at the data acquisition level by requiring that a threshold be reached by the number of ionisation clusters within a reasonable time window. In addition, charge strings with holes longer than the average cluster separation can be interpreted as due to separate signals, thus avoiding pilling up of any remaining photon induced background. With this effective suppression of photon induced signals, the background from IPC is expected to remain low and is unlikely to cause adverse issues for the track reconstruction.

4.4.6 Constraints on the readout system

With a drift chamber, all digitised hits generated at the occurrence of a trigger are usually transferred to data storage. The IDEA drift chamber transfers 2 B/ns from both ends of all wires hit, over a maximum drift time of 400 ns. With 20 tracks/event and 130 cells hit for each track, the size of a hadronic Z decay in the DCH is therefore about 4 MB, corresponding to a bandwidth of 40 GB/s at the Z pole (at a trigger rate of approximately 10 KHz). The contribution from $\gamma\gamma$ to hadrons amounts to 6 GB/s. As mentioned in the previous paragraph, the IPC background causes the read-out of additional 1400 wires on average for every trigger, which translates into a bandwidth of 25 GB/s. A similar bandwidth is taken by the noise induced by the low single electron detection threshold necessary for an efficient cluster counting. Altogether, the various contributions sum up to a data rate of about 0.1 TB/s. Reading out these data and sending them into an "event

builder" would not be a challenge, but the data storage requires a large reduction. Such a reduction can be achieved by transferring, for each hit drift cell, the minimal information needed by the cluster timing/counting, i.e., the amplitude and the arrival time of each peak associated with each individual ionisation electron, each encoded in 1 Byte, instead of the full signal spectrum. The data generated by the drift chamber, subsequently digitised by an ADC, can be analysed in real time by a fast read-out algorithm implemented in a FPGA[57]. This algorithm identifies, in the digitised signal, the peaks corresponding to the different ionisation electrons, stores the amplitude and the time for each peak in an internal memory, filters out spurious and isolated hits and sends these reduced data to the acquisition system at the occurrence of a trigger. Each hit cell integrates the signal of up to 30 ionisation electrons, which can thus be encoded within 60 B per wire end instead of the aforementioned 800 B. Because the noise and background hits are filtered out by the FPGA algorithm, the data rate induced by Z hadronic decays is reduced to 3 GB/s, for a total bandwidth of about 3.6 GB/s, roughly a factor 30 reduction.

References

[1] P. M. De Freitas and H. Videau, *Detector simulation with MOKKA/GEANT4: Present and future*, in *International Workshop on Linear Colliders (LCWS 2002), Jeju Island, Korea*, pp. 26–30. 2002.

[2] M. Regler, M. Valentan, and R. Frühwirth, *The LiC detector toy program*, Nuclear Instruments and Methods in Physics Research Section A:Accelerators,Spectrometers,Detectors and Associated Equipment **581** (2007) no. 1, 553–556.

[3] M. Battaglia, C. Da Viá, D. Bortoletto, R. Brenner, M. Campbell, P. Collins, G. Dalla Betta, M. Demarteau, P. Denes, H. Graafsma, et al., *R&D paths of pixel detectors for vertex tracking and radiation imaging*, Nuclear Instruments and Methods in Physics Research Section A:Accelerators,Spectrometers,Detectors and Associated Equipment **716** (2013) 29–45.

[4] G. Contin, E. Anderssen, L. Greiner, J. Schambach, J. Silber, T. Stezelberger, X. Sun, M. Szelezniak, C. Vu, H. Wieman, et al., *The MAPS based PXL vertex detector for the STAR experiment*, Journal of Instrumentation **10** (2015) no. 03, C03026.

[5] C. Lacasta, *The DEPFET pixel detector for the Belle II experiment at SuperKEKB*, PoS (2014) 005.

[6] B. Abelev, J. Adam, D. Adamova, M. Aggarwal, G. A. Rinella, M. Agnello, A. Agostinelli, N. Agrawal, Z. Ahammed, N. Ahmad, et al., *Technical design report for the upgrade of the ALICE inner tracking system*, Journal of Physics G: Nuclear and Particle Physics **41** (2014) no. 8, .

[7] I. Valin, C. Hu-Guo, J. Baudot, G. Bertolone, A. Besson, C. Colledani, G. Claus, A. Dorokhov, G. DoziÃšre, W. Dulinski, M. Gelin, M. Goffe, A. Himmi, K. Jaaskelainen, F. Morel, H. Pham, C. Santos, S. Senyukov, M. Specht, G. Voutsinas, J. Wang, and M. Winter, *A reticle size CMOS pixel sensor dedicated*

to the STAR HFT, Journal of Instrumentation **7** (2012) no. 01, C01102. http://stacks.iop.org/1748-0221/7/i=01/a=C01102.

[8] G. A. Rinella, *The ALPIDE pixel sensor chip for the upgrade of the ALICE Inner Tracking System*, Nuclear Instruments and Methods in Physics Research Section A: Accelerators, Spectrometers, Detectors and Associated Equipment **845** (2017) 583 – 587. http://www.sciencedirect.com/science/article/pii/S0168900216303825. Proceedings of the Vienna Conference on Instrumentation 2016.

[9] Y. Lu, Q. Ouyang, Y. Arai, Y. Liu, Z. Wu, and Y. Zhou, *First results of a Double-SOI pixel chip for X-ray imaging*, Nuclear Instruments and Methods in Physics Research Section A: Accelerators, Spectrometers, Detectors and Associated Equipment **831** (2016) 44 – 48. http://www.sciencedirect.com/science/article/pii/S0168900216301851. Proceedings of the 10th International Hiroshima Symposium on the Development and Application of Semiconductor Tracking Detectors.

[10] I. Kurachi, K. Kobayashi, M. Mochizuki, M. Okihara, H. Kasai, T. Hatsui, K. Hara, T. Miyoshi, and Y. Arai, *Tradeoff Between Low-Power Operation and Radiation Hardness of Fully Depleted SOI pMOSFET by Changing LDD Conditions*, IEEE Transactions on Electron Devices **63** (2016) no. 6, 2293–2298.

[11] Z. Wu, *A prototype SOI pixel sensor for CEPC vertex*, https://indico.cern.ch/event/577879/contributions/2741627/attachments/1575067/2486910/A_prototype_SOI_pixel_sensor_for_CEPC_vertex.pdf.

[12] S. Ono, M. Togawa, R. Tsuji, T. Mori, M. Yamada, Y. Arai, T. Tsuboyama, and K. Hanagaki, *Development of a pixel sensor with fine space-time resolution based on SOI technology for the ILC vertex detector*, Nuclear Instruments and Methods in Physics Research Section A: Accelerators, Spectrometers, Detectors and Associated Equipment **845** (2017) 139 – 142. http://www.sciencedirect.com/science/article/pii/S0168900216303783. Proceedings of the Vienna Conference on Instrumentation 2016.

[13] M. Idzik, *SOI-Cracow*, https://agenda.linearcollider.org/event/7450/contributions/38595/attachments/31561/47538/2017_LCVertex_Idzik.pdf.

[14] S. Spannagel, *Silicon technologies for the CLIC vertex detector*, Journal of Instrumentation **12** (2017) no. 06, C06006. http://stacks.iop.org/1748-0221/12/i=06/a=C06006.

[15] H. Wieman, E. Anderssen, L. Greiner, H. Matis, H. Ritter, X. Sun, and M. Szelezniak, *STAR PIXEL detector mechanical design*, Journal of Instrumentation **4** (2009) no. 05, P05015.

[16] H. Abramowicz et al., *The International Linear Collider Technical Design Report - Volume 4: Detectors*, arXiv:1306.6329 [physics.ins-det].

[17] Belle-II Collaboration, T. Abe et al., *Belle II Technical Design Report*, arXiv:1011.0352 [physics.ins-det].

[18] Y. Zhang, H. Zhu, L. Zhang, and M. Fu, *Charge collection and non-ionizing radiation tolerance of CMOS pixel sensors using a 0.18* µm *CMOS process*, Nuclear Instruments and Methods in Physics Research Section A: Accelerators, Spectrometers, Detectors and Associated Equipment **831** (2016) 99 – 104. http://www.sciencedirect.com/science/article/pii/S0168900216300481. Proceedings of the 10th International Hiroshima Symposium on the Development and Application of Semiconductor Tracking Detectors.

[19] Y. Zhou, *Development of highly compact digital pixels for the vertex detector of the future e+e- collider*, https://indico.cern.ch/event/577879/contributions/2740073/.

[20] Y. Zhang, *A Monolithic Active Pixel Sensor prototype for the CEPC vertex detector*, https://indico.cern.ch/event/577879/contributions/2740125/attachments/1574470/2485730/P15_ZY_POSTER_Final.pdf.

[21] Y. Lu, *Study of SOI Pixel for the Vertex*, http://indico.ihep.ac.cn/event/6433/.

[22] M. Motoyoshi, T. Miyoshi, M. Ikebec, and Y. Arai, *3D integration technology for sensor application using less than 5ÎŒm-pitch gold cone-bump connpdfection*, Journal of Instrumentation **10** (2015) no. 03, C03004. http://stacks.iop.org/1748-0221/10/i=03/a=C03004.

[23] W. Snoeys, G. A. Rinella, H. Hillemanns, T. Kugathasan, M. Mager, L. Musa, P. Riedler, F. Reidt, J. V. Hoorne, A. Fenigstein, and T. Leitner, *A process modification for CMOS monolithic active pixel sensors for enhanced depletion, timing performance and radiation tolerance*, Nuclear Instruments and Methods in Physics Research Section A: Accelerators, Spectrometers, Detectors and Associated Equipment **871** (2017) 90 – 96. http://www.sciencedirect.com/science/article/pii/S016890021730791X.

[24] F. Shen, S. Wang, C. Yang, and Q. Xu, *MWPC prototyping and testing for STAR inner TPC upgrade*, JINST **12** (2017) no. 06, C06008.

[25] ALICE Collaboration, D. Rohr, *Tracking performance in high multiplicities environment at ALICE*, in *5th Large Hadron Collider Physics Conference (LHCP 2017) Shanghai, China, May 15-20, 2017*. 2017. arXiv:1709.00618 [physics.ins-det]. https://inspirehep.net/record/1621494/files/arXiv:1709.00618.pdf.

[26] P. Bhattacharya, S. S. Sahoo, S. Biswas, B. Mohanty, N. Majumdar, and S. Mukhopadhyay, *Numerical Investigation on Electron and Ion Transmission of GEM-based Detectors*, EPJ Web Conf. **174** (2018) 06001.

[27] M. Posik and B. Surrow, *Construction of a Triple-GEM Detector Using Commercially Manufactured Large GEM Foils*, 2018. arXiv:1806.01892 [physics.ins-det].

[28] ATLAS Muon Collaboration, D. Sampsonidis, *Study of the performance of Micromegas detectors in magnetic field*, EPJ Web Conf. **174** (2018) 05003.

[29] S. Dalla Torre, E. Oliveri, L. Ropelewski, and M. Titov, *R&D Proposal: RD51 Extension Beyond 2018*, arXiv:1806.09955 [physics.ins-det].

[30] M. Zhao, M. Ruan, H. Qi, and Y. Gao, *Feasibility study of TPC at electron positron colliders at Z pole operation*, JINST **12** (2017) no. 07, P07005, arXiv:1704.04401 [physics.ins-det].

[31] CEPC-SPPC Study Group, *CEPC-SPPC Preliminary Conceptual Design Report. Volume I - Physics & Detector*, .

[32] Particle Data Group Collaboration, C. Patrignani et al., *Review of Particle Physics*, Chin. Phys. **C40** (2016) no. 10, 100001.

[33] J. E. Augustin et al., *A silicon envelope for the TPC*, .

[34] A. Affolder et al., *DC-DC converters with reduced mass for trackers at the HL-LHC*, JINST **6** (2011) C11035.

[35] S. Diez, *System Implications of the Different Powering Distributions for the ATLAS Upgrade Strips Tracker*, Phys.Procedia **37** (2012) 960–969.

[36] K. Klein et al., *DC-DC conversion powering schemes for the CMS tracker at Super-LHC*, JINST **5** (2010) C07009.

[37] A. Nomerotski et al., *Evaporative CO2 cooling using microchannels etched in silicon for the future LHCb vertex detector*, JINST **8** (2013) P04004, arXiv:1211.1176 [physics.ins-det].

[38] The ATLAS Collaboration, A. Affolder, *Silicon Strip Detectors for the ATLAS HL-LHC Upgrade*, Phys.Procedia **37** (2012) 915–922.

[39] V. Blobel, *Software alignment for tracking detectors*, Nucl.Instrum.Meth. **A566** (2006) 5–13.

[40] A. Savoy-Navarro, *Large Area Silicon Tracking: New Perspectives*, arXiv:1203.0736 [physics.ins-det].

[41] N. Calace and A. Salzburger, *ATLAS Tracking Detector Upgrade studies using the Fast Simulation Engine*, J. Phys.:Conf. Ser. **664** (2015) 072005.

[42] M. Regler et al., *The LiC Detector Toy program*, J. Phys.:Conf. Ser. **119** (2008) 032034.

[43] P. Mora de Freitas and H. Videau, *Detector simulation with Mokka/GEANT4: Present and future, LC-TOOL-2003-010, 623-627 (2002).*, (2002) .

[44] N. Graf and J. McCormick, *LCSIM: A detector response simulation toolkit*, in *2012 IEEE Nuclear Science Symposium and Medical Imaging Conference Record (NSS/MIC)*, p. 1016. Oct, 2012.

[45] C. Adolphsen et al., *The International Linear Collider Technical Design Report - Volume 3. II: Accelerator Baseline Design* , 2013. arXiv:1306.6328 [physics.acc-ph].

[46] H. Abramowicz et al., *The International Linear Collider Technical Design Report - Volume 4: Detectors* , 2013. arXiv:1306.6329 [physics.ins-det].

[47] S. V. Chekanov, *Public repository with Monte Carlo simulations for high-energy particle collision experiments*, PoS **ICHEP2016** (2016) 229, arXiv:1609.04455 [hep-ex].

[48] S. V. Chekanov, M. Beydler, A. V. Kotwal, L. Gray, S. Sen, N. V. Tran, S. S. Yu, and J. Zuzelski, *Initial performance studies of a general-purpose detector for multi-TeV physics at a 100 TeV pp collider*, JINST **12** (2017) no. 06, P06009, arXiv:1612.07291 [hep-ex].

[49] N. Graf and J. McCormick, *Simulator for the linear collider (SLIC): A tool for ILC detector simulations*, AIP Conf. Proc. **867** (2006) 503–512.

[50] J. Allison et al., *Recent developments in Geant4*, Nuclear Instruments and Methods in Physics Research A **835** (2016) 186.

[51] M. J. Charles, *PFA Performance for SiD*, in *Linear colliders. Proceedings, International Linear Collider Workshop, LCWS08, and International Linear Collider Meeting, ILC08, Chicago, USA, Novermber 16-20, 2008* . 2009. arXiv:0901.4670 [physics.data-an].

[52] J. S. Marshall and M. A. Thomson, *Pandora Particle Flow Algorithm*, in *Proceedings, International Conference on Calorimetry for the High Energy Frontier (CHEF 2013)*, pp. 305–315. 2013. arXiv:1308.4537 [physics.ins-det].

[53] S. V. Chekanov and M. Demarteau, *Conceptual Design Studies for a CEPC Detector*, Int. J. Mod. Phys. **A31** (2016) no. 33, 1644021, arXiv:1604.01994 [physics.ins-det].

[54] M. Adinolfi et al., *The tracking detector of the KLOE experiment*, Nucl. Instrum. Meth. **A488** (2002) 51–73.

[55] A. M. Baldini et al., *MEG Upgrade Proposal*, arXiv:1301.7225 [physics.ins-det].

[56] A. M. Baldini et al., *Single-hit resolution measurement with MEG II drift chamber prototypes*, arXiv:1605.07970 [physics.ins-det].

[57] G. Chiarello, C. Chiri, G. Cocciolo, A. Corvaglia, F. Grancagnolo, M. Panareo, A. Pepino, and G. F. Tassielli, *The Use of FPGA in Drift Chambers for High Energy Physics Experiments*, 2017. http://inspirehep.net/record/1663851/files/53616.pdf.

CHAPTER 5

CALORIMETRY

5.1 Introduction to calorimeters

A calorimetry system is employed in the CEPC detector to provide hermetic coverage for high-resolution energy measurements of electrons, photons, taus and hadronic jets. To fully exploit the potential of the CEPC physics program for Higgs and electroweak physics, all possible final states from decays of the intermediate vector bosons, W and Z, and the Higgs boson need to be separately identified and reconstructed with high sensitivity. In particular, to clearly discriminate the $H \to ZZ^* \to 4j$ and $H \to WW^* \to 4j$ final states, the energy resolution of the CEPC calorimetry system for hadronic jets needs to be pushed quite beyond today's limits. Indeed, in order to distinguish the hadronic decays of W and Z bosons, a 3%-4% invariant mass resolution for two-jet systems is required. Such a performance needs a jet energy resolution of $\sim 30\%/\sqrt{E}$, at energies below 100 GeV. This would be about a factor of two better than that provided by the LEP detectors and the currently operating calorimeters at the LHC, and would significantly improve the separation of the W and Z bosons in their hadronic decays, as shown in Figure 5.1. Two different technology approaches are pursued for the CEPC calorimetry system, the first one aiming to measure individual particles in a jet using a calorimetry system with very high granularity based on the particle flow concept, while the second aiming at a homogeneous and integrated solution based on the dual-readout concept. Both approaches will be described in this chapter, while the first approach is the current baseline for the design of the CEPC calorimetry system in that it is integrated in the full CEPC detector simulation.

The particle flow algorithm (PFA [1]) is a very promising approach to achieve the unprecedented jet energy resolution of 3%-4%. The basic idea of the PFA is to make use

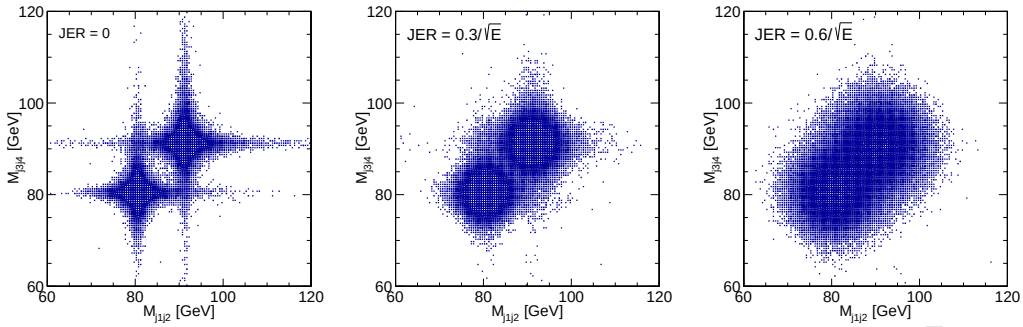

Figure 5.1: Separation of W and Z bosons in their hadronic decays with different jet energy resolutions, $0/\sqrt{E}$ (left plot), $30\%/\sqrt{E}$ (middle plot), and $60\%/\sqrt{E}$ (right plot).

of the optimal sub-detector in a detector system to determine the energy/momentum of each particle in a jet. An essential prerequisite for realization of this idea is to distinguish among energy deposits of individual particles from a jet in the calorimetry system. High, three-dimensional spatial granularity is required for the calorimetry system to achieve this. Therefore, PFA calorimeters feature finely segmented, three-dimensional granularity and compact, spatially separated, particle showers to facilitate the reconstruction and idenfication of every single particle shower in a jet. It is for this feature PFA calorimeters are usually also called imaging calorimeters. A PFA calorimetry system generally consists of an electromagnetic calorimeter (ECAL), optimized for measurements of photons and electrons, and a hadronic calorimeter (HCAL) to measure hadronic showers.

In a typical jet, 65% of its energy is carried by charged particles, 25% by photons and 10% by neutral hadrons. The charged particles in a jet can be precisely measured with a tracking system, especially for low momentum particles where the relatively small, multiple scattering term dominates in the resolution, and their tracks can be matched to their energy deposits in a PFA calorimetry system. This combination maximizes the overall resolution of the jet energy measurement by compensating for the worsening of calorimeter-only energy resolution for low energy particles by leveraging the improved resolution from the tracking system. Energy deposits in the PFA calorimetry system without matched tracks are considered to originate from the neutral particles of photons and neutral hadrons in the jet. Among these neutral particles, photons are measured using the ECAL with good energy resolution, while only the neutral hadrons are primarily measured using a combination of the ECAL and HCAL with a limited energy resolution. Therefore, in the PFA, the jet energy is determined by combining the best measurement in a detector system of each single particle in the jet: the track momenta of charged particles measured using the tracking system, the energies of photons measured using the ECAL and the energies of neutral hadrons measured primarily using the HCAL.

Extensive studies have been carried out within the CALICE collaboration [2] to develope compact PFA calorimeters. Various detector technology options have been explored to address challenges from stringent performance requirements as shown in Figure 5.2. Prototypes with high granularity using several technological options have been developed and exposed to particle beams, which have demonstrated the in-depth understanding of the PFA calorimetry performance.

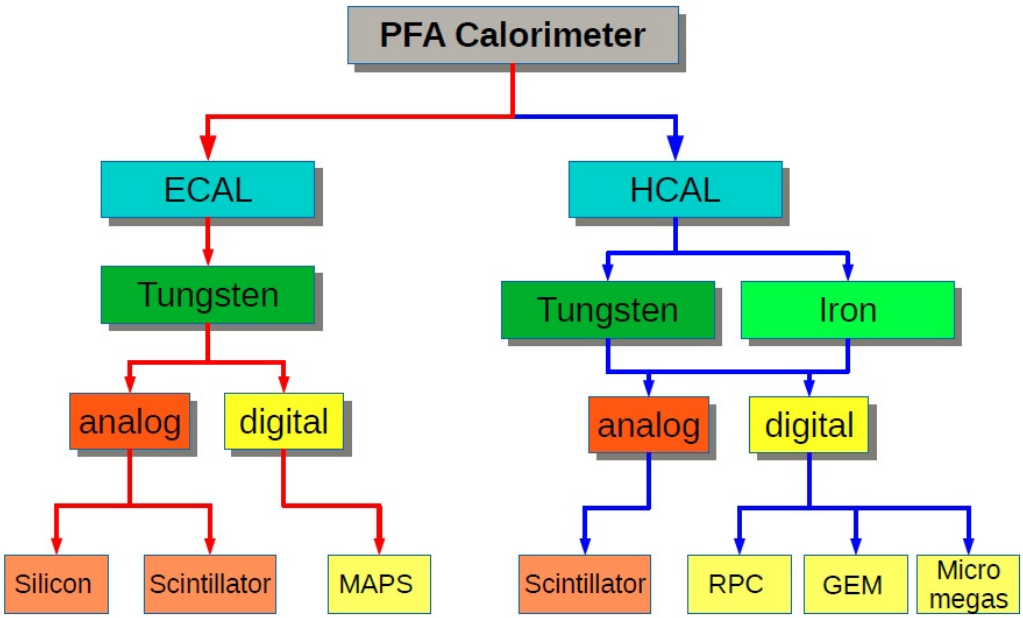

Figure 5.2: PFA: Imaging calorimeters being developed by the CALICE collaboration since 2000.

An alternative approach for a combined, high-performance, electromagnetic and hadronic calorimeter aims at reaching an even better (standalone) hadronic resolution, without spoiling the electromagnetic one, by exploiting the dual-readout (DR) technique. Indeed the main limiting factor to the energy resolution in hadron calorimetry arises from the fluctuations of the electromagnetic component (f_{em}) that each hadronic shower develops as consequence of π^0 and η production. Since typically the detector response to the hadronic and em components is very different ($h/e \neq 1$), the reconstructed signal heavily depends on the actual value of f_{em}. By using two independent processes (namely, scintillation and Čerenkov light production) that have a very different sensitivity to the hadronic and em components, it is possible to reconstruct f_{em}, event by event, and eliminate the effects of its fluctuations.

Among the possible DR implementations, a fiber-sampling DR calorimeter, based on either copper or lead as absorber material, looks the most suitable to provide the required performance in a cost-effective way. Preliminary results of GEANT4 simulations point to possible resolutions better than 15% and around $30\% - 40\%$ (over $\sqrt{E}$), for electromagnetic and hadronic showers, respectively (see Section 5.5.6).

Moreover, if the fibers are readout with Silicon PhotoMultipliers (SiPMs), the high detector granularity and the possibility of longitudinal segmentation will make this solution easily compatible with Particle Flow Algorithms.

In the following sections, several possible concrete implementations of a calorimeter system are discussed in sufficient detail to describe the readiness of the technologies and the performance of these systems in current test beams and prototypes and their corresponding general implementation in the simulation permformance studies of the physics objects and benchmarks presented in subsequent chapters.

5.2 General design considerations for the PFA Calorimetry system

The CEPC PFA calorimetry system is longitudinally composed of two separate sampling calorimeters: ECAL and HCAL, both of which are installed inside the solenoid coil of the CEPC detector system to minimize the inactive material in front of the calorimetry system and to reliably associate tracks to energy deposits. Following the geometry of the CEPC detector, each of two calorimeters is organised into one cylindrical barrel and two disk-like end-cap sections.

The ECAL, considered here, has analog readout, consisting of sensitive layers of either silicon pads or scintillator tiles interleaved with tungsten absorber plates. As for the HCAL, steel plates are adopted as absorber, and both digital and analog readout is considered. The digital HCAL (DHCAL) uses either Glass Resistive Plate Chambers (GRPC) or Thick Gas Electron Multiplier detectors (THGEM) as the active medium, while the analog HCAL (AHCAL) uses scintillator tiles coupled to SiPMs.

The calorimeters for these options are all highly segmented both transversely and longitudinally, which is driven by the requirement from the particle flow algorithm of excellent particle shower separation capability. The baseline technology options for the CEPC PFA ECAL and HCAL that have been integrated into the full CEPC detector simulation are silicon-tunsgten and steel-GRPC, respectively. In the baseline design of the calorimeters, the ECAL is segmented into 30 longitudinal layers with a total depth of $24\ X_0$, and the silicon plate in each layer is divided into square cells each of $5 \times 5\ \mathrm{mm}^2$. The HCAL consists of 40 longitudinal layers each containing 2 cm thick steel with a thin layer of GRPCs read out in a cell size of $10 \times 10\ \mathrm{mm}^2$. Further optimization on cell sizes for both the ECAL and HCAL based on benchmark physics processes is underway.

5.3 Electromagnetic Calorimeter for Particle Flow Approach

The particle flow paradigm has tremendous impact on the design of the ECAL. With excellent capability of pattern recognition, the ECAL is expected to identify photons from close-by showers, reconstruct detailed properties of a shower (i.e. shower shape, starting point and energy distribution), and distinguish electromagnetic showers from hadronic ones. Thus, shower imaging capability of the calorimeter is more important than its intrinsic energy resolution, although the latter is still important to the particle flow performance for electrons, photons and jets. Due to the fact that about half of hadronic showers start inside the ECAL, excellent three dimensional granularity is of primary importance to the ECAL. In order to have the power of separating close-by showers in the calorimeter, absorber material with small Moliere radius is required for the ECAL. And a large ratio of the interaction length over the radiation length of the absorber material is advantageous to separation between electromagnetic and hadronic showers because a short radiation length makes an electromagnetic shower start early in the ECAL, while a long interaction length reduces the fraction of a hadronic shower in the ECAL. A short radiation length also makes a compact ECAL, which is highly desirable from the cost saving point of view.

In short, requirements for the ECAL on high granularity, compactness and shower separation lead to the choice of a sampling calorimeter with tungsten (the radiation length $\mathrm{X}_0 = 3.5\ \mathrm{mm}$, the Molière Radius=9 mm and the interaction length $\lambda_\mathrm{I} = 99\ \mathrm{mm}$) as absorber material. This ensures a compact ECAL with a depth of around $24\ X_0$ within $20\ \mathrm{cm}$.

Two options for active material are considered for the ECAL: silicon and scintilator. The silicon option is taken as the baseline, while the scintilator option is also being investigated as alternative. Both options are presented in this section.

The baseline design of the ECAL consists of a layout of 30 longitudinal layers of silicon sensors sandwiched between tungsten plates with a sensor size of $5 \times 5\ \mathrm{mm}^2$ and a total depth of $24\ X_0$.

5.3.1 Silicon-Tungsten Sandwich Electromagnetic Calorimeter

5.3.1.1 Silicon sensors

Among several sensor techniques, silicon PIN diodes with high resistivity offer several unique intrinsic advantages as follows.

- Stability: under a reasonable bias voltage, a completely depleted silicon PIN diode has unity gain, and a signal response to a Minimum Ionizing Particle (MIP) mostly defined by the sensor thickness, with a relatively low dependence on the operating environment including temperature, humidity, etc.
- Uniformity: the control of the sensor thickness within large production batches (typically to less than a percent) ensures uniform responses within a wafer and between different wafers. The non-sensitive area between wafers has recently been reduced by the use of laser cutting, thinned guard-ring design [3], and would benefit from the use of larger ingot size (8“ becoming the standard).
- Flexibility: the dimension and geometry of the cells can be flexibly defined. The readout pads on the PCB need to be compatible.
- High signal-to-noise (S/N) ratio: for a MIP, the most probable number of electron-hole pairs generated in $1\mu m$ thick silicon is around 76 (while the average number is 108), which yields an excellent S/N ratio of silicon sensors. Thus, MIP tracks can be easily tracked in the calorimeter, which is critical to the good performance of the ECAL.

Currently the only drawback of the silicon sensors is the price, which is expected to be around $2 - 3\ \mathrm{cm}^2$.

By integrating the silicon sensors with tungsten plates and carbon fiber structures, the SiW-ECAL offers an excellent option for the PFA optimized calorimetry.

5.3.1.2 Geometry and mechanical design

A key requirement for the calorimeter system is to ensure the best possible hermeticity. Three regions need to be taken account, including the boundaries of mechanical modules, the overlap between the barrel and endcap parts, and the small angle region near the lumonisity monitor (or other forward detectors). A design with large ECAL modules is preferred to minimize the number and effect of cracks in the barrel part. The inter-module boundaries should not point back to the interaction point (IP). As shown in Figure 5.3, an octagonal shape is used to approximate the cylindrical symmetry and the modules are so designed that that the cracks are at a large angle with respect to the radial direction. One eighth of the barrel ECAL is named a stave. Each stave will be fastened to the HCAL front face with a precise system of rails. Some space will be left between the ECAL and

HCAL to accommodate services including cooling, power and signal cabling. Along the beam direction, a stave is divided into five modules. The two ECAL endcap parts will be fastened to the front face of HCAL endcap parts using a similar rail system.

ECAL longitudinal arrangement In the ECAL baseline design featuring 30 layers in the longitudinal direction, split into 2 sections. The first section contains 12 radiation lengths and are filled with 20 layers of $0.6X_0$ (or 2.1 mm) thick tungsten plates. Each sensitive layer is equipped with $525\ \mu\mathrm{m}$ thick silicon sensors. It is followed by the second section with another 11 radiation lengths made from 9 layers of $1.2X_0$ thick (4.2 mm) tungsten plates. The ECAL starts with an active layer. The choice of the silicon layer granularity is fixed at $5 \times 5\mathrm{mm}^2$. The first and second sections are both held on a base plate (carbon-fiber) of 20 mm thick, and are 223 mm, 191 mm thick in total, respectively.

ECAL dimensions The ECAL barrel part consists of 8 staves, each with 5 trapezoidal modules. A barrel module contains 5 columns (a column is also named alveolus). The numbers of modules and alveoli are positional along the beam axis and chosen to be odd in number and symmetrically placed in order to avoid any pointing-like dead region at the azimuthal plane perpendicular to the beam direction at the interaction point (IP). The alveolus size is fixed to 186 mm by mechanical limits and by cost optimization considerations, in order to contain exactly two 6-inch wafers or one and a half 8-inch wafers. Integrating the alveolus size, walls of modules and contingencies, the barrel length adds up to 4700 mm in the beam direction (4900mm is used in the CEPC simulation). A gap of typically 70 mm (100 mm in the CEPC simulation) is left between the barrel sides and end-cap front parts. The precise dimension will depend on the amount of services for the ECAL, the HCAL and the tracker system (including power and DAQ cabling, cooling pipes, patch panels, etc.).

The end-caps are made of quadrants of 2 modules one of 4 and one of 3 alveoli columns. Their inner radius is fixed by the ECAL ring at 400mm. With 7 alveoli columns, the end-cap outer radius is 1755mm. An overshoot of 32mm is left between the outer radius of the barrel and of the end-caps, in order to contain the EM shower impinging the region of overlap. This fixes the inner radius size of the ECAL barrel at 1498mm or 1530mm. For such a geometry, summing the barrel (200) and end-caps (56), 256 alveoli columns are needed. For 22 (resp. 30) layers, and this yields 5632 (7680) alveoli, and as many detector slabs.

ECAL slab Several slabs are inserted into each column of the ECAL modules. Each slab consists of two symmetric sensitive layers and one tungsten plate. Each sensitive layer contains a layer of silicon sensors glued on a PCB, equipped with readout ASICs, a high voltage distribution by a Kapton foil and copper layers for passive cooling. The components are attached on both sides of an H-shaped carbon fiber cradle, with a tungsten core, and shielded by an aluminum cover. To insure scalability and industrial production, the design has been made as modular as possible: each basic unit is an ASU (Active Sensor Unit), which currently has a $18 \times 18\ \mathrm{mm}^2$ PCB glued with 4 pieces of $90 \times 90\ \mathrm{mm}^2$ silicon wafers. Each ASU will handle 256 silicon pads with 4 ASIC chips, for the cell size of approximately $11 \times 11\ \mathrm{mm}^2$.

The ASUs are chained together for the clock and configuration distributions and data collection. For a radius of 1498mm the longest (shortest) barrel slabs measure 1146mm (955mm).

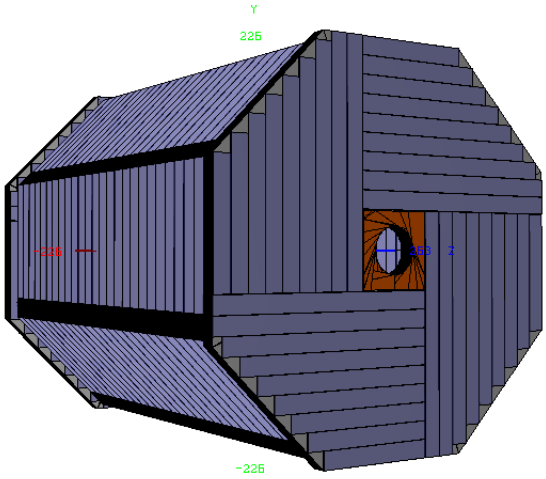

Figure 5.3: Schematic of the CEPC ECAL layout.

5.3.1.3 SiW-ECAL electronics

One of the most critical elements of the CEPC calorimeters is the readout electronics which is defined by the dynamic range, the effective digitisation, mode of trigger, the rate of working and power consumption per channel.

Dynamic range: A MIP going through a 725 μm silicon diode will produce around 60000 electron-pairs holes (or a charge of 9.6 fC) as the most probable value (MPV). To record MIPs with an efficiency higher than 95%, this determines the lower limit of the dynamic range to a 1/3 of the MPV. The higher limit is given by the number of MIP equivalents at the core of the high-energy EM showers, which can reach up to 10000 MIPs (or 96pC) within a 11×11 mm^2 cell.

Timing: Time measurements of energy depositions in the calorimeters can be useful to Particle Flow algorithms to help disambiguate particle contributions. For the CEPC as a lepton collider, normally with a single primary vertex, precision timing of individual cells - or group of cells - could still be useful to reduce the confusion in the calorimeters and improve the energy resolution, which however needs further studies to quantitatively explore this potential. A SiW-ECAL ASIC with the most recent version (SKIROC2A) has been tested on a test board and reached a measure of timing resolution close to 1.1 ns for a signal amplitude corresponding to 5 MIPs [4].

Power consumption: The running conditions of a circular collider exclude pulsed operation as is planned for the linear colliders. As a point of reference, the current power consumption for the SKIROC2 chip is around 5 mW per channel in the continuous operating mode.

Occupancy: The occupancy of the calorimeters is expected to be very low. This offers room for an ultra-low power electronics design when there is no signal.

5.3.1.4 SiW-ECAL power consumption and cooling

To the first order, the amount of the power dissipation scales up with the number of electronics channels. One critical issue for the calorimeters is the cooling scheme. As for now there are two options. The CEPC ECAL is at the boundary of both options, with a limit for

the purely passive option of the order of $20 \times 20\ \mathrm{mm}^2$ cells for a increase of temperature limited to $\Delta\mathrm{T} \sim 10\ ^\circ\mathrm{C}$ at the far end of the slab.

- Passive cooling: this option requires a reduced number of channels in order to use only passive cooling at the rear of the detector. As an example, a $400\ \mu\mathrm{m}$ thick copper sheet will drain the heat to the end of an ECAL slab, where it is then removed by an active cooling system installed near boundaries between barrel and endcap parts. A leakless water cooling system can be such an option to extract the heat at the end of each slab from the copper. Details of implementation can be found in [5]. Full simulation studies based on PFA should be performed to provide the quantitative impact from a reduced granularity and the corresponding calorimeter performance.
- Active cooling: this option is the baseline high granularity design and requires the cooling system to provide cooling near the sensors and front-end electronics throughout the entire calorimeter system. A two-phase, low mass CO_2 cooling system is a promising option, which can be embedded in the absorber plates. There are already some simulation studies on a similar system adapted to the SiW-ECAL [6], where 3 mm thick copper plates, equipped with 1.6 mm inner diameter pipes for CO_2 circulation, with the ASICs glued on both sides of the slab. The study assumed a fully transversally isolated system, with ASICs as the primary heat source at equilibrium dissipating 0.64 W (10 mW per channel times 64 channels), and a fixed working point of $20\ ^\circ\mathrm{C}$ for CO_2 (i.e. assuming perfect heat absorption). A doubled-sided module of $252 \times 252\ \mathrm{mm}^2$ holding 32 chips cooled by 2×2 pipes was simulated. Preliminary simulations in "ideal conditions" show a difference of $\Delta\mathrm{T} \sim 2\ ^\circ\mathrm{C}$ mostly centered on the ASICs (and only $0.3\ ^\circ\mathrm{C}$ in the heat exchanger).

5.3.1.5 SiW-ECAL R&D status

The performances of a SiW-ECAL have beed explored using the “physical prototype“ developed within the CALICE collaboration, with extensive beam tests during the years 2005- 2011 [7–9]. Some ASUs have been operated in beam test campaigns: first at CERN in 2015, where 3 ASUs were mounted on test boards which behaved as expected [10]; a signal to noise ratio (SNR) (defined as the Most Probable Value of a Landau fit on data, divided by the Gaussian width of the noise) reached typical values of 15-18, with a very limited number of masked channels.

In a recent a beam test at DESY with 1-5 GeV electrons, "short slabs" (featuring all the elements as required but limited to a single ASU on a single side) could reach a SNR of around 20 on average [11].

The collected data is still under analysis, but they are expected to be similar to the SiW-ECAL physical prototype. The construction of a “long slab“ is being actively pursued, and should be completed toward the end of year 2019; the R&D involves all the power, cooling and frond-end electronics issues. The results and design will have to be optimized for a circular collider, where the power-pulsing operation is not allowed.

5.3.2 Scintillator-Tungsten Sandwich Electromagnetic Calorimeter

5.3.2.1 Introduction

Alternatively, a sampling calorimeter with scintillator-tungsten structure is proposed. It can be built in a compact and cost effective way. The structure of the ScW-ECAL is similar

to the SiW-ECAL. The major geometry parameters of the ScW-ECAL are also studied and optimized, with results that are similar to the SiW-ECAL. The primary difference is in the thickness of the active layers. The active layers of the ScW-ECAL consists of $5 \times 45\ \mathrm{mm}^2$ scintillator strips. The scintillator strips in adjacent layers are perpendicular to each other to achieve a $5 \times 5\ \mathrm{mm}^2$ effective transverse readout cell size. Each strip is covered by a reflector film to increase light collection efficiency and improve uniformity of the scintillation light as a function of impact position on the strip. Photons from each scintillator strip are read out by a very compact photo-sensor, SiPM, attached at the end of the strip. The SiPM and highly integrated readout electronics make the dead area in the ScW-ECAL almost negligible. The possibility of attaching an SiPM on both ends of the strips is also considered.

Plastic scintillator is a robust material which has been used in many high energy physics experiments. Production of the scintillator strips can be performed at low cost by the extrusion method. Moreover, the number of readout channels can also be significantly reduced due to the strip structure. So the total construction cost of the ScW-ECAL is lower than the SiW-ECAL. Some key issues which might affect the performance of the ScW-ECAL were studied and optimized.

5.3.2.2 SiPM dynamic range study

Because each pixel on a SiPM can only detect one photon at once and a few nanoseconds are needed before recovery, the SiPM is not a linear photon detection device, especially in the case of high intensity light input. The application of the SiPM in the CEPC ScW-ECAL is a challenge to its dynamic range, which needs to be studied.

For a short time light pulse, the response of the SiPM can be theoretically calculated as

$$N_{fired} = N_{pixel}(1 - e^{-N_{pe}/N_{pixel}}) \tag{5.1}$$

However, for the ScW-ECAL, the width of the light pulse should not be ignored, and some pixels of the SiPM can detect more than one photon in an event. The response of the SiPM should be modified as

$$N_{fired} = N_{eff}(1 - e^{-N_{pe}/N_{eff}}) \tag{5.2}$$

The N_{eff} stands for the effective number of pixels on a SiPM, which is relative to the width of the input light pulse. The response curve of 10000-pixel (10μm pitch size)and 1600-pixel (25μm pitch size) SiPMs with an area of $1 \times 1\ \mathrm{mm}^2$ for different light pulse durations have been measured. As shown in Figure 5.4, the output linearity of the device is improved by the increase in the incident light width and by the total number of pixels. Larger area SiPMs are considered for this, as the price per cm^2 has dropped considerably.

5.3.2.3 Scintillator strip test

When the scintillator stip is coupled to an SiPM at only one end, the light output will be non-homogeneous along the length of the scintillator, which will affect the performance of the ScW-ECAL. By moving a Sr^{90} source along the length of the scintillator, we test the light pulses height read out by the SiPM to study the non-uniformity of the scintillator detector. Figure 5.5(left) is a typical test result of a scintillator module whose light output non-uniformity is 23%. The uniformity can be improved by optimizing the reflection material or the coupling methods of the SiPM to the scintillator strip. SiPM readout on

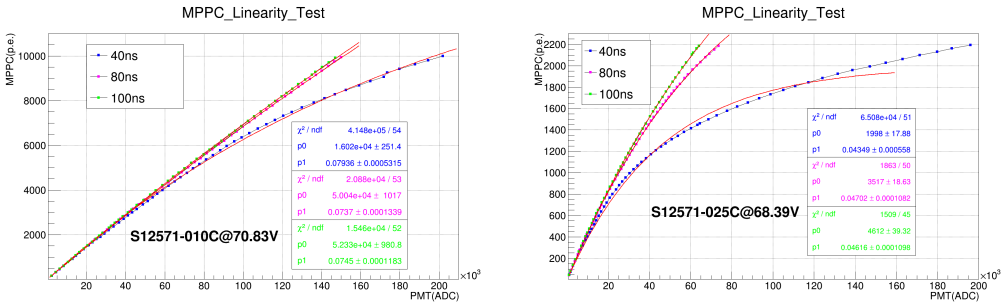

Figure 5.4: The response curve of 10000-pixel(left) and 1600-pixel(right) SiPMs for different illuminating durations.

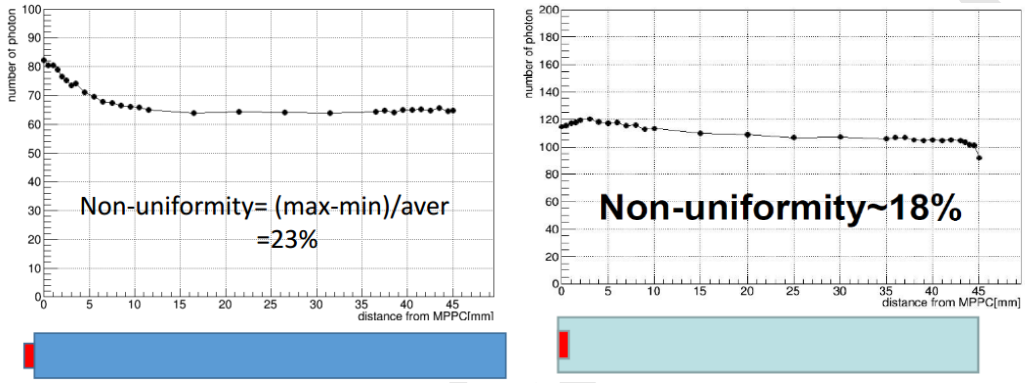

Figure 5.5: Uniformity of scintillator strips with an SiPM coupled on side surface (left) or embedded into one side (right).

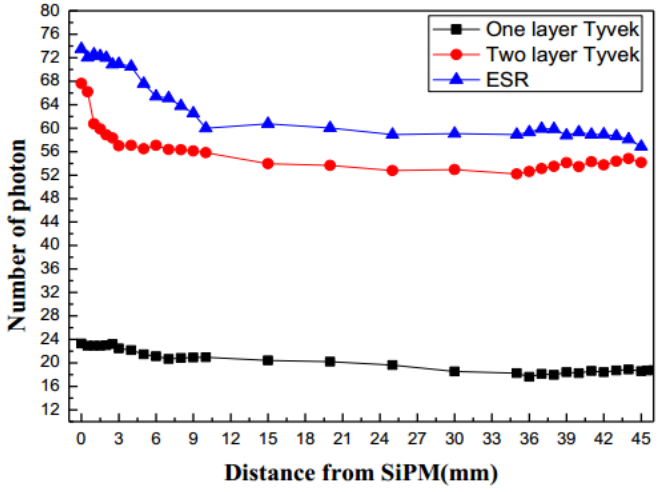

Figure 5.6: Light output of scintillators with different reflectors.

both ends of the strip could also be used to correct for the uniformity of the light output. Figure 5.5(right) shows a result of a scintillator module with the SiPM embedded into the scintillator strip, and Figure 5.6 is the light output of another scintillator module with a different reflector. Scintillators with ESR reflector can give much more light output. We have also measured the light output of a scintillator coupled with the SiPM with different pitch sizes. The two kinds of SiPM have the same photodetection area ($1 \times 1\ \mathrm{mm}^2$). The light output of the scintillator with 10μm pitch SiPM is about 1/3 of the scintillator

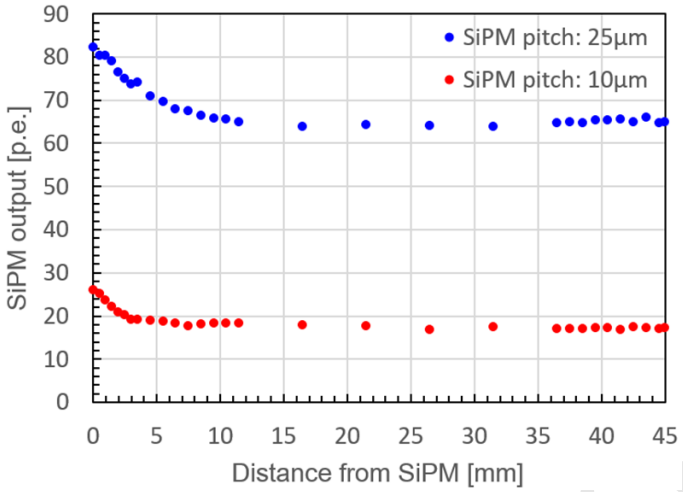

Figure 5.7: light output of scintillators with 10μm (red dots) and 25μm (blue dots) SiPMs pitch.

with 25μm pitch SiPM, shown in Figure 5.7. The photodetection efficiency (PDE) is a strong function of fill-factor for pitch sizes of 10μm and smaller. This ultimately limits the amount of collected light for a given pitch size and total photodetection area for a fast pulse.

5.3.2.4 SiPM readout electronics

The readout electronics of the ECAL has to provide high dynamic range for energy measurements. A 100 GeV photon shower may leave an energy deposit of 1∼800 MIP-equivalent in a single cell. A high spatial granularity of the ECAL readout, typically 10 mm, is required for the Particle Flow Algorithm (PFA). This, in turn, results in a large total channel count and a high density of channels. For this reason, multi-channel readout chips are considered.

The full readout chain of the electronics consists of two parts: Front-End and Back-End. The Front-End electronics (FE) is embedded into the layers of ECAL. It performs amplification, auto-triggering, digitization and zero-suppression, with local storage of data between the working phases. The Back-End electronics (BE) collects data and configures the readout chips before system running.

Several studies and existing calorimeter readout electronics have shown that one can obtain optimized energy resolutions using a preamplifier-shaper and digitizing the pulse at the peak amplitude. For instance, a preamp-shaper-SCA structure of analog circuit was applied on an ILC HCAL and implemented in an ASIC names SPIROC2b. A similar approach can be applied for the CEPC-ECAL. The analog part of the SPIROC2b is schematically depicted in Figure 5.8. This ASIC is presently under consideration for the CEPC-ECAL.

The basic principle consists of a readout chain with an amplifier-shaper using a RCn-CRp filter delivering a pulse length of about 50-200ns duration for a SiPM pulse signal. This signal is also shaped by a fast shaper in parallel to generate fast and narrow pulse for pulse discrimination. Then, the discriminator sends the trigger to a Switched-Capacitor-Array (SCA) for locking the peak value of the slowly shaped signal. The locked voltage value corresponds to the charge that the circuit received. A 12bit Wilkinson ADC is used for digitizing the analog voltage in the SCA. Future detailed implementations of the

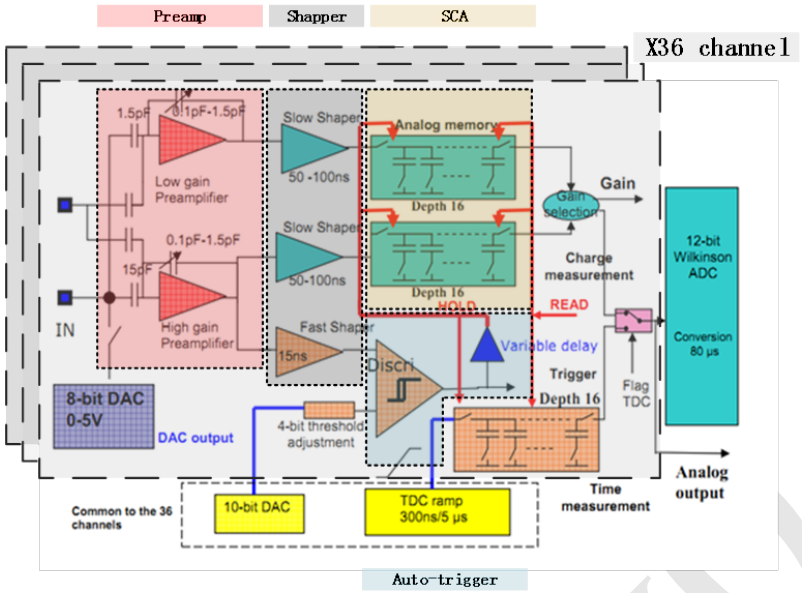

Figure 5.8: Schematic of the SPIROC2b ASIC chip.

calorimeter front-end electronics for CEPC is still considered using the ROC series ASIC but newer versions.

The maximum data rate to the Back-End electronics can be estimated as follows. Assuming continuous operation, the SPIROC2b will be switched between three states called Acquisition, AD Converting and Readout. Only in the Acquisition state can SPIROC2b receive signal from the SiPM and store in received charge in the SCA at a rate of about 5MHz. The two other states contribute to the “dead-time" status. There is depth of 16 in the SCA corresponding to 4μs for Acquisition, and an additional ~ 4 ms for ADC and Readout. Therefore, the maximum data rate is 16 events per 4ms which corresponds to 4 kHz. Each data package is 2 Kbytes in size.

The number of chips readout in series in a single layer will multiply the duration of Readout. Assuming that there are 4 chips in one layer, there is 16ms for Readout. The maximum events rate is reduced to 1 kHz and leads to about a transmission of 5 Mbyte/s. This can easily be managed with 100Mbps links.

The power consumption in the front-end will be dominated by the ASIC and more specifically by the analog part of the ASIC. One SPIROC2b consumes 250.8mW of which about 150mW is consumed by the analog part. In actual use, most of the cycle is in ADC and Readout. This leads to about 150mW power consumption per chip and 4mW per channel.

The electronic calibration and cosmic ray tests have been done. From these electronic calibrations we have obtained that the noise of readout system is 46 fC in RMS. The least-significant bit of the ADC in high gain and low gain is 151/pC and 10.3/pC, respectively, while the maximum ADC range is 4096. A dynamic range of 100fC-300pC of the readout system is measured with this method. Cosmic ray results show that the system can distinguish a MIPs signal from pedestal well with a measured charge of approximately 1 pC.

5.4 Hadronic Calorimeter for Particle Flow Approach

5.4.1 Introduction

High-granularity hadronic calorimetry is an essential concept in PFA-based experiments such as those proposed for CEPC. The high spatial granularity provides a means to separate the deposits of charged and neutral hadrons and to precisely measure the energy of the neutrals. The contribution of the neutrals to the jet energy, around 10% on average, fluctuates in a wide range from event-to-event, and the accuracy of the measurement is the dominant contribution to the particle flow resolution for jet energies up to about 100 GeV. For higher energies, the performance is dominated by a term in the PFA resolution called the confusion term. This term originates from failures in both the topological pattern recognition and energy information that are important for correct track cluster assignment. A high-granularity hadronic calorimeter is thus needed to achieve excellent jet energy resolution.

THE HCAL systems considered here are sampling calorimeters with steel as the absorber and scintillator tiles or gaseous devices with embedded electronics for the active part. The steel was chosen due to its rigidity which allows to build self-supporting structures without auxiliary supports (dead regions). Moreover, the moderate ratio of hadronic interaction length ($\lambda_I = 17$ cm) to electromagnetic radiation length ($X_0 = 1.8$ cm) of iron, allows a fine longitudinal sampling in terms of X_0 with a reasonable number of layers in λ_I, thus keeping the detector volume and readout channel count small. This fine sampling is beneficial both for the measurement of the sizable electromagnetic energy part in hadronic showers and for the topological resolution of shower substructure, needed for particle separation.

The active detector element has finely segmented readout pads, with 1×1 cm^2 size, for the entire HCAL volume. Each readout pad is readout individually, so the readout channel density is approximately 4×10^5/m^3. For the entire HCAL, with $\sim$100 m^3 total volume, the total number of channels will be 4×10^7 which is one of the biggest challenges for the HCAL system. On the other hand, simulation suggests that, for a calorimeter with cell sizes as small as 1×1 cm^2, a simple hit counting is already a good energy measurement for hadrons. As a result, the readout of each channel can be greatly simplified and just record 'hit' or 'no hit' according to a single threshold (equivalent to a '1-bit' ADC). A hadron calorimeter with such kind of simplified readout is called a Digital Hadron Calorimeter (DHCAL). In a DHCAL, each readout channel is used to register a 'hit', instead of measure energy deposition, as in traditional HCAL systems. In this context, gas detectors (such as RPC, GEM) become excellent candidates for the active element of a DHCAL. Another technology option is the Analog Hadron Calorimeter (AHCAL) which is based on scintillator with SiPMs as the active sensor.

A drawing of the HCAL structure is shown in Figure 5.9, the barrel part is made of 5 independent and self-supporting wheels along the beam axis. The segmentation of each wheel in 8 identical modules is directly linked with the segmentation of the ECAL barrel. A module is made of 40 stainless steel absorber plates with independent readout cassettes inserted between the plates. The absorber plates consist of a total of 20 mm stainless steel: 10 mm absorber from the welded structure and 10 mm from the mechanical support of the detector layer. Each wheel is independently supported by two rails on the inner wall of the cryostat of the magnet coil. The cables as well the cooling pipes will be routed outside

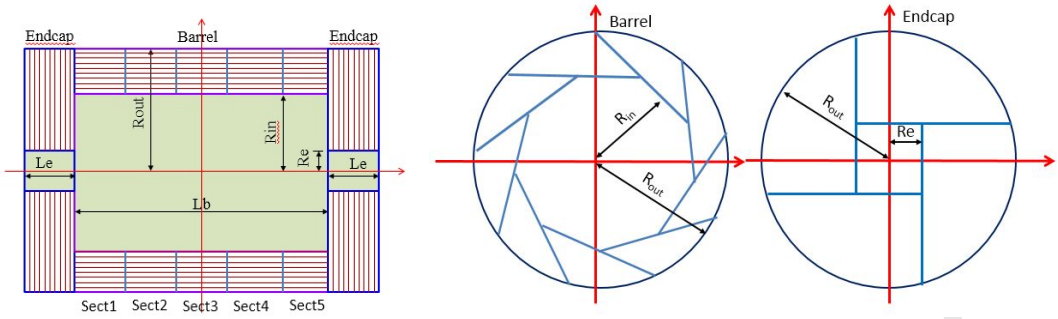

Figure 5.9: HCAL layout in Y-Z plane (left plot), HCAL Barrel layout in X-Y plane (middle plot) and HCAL Endcap layout in X-Y plane (right plot).

the HCAL in the space left between the outer side of the barrel HCAL and the inner side of the cryostat.

5.4.2 Semi-Digital Hadronic Calorimeter (SDHCAL)

5.4.2.1 Introduction

For the CEPC, a SDHCAL based on gaseous detecor is proposed. This is motivated by the excellent efficiency and very good homogeneity the gaseous detectors could provide. Another important advantage of gaseous detectors is the possibility to have very fine lateral segmentation. Indeed, in contrast to scintillator tiles, the lateral segmentation of gaseous devices is determined by the readout electronics and not by the detector itself. Active layer thickness is also of importance for what concerns the CEPC hadronic calorimeter to be placed inside the magnetic field. Highly efficient gaseous detectors can indeed be built with a thickness of less than 3 mm. While other detectors could achieve such performance, gaseous detectors have the advantage of being cost-effective and discharge free. They are also known for their fast timing performance which could be used to perform 4D construction of the hadronic showers. Such a construction can improve on hadronic shower separation by better associating the energy deposits belonging to the same shower from those of other showers. It can also improve on the energy reconstruction by identifying the delayed neutrons and assigning them a different weight.

To obtain excellent resolution in the hadronic shower energy measurement a binary readout of the gaseous detector is the simplest and most effective scenario. However, a lateral segmentation of a few millimeters is needed to ensure good linearity and resolution of the reconstructed energy. Such a lateral segmentation leads to a huge number of electronic channels resulting in a complicated readout system design and excessive power consumption. A cell size of $1 \times 1\ \mathrm{cm}^2$ are found to be a good compromise that still provides a very good resolution at moderate energies. However, simulation studies show that saturation effects are expected to show up at higher energies ($> 40\,\mathrm{GeV}$). This happens when many particles cross one cell in the center of the hadronic shower. To reduce these effects, multi-threshold electronics (Semi-Digital) readout is chosen to improve on the energy resolution by exploiting the particle density in a more appropriate way. These elements were behind the development of a Semi-Digital Hadronic CALorimeter (SDHCAL) that we propose to equip one of the CEPC future experiments.

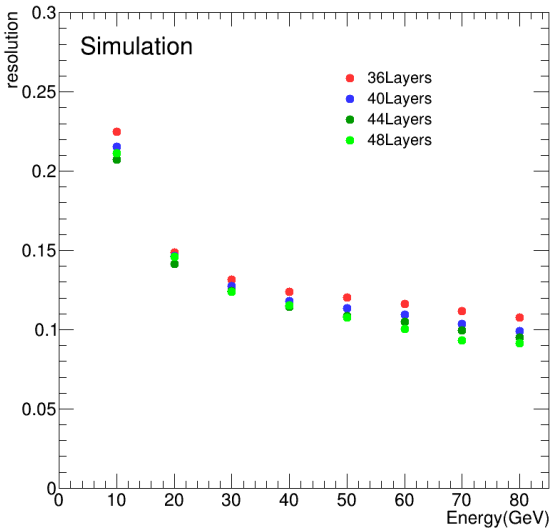

Figure 5.10: The energy resolution of SDHCAL with different number of layers using simulated pion samples.

Even with a 1x1 cm^2 lateral granularity of the readout system, a large number of electronic channels is still needed. This has two important consequences. The first is the power consumption and the resulting increase of temperature which affects the behavior of the active layers. The other consequence is the number of service cables needed to power and readout these channels. These two aspects can deteriorate the performance of the HCAL and destroy the principle of PFA if they are not addressed properly.

The R&D pursued by the CALICE SDHCAL groups has succeeded to pass almost all the technical hurdles of the PFA-based HCAL. The SDHCAL groups have succeeded to build the first technological prototype [12] of these new-generation calorimeters with 48 active layers of GRPC, 1m^2 each. The prototype validates the concept of the high-granularity gaseous detector and permits to study the energy resolution of hadrons one can obtain with such calorimeter. Figure 5.10 shows the energy resolution of SDHCAL with different numbers of layers using simulated pion samples. It indicates that SDHCAL with 40 layers yield decent performance with pion energies up to 80 GeV which is suitable for a CEPC detector.

A baseline detector of SDHCAL has been designed with 40 layers in total. Each layer contains 20 mm thick stainless steel, 3 mm thick GRPC and 3 mm for readout electronics with 1×1 cm^2 readout pads on PCB board.

In order to investigate appropriate options for the active detector of the SDHCAL, two parallel detector schemes, the Glass Resistive Plate Chamber (GRPC) and the Thick Gaseous Electron Multiplier (THGEM) are proposed for the active layers of the SDHCAL.

5.4.2.2 GRPC based SDHCAL

The GRPC scheme The structure of GRPC proposed as an active layer of the HCAL for CEPC is shown in Figure 5.11. It is made out of two glass plates of 0.7 mm and 1.1 mm thickness. The thinner plate is used to form the anode while the the thicker one forms the cathode. Ceramic balls of 1.2 mm diameter are used as spacers between the glass plates. The balls are glued on only one of the glass plates. In addition to those balls, 13 cylindrical fiber-glass buttons of 4 mm diameter are also used. Contrary to the ceramic

balls the buttons are glued to both plates ensuring thus a robust structure. Special spacers (ceramic balls) were used to maintain uniform gas gap of 1.2 mm. Their number and distribution were optimized to reduce the noise and dead zones (0.1%).

The distance between the spacers (10 cm) was fixed so that the deviation of the gap distance between the two plates under the glass weight and the electric force does not exceed 45 microns. The choice of these spacers rather than fishing lines was intended to reduce the dead zones (0.1%). It was also aimed at reducing the noise contribution observed along the fishing lines in standard GRPC chambers. The gas volume is closed by a 1.2 mm thick and 3 mm wide glass-fiber frame glued on both glass plates. The glue used for both the frame and the spacers was chosen for its chemical passivity and long term performance. The resistive coating on the glass plates which is used to apply the high voltage and thus to create the electric field in the gas volume was found to play important role in the pad multiplicity associated to a MIP [13]. A product based on colloids containing graphite was developed. It is applied on the outer faces of the two electrodes using the silk screen print method, which ensures very uniform surface quality. The measured surface resistivity at various points over a 1m^2 glass coated with the previous paint showed a mean value of 1.2 $\text{M}\Omega/\text{cm}^2$ and a ratio of the maximum to minimum values of less than 2 ensuring a good homogeneity of the detector.

Another important aspect of this development concerns the gas circulation within the GRPC taking into account that for the CEPC SDHCAL, gas outlets should all be on one side. A realization of this system was developed. It is based on channeling the gas along one side of the chamber and releasing it into the main gas volume at regular intervals. A similar system is used to collect the gas on the opposite side. A finite element model has been established to check the gas distribution. The simulation confirms that the gas speed is reasonably uniform over most of the chamber area. The GRPC and its associated electronics are housed in a special cassette which protects the chamber and ensures that the readout board is in close contact with the anode glass. The cassette is a thin box consisting of 2.5 mm thick stainless steel plates separated by 6 mm wide stainless steel spacers. Its plates are also a part of the absorber.

The electronics board is assembled with a polycarbonate spacer which is also used to fill the gaps between the readout chips and to improve the overall rigidity of the detector. The electronics board is fixed on the small plate of the cassette with tiny screws. The assembled set is fixed on the other plate which hosts the detector and the spacers. The total thickness of the cassette is 11 mm with 6 mm of which due to the sensitive medium including the GRPC detector and the readout electronics.

GRPC technological prototype An SDHCAL prototype fulfilling the efficiency, robustness and the compactness requirements of the future PFA-based leptonic collider experiments [12] was built. A total of 48 cassettes as the one described above were built. They fulfilled a stringent quality control. It is worth mentioning that 10500 HR ASICs were produced and tested using a dedicated robot for this purpose. The yield was found to be higher than 92%. The ASICs were then fixed on the PCBs over a surface area of 1m^2 and then subsequently fixed on the cassette cover once successfully tested. The cassettes were inserted in a self-supporting mechanical structure that was conceived and built in collaboration with the Spanish group of CIEMAT. The structure is made of Stainless Steel plates of 1.5 cm each. The plates were machined to have an excellent flatness and well controlled thickness. The flatness of the plates was measured using a laser-based inter-

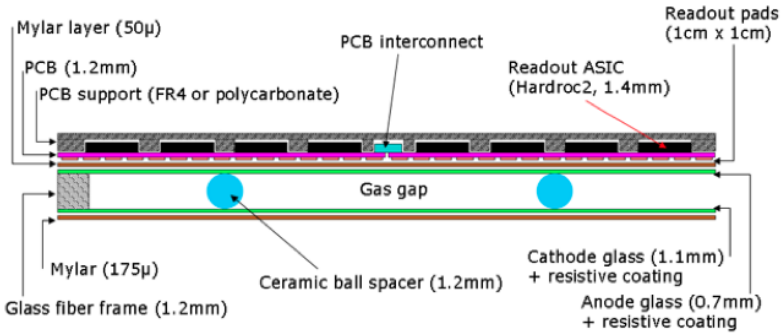

Figure 5.11: Cross-sectional view of an active layer with GRPC and readout layer.

ferometer system. It was found that the flatness of the plates are less than 500 microns. In April 2012 the prototype was exposed to pion, muon, electron beams of both the PS and the SPS of CERN as shown in Figure 5.12. The data were collected continuously in a triggerless mode. Figure 5.13 shows the efficiency (left) and pad multiplicity (right) of the prototype GRPC chambers measured using the muon beam. Figure 5.14 shows a display of two events collected in the SDHCAL. One is a produced by a pion interaction (left) and the other by an electron interaction (right).

The SDHCAL prototype results obtained with a minimum data treatment (no gain correction) show clearly that excellent linearity and good resolution [14] could be achieved on large energy scale as can be shown in Figure 5.15 where results obtained in two different beam lines are obtained using the same detector configurations. As is clearly demonstrated from this data, the high granularity of the SDHCAL allows one to study thoroughly the hadronic showers topology and to improve on the energy resolution by, among others, separating the electromagnetic and the hadronic contribution. The separation between close-by showers will also benefit from the high granularity on the one hand and the very clean detector response (< 1 Hz/cm^2) on the other. The results obtained with the SDHCAL [15] confirm the excellent efficiency of such separation due to the SDHCAL performance.

The quality of data obtained during several campaigns of data taking at the CERN PS and SPS beam lines validates completely the SDHCAL concept. This is especially encouraging since no gain correction was applied to the electronics channels to equalize their response. Still, improvement was further achieved by applying gain and threshold correction schemes in terms of the calorimeter response homogeneity.

A digitizer describing the response of the GRPC within the SDHCAL was developed [16]. It allows to study the SDHCAL behavior in a realistic manner in the future experiments.

In parallel to the prototype construction, a single cassette was tested in a magnetic field of 3 Tesla (H2 line at CERN) applying the power-pulsed mode. The test beam results [17] indicated clearly that the use of the power-pulsed mode in such a magnetic field is possible. The behavior of the detector in terms of efficiency, multiplicity, and other factors was found to be similar to those obtained in the absence of both the magnetic field and the power-pulsed mode.

Current SDHCAL R&D Large GRPC of 1m^2 were developed and built for the technological prototype. However, larger GRPC are needed in the SDHCAL proposed for future

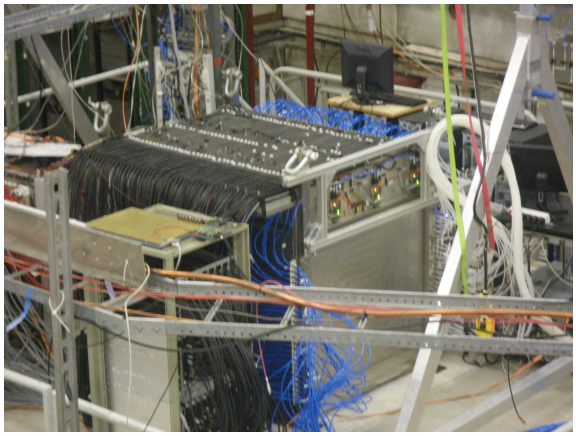

Figure 5.12: The SDHCAL prototype in beam test at CERN.

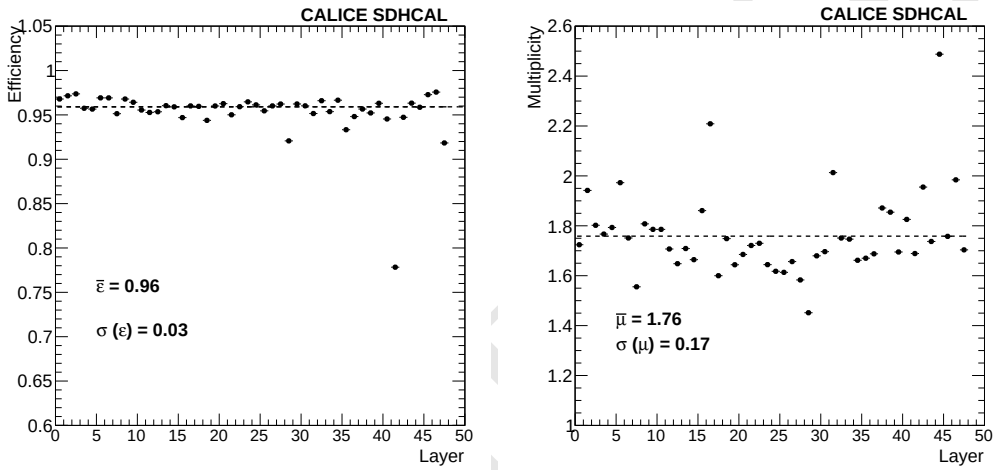

Figure 5.13: Left: Efficiency of the GRPC detectors of the SDHCAL. Right: the pad multiplicity of the GRPCs. One third of the chamber 42 was not instrumented. (Note: Figures taken from [14].)

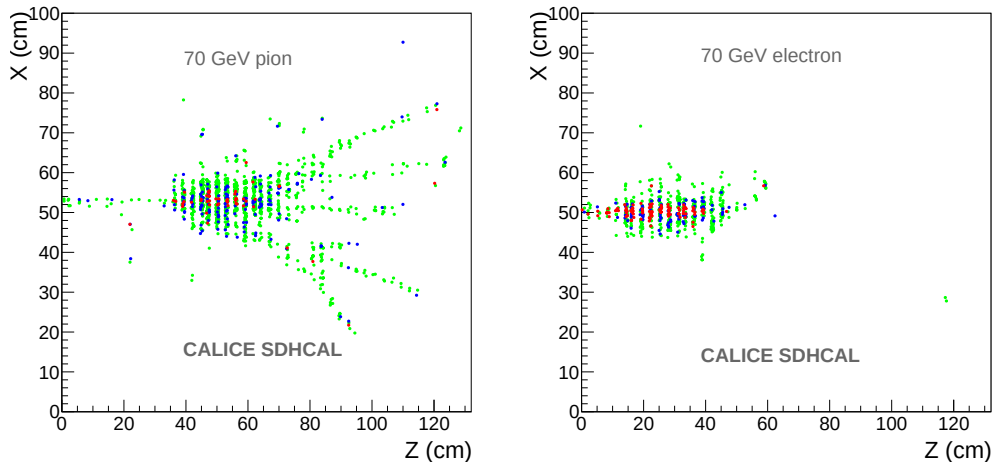

Figure 5.14: Left: event display of an 70 GeV pion interaction in the SDHCAL prototype. Right: Event display of a 70 GeV electron interaction in the SDHCAL prototype. (Note: Figures taken from [14].)

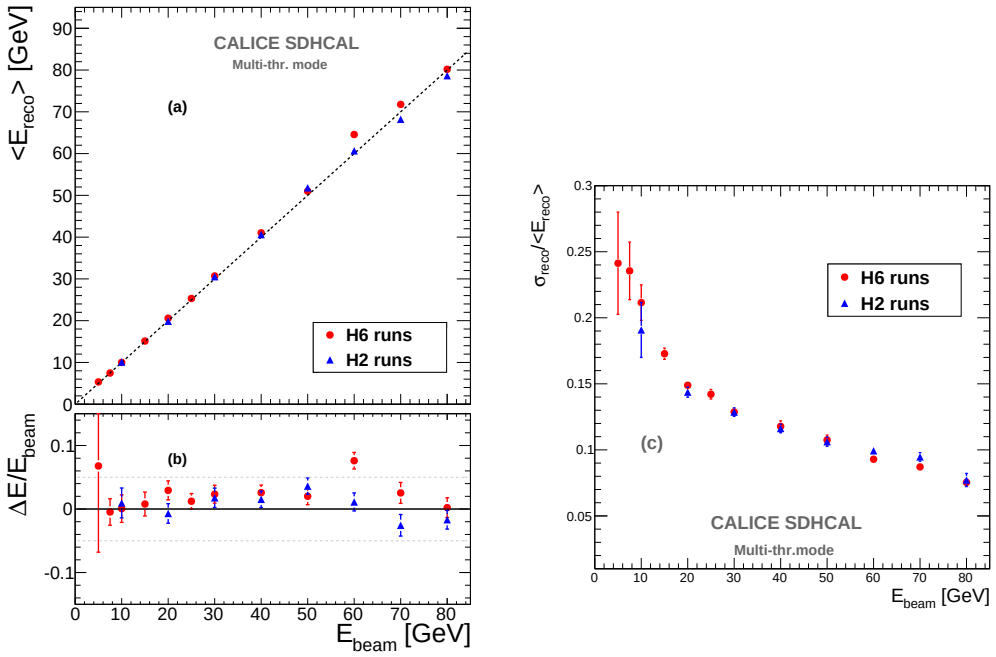

Figure 5.15: Left: a) Reconstructed energy of the hadronic showers collected in both H2 and H6 SPS beamlines. b) The relative deviation of the reconstructed energy with respect to the beam energy. Right: Relative energy resolution of the reconstructed hadronic shower. The pion beam of H6 beamline is largely contaminated by protons at high energy (>50 GeV). (Note: Figures taken from [14].)

leptonic collider experiments. These large chambers with gas inlet and outlet on one side need a dedicated study to guarantee a uniform gas gap everywhere notwithstanding the angle of the plate. It is necessary also to ensure an efficient gas distribution as it was done for the 1m2 chambers. To obtain this different gas distribution systems were studied. A new scheme with two gas inlets and one outlet was found to ensure an excellent homogeneity of the gas distribution. This system will be used in the near future to build large detectors exceeding $2m^2$.

To cope with the heating produced by the embedded readout system in case of limited or even the absence of use of the Power Pulsing system, a new active cooling system is being studied. Figure 5.16 shows a study of a water-based cooling system to absorb the excess of heat in the SDHCAL. The cooling system is very simple but very effective as well. It allows to keep the average temperature as well as the temperature dispersion of the GRPC well under control.

5.4.2.3 THGEM-based DHCAL

The THGEM scheme The THGEM can be built in large quantities at low cost, which might make them suitable for the large CEPC HCAL. THGEM detectors can provide flexible configurations, which allow small anode pads for high granularity. They are robust and fast, with only a few nano-seconds rise time, and have a short recovery time which allows a higher rate capability compared to other detectors. They are operated at a relatively low voltage across the amplification layer with stable high gain. The ionisation signal from charged tracks passing through the drift section of the active layer is amplified using a single layer or WELL-type THGEM structure. The amplified charge is collected

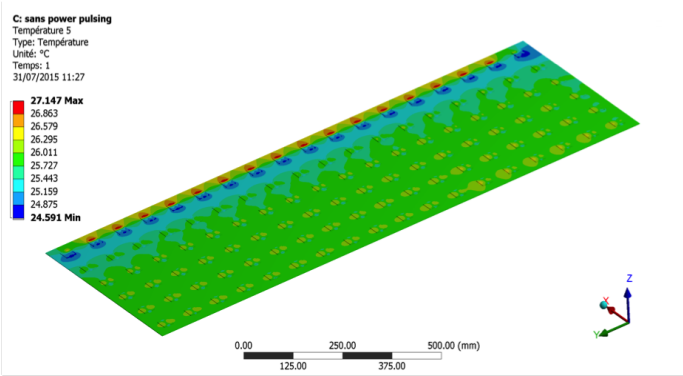

Figure 5.16: Temperature distribution in an active layer of the SDHCAL operated with no power-pulsing. The cooling system is based on circulating water inside copper tubes in contact with the ASICs.

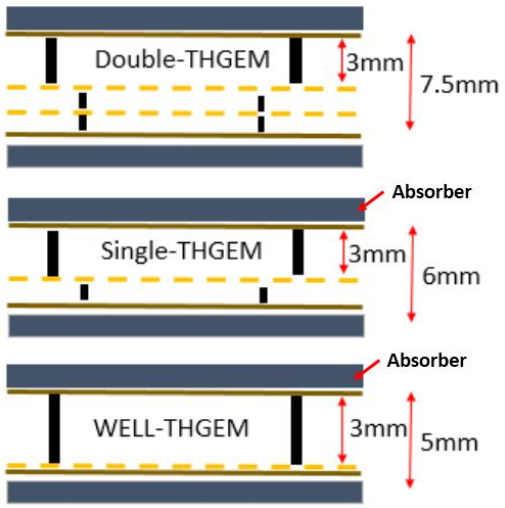

Figure 5.17: Schematic of three different types of THGEMs, eg. doubly-THGEM, single-THGEM and well-THGEM.

at the anode layer with pads at zero volts. As the HCAL is located within the coil, WELL-THGEM, a single layer structure with thinner thickness, as shown in Figure 5.17, can be considered as the sensitive medium, to keep the HCAL compact.

Digital readout has been proposed to limit the total amount of data, which simplifies the data treatment without comprising the energy resolution performance. The readout electronics of the DHCAL will be integrated into the sensitive layer of the system, thus minimizing dead areas. Large electronics boards are assembled together to form extra large boards before being attached to the THGEM. The board assembly will utilise a mechanical structure made of 4 mm stainless steel plates. In addition, to keep the HCAL as compact as possible, the fully equipped electronic boards are designed to be less than 2 mm thick in total.

A THGEM based detector for DHCAL has been designed with 40 layers in total. Each layer contains 2.0 cm thick stainless steel, 0.8 cm thick THGEM and readout electronics with 1×1 cm^2 readout pads. As THGEM production technology matures, the maximum area of THGEM is limited only by the size of the CNC drilling area. The low cost of materials and fabrication, robustness against occasional discharges, high gain and count rate

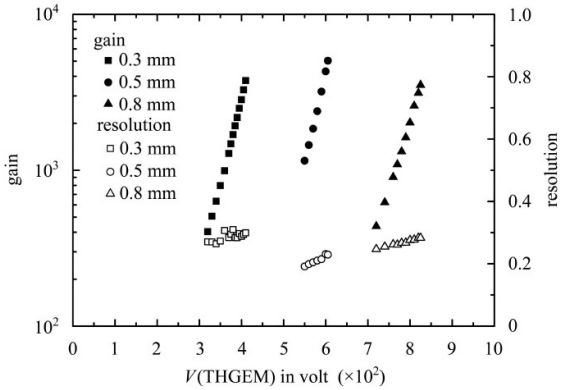

Figure 5.18: Gain and energy resolution of THGEM detector obtained with ^{55}Fe.

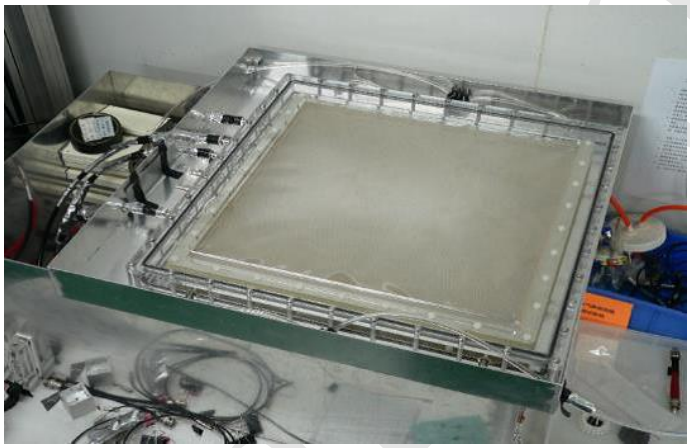

Figure 5.19: A THGEM was produced with a size of 40×40 cm^2.

capability of up to 10MHz/cm^2 make THGEM very attractive for building the DHCAL. As illustrated in Figure 5.17, the total thickness of the sensitive medium is 5 mm, which consists of 3 mm drift gap, 1 mm transfer gap and 1 mm induction gap. The absorber between the active layers is made of 20 mm thick stainless steel. The thickness of the readout electronics board is about 3 mm, and the total thickness of a single sensitive layer is less than 10 mm. Each layer corresponds to about 1.2 radiation lengths and 0.65 nuclear interaction lengths. The whole DHCAL detector is evenly divided into 40 layers, with a total stainless steel absorber thickness of 4.7 nuclear interaction lengths.

THGEM prototype A THGEM with an area of 40×40 cm^2 has been successfully fabricated, as shown in Figure 5.19, and a gain of 2×10^5 has been achieved with a double THGEM, with an energy resolution of about 20% for an ^{55}Fe source. The THGEM produced has the following features:

1. Standard PCB processes are used, which keeps the cost low;
2. Excellent performance in terms of energy resolution, gas gain and stability (as shown in Figure 5.18);
3. Rim around the hole formed by full-etching process, the size of which can be varied between 10 μm and 90 μm, as depicted in Figure 5.18 - this allows adjustment according to gas requirements.

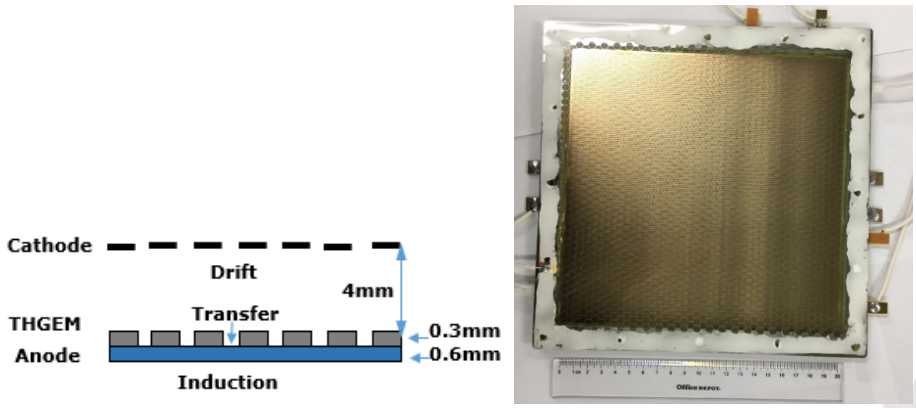

Figure 5.20: The schematic diagram of the WELL-THGEM (left plot) and a $20\text{cm} \times 20\text{cm}$ WELL-THGEM detector (right plot).

Figure 5.20 shows the schematic diagram of a new THGEM detector, where a micro-plate directly attached to the readout plate. Since the micro-porous structure is similar in shape to a well, these detectors are known as well-type THGEM (WELL-THGEM). This structure contains a single-layer THGEM, so that the thickness of detector can be reduced to $4 \sim 5$ mm, and the total thickness of the detector including ASIC electronics could be lowered to about 6 mm. A $20\text{cm} \times 20\text{cm}$ WELL-THGEM detector using thin-type THGEM has been developed as shown in the right plot of Figure 5.20

In addition, large THGEM detectors have been studied. Single THGEM detectors and WELL-THGEM detectors are being developed to reduce detector instability and inefficiency. Gas recycling systems are built to lower gas consumption and pollution. The achieved THGEM detection rates of 1 MHz/cm^2 with efficiencies greater than 95% already meet the CEPC requirements.

THGEM digital readout system A MICRO-mesh gaseous structure Read-Out Chip (MICROROC), which is developed at IN2P3 by OMEGA/LAL and LAPP microelectronics groups was used to readout the THGEM-based SDHCAL. The MICROROC is a 64-channel mixed-signal integrated circuit based on 350 nm SiGe technology. Each channel of the MICROROC chip contains a very low noise fixed gain charge preamplifier which is optimized to cover a dynamic range from 1 fC to 500 fC and allow an input detector capacitance of up to 80 pF, two gain-adjustable shapers, three comparators for triple-threshold readout and a random access memory used as a digital buffer. In addition, the chip has a 10-bit DAC, a configuration register, a bandgap voltage reference, a LVDS receiver shared by 64 channels and other features. A 1.4 mm total thickness is achieved by using the Thin Quad-Flat Packaging (TQFP) technology.

5.4.3 AHCAL based on Scintillator and SiPM

A high-granularity hadronic calorimeter plays an essential role in PFA-based experiments such as CEPC. It allows separation of the energy deposits from charged and neutral hadrons. The contribution of the neutrals to the jet energy, around 10% on average, fluctuates over a wide range from event-to-event. Improved resolution on the measurement of neutrals and therefore on the overall jet energy resolution performance with PFA can be achieved with analog instrumentation. The AHCAL (Analog Hadron CALorimeter)

is a sampling calorimeter with steel as the absorber and scintillator tiles with embedded electronics. The moderate ratio of hadronic interaction length (I=17cm) to electromagnetic radiation length (X_0 = 1.8 cm) of steel, allows a fine longitudinal sampling in terms of X_0 with a reasonable number of layers. Within the CALICE collaboration, a large technological prototype [18] using scintillator tiles and SiPMs is currently being built to demonstrate the scalability to construct a final detector via automated mass assembly. The outcome of CALICE-AHCAL R&D activities can be an essential input for the conceptual design of the hadron calorimeter system at CEPC.

5.4.3.1 AHCAL geometry and simulation

The AHCAL will consist of 40 sensitive and absorber layers, and the total thickness is about 100 cm. The AHCAL barrel consists of 32 super modules, each super module consists of 40 layers (Figure 5.21 shows the AHCAL structure). Figure 5.22 shows the single layer structure of AHCAL. The scintillator tiles wrapped by reflective foil are used as sensitive medium, interleaved with stainless steel absorber. The thickness of active layer including the scintillator and electronics is about $4 \sim 5$ mm.

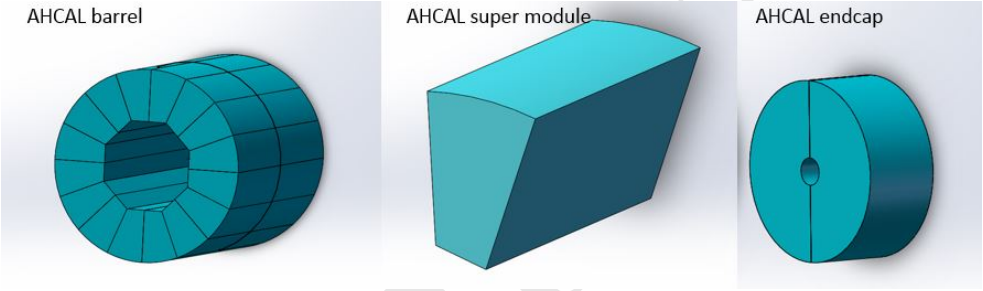

Figure 5.21: The layout of AHCAL barrel (left) and endcap regions (right), the middle plot shows a super module of AHCAL.

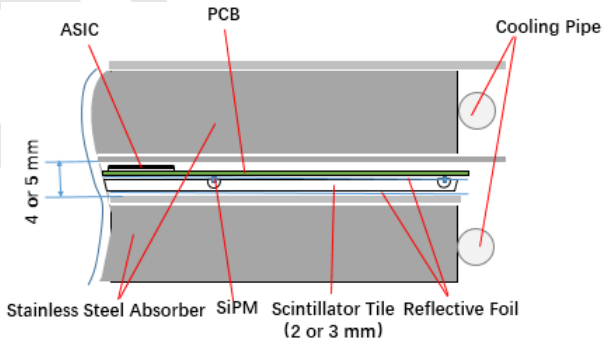

Figure 5.22: Cross-sectional view of a single layer of AHCAL.

The structure of scintillator tiles is shown in Figure 5.23. A dome-shaped cavity was processed in the center of the bottom surface of each tile by injection molding technology. The diameter and height of the cavity [19] are 6mm, 1.5mm, respectively, as shown in Figure 5.23 (right). Good response uniformity and low dead area will be achieved by the design of the cavity. More optimizations of the cavity structure will be done by GEANT4 simulation.

The AHCAL prototype detector was simulated by GEANT4. The detector model used here was the CEPC_v1 detector model. The geometry information was extracted by

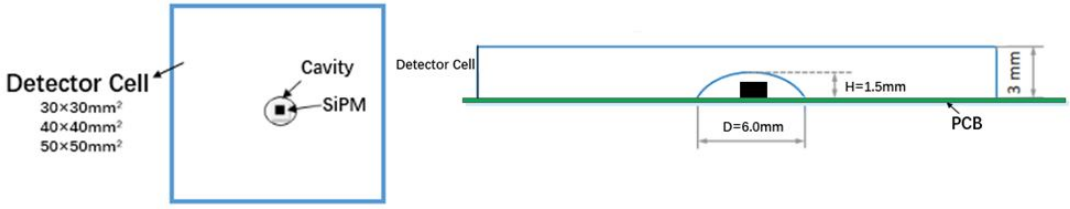

Figure 5.23: Top view of a detector cell (left) and cross-sectional view of a detector cell with a dome-shaped cavity (right)

Mokka at runtime and the generated events were stored in Slcio, which contains primary information regarding the energy deposition, hit position, time and Monte Carlo particle causing the energy deposition. The ECAL was simulated with 30 layers, and the HCAL has 40 active layers interleaved with 20 mm stainless steel as absorber plates. Each active layer consists of plastic scintillator (3mm) and readout layer (2mm PCB). The detector cell size is $30\times30\times3$ mm^3, as shown in Figure 5.24.

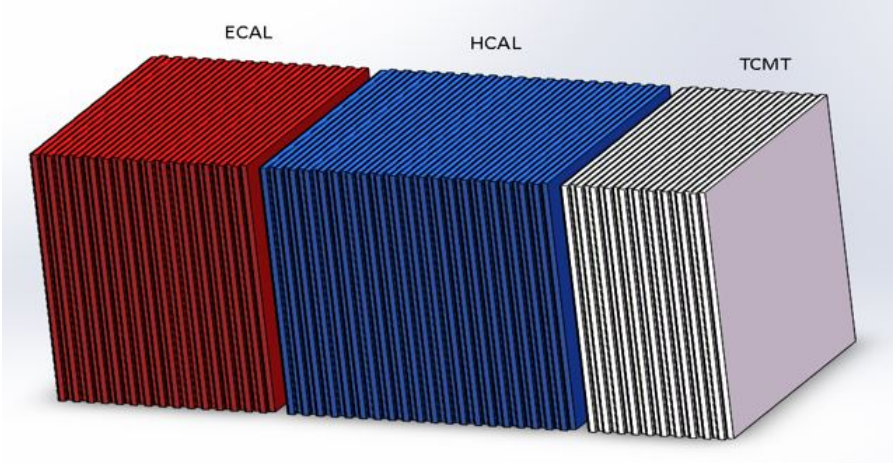

Figure 5.24: The structure of simulated calorimeters which is a part of the simplified geometry. Red part is the Silicon ECAL, Blue part is the scintillator AHCAL.

In order to obtain the resolution of calorimeters (ECAL and AHCAL) as shown in figure 5.24, the energy reconstruction formula 5.3 is employed [20], the coefficients a and b in this formula represent ECAL and HCAL calibration constants, respectively. After optimization, the calibration constants are a=44.4 and b=44.2, respectively, which were corrected to the energy scale of 60 GeV pions. The calibration constants compensate for the energy leakage from the calorimeters. The formula 5.4 [20] is used to fit for the energy resolution, as shown in Figure 5.25.

$$E_{REC} = a \times E_{ECAL} + b \times E_{HCAl} \tag{5.3}$$

$$\frac{\sigma}{E} = \frac{p_0}{\sqrt{E}} + p_1 \tag{5.4}$$

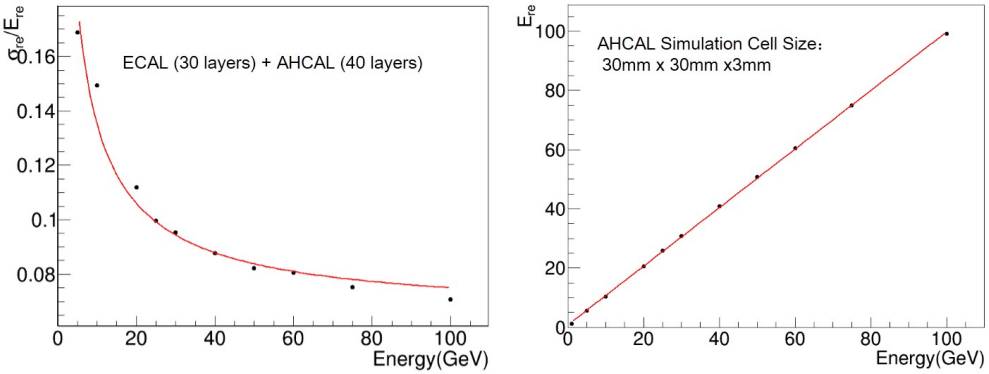

Figure 5.25: The left plot is the energy resolution from the SiW-ECAL and AHCAL for pions. The right plot is the corresponding results of reconstruction energy linearity.

5.4.3.2 Plastic Scintillator detector cell design and test

According to studies by the CALICE collaboration, a scintillator detector cell size of 30 × 30mm^2 is an optimal size. The simulation results of the CALICE collaboration [21] also suggest that it is possible to use the detector cells of larger sizes. A large detector cell size of 40 × 40mm^2 would reduce by nearly half the number of electronics channels compared to the 30 × 30mm^2 size. Therefore, the construction costs can be greatly reduced if the larger detector cells can meet the physics requirements. Two larger sizes of detector cells were considered. Four kinds of scintillator tiles with different sizes were fabricated and tested.

The SiPM is soldered onto a readout Printed Circuit Board (PCB) and the scintillator tile wrapped by ESR reflective foil is directly glued onto the PCB. A cavity design provides enough space for the SiPM package and improves collection efficiency of the light produced by incident particles penetrating the tile at different positions.

A strongly non-uniform tile response can lead to a distortion of the energy reconstruction in a complete calorimeter, and also compromises the calibration of the detector cells based on single particle signals. Three different sizes tiles (30×30×3mm^3, 30×30×2mm^3 and 50×50×3mm^3) were tested with the Hamamatsu MPPC S12571-025P and S13360-025PE. The spatial distribution of photon equivalents number (p.e.) with different detector cell areas are shown in Figure 5.26. The result shows that the number of p.e. in the center area is slightly larger than that of the surrounding area. The three detector cells show good response uniformity, within 10% deviation from their mean response.

Seven detector cells of different sizes, polishing methods and wrapping foil types were measured. The larger the area of the cell is, the less p.e. are detected, and the results of same size cells varied greatly because of the polishing methods.

The detection efficiency of 30×30×3mm^3 and 50×50×3mm^3 were measured with cosmic rays. The detection efficiency of 30×30×3mm^3 and 50×50×3mm^3 cells are 99% and 98.2%, respectively. According the cosmic-ray test result, the detection efficiency of 30×30×2mm^3 with S13360-025PE MPPC also can reach 98%.

The good response uniformity and high detection efficiency results indicate that scintillator detector cells are acceptable for AHCAL. The size of 30×30×3mm^3 detector cell

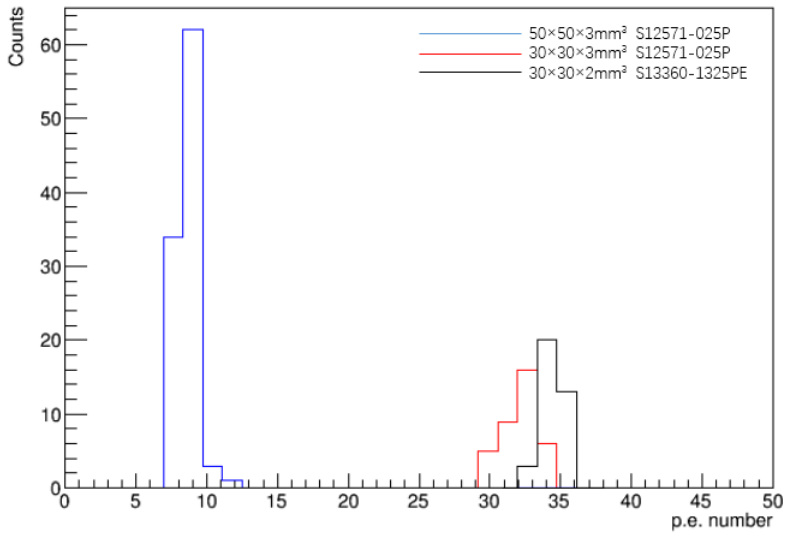

Figure 5.26: The uniformity measurement result of $30\times30\times3mm^3$, $50\times50\times3mm^3$ and $30\times30\times2mm^3$ detector cell.

is the baseline of AHCAL and more optimization of the detector cell size will be done by the simulation and test beam measurements.

5.4.3.3 Development of SiPM

Several kinds of SiPM were developed by Hamamatsu and other companies, they have been used for scintillator ECAL systems. The SiPM with epitaxial quenching resistors (EQR SiPM) is one of the main SiPM technologies under development in China. As shown in Figure 5.27, each APD cell (pixel) forms a high electric field, composing an enriched region between N-type epitaxial silicon substrate and P++ cap layer, and it employs the un-depleted region in the epitaxial silicon layer below P/N junction as the quenching resistor. Compared to conventional SiPM configurations that employ poly-silicon quenching resistors on the device surface, it is easier to achieve high density and small micro-APD cells, thus obtaining a small junction capacitor; the EQR SiPMs are expected to have short recovery time and high counting rate capability.

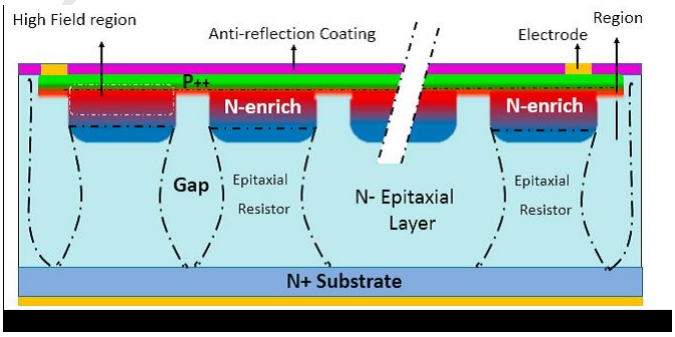

Figure 5.27: Schematic structure of EQR SiPM. APD cell consists of N-enriched regions forming high electric fields between the N-type epitaxial silicon wafer and the P++ surface layer, the un-depleted region in the epitaxial silicon layer below the P/N junction as the quenching resistor. The APD cells are isolated from each other by the Gap depletion region.

5.4.3.4 Electronics and DAQ

Front-end electronics ASIC: High-density electronics is indispensable to the instrumentation of high-granularity calorimetry. An ASIC chip named SPIROC, developed by the OMEGA group, is capable of handling 36 SiPMs. For each channel, it can be operated in an auto-trigger mode and has a dual-gain charge preamplifier with high dynamic range. It allows to measure the charge from 1 to 2000 photo-electron and the time to within 1 ns using a 12-bit digitizing circuit. With one 8-bit 5V input DAC per channel, the bias voltage for each SiPM can be adjusted to reach its optimum. In each channel, there are 16 analog memory cells that can buffer both charge and timing signals to be digitized afterwards consecutively. The digitization circuit is shared for both charge and timing measurements to minimize the power consumption, which needs to be as low as 25 μW per channel.

5.4.3.5 Cooling system

Inside the active layers of the calorimeter, the total power consumption of SPIROC ASIC chip and SiPM is about 5 mW/channel [22]. The scintillator detector cell size is 30×30mm^2, and the total channel number is about 5 million. For whole AHCAL, the total power consumption from ASIC chips is about 30kW. The copper cooling water pipes are expected to embedded in the stainless steel absorber. The cooling pipes are in the layer structure, as shown in Figure 5.22. Detailed design and optimization of a cooling system is needed.

5.5 Dual-readout calorimetry

5.5.1 Introduction

The dual-readout approach envisages designing a combined, homogeneous, detector with excellent performance for both electromagnetic and hadronic particle showers.

With conventional calorimeters, the performance obtained in hadronic energy measurements is by far worse than for the electromagnetic ones. The origin of this disparity is in the showers from single hadrons or jets of hadrons. Hadronic showers develop an electromagnetic component, from π^0 and η production, that exhibits large event-by-event fluctuations and dependence on the particle type and energy [23]. The em and non-em components of a hadronic shower are normally sampled with very different sensitivity, producing large differences in the measured signals, heavily affecting the energy resolution capability.

The variation of the em fraction is intrinsic to hadronic showers. As a matter of fact, the em fraction depends on the kind of particle initiating the shower (e.g., π, K, p) since, for example, impinging $\pi^{\pm}$ mesons can undergo a charge-exchange reaction with a nucleon as first interaction and generate a pure em shower, while a p cannot do the same due to baryon number conservation. Moreover, since π^0 production happens at any stage of shower development, the average em fraction $< f_{em} >$ increases with the energy as well as with the depth ("age") of the shower.

To overcome the problem two methods have been exploited: compensation and dual readout (DR). The first relies on equalizing the detector response to electromagnetic (e) and non-electromagnetic (h) shower particles (i.e. $h/e = 1$), but this requires a fixed ratio of absorber-to-sensor volumes, which limits the electromagnetic energy resolution, and the integration of the signals over large volumes and long times, to increase the response to the h component. The dual-readout method avoids these limitations by directly mea-

suring f_{em} on an event-by-event basis. The showers are sampled through two independent processes, namely scintillation (S) and Čerenkov (C) light emissions. The former is sensitive to all ionizing particles, while the latter is produced by highly relativistic particles only, almost exclusively found inside the em shower component. By combining the two measurements, energy and f_{em} of each shower can be simultaneously reconstructed. The performance in hadronic calorimetry may be boosted toward its ultimate limit.

The results obtained so far with prototypes, support the statement that fiber-sampling DR calorimeters may reach resolutions of the order of $10\%/\sqrt{E}$ or better for em showers and around $30-40\%/\sqrt{E}$ for hadronic showers and jets, coupled with strong standalone particle identification (PID) capabilities. One of the strengths of a DR calorimeter is that it achieves excellent jet energy resolution while not sacrificing performance in electromagnetic energy measurements. This would allow $W \to jj$ separation from $Z \to jj$ by invariant mass, high-precision missing three-momentum reconstruction by subtraction, e-μ-π separation and particle tagging.

While the dual-readout concept has been extensively demonstrated and experimentally validated in a series of beam tests, the use of standard PhotoMultiplier (PM) tubes to readout the S and C light has so far limited its development towards a full-scale system compliant with the integration in a particle detector at a colliding beam machine. These limitations should be overcome using SiPMs, low-cost solid-state sensors of light with single photon sensitivity, magnetic field insensitivity and design flexibility.

As it will be shown in the following, the high readout granularity in the plane perpendicular to the shower development and few other signal properties will probably make redundant or even inessential the need of a longitudinal segmentation into em and hadronic compartments (that is anyway possible). In case of a segmented calorimeter, both compartments need to provide dual-readout signals, in order to allow for the measurement of $< f_{em} >$.

5.5.2 Principle of dual-readout calorimetry

The independent sampling of hadronic showers, through scintillation and Čerenkov light emission, allows one to fully reconstruct, at the same time, energy and f_{em} of hadronic showers. In fact, the total detected signals, measured with respect to the electromagnetic energy scale, can be expressed as:

$$S \;=\; E\,[\; f_{em} \;+\; \eta_S \cdot (1 - f_{em})\;] \tag{5.5}$$

$$C \;=\; E\,[\; f_{em} \;+\; \eta_C \cdot (1 - f_{em})\;] \tag{5.6}$$

where $\eta_S = (h/e)_S$ is the ratio of the average S response for the non-em component to the em component in hadronic showers. The response being defined as the average signal per unit of deposited particle energy. The parameter $\eta_C = (h/e)_C$ is the response ratio for the C signal. In a typical dual-readout calorimeter, $\eta_S \approx 0.7$ and $\eta_C \approx 0.2$. These two equations are easily solved giving:

$$\frac{C}{S} \;=\; \frac{[\; f_{em} \;+\; \eta_C \cdot (1 - f_{em})\;]}{[\; f_{em} \;+\; \eta_S \cdot (1 - f_{em})\;]} \tag{5.7}$$

$$E \;=\; \frac{S \;-\; \chi C}{1 \;-\; \chi} \tag{5.8}$$

where:

$$\chi = \frac{1-\eta_S}{1-\eta_C} = \cot\,\theta \tag{5.9}$$

This is the simplest formulation of hadronic calorimeter response: an em part with relative response of unity, and a non-em part with relative response η.

There are two unknowns for each shower, E and f_{em}, and two measurements, S and C. The electromagnetic fraction, f_{em}, is determined entirely by the ratio C/S, and the shower energy calculated as in Eq. 5.8. Both, S and C, $\eta = (h/e)$ ratios have event-by-event fluctuations and should be considered stochastic variables, nevertheless the average $<h/e>$ values are essentially independent of hadron energy and species [24–26]. The global parameter χ can be extracted with a fit to calibration data:

$$\chi = \frac{E_0 - S}{E_0 - C} \tag{5.10}$$

$$S = (1-\chi)E_0 + \chi C \tag{5.11}$$

where E_0 is the beam energy.

The geometrical meaning of the θ angle in Eq. 5.9 can be understood by looking at the scatter plot of C versus S signals in Figure 5.28. An illustration of the prediction for the scatter plot for protons and pions is shown in Figure 5.28(a) and the scatter plot for 60 GeV pions measured in the RD52 lead-fiber calorimeter is shown in Figure 5.28(b).

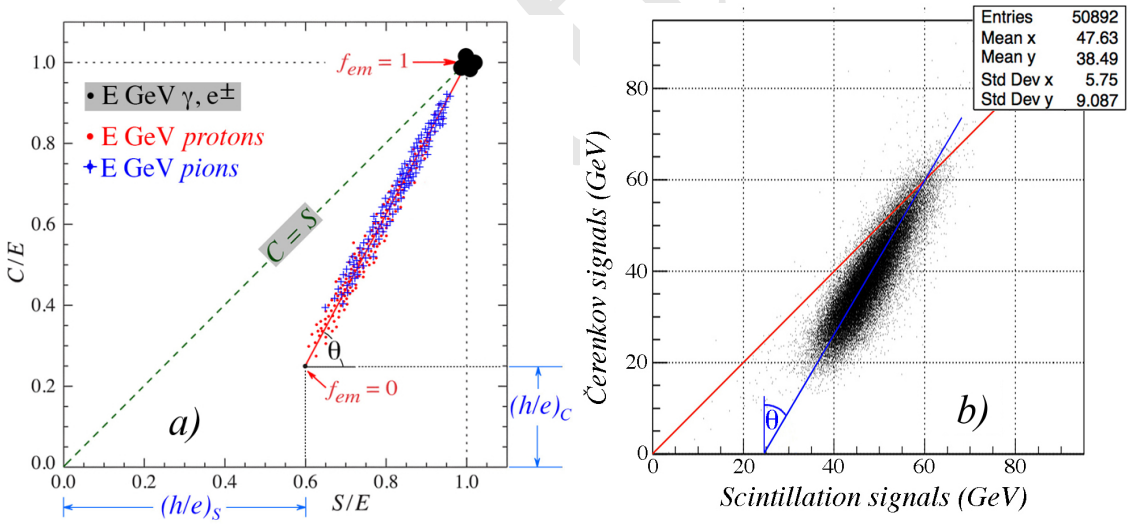

Figure 5.28: (a) Scatter plot of C/E versus S/E in a dual-readout calorimeter for p and π; (b) scatter plot of C and S signals for 60 GeV pions in the RD52 lead-fiber calorimeter.

The plot in Figure 5.28(b) shows that the data points are located on a locus, clustered around a line that intersects the $C/S = 1$ line at the beam energy of 60 GeV. In first approximation, the signal generated in the Čerenkov fibers is produced only by the em components of the hadron showers. The smaller the em fraction f_{em}, the smaller the C/S signal ratio. All signals are relative to the em scale meaning that both the Čerenkov and the scintillation responses are calibrated with beam electrons only, i.e. no hadronic calibration is required. This is one of the most qualifying and important points of dual-readout calorimetry.

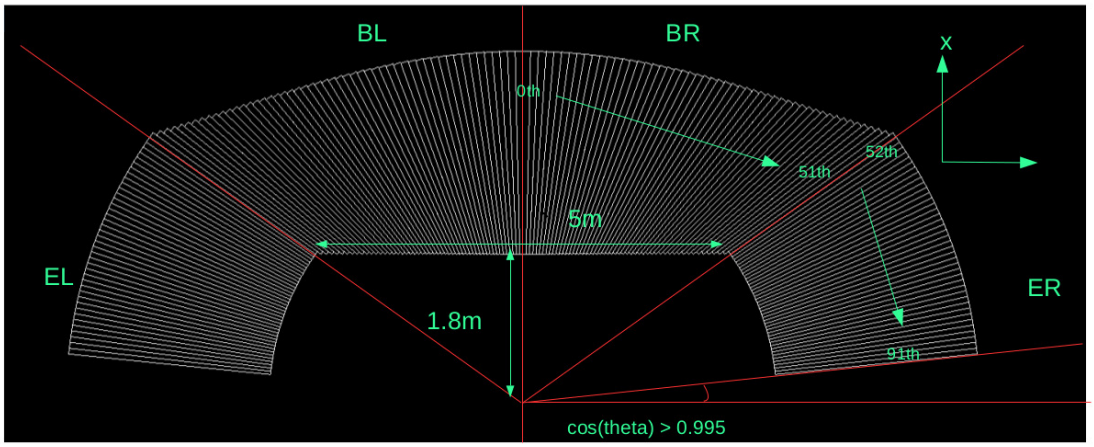

Figure 5.29: A possible 4π solution (called "wedge" geometry).

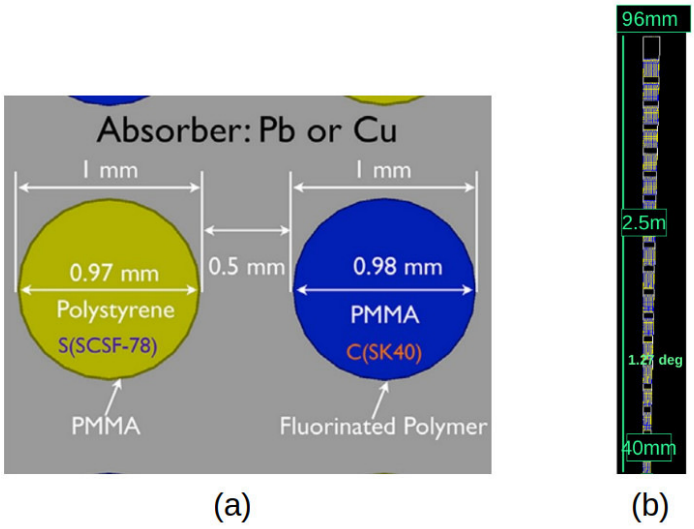

Figure 5.30: (a) Fiber arrangement inside the modules. (b) Dimensions of a module in the barrel region (at $\eta = 0$): from inside to outside the number of fibers more than doubles.

The effectiveness of this approach has been demonstrated by the DREAM/RD52 collaboration over a 15-year research program with a variety of detector solutions. Results and simulations [27–32] provide, so far, confidence that a fiber-sampling calorimeter, even without longitudinal segmentation, may meet the requirements of the CEPC physics program in a cost-effective way. Linearity and energy resolution, for both em and hadronic showers, $e/\pi/\mu$ separation, spatial resolution, all show adequate performance.

5.5.3 Layout and mechanics

5.5.3.1 Layout

A possible projective layout ("wedge" geometry, Figure 5.29) has been implemented in the simulations. Based on the work done for the 4th Detector Collaboration (described in its Letter of Intent [33]), it covers, with no cracks, the full volume up to $|cos(\theta)| = 0.995$, with 92 different types of towers (wedges). A typical one in the barrel region is shown in

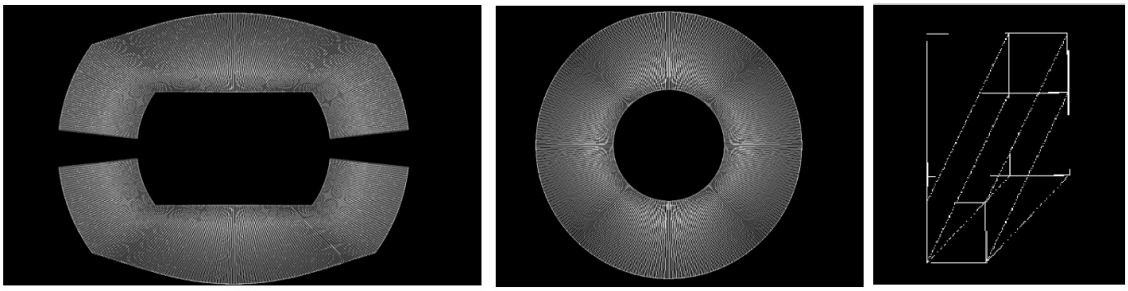

Figure 5.31: An alternative 4π solution (called "wing" geometry).

Figure 5.30(b), together with the fiber arrangement (Figure 5.30(a)): it has a granularity of $\Delta\theta \times \Delta\phi = 1.27^\circ \times 1.27^\circ$, a depth of about 250 cm ($\sim 10\ \lambda_{\rm Int}$), and contains a total of about 4000 fibers. The sampling fraction is kept constant by fibers starting at different depths inside each tower. This layout has been already imported in the simulations for the CEPC detector. Preliminary results on performance are shown in the next chapters.

A different layout implementing the "wing" geometry (see Figure 5.31) is also under study and preliminary results on the em performance will also been shown in the next chapters. In this case, the calorimeter is made of rectangular towers coupled with triangular ones.

In both cases, the total number of fibers is of the order of 10^8 for a complete 4π calorimeter.

5.5.3.2 Mechanics (material choice and machining)

Copper, lead and brass (Cu260) have been used as absorber materials by the DREAM/RD52 collaboration. Their main properties are shown in the Table 5.1, that also reports the calculation for the RD52 lead-prototype geometry. The values for iron are also shown, for comparison. From the table it can be seen that, for hadronic showers, a full-coverage solution with lead will give 6% broader and longer showers and a total mass 56% heavier than using brass. A full-containment $3 \times 3 \times 10\ \lambda^3$ prototype will need ~ 5 tons of material with lead and ~ 3.2 tons with brass.

material	ρ (g/cm^3)	X_0 (cm)	$R_{\rm Molière}$ (cm)	$\lambda_{\rm Int}$ (cm)	$\rho \times \lambda^3_{\rm Int}$ (kg)
Copper (Cu)	8.96	1.44	1.57	15.3	32.2
Brass (Cu260)	8.53	1.49	1.64	16.4	37.8
Lead (Pb)	11.35	0.56	1.60	17.6	61.8
Iron (Fe)	7.874	1.76	1.72	16.8	37.1
Fibers:Copper (38:62)	5.98	2.26	2.28	21.9	62.8
Fibers:Brass (38:62)	5.72	2.35	2.38	23.3	72.1
Fibers:Lead (38:62)	7.46	0.90	2.33	24.7	112.8
Fibers:Iron (38:62)	5.31	2.75	2.48	23.7	70.8

Table 5.1: Main properties of lead, copper, brass and iron absorber material and of fiber sampling matrices (RD52 lead-fiber prototype geometry).

A possibly stronger reason in favor of copper/brass is the fact that, since the e/mip ratio is 50% higher for copper than for lead, the Čerenkov light (almost exclusively produced by the em component of the shower) has a larger yield for copper, resulting in a better hadronic resolution [23]. However this statement needs to be quantified since it depends on the absolute level of the Čerenkov light yield(s).

On the other hand, lead is easily and accurately extruded, whereas forming copper into the desired shape, either by extrusion, molding, or machining, with the required tolerances in planarity and groove parallelism, is not yet an established industrial process. A variety of techniques (extrusion, rolling, scraping, and milling) for forming the converter layers have been tested. None has been qualified for a large-scale production and identifying an industrial and cost-effective process, including moulding, is a key point.

Alternative copper alloys (e.g. bronze) and/or materials (e.g. iron) may be investigated as well, both for addressing the production process issues and for optimizing the detector performance.

5.5.4 Sensors and readout electronics

To separately read out the signals from the S and C fiber forest and avoid oversampling of late developing showers is an issue that may be successfully addressed through the use of Silicon PhotoMultipliers (SiPMs). They would allow the separate reading of each fiber and provide magnetic field insensitivity. In principle, assuming powering and cooling do not pose issues, the transverse segmentation could be made as small as a fiber spacing, or 1.5 mm.

SiPMs are low-cost solid state light sensors with single photon sensitivity that underwent an impressive development over the last few years. Tests done in the last two years by the RD52 collaboration indicate that effective solutions for small-scale prototypes are very close already now. Thanks to their higher photon detection efficiency with respect to a standard PM, the higher number of Čerenkov (pe) should result in an improved resolution for both em and hadronic showers. On the other hand, the scintillation light spans a very large dynamic range and saturation and non-linearity effects were observed already for low-energy em showers.

In Figure 5.32, the number of photoelectrons per GeV ($\mathrm{pe/GeV}$) measured, in July 2017, with a very small module ($\sim 1.44\ \mathrm{cm}^2$ cross section, 32 + 32 fibers), is shown. The most relevant sensor characteristics are 1600, $25 \times 25\ \mu m^2$, cells, and a 25% nominal PDE. Due to the large S light yield, the data for the S signal were obtained at an (ultra low) PDE of $\sim 2\%$, and corrected for non-linearity. Rescaled to a 25% efficiency, the yield of S photoelectrons results in $\sim 108 \times 12.5 = 1350\ \mathrm{pe/GeV}$. By removing from the sum the hottest fiber, more heavily affected by non-linearity effects, the estimate grows to $\sim 1530\ \mathrm{pe/GeV}$.

The C signals show a linear response at $\sim\ 30\ pe/GeV$. It should be mentioned that the shower containment was estimated from GEANT4 simulations to be $\sim\ 45\%$. In addition, the problem of large light leaks from the S fibers into the neighboring C SiPM channels, observed in the 2016 tests, seems to be largely but not completely solved by a staggered readout of the S and C fibers (Figure 5.33). The contamination of the C signal was estimated to be $\sim 16\% \pm 6\%$.

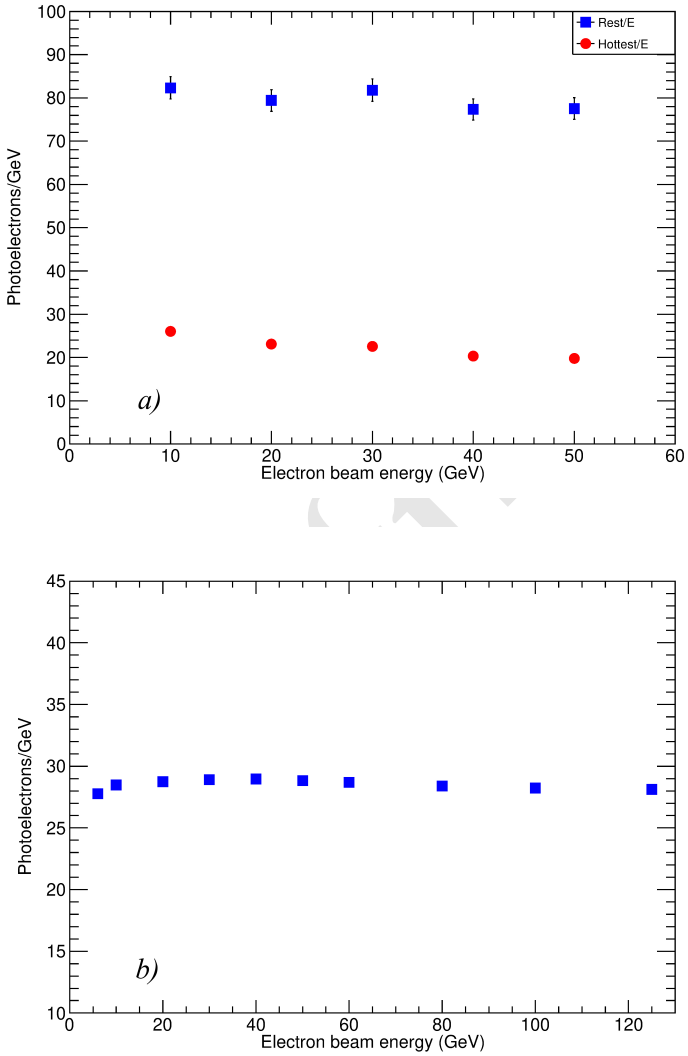

Figure 5.32: Number of photoelectrons per GeV $(\mathrm{pe/GeV})$ for (a) S and (b) C signals, as a function of the electron energy, from 10 to 50 GeV, in a small 64-fiber brass module. In (a), the results are shown separately for the hottest fiber and for the sum of the signals measured by the other 31 scintillating fibers obtained at the (ultra low) PDE of $\sim 2\%$. The main sensor specifications were: 1600, 25×25 μm^2, cells, and a 25% nominal PDE.

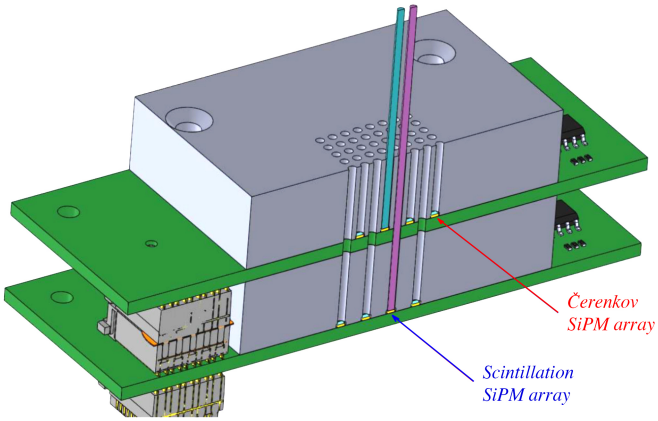

Figure 5.33: Staggered readout scheme: the scintillation and Čerenkov fibers are readout at different planes to minimize light leakage into neighboring channels.

5.5.4.1 Sensor choice

As far as the scintillation light detection is concerned, saturation and non-linearity should be solvable using higher density devices (e.g. with 10000, 10×10 μm^2, cells) in combination with some light filtering. The definition of the optimal dynamic range and the qualification of existing SiPMs in that regard, will be likely addressed in a short-term R&D phase.

For the Čerenkov light, improvements of the photon collection are possible with the use of an aluminized mirror on the upstream end of the fibers. The acceptance cone may also be enlarged with the use of cladding with a different refractive index. Over a longer term, it could be possible that the R&D on new devices, such as Silicon Carbide (SiC) sensors, expected to provide exclusive UV sensitivity (i.e. visible-light blindness), will allow us to obtain significantly larger pe yields.

5.5.4.2 Front-end electronics and readout

Concerning the front-end, the development shall certainly evaluate the use of Application Specific Integrated Circuits (ASIC) to handle and reduce the information to be transferred to the DAQ system. A major question is finding the optimal way for summing signals from a plurality of sensors into a single output channel. A dedicated feature-extracting processor, capable of extracting timing information such as time-over-threshold, peaking, leading and/or falling times, may allow to disentangle overlapping em and hadronic showers without the need for longitudinal segmentation. With the present fibers, a resolution of the order of 100 ps corresponds to a spatial resolution of about ~ 6 cm along the fiber axis (relativistic particles take 200 ps to cover 6 cm while light needs 300 ps).

5.5.5 Performance studies with fiber-sampling prototypes

Different prototypes were built and studied by the DREAM/RD52 collaboration, with copper or lead as absorber and photomultipliers as light sensors [27–32]. With electrons and pions, in the range of $\sim$ 10-150 GeV, the response linearity was found at the level of 1% for both the em and the hadronic energy reconstruction (having applied the dual-readout formula, equation 5.8, for hadronic showers). The em resolution was estimated to be close to $\sim 10\%/\sqrt{E}$, while the hadronic resolution was found to be at the level of $60\text{-}70\%/\sqrt{E}$,

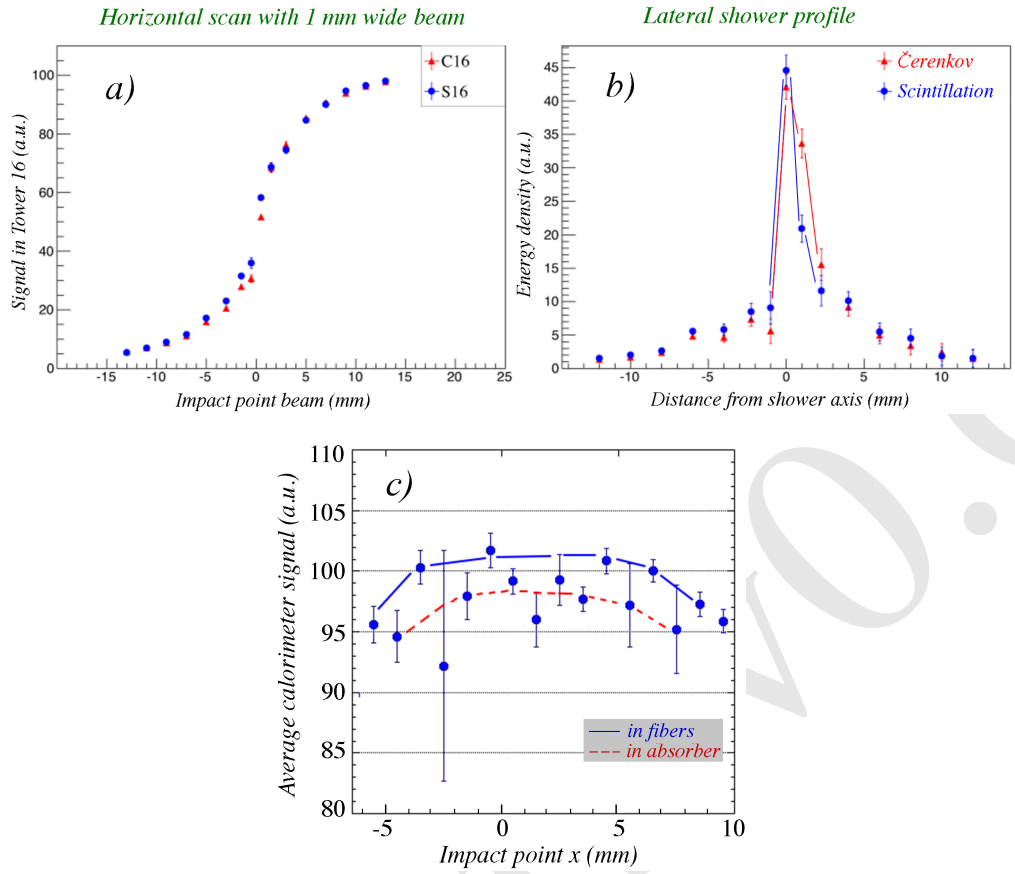

Figure 5.34: (a) The signal from a 1 mm wide beam of 100 GeV electrons, in the RD52 lead-fiber prototype, as a function of the impact point; (b) the lateral shower profiles derived from this measurement; (c) the dependence of the scintillation signal on impact point for a beam impinging parallel to the fibers.

to be corrected for the fluctuations introduced by lateral leakage and light attenuation in the fibers. None of the prototypes built thus far were large enough to substantially contain hadronic showers and an R&D program to assess the hadronic performance of a real detector, is under way. Preliminary simulations of standalone modules indicate a possible ultimate resolution of $\sim 30-40\%/\sqrt{E}$. More details can be found in the next paragraphs.

5.5.5.1 Electromagnetic performance

Figure 5.34(a) and 5.34(b) show the radial shower profile and the sensivity to the impact point: the core of the signal spans just a few mm. Figure 5.34(c) shows the dependence of the S signal on the impact point for particles entering parallel to the fibers. This introduces a constant term in the resolution that can be avoided with a small tilt of the fiber axis. In the C fibers, the problem does not show up since the early (collimated) part of the shower produces photons outside the fiber numerical aperture.

For the reconstruction of the energy of em showers, S and C signals provide independent uncorrelated measurements, with different sensitivity of the response. They are affected by different problems: S signals have photoelectron statistics one or two orders of magnitude higher than C signals, and their fluctuations are largely dominated by the sampling fluctuation of the energy deposits. C signal fluctuations are generally dominated

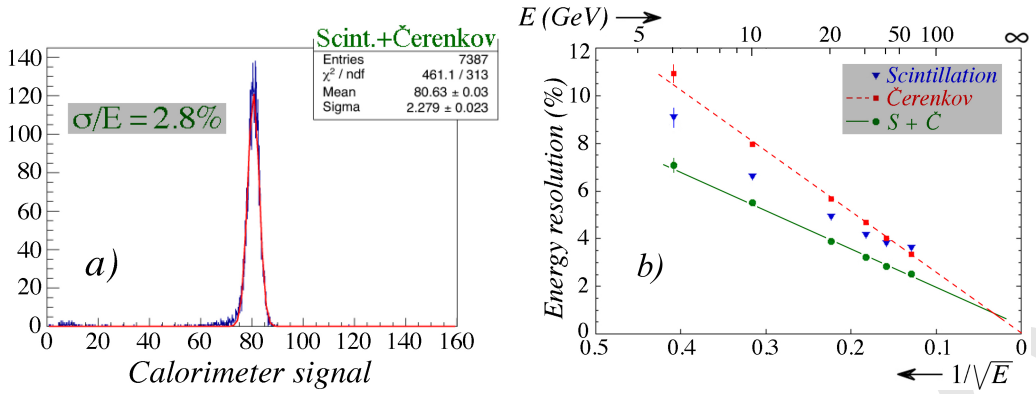

Figure 5.35: In the RD52 copper-fiber module: (a) signal distribution of the sum of all fibers for 40 GeV electrons; (b) the em energy resolution as a function of the beam energy. Shown are the results for the two types of fibers, and for the average combined signal.

by the limited photoelectron statistics, especially at low energies. Nevertheless, at high energies, the constant term for C signals is negligible, giving a better resolution. Averaging the two measurements improves the resolution up to a factor of $\sqrt{2}$. For the copper matrix, in Figure 5.35(a) the sum of S and C signals for 40 GeV electrons is plotted, while Figure 5.35(b) shows the em resolution, for S, C and the (average) combined signal.

5.5.5.2 Hadronic performance

The response of a lead-fiber matrix was studied with pion and proton beams [32]. The energy was reconstructed with the dual-readout relation (Eq. 5.8) and shows a restored gaussian response function (Figure 5.36) and linearity of the mean response.

The comparison of p and π^+ signals confirms that the dual-readout method largely compensates for the differences in shower composition, i.e., differences in the electromagnetic fraction, f_{em}, and between baryon-initiated and pion-initiated hadronic showers.

Due to the limited lateral size of the matrix (the effective diameter was $\sim 1\lambda_{\rm Int}$), the containment for hadronic showers was $\sim 90\%$ so that leakage fluctuations dominated the energy resolution. Selecting contained showers improved the resolution by a factor of ~ 2. Although that selection was introducing a bias in favor of high f_{em} showers, a significant improvement is expected for a realistic-size module.

The resolution was also affected by the finite light attenuation length of the fibers, causing early starting showers to be observed at lower signal values. The hadronic resolution, yet to be corrected for both effects, was reconstructed to be $\sim 70\%/\sqrt{E}$.

5.5.5.3 e/π separation

Four discriminating variables were identified for implementing e/π separation: the fraction of energy in the central tower, the C/S signal ratio, the signal starting time and the total charge/amplitude ratio, shown in Figure 5.37. The plots are relative to testbeam data taken with the RD52 lead-fiber prototype [27].

A multivariate neural network analysis showed that the best e/π separation achievable for 60 GeV beams was 99.8% electron identification efficiency with 0.2% pion misidentification. Further improvements may be expected by including the full time structure information of the pulses, especially if the upstream ends of the fibers are made reflective.

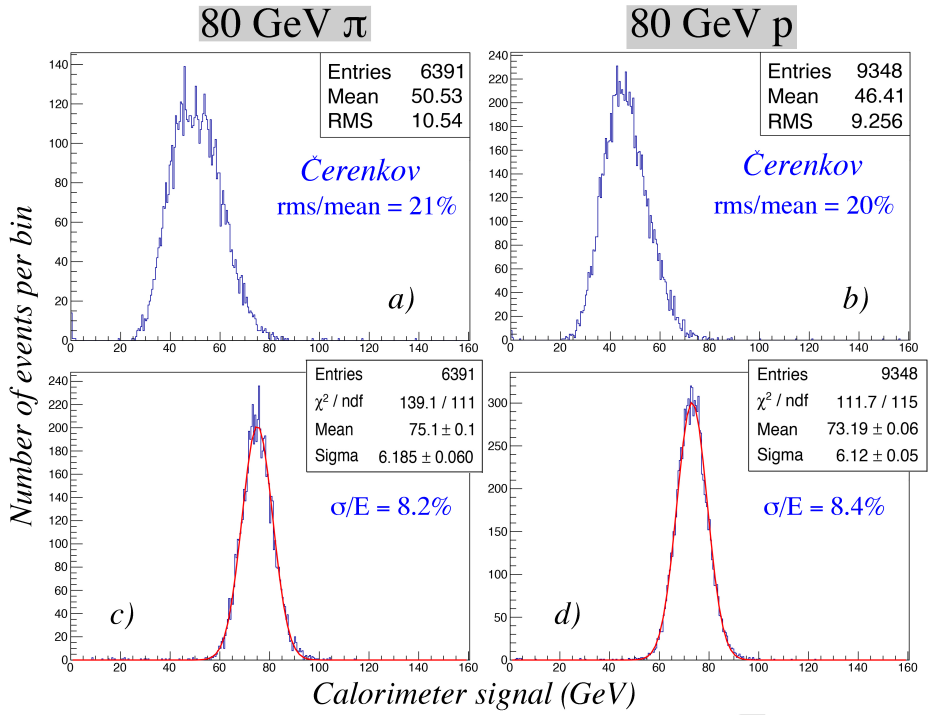

Figure 5.36: Signal distributions for 80 GeV pions and protons measured with the RD52 lead-fiber calorimeter. Shown are the distributions for the Čerenkov signals from 80 GeV (a) pi^+ and (b) protons, as well as the dual-readout total signals for 80 GeV(c) pi^+ and (d) protons. The dual-readout signals were obtained by applying Equation 5.8 with $\chi = 0.45$.

5.5.6 Monte Carlo simulations

GEANT4 simulations[1] are under development and analysis for understanding the performance of both testbeam modules and a 4π calorimeter integrated in a detector, with magnetic field, tracking and preshower elements.

5.5.6.1 Electromagnetic performance

A Cu matrix of dimensions $\sim 31 \times 31 \times 100$ cm^3 , with 1 mm fibers at 1.4 mm distance, compatible with the RD52 prototypes, has been simulated for the evaluation of the electromagnetic performance. PMMA clear fibers and Polystyrene scintillating fibers, with a 3% thick cladding (C_2F_2 Fluorinated Polymer for clear and PMMA for scintillating fibers), were the sensitive elements.

A small ($\lesssim 1°$) tilt angle was introduced to avoid large non-Gaussian tails in the scintillation signal due to channeling.

The energy containment for 20 GeV electrons was estimated to be $\geq 99\%$, with sampling fractions of 5.3% and 6.0% for scintillating and clear fibers, respectively.

Given the integral sampling fraction of 11.3% and the 1 mm diameter fibers, the contribution to the energy resolution due to sampling fluctuations can be estimated to be $\sim 9\%/\sqrt{E}$, ultimate limit on the em resolution for this detector.

The scintillation light yield is so large ($\sim$ 5500 pe/GeV) that the fluctuations of the S signals are dominated by the energy sampling process (Figure 5.38(a)). This is

[1] version 10.02.p01-10.03.p01, with FTFP_BERT_HP physics list

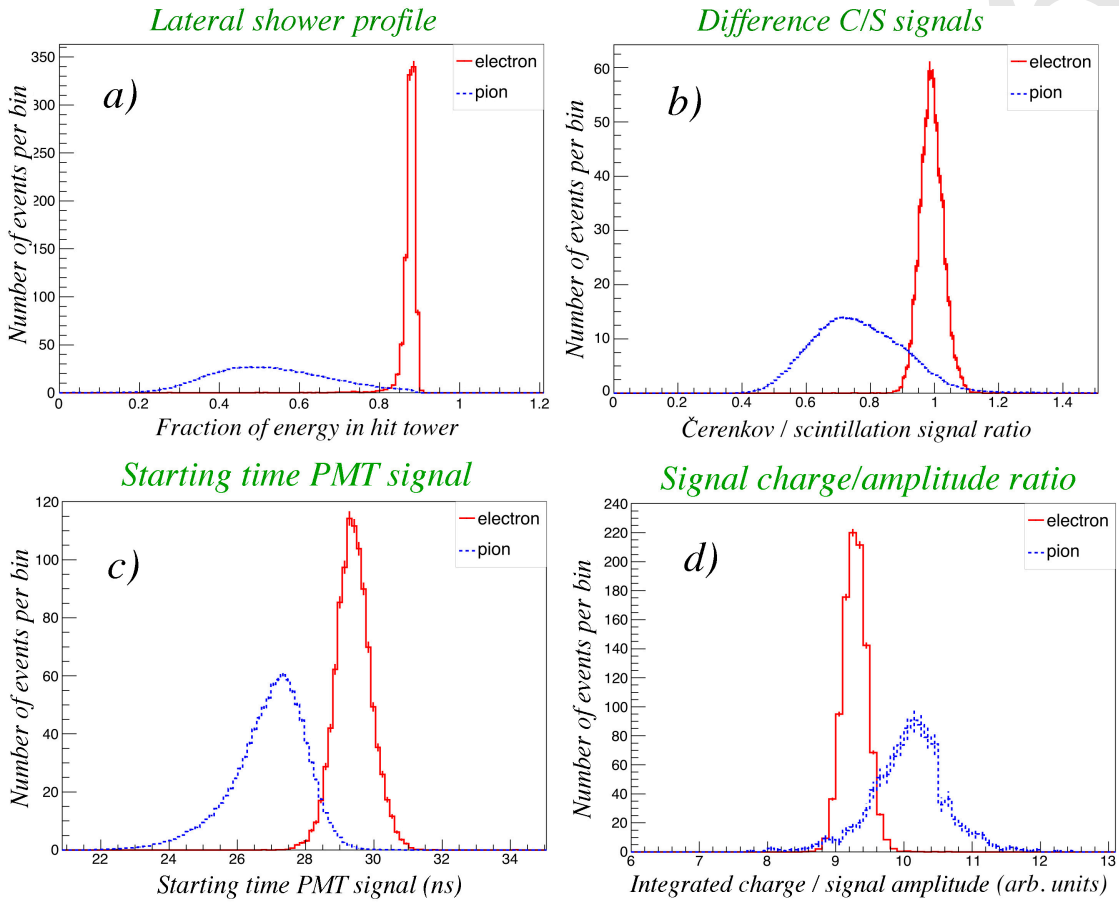

Figure 5.37: Distribution of four discriminating variables for 60 or 80 GeV electrons and pions, as measured with the RD52 lead-fiber prototype: (a) energy fraction deposited in the hit tower; (b) C/S signal ratio in the hit tower; (c) starting time of the PM signal; (d) ratio of the integrated charge and the amplitude of the signals.

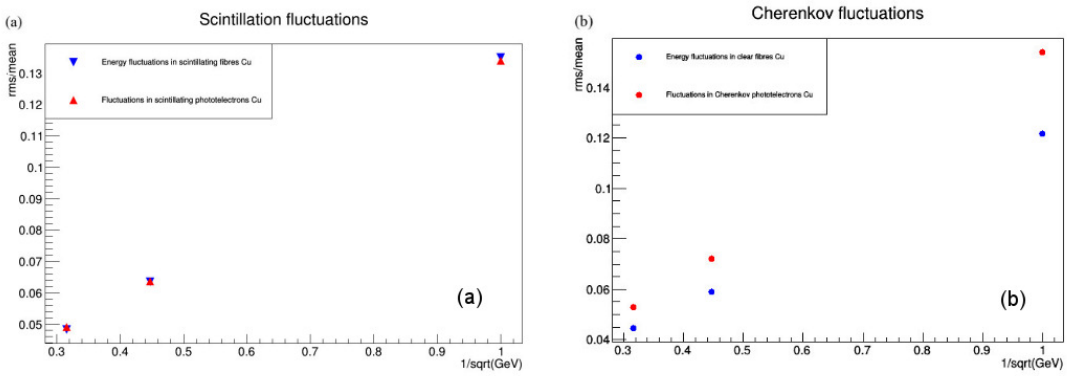

Figure 5.38: Relative fluctuation of the total signal detected in the (a) scintillating and (b) Čerenkov fibers, for both the energy deposit and the number of photoelectrons (MC simulations).

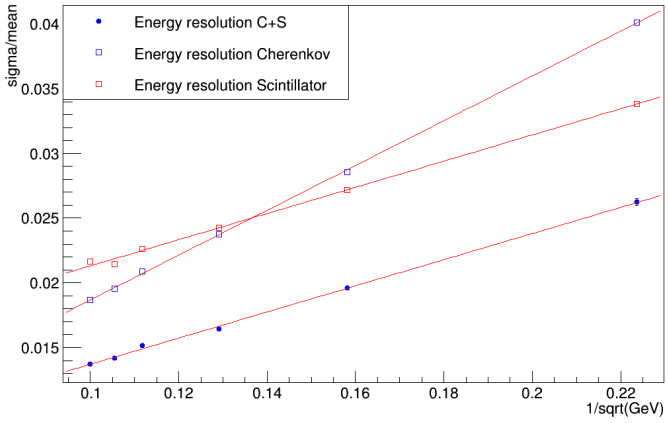

Figure 5.39: Relative resolution for em showers for the C and S signals, independently, and for the average of the two (MC simulations).

not true for the Čerenkov signals (Figure 5.38(b)), whose sensitivity is estimated to be $\sim 100\ pe/GeV$.

In the simulations, the process of generation and propagation of the scintillation light was switched off and the energy deposited in the fibers was taken as signal since this does not introduce any bias to the detector performance. This statement does not apply to the Čerenkov photons for which a parameterization that convolutes the effect of light attenuation, angular acceptance and PDE, was introduced.

In Figure 5.39 the resolutions are shown for both C and S signals, separately, and for the unweighted average value of the two. The variable on the horizontal axis and in the formulae for the fitted resolutions is the beam energy. The results of the fit to the data points are shown in Table 5.2. A slightly better result may be obtained with a weighted average.

5.5.6.2 Hadronic performance

A simulation of larger ($\sim 72 \times 72 \times 250\ cm^3$) matrices was implemented in order to get a hadronic shower containment of $\sim 99\%$. Calibration was done with 40 GeV electron beams.

fibers used	Fitted Gaussian em energy resolution
S-fibers only	$\sigma/E = 10.1\%/\sqrt{E} \oplus 1.1\%$
C-fibers only	$\sigma/E = 17.3\%/\sqrt{E} \oplus 0.1\%$
S-fibers and C-fibers	$\sigma/E = 10.1\%/\sqrt{E} \oplus 0.4\%$

Table 5.2: Fit to the em resolution (MC simulations)

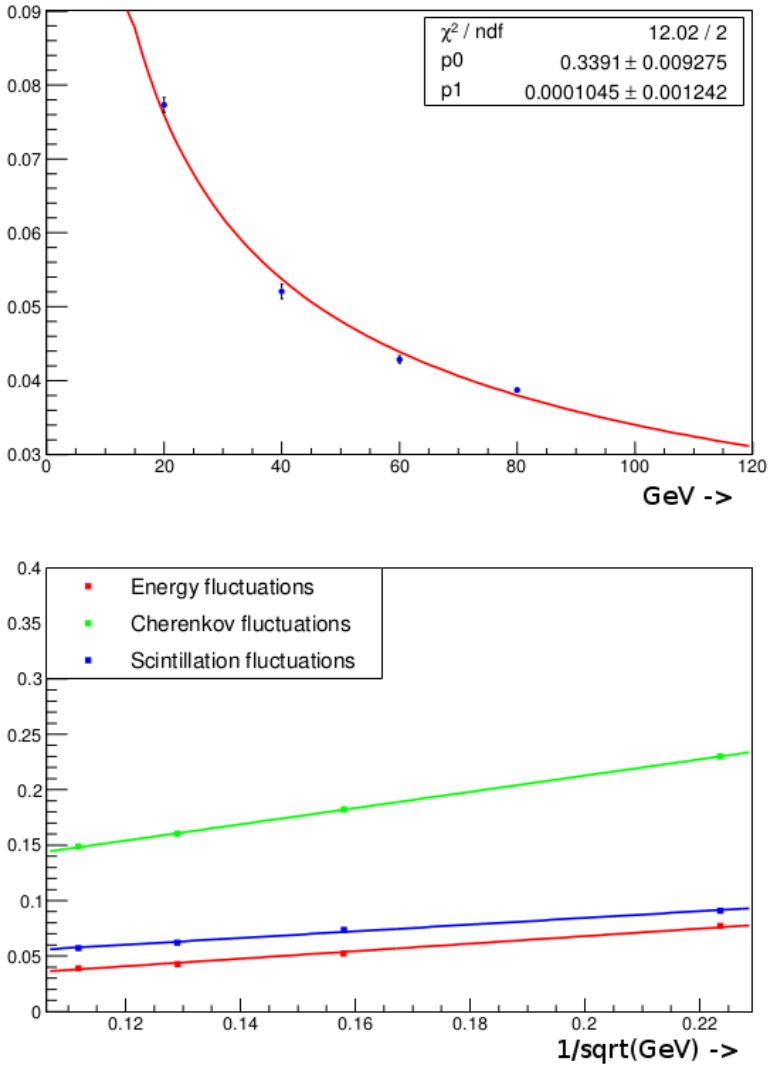

Figure 5.40: Monte Carlo simulations showing: (top) the relative hadronic resolution as reconstructed with the dual-readout formula; (bottom) the relative hadronic resolution independendly for the C and S signals and for the dual-readout combination of the two.

fibers used	Fitted Gaussian hadronic energy resolution
S-fibers only	$\sigma/E = 30\%/\sqrt{E} \oplus 2.4\%$
C-fibers only	$\sigma/E = 73\%/\sqrt{E} \oplus 6.6\%$
Dual-readout S-fibers and C-fibers	$\sigma/E = 34\%/\sqrt{E} \oplus$ (negligible)%

Table 5.3: Fit to the hadronic resolution (MC simulations)

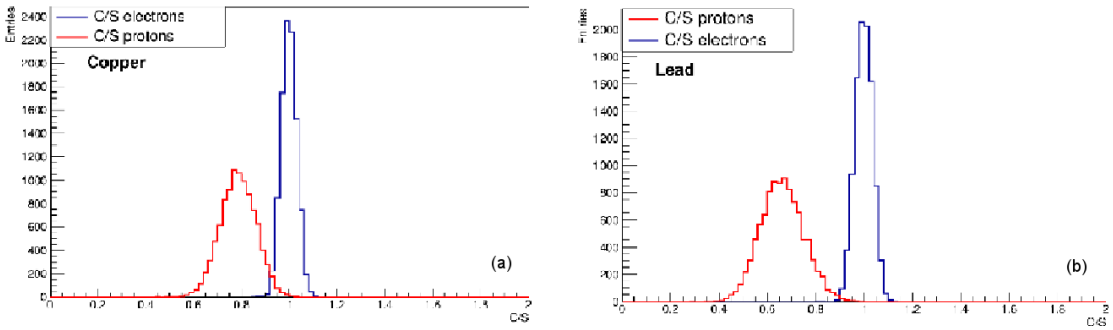

Figure 5.41: C/S ratio (MC simulations) for 80 GeV e^- and protons in (a) copper and (b) lead.

In Figure 5.40 GEANT4 predictions for the hadronic energy resolution, with copper absorber, are shown. Table 5.3 lists the results of the fit to the curves.

The large constant terms, for both S and C signals, are generated by the f_{em} correlated fluctuations. Simulations with lead absorber give equivalent but even slightly better results. The energy E in the plot (and in the expressions for the fitted resolutions) is the beam energy, corresponding in average to the energy reconstructed with the Equation 5.8 when the containment is properly accounted for (i.e., the reconstructed energy corresponds, in average, to the beam energy times the average containment). The fact that the experimental resolution was, so far, about a factor of two worse than simulations, is in our understanding, largely due to the small lateral size of the prototypes. In order to fully validate the MC predictions, an R&D programme is being pursued.

The correlation of the invisible energy with all the other components of hadronic showers was also analysed. Preliminary results seem to indicate that the most appropriate variable to account for the fluctuations of the invisible energy component is, by far, the f_{em}, with correlation coefficients of 90%, 92%, 94%, for copper, iron and lead respectively. The kinetic energy of the neutrons is predicted to be, at best, correlated at the 76% level. If confirmed, this would prove that compensation through neutron signal pickup or amplification will anyway give worse results than the dual-readout method [34].

In terms of particle ID capabilities, in Figure 5.41 the C/S ratio is shown for 80 GeV e^- and protons in copper (left) and lead (right). For an electron efficiency of $\sim 98\%$, the rejection factor for protons is ~ 50 in copper and ~ 600 in lead. Of course, this is an ideal

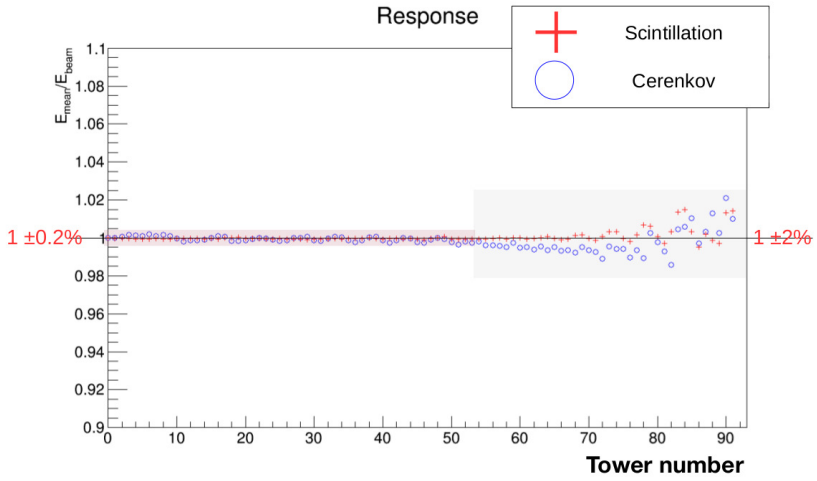

Figure 5.42: Ratio of reconstructed energy to the beam energy for 20 GeV e^-, as a function of the tower number, in the wedge geometry (MC simulations).

detector and in reality it is likely that the numbers will be worse. On the other hand, there are more variables that can be easily used in order to enhance the particle ID performance (namely the lateral shower profile, the starting time of the signal, the charge-to-amplitude ratio).

5.5.6.3 Projective geometry

Each tower, in the wedge geometry implementation, was exposed to 20 GeV electron beams, with an incident angle of $(1°, 1.5°)$, and the calibration constants calculated as the average deposit energy (in each tower) divided by the average C or S signal (of each tower). The response to an electron beam of the same energy is plotted in Figure 5.42. In the barrel region the response of all towers is within 0.2%, while in the forward the systematics are within 2%. All results were obtained with the quantum efficiency for the Čerenkov channel of each tower tuned to a light yield of $\sim 30\ pe/GeV$, as estimated in the RD52 beam tests.

The performance of a few towers was studied with electron beams in the range of 10-100 GeV. Figure 5.43 shows the linearity and em energy resolutions for towers #0 and #45. In both cases, the combined S and C signal shows a resolution of $\sim 14\%/\sqrt{E}$ with a constant term of $\sim 0.1\%$ while the average response is constant within 0.4%.

The hadronic resolution was studied with pions in the same energy range. A χ value of 0.29, the value measured for the DREAM calorimeter [35], was used to reconstruct the shower energy with Eq. 5.8. In the linearity plots for both tower #0 and #45 in Figure 5.44(a), the C and S responses to single pions increase non-linearly as the pion beam energy increases. On the other hand, the value reconstructed with the dual-readout formula shows a constant response to single pions $\sim 8\%$ lower than that to electrons (the reason being the shower containment). This effect in the GEANT4 simulations is described in reference [36]. In addition, the energy resolution after the correction (shown in Figure 5.44(b) for towers #0 and #45) is $\sim 26\%/\sqrt{E}$, with a constant term of less than 1%. These results support the statement that the hadronic energy resolution and the response to single hadrons should be constant (and appropriate) over the full barrel region. We may reasonably expect to obtain good performance over the entire 4π detector.

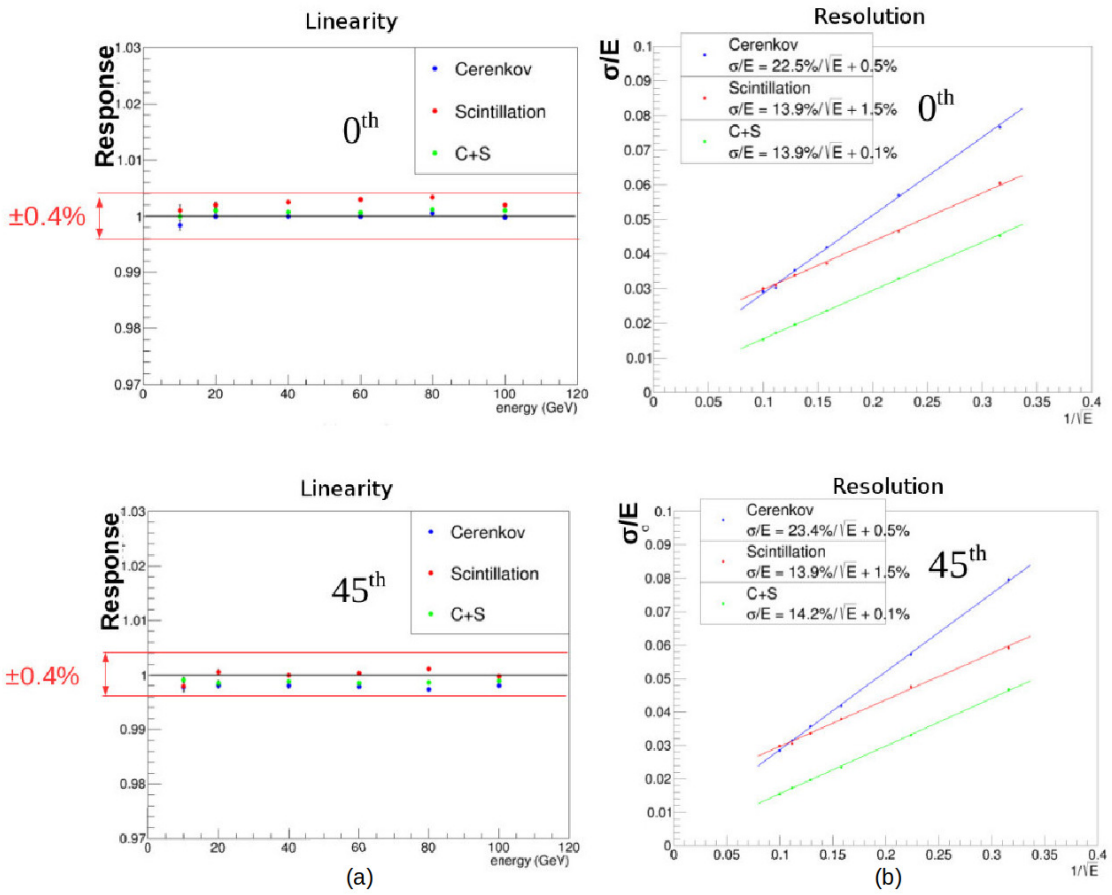

Figure 5.43: Linearity and em energy resolution for towers #0 (top) and #45 (bottom), in the wedge geometry (MC simulations).

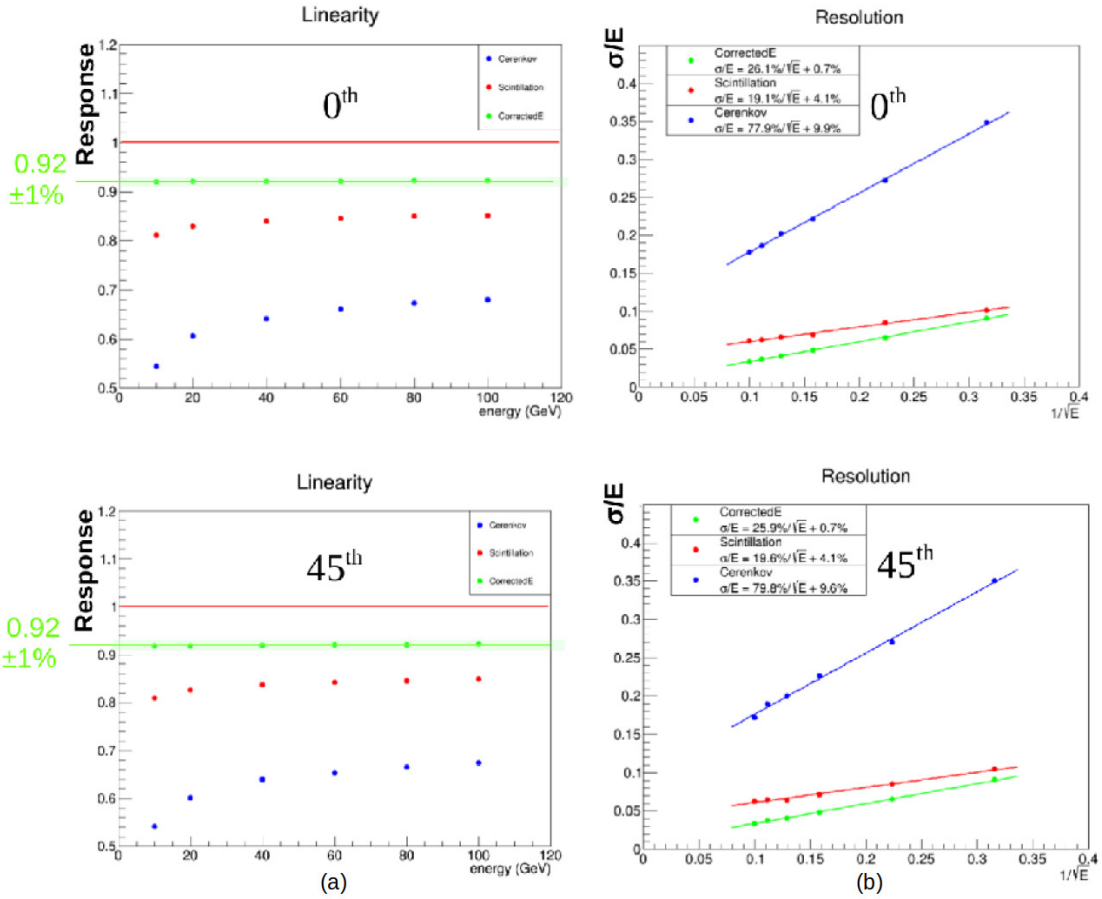

Figure 5.44: Linearity and energy resolution with pions, for towers #0 (top) and #45 (bottom), in the wedge geometry (MC simulations).

For the wing geometry, the results, at present, are limited to the em performance of few towers and the results (linearity and em resolution) substantially reproduce the wedge geometry ones.

5.5.6.4 Short term planning and open issues

The performance for single hadrons, jets and τ leptons has to be understood and the work has just started. For validation, the comparison with a prototype with a non-marginal hadronic shower containment, like the RD52 lead matrix, will be pursued.

For the em simulations, a program for the comparison with the 2017 RD52 data is ongoing. Some initial understanding of the absolute photoelectron scale for the Čerenkov light should be available in a very short time.

In general, light attenuation effects need also to be considered, for a $\sim 2-2.5m$ long fiber detector, that may introduce a constant term in the hadronic resolution as a function of the shower development point (late starting showers will give bigger and earlier signals).

The evaluation of advantages and disadvantages of filters (to dump the short attenuation-length components) and mirrors (to increase the number of photons that reach the photodetectors) may be relevant in this context.

The effects of the integration of a preshower detector have to be evaluated and the e/π separation capability assessed and quantified, for both isolated particles and particles within jets.

5.5.7 Final remarks

The 15-year-long experimental research program on dual-readout calorimetry of the DREAM/RD52 collaboration has yielded a technology that is mature for application at CEPC. The results show that the parallel, independent, readout of scintillation and Čerenkov light, makes it possible to cancel the effects of the fluctuations of the electromagnetic fraction in hadronic showers, dominating the energy resolution of most (if not all) the calorimeters built so far. In conjunction with high-resolution em and hadronic energy measurements, excellent standalone particle-ID capability has been demonstrated as well.

Those results give increasing support to the conviction that a matrix of alternating scintillating and clear fibers, inserted in copper or lead strips and readout by Silicon PhotoMultipliers (SiPMs), will be able to provide performance more than adequate for the physics programs at the CEPC collider.

Nevertheless, there is a series of technical and physics issues that need to be solved, within the next 2-3 years in order to arrive up to the design of a realistic 4π detector. A non-exhaustive list must include:

1. The industrial machining of foils of copper, lead or some other material, with the required precision.

2. The development of a mechanical integration design.

3. The readout of the high granularity matrices of SiPM that, in order to be effective, will require the development of a dedicated Application Specific Integrated Circuit (ASIC). Possible aggregations of more fiber outputs into a single channel have also to be implemented and studied.

4. The need and, in case, the way for a longitudinally segmented calorimeter system and the performance of Particle Flow Algorithms to further boost the performance of dual-readout.

5. The development of a modular solution and the assessment, at all levels, of its performance, through beam tests of small modules and simulations. An intensive program of simulations is already ongoing for a dual-readout calorimeter system at CEPC. The response to single particles and jets is under study, in standalone configurations. The work for understanding the behavior of a 4π calorimeter integrated in a full detector, with a tracking and a magnetic system, has also started. This will include, as well, the evaluation of the combined performance with a preshower detector in front.

References

[1] J.-C. Brient, *Improving the jet reconstruction with the particle flow method: An introduction*, in *Calorimetry in Particle Physics*, pp. 445–451. World Scientific, 2005.

[2] CALICE Wikipage. https://twiki.cern.ch/twiki/bin/view/CALICE/.

[3] CALICE Collaboration, R. Cornat, *Semiconductor sensors for the CALICE SiW EMC and study of the cross-talk between guard rings and pixels in the CALICE SiW prototype*, in *Proceedings CALOR'08*, vol. 160, p. 012067. 2009.

[4] T. S. et al., *Performance study of SKIROC2/A ASIC for ILD Si-W ECAL*, in *proceeding of the International Conference on Calorimetry for the High Energy Frontier (CHEF 2017)*. 2017.

[5] D. Grondin, J. Giraud, and J.-Y. Hostachy, *CALICE Si/W ECAL: Endcap structures and cooling system*, in *Proceedings, International Workshop on Future Linear Colliders 2016 (LCWS2016): Morioka, Iwate, Japan, December 05-09, 2016*. 2017. arXiv:1702.03770 [physics.ins-det]. http://inspirehep.net/record/1513187/files/arXiv:1702.03770.pdf.

[6] V. Boudry, *SiW ECAL R&D*, in *Fourth International Workshop on Future High Energy Circular Colliders (CEPC2014)*. 2014. http://indico.ihep.ac.cn/event/4338/session/2/contribution/35/material/slides/0.pdf.

[7] CALICE Collaboration, J. Repond et al., *Design and Electronics Commissioning of the Physics Prototype of a Si-W Electromagnetic Calorimeter for the International Linear Collider*, JINST **3** (2008) P08001, arXiv:0805.4833 [physics.ins-det].

[8] C. Adloff et al., *Response of the CALICE Si-W electromagnetic calorimeter physics prototype to electrons*, Nucl. Instrum. Meth. **A608** (2009) 372–383.

[9] CALICE Collaboration, R. Poschl, *A large scale prototype for a SiW electromagnetic calorimeter for a future linear collider*, in *Proceedings of*

International Workshop on Future Linear Colliders (LCWS11) 26-30 Sep 2011. Granada, Spain. 2012. arXiv:1203.0249 [physics.ins-det].

[10] V. Balagura et al., *SiW ECAL for future e^+e^- collider*, in *Proceedings, International Conference on Instrumentation for Colliding Beam Physics (INSTR17): Novosibirsk, Russia*. 2017. arXiv:1705.10838 [physics.ins-det]. http://inspirehep.net/record/1601898/files/arXiv:1705.10838.pdf.

[11] A. Irles, *Latest R&D news and beam test performance of the highly granular SiW-ECAL technological prototype for the ILC*, in *proceeding of the International Conference on Calorimetry for the High Energy Frontier (CHEF 2017)*. 2017.

[12] G. B. *et.al.*, *Conception and construction of a technological prototype of a high-granularity digital hadronic calorimeter*, JINST **10** (2015) P10039.

[13] M. B. *et al.*, *Performance of Glass Resistive Plate Chambers for a high granularity semi-digital calorimeter*, JINST **6** (2011) P02001.

[14] CALICE Collaboration, *First results of the CALICE SDHCAL technological prototype*, JINST **11** (2016) P04001.

[15] CALICE Collaboration, *Separation of nearby hadronic showers in the CALICE SDHCAL prototype detector using ArborPFA*, CAN-054 (2016) .

[16] CALICE Collaboration, *Resistive Plate Chamber Digitization in a Hadronic Shower Environment*, JINST **11** (2016) P06014.

[17] L. Caponetto*et al.*, *First test of a power-pulsed electronics system on a GRPC detector in a 3-Tesla magnetic field*, JINST **7** (2012) P04009.

[18] F. Sefkow, *Prototype tests for a highly granular scintillator-based hadron calorimeter*, CHEF2017. https://indico.cern.ch/event/629521/contributions/2702990/.

[19] The CALICE Collaboration, Y. Liu et al., *A design of scintillator tiles read out by surface-mounted SiPMs for a future hadron calorimeter*, (NSS/MIC), IEEE (2014) 1–4.

[20] The CALICE Collaboration, C. Adloff et al., *hadronic energy resolution of a highly granular scintillator-steel hadron calorimeter using software compensation techniques*, Journal of Instrumentation **7(09)** (2012) 1–23.

[21] K. Krueger, *Software compensation and particle flow*, CHEF2017. https://indico.cern.ch/event/629521/contributions/2703038/.

[22] M. Bouchel et al., *Second generation Front-end chip for H-Cal SiPM readout :SPIROC*, ILC website. https://agenda.linearcollider.org/event/1354/contributions/2542/attachments/1826/3054/SPIROC_presentation_13_02_2007.pdf.

[23] R. Wigmans, *Calorimetry, Energy Measurement in Particle Physics*, vol. 168 (second edition). International Series of Monographs on Physics, Oxford University Press, 2017.

[24] C. Patrignani et al. (Particle Data Group) Chin. Phys. C **40** (2016) 479–482.

[25] D. E. Groom, *Energy flow in a hadronic cascade: Application to hadron calorimetry*, Nucl. Instrum. Methods A **572** (2007) 633–653.

[26] D. E. Groom, *Erratum to "Energy flow in a hadronic cascade: Application to hadron calorimetry" [Nucl. Instr. and Meth. A 572 (2007) 633-653]*, Nucl. Instrum. Methods A **593** (2008) 638.

[27] N. Akchurin et al., *Particle identification in the longitudinally unsegmented RD52 calorimeter*, Nucl. Instrum. Methods A **735** (2014) 120.

[28] N. Akchurin et al., *The electromagnetic performance of the RD52 fiber calorimeter*, Nucl. Instrum. Methods A **735** (2014) 130.

[29] N. Akchurin et al., *Lessons from Monte Carlo simulations of the performance of a dual-readout fiber calorimeter*, Nucl. Instrum. Methods A **762** (2014) 100.

[30] A. Cardini et al., *The small-angle performance of a dual-readout fiber calorimeter*, Nucl. Instrum. Methods A **808** (2016) 41.

[31] R. Wigmans, *New results from the RD52 project*, Nucl. Instrum. Methods A **824** (2016) 721.

[32] S. Lee et al., *Hadron detection with a dual-readout fiber calorimeter*, Nucl. Instrum. Methods A **866** (2017) 76.

[33] 4th Detector Collaboration Letter of Intent: http://www.4thconcept.org/4LoI.pdf.

[34] S. Lee, M. Livan, and R. Wigmans, *On the limits of the hadronic energy resolution of calorimeters*, Nucl. Instrum. Methods A **882** (2018) 148.

[35] N. Akchurin et al., *Hadron and jet detection with a dual-readout calorimeter*, Nucl. Instrum. Methods A **537** (2005) 537.

[36] N. Akchurin et al., *Lessons from Monte Carlo simulations of the performance of a dual-readout fiber calorimeter*, Nucl. Instrum. Methods A **762** (2014) 100.

CHAPTER 6

DETECTOR MAGNET SYSTEM

The CEPC detector magnet is an iron-yoke-based solenoid to provide an axial magnetic field of 3 Tesla. A room temperature bore is required with a diameter of 6.8 m. This chapter describes the conceptual design of magnet, including the design of field distribution, solenoid coil, cryogenics, quench protection, power supply and the yoke. In the end of this chapter, the R&D section 6.5 brings up other concept options and some reach projects.

Compensation magnets are discussed in the Accelerator CDR chapter 9.2.

6.1 Magnetic field design

6.1.1 Main parameters

The CEPC detector magnet follows the same design concepts of the CMS and ILD detector magnets [1, 2]. The magnet system consists of the superconducting coil and the iron yoke with a barrel yoke and two end-cap yokes. The superconducting coil is designed with 5 modules wound with 4 layers. The three middle coil modules and the two end coil modules are wound with 78 and 44 turns, respectively. The operating current is 15,779 A for each turn corresponding to 3 T at the interaction point. The geometrical layout of magnet are shown in Figure 6.1. The main magnetic and geometrical design parameters are given in Table 6.1.

6.1.2 Magnetic field design

The magnetic field simulation has been calculated in 2D FEA model, with fine structure of the barrel yokes and end-cap yokes. Figure 6.2 shows the magnetic field contour of the

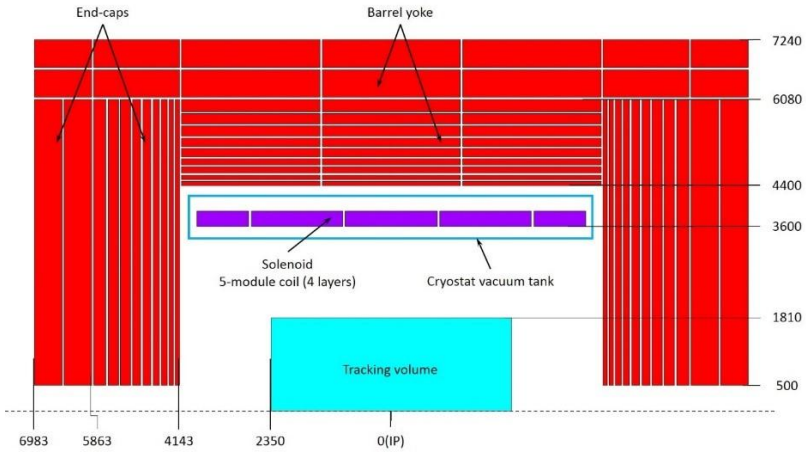

Figure 6.1: 2D layout of CEPC detector magnet (mm)

The solenoid central field (T)	3	Working current (A)	15779
Maximum field on conductor (T)	3.485	Total ampere-turns of the solenoid (MAt)	20.323
Coil inner radius (mm)	3600	Inductance (H)	10.46
Coil outer radius (mm)	3900	Stored energy (GJ)	1.3
Coil length (mm)	7600	Cable length (km)	30.35

Table 6.1: Main parameters of the solenoid coil

magnet. The maximum field on NbTi cable is 3.5 Tesla. The edge of 50 Gauss stray field is at 13.6 m from the beam axis and axial direction 15.8 m from the IP.

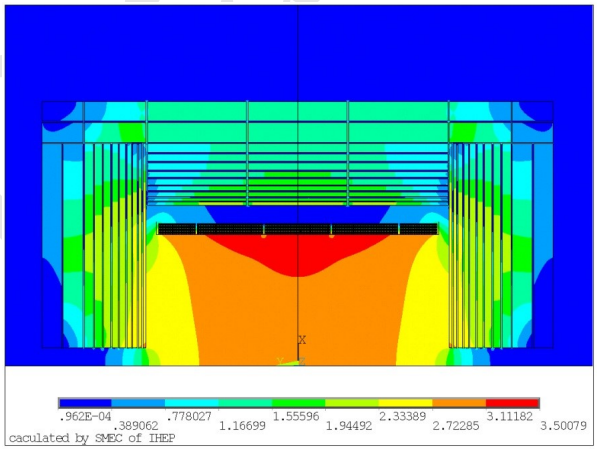

Figure 6.2: Field map of the magnet (T)

6.2 Solenoid coil

The conceptual superconducting conductor is based on the self-supporting conductor design of CMS detector magnet, composed of NbTi Rutherford cable, the pure aluminum stabilizer and aluminum alloy reinforcement.

The coil windings is wound by inner winding technique with the support aluminum-alloy cylinder, which acts as an external supporting mandrel and taking away the heat energy induced by quench. In order to maintain the operating temperature of LTS detector magnet, the cooling tubes for circular flow of LHe are welded on the outer surface of the aluminum-alloy cylinder.

6.3 Ancillaries (cryogenics, power supply, quench protection)

6.3.1 Cryogenics system

The coil cryogenic system is based on the CMS cryogenic system. The magnetic stored energy is 1.3 GJ. The thermosiphon principle is used for the coil indirect cooling mode using saturated liquid helium. A horizontal cryostat is designed, including a vacuum tank, an inner thermal shield, an outer thermal shield. The stainless steel vacuum vessel is 8.05 m length cylinder with diameter of 8.5 m. Two service towers are designed on the top of the cryostat in the central ring of the barrel yoke.

6.3.2 Power supply

A low ripple DC current-stabilized power supply, with low output voltage and high output current, is requested for CEPC detector magnet. The power supply is expected to have a free-wheel diode system and to be cooled with demineralized water.The main circuit of a standard power supplyincludes 12 pulse diode rectifiers and 4 IGBT chopper units with a switching frequency of 10 kHz.

6.3.3 Quench protection and istrumentation

Selected voltage signals from the CEPC detector magnet coil and current leads are monitored by an FPGA board for quench detection. If a quench happened, the power supply is switched off and a dump resistor is switched into the electrical circuit, the huge stored energy will be extracted mainly by the dump resistor and partially by the coil itself.

6.4 Iron yoke design

The iron yoke is designed not only for field quality but also for resisting magnetic forces, as well as the mechanical support of the sub-detectors. Therefore high permeability material with high mechanical strength is required for the yoke material in account of mechanical performance and magnetic field. The yoke also provides room for the muon detector, which will sit between layers of the yoke, and allows space for data cables, cooling pipes, gas pipes and etc. through the yoke. The yoke is divided into two main components, one cylindrical barrel yoke and two end-cap yokes. The total weight of the yoke assembly is about 10,000 tons.

The barrel yoke is a dodecagonal shape structure with a length of 8,200 mm (Figure 6.3). The outer diameter of the dodecagon and the inner diameter are 13,300 mm and 7,800 mm. The barrel yoke is subdivided along the beam axis into 3 rings, with 11 layers in each ring. Each ring of the barrel yoke is composed of 12 segments. 40 mm gap is designed between the rings and the layers for placing the muon detector and the electronics cables and services. From the inner to the outer, the layer thicknesses are 80 mm, 80 mm,

120 mm, 120 mm, 160 mm, 160 mm, 200 mm, 200 mm, 240 mm, 540 mm, 540 mm, respectively.

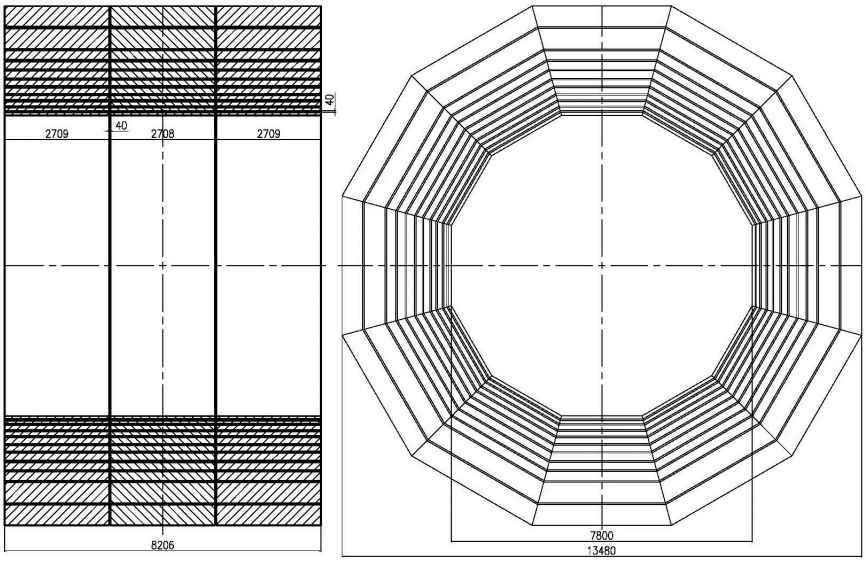

Figure 6.3: The barrel yoke design

The end-cap yokes is designed to dodecagonal structure with the out diameter of 13,300 mm. Each end-cap yoke will consist of 11 layers and one pole tip (Figure 6.4). Each end-cap yoke is composed of 12 segments. The thickness of pole tip is 600 mm, and from the inner to the outer, the layer thicknesses are 80 mm, 80 mm, 120 mm, 120 mm, 160 mm, 160 mm, 200 mm, 200 mm, 240 mm, 540 mm, 540 mm, respectively.

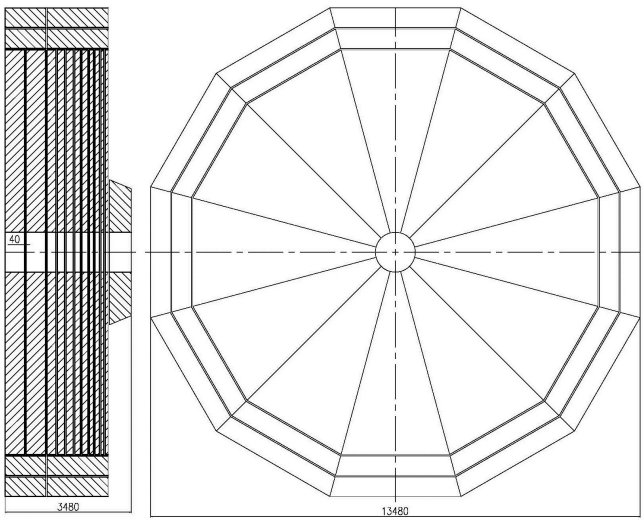

Figure 6.4: The end-cap yokes design

6.5 Thin solenoid for the IDEA detector

A "thin" 6 m long solenoid with an inner bore of 2.1 m radius and a field of 2 Tesla is a key element of the IDEA detector, where the calorimeter is located outside of the solenoid, allowing the maximum possible volume for tracking, but requiring maximum transparency. By "thin" we mean that the magnet should give minimal perturbation to the calorimetric measurements. The current design is mostly derived by scaling the present 2 Tesla solenoid of the ATLAS detector and uses a self-supporting aluminum stabilized NbTi conductor. Preliminary engineering studies [3, 4] indicate that the coil and the cryostat can fit in a total thickness of 30 cm using current technology; for a total of 0.74 radiation lengths or 0.16 interaction lengths at normal incidence. Up to 20% additional reduction in the overall thickness may be achieved with more R&D and engineering.

6.5.1 HTS solenoid concept for IDEA detector

A large HTS solenoid concept is also being studied for the IDEA detector. The HTS solenoid is supposed to use YBCO stacked-tape cable as the conductor. The radiation length of single YBCO tape coated with 10 μm copper is about 0.004 X_0. Each tape carries 700 A at 20 K. 35 YBCO tapes stacked together allows 24.5 kA. These tapes are embedded in 5 mm pure aluminium. The radiation length of this YBCO stacked-tape cable is estimated to be 0.2 X_0. If the operation temperature of the cold mass is raised to 20 K, the heat conductivity parameters of all components are improved. In addition, the electricity consumption of cooling station is much lower than that at 4.2 K. Therefore, the YBCO stacked-tape cable and the cryogenics are brought into R&D.

6.6 R&D

6.6.1 Dual solenoid design

The dual solenoid design is presented for a conceptual option for CEPC detector magnet, which contains two series connected superconducting solenoids carrying the opposite direction current, based on FCC twin solenoid [5]. The main solenoid provides central field within the room temperature bore. The outer solenoid provides the stray field shielding and a magnetic field between the two solenoids to facilitate muon tracking. The main advantage of this dual solenoid is that the system becomes comparatively light-weight and cost saving without iron yoke. The sketch is shown in Figure 6.5.

6.6.2 Superconducting conductor

The coil is simulated with an elasto-plastic 2D FE model. Mechanical analysis requires the experimental material properties of all conductor components. We have developed a 10 m long NbTi Rutherford cable embedded inside stabilizer which provides Ic 5 kA at 4 T background magnetic field. Meanwhile we measured the material properties and the tensile stress of 10 m cable. Longer conductor with higher Ic 15 kA at 4 T background is ongoing.

Figure 6.5: The sketch of dual solenoid design

6.6.3 Thermosyphon circuit

Thermosyphon principle is used to cool CEPC detector superconducting magnet by the U-shaped circuit configuration carrying LHe on the outer surfaces of the coil supporting cylinders. The thermosyphon circuit consists of helium phase separator located in an elevated position and the cooling tubes. In order to study the phase transition process of helium in the circuit, the changes of the temperature distribution and the density distribution over the time, a 1:10 scale thermosyphon circuit will be established for simulation and experiment.

References

[1] T. Behnke, J. E. Brau, P. N. Burrows, J. Fuster, M. Peskin, M. Stanitzki, Y. Sugimoto, S. Yamada, and H. Yamamoto, *The International Linear Collider Technical Design Report*, vol. Detector. 2013.

[2] C. Collaboration, *The CMS magnet project: Technical Design Report*, CERN/LHCC, 1997.

[3] M. Mentink, A. Dudarev, H. F. P. D. Silva, C. P. Berriaud, G. Rolando, R. Pots, B. Cure, A. Gaddi, V. Klyukhin, H. Gerwig, U. Wagner, and H. ten Kate, *Design of a 56-GJ Twin Solenoid and Dipoles Detector Magnet System for the Future Circular Collider*, IEEE TRANSACTIONS ON APPLIED SUPERCONDUCTIVITY **26** (2016) no. 3, 4003506.

[4] H. ten Kate, *Ultra-light 2T/4m bore Detector Solenoid for FCCee*, FCC Annual meeting. Amsterdam, Apirl 9-14th, 2018.

[5] M. Caccia, *An International Detector for Electron-Positron Accelerator(IDEA)*, Workshop on Circular Electron-Positron Colliders. Roma, May 24-26th, 2018.

CHAPTER 7

MUON SYSTEM

The muon system for a CEPC detector is designed to identify and measure muons, and will be located within the solenoid flux return yoke of the whole spectrometer. Two detector concepts are envisaged for the CEPC collider and they will likely employ different muon systems. A common requirement for the muon detectors will be to identify muons with very high efficiency ($\geq$95%) and high purity, over the largest possible solid angle and down to low p_T values ($\geq$3 GeV/c). A standalone muon momentum resolution from the muon detector could be required, translating in a good position resolution along the muon track which would add robusteness and redundancy to the whole detector design. In particular the muon system will significantly help in identifying muon produced within jets, for example from b decays.

The muon system plays an important role in measuring physics processes involving muon final states, e.g. $e^+e^- \to ZH$ with $Z \to e^+e^-$ or $\mu^+\mu^-$ and also for studying long-lived particles that would decay far from the primary vertex but still within the detector. In addition, the muon system compensates for leaking energetic showers and late showering pions from the calorimeters, which could help to improve the relative jet energy resolution[1].

In this chapter the baseline muon system design is described and then two possible technologies for realising the muon detector are presented, specifically the Resistive Plate Chamber (RPC) and an innovative type of Micro Pattern Gas detector (MPGD), the μ-RWELL detector. The main difference between the two technologies lies in the position resolution and the cost. More layers of RPC detectors are needed to achieve a good momentum resolution on the muon tracks with respect to the μ-RWELL case, where 3-4 layers would be sufficient. In terms of rate capability both technologies are more than adequate for the CEPC environment. If the requirement of a standalone muon momentum

resolution from the muon detector is relaxed, the number of layers of the RPC solution could be greatly reduced. Other gas detectors are also being considered as possible options, such as Gas Electron Multiplier (GEM), MicroMegas and Monitored Drift Tubes (MDT), although they are not described here.

7.1 Baseline Design

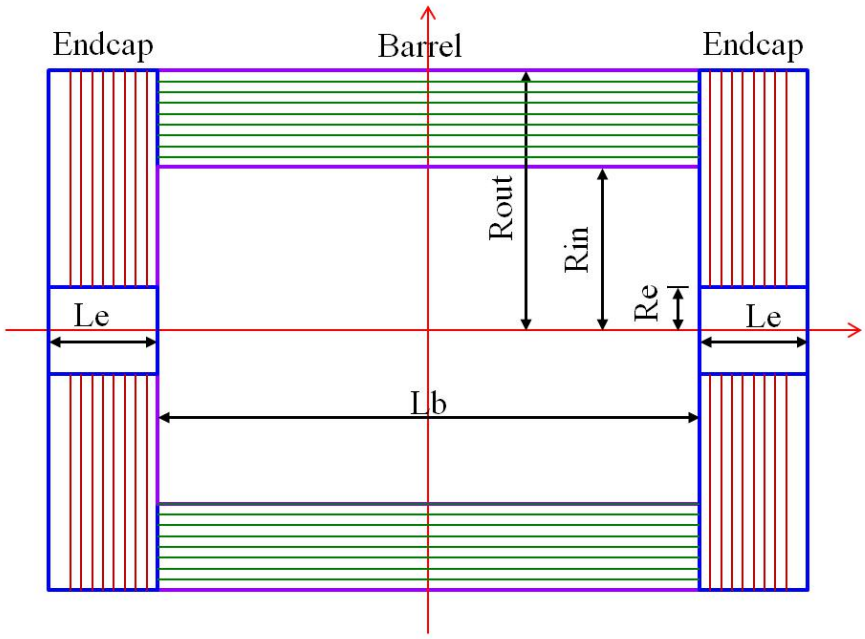

Figure 7.1: The basic layout of the muon system.

The CEPC muon system is the outermost component of the whole detector. It is divided into barrel and end-caps, as shown in Figure 7.1. Both the barrel and end-caps consist of segmented modules. The segmentation is constrained by the maximum sizes of the module and sensitive unit (more segments are required for a larger detector), dodecagon segmentation is selected for the baseline design of the CEPC muon system. All baseline design parameters are summarised in Table 7.1. These parameters will be further optimised together with the inner detectors, in particular the ECAL and the HCAL.

The number of sensitive layers and the thickness of iron (or tungsten) in the absorbers are two critical parameters. For the baseline design, the total thickness of iron absorber is chosen to be 8λ (the nuclear interaction length of iron) distributed in 8 layers, which should be sufficient for effective muon tracking together in combination with the calorimeters. Gaps of 4 cm between neighbouring iron layers give adequate space for installing sensitive detectors.

The solid angle coverage of the CEPC muon system should be up to $0.98 \times 4\pi$ in accordance with the tracking system. Minimum position resolutions of $\sigma_{r\phi} = 2.0$ cm and $\sigma_z = 1.5$ cm are required. Since the particle flow algorithm calorimetry provides very good particle identification capabilities, the detection efficiency of 95% ($E_\mu > 5$ GeV) of the CEPC muon system should provide enough redundancy and complement in muon detection for most physics processes related to muons. The muon system should provide

Table 7.1: The baseline design parameters of the CEPC muon system

Parameter	**Possible range**	**Baseline**
Lb/2 [m]	3.6 – 5.6	4.0
Rin [m]	3.5 – 5.0	4.4
Rout [m]	5.5 – 7.2	7.0
Le [m]	2.0 – 3.0	2.6
Re [m]	0.6 – 1.0	0.8
Segmentation	8/10/12	12
Number of layers	3 – 10	8
Total thickness of iron	6 – 10λ ($\lambda = 16.77$ cm)	8λ (136 cm) (8/8/12/12/16/16/20/20/24) cm
Solid angle coverage	(0.94 – 0.98)$\times 4\pi$	0.98
Position resolution [cm]	$\sigma_{r\phi}$: 1.5 – 2.5	2
	σ_z : 1 – 2	1.5
Time resolution [ns]	< 10	1 – 2
Detection efficiency ($E_\mu > 5$ GeV)	92% – 99%	95%
Fake($\pi \to \mu$)@30GeV	0.5% – 3%	$< 1\%$
Rate capability [Hz/cm^2]	50 – 100	$\sim$60
Technology	RPC	RPC (super module, 1 layer readout, 2 layers of RPC)
	μRWell	
Total area [m^2]	Barrel	$\sim$4450
	Endcap	$\sim$4150
	Total	$\sim$8600

several hits each with a spatial resolution of a few cm, a time resolution of a few ns and a rate capability of 50 – 100 Hz/cm^2. Based on the dimensions and segmentation of the baseline design, the total sensitive area of the muon system amounts to 8600 m^2.

7.2 The Resistive Plate Chamber technology

Resistive Plate Chamber (RPC) is suitable for building large area detectors with centimeter spatial resolution. It has been applied in muon systems for experiments including BaBar [2], Belle [3], CMS [4] , ATLAS [5], BESIII [6], and Daya Bay [7]. It provides a common solution with the following advantages: low cost, robustness, easy construction of large areas, large signal, simple front-end electronics, good time and spatial resolution. It is chosen as the baseline design of the CEPC muon system.

RPCs can be built with glass or Bakelite, and run in avalanche or streamer mode. Bakelite RPCs of about 1200 m^2 and 3200 m^2 were produced for the BESIII and Daya Bay muon systems, respectively. Compared with glass RPC, Bakelite RPC has the advantages of easier construction, lower density, larger cell size and lower cost, especially if the event rate is below 100 Hz/cm^2 as required by the CEPC muon system. The characteristics of Bakeliete and glass RPCs are compared in Table 7.2. Further improvements are required for Bakelite RPCs, however, in terms of long-term stability, detection efficiency, readout technologies, lower resistivity ($< 10^{10}$) and higher rate capability.

Table 7.2: Comparison of Bakelite and glass RPC.

Parameters		Bakelite	Glass
Bulk resistivity [$\Omega\cdot$ cm]	Normal	$10^{10} \sim 10^{12}$	$> 10^{12}$
	Developing	$10^8 \sim 10^9$	
Max unit size (2 mm thick) [m]		1.2×2.4	1.0×1.2
Surface flatness [nm]		< 500	< 100
Density [g/cm^3]		1.36	2.4∼2.8
Min board thickness [mm]		1.0	0.2
Mechanical performance		Tough	Fragile
Rate capability [Hz/cm^2]	Streamer	100@92%	
	Avalanche	10K	100@95%
Noise rate [Hz/cm^2]	Streamer	< 0.8	0.05

7.3 The μ-RWELL technology

The μ-RWELL is a compact, spark-protected and single amplification stage Micro-Pattern Gas Detector (MPGD). A μ-RWELL detector [8] is composed of two PCBs: a standard GEM Drift PCB acting as the cathode and a μ-RWELL PCB that couples in a unique structure the electron amplification (a WELL patterned matrix) and the readout stages. The layout is shown in Figure 7.2a). A standard GEM 50 μm polyimide foil is copper clad on one side and Diamond Like Carbon (DLC) sputtered on the opposite side. The

thickness of the DLC layer is adjusted according to the desired surface resistivity value (50-200 MΩ/□) and represents the bottom of the WELL matrix providing discharge suppression as well as current evacuation. The foil is then coupled to a readout board.(as shown in Figure 7.2b)). A chemical etching process is then performed on the top surface of the overall structure in order to create the WELL pattern (conical channels 70 um (50 um) top (bottom) in diameter and 140 μm pitch) that constitutes the amplification stage. The process is shown in Figure 7.3. The high voltage applied between the copper and the resistive DLC layers produces the required electric field within the WELLs that is necessary to develop charge amplification. The signal is capacitively collected at the readout strips/pads. Two main schemes for the resistive layer can be envisaged: a *low-rate* scheme (for particles fluxes lower than 100 kHz/cm^2) based on a simple resistive layer of suitable resistivity; and an *high-rate* scheme (for a particle flux up to 1 MHz/cm^2) based on two resistive layers intra-connected by vias and connected to ground through the readout electrodes. Finally, a drift thickness of 3-4 mm allows for reaching a full efficiency while maintaining a versatile detector compactness.

A distinctive advantage of the proposed μ-RWELL technology is that the detector does not require complex and time-consuming assembly procedures (neither stretching nor gluing), and is definitely much simpler than many other existing MPGDs, such as GEMs or MicroMegas. Being composed of only two main components, the cathode and anode PCBs, is extremely simple to be assembled. This makes the cost of a μ-RWELL detector typically less than half the cost of a triple-GEM detector of the same size and the same strip pitch.

The μ-RWELL technology, especially in its *low-rate* version, is a mature solution, with whom single detectors of a 0.5 m^2 have been realised and succesfully operated in the laboratory as well as in test beams. They can withstand particle rates up to a few tens of kHz/cm^2, providing a position resolution as good as $\sim$60 μm with a time resolution of 5-6 ns. The detailed results are presented in the Appendix. The requirements of a muon detector for CEPC are not as stringent and therefore can be easily and cost-effectively achieved with the μ-RWELL technology. Moreover the μ-RWELL technology is a robust solution, intrinsically safer against sparks than, for example, the widely used GEM detectors. The muon system could be realised by using tiles of μ-RWELL detectors of a size 50x50 cm^2. This would make the whole muon detector very modular with components bought directly from industry. A CEPC muon detector made of μ-RWELL tiles could consist of three or four detector layers stations, each equipped with a couple of layers of μ-RWELL detectors in order to provide a very precise, of the order of 200-300μm, position resolution on the coordinates of a muon track.

7.4 Future R&D

The baseline conceptual design and most promising technologies for the CEPC muon system have been discussed. Future R&D requires detailed studies of different technologies and further optimization of baseline design parameters. Several critical R&D items have been identified, including:

- **Long-lived particles optimization**: Explore new physics scenario of long-lived particles and exotic decays. Optimize detector parameters and technologies.

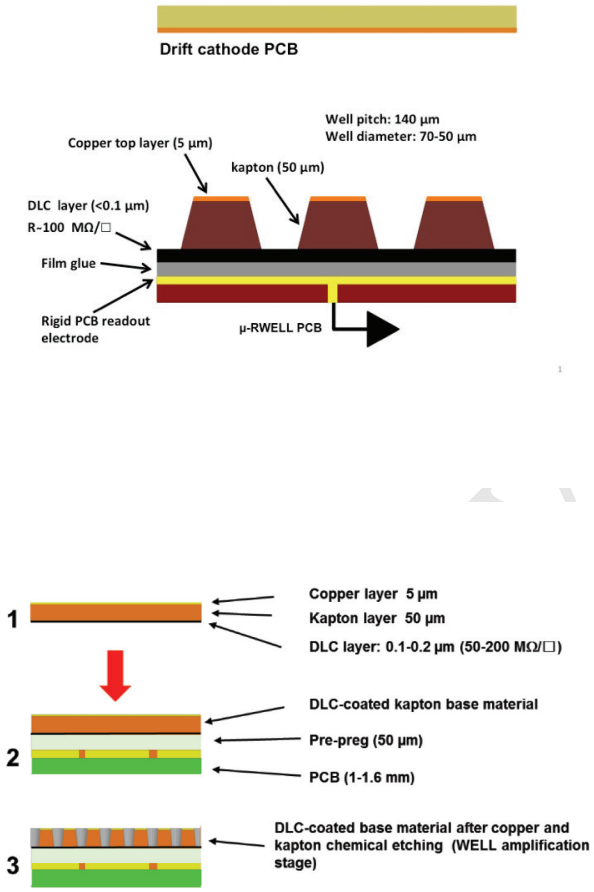

Figure 7.2: a) Layout of a μ-RWELL detector module; b) Coupling steps of the μ-RWELL PCB c) Amplification stage directly coupled with the readout.

- **Layout and geometry optimization**: Detailed studies on the structure of the segments and modules need to be carried out to minimise the dead area and to optimise the interface for routing, support and assembly. The geometry and dimensions need to be optimized together with the inner detectors, in particular the ECAL and the HCAL.

- **Detector optimization**: Study aging effects, improve long-term reliability and stability, readout technologies.

- **Detector industrialization**: Improve massive and large area production procedures for all technologies. One example is the engineering and the following industrialization of the μ-RWELL technology. The engineering of the detector essentially coincides with the technological transfer of the manufacturing process of the anode PCB and the ecthing of the kapton foil to suitable industrial partners.

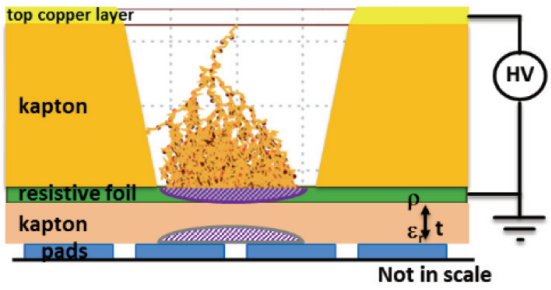

Figure 7.3: Amplification stage directly coupled with the readout.

References

[1] CALICE Collaboration, *Construction and performance of a silicon photomultiplier/extruded scintillator tail-catcher and muon-tracker*, JINST **7** (2012) no. 04, P04015, arXiv:1201.1653. http://stacks.iop.org/1748-0221/7/i=04/a=P04015.

[2] Babar Collaboration, *The BaBar detector*, Nucl. Instrum. Meth. **A479** (2002) 1–116, arXiv:hep-ex/0105044.

[3] A. Abashian et al., *The Belle Detector*, Nucl. Instrum. Meth. **A479** (2002) 117–232. KEK-PROGRESS-REPORT-2000-4.

[4] CMS Collaboration, *The CMS muon project: Technical Design Report*. Technical Design Report CMS. CERN, Geneva, 1997. http://cds.cern.ch/record/343814.

[5] ATLAS Collaboration, *ATLAS muon spectrometer: Technical Design Report*. Technical Design Report ATLAS. CERN, Geneva, 1997. http://cds.cern.ch/record/331068.

[6] Y.-G. XIE, J.-W. ZHANG, Q. LIU, J.-F. HAN, S. QIAN, N. YAO, J.-B. ZHAO, J. CHEN, and J.-C. LI, *Performance Study of RPC Prototypes for the BESIII Muon Detector*, Chinese Physics C **31** (2007) no. 01, 70–75. http://cpc-hepnp.ihep.ac.cn:8080/Jwk_cpc/EN/abstract/abstract7618.shtml.

[7] J.-L. Xu, M.-Y. Guan, C.-G. Yang, Y.-F. Wang, J.-W. Zhang, C.-G. Lu, K. McDonald, R. Hackenburg, K. Lau, L. Lebanowski, C. Newsom, S.-K. Lin, J. Link, L.-H. Ma, and P. Viktor, *Design and preliminary test results of Daya Bay*

RPC modules, Chinese Physics C **35** (2011) no. 9, 844. http://stacks.iop.org/1674-1137/35/i=9/a=011.

[8] G. Bencivenni, R. D. Oliveira, G. Morello, and M. P. Lener, *The micro-Resistive WELL detector: a compact spark-protected single amplification-stage MPGD*, Journal of Instrumentation **10** (2015) no. 02, P02008. http://stacks.iop.org/1748-0221/10/i=02/a=P02008.

CHAPTER 8

READOUT ELECTRONICS AND DATA ACQUISITION

The readout electronics and data acquisition (DAQ) systems for the detectors at the CEPC need to operate synchronously with the circular collider time structure for beam collisions and deliver high efficiency for recording all events without compromising on rare or yet unknown physics processes. The beam conditions and time structure are adjusted to operate in three different modes, corresponding to three different center-of-mass energies ($\sqrt{s}$): Higgs factory ($e^+e- \rightarrow ZH$) at $\sqrt{s} = 240$ GeV, Z boson factory ($e^+e- \rightarrow Z$) at $\sqrt{s} = 91.2$ GeV and W threshold scan ($e^+e- \rightarrow W^+W^-$) at $\sqrt{s} =\sim 160$ GeV. The instantaneous luminosities are expected to reach 3×10^{34}, 32×10^{34} and 10×10^{34} cm^{-2}s^{-1}, respectively, as shown in Table 1.1. The current tentative operation plan will allow the CEPC to collect one million Higgs particles or more, close to one trillion Z boson events, and ten million W^+W^- event pairs.

In conjunction with the recording of central events, the forward luminosity monitors are required to measure Bhabha scattering events to determine the delivered integrated luminiosity to a relative accuracy of 0.1% for the Higgs factory operation, and 10^{-4} for the Z line shape scan. This imposes dedicated readout capabilities to maintain the high rates of the luminosity calorimeter (LumiCal).

The following sections detail specifications for the on-detector front-end electronics and off-detector back-end electronics for the detector sub-systems and their interface to the central DAQ, trigger, clock and control systems. The event builders provide data to the event filters to determine the final event selection and data storage.

8.1 Readout electronics

The readout electronics of each detector sub-system consists of on-detector front-end electronics and off-detector back-end electronics. The front-end electronics directly receive the analog signals from the sensors. These signals are fed into Application Specific Integrated Circuits (ASIC) to produce digital signals that are further processed by configurable front-end chips, such as digital signal processors (DSP) and field-programmable gate arrays (FPGA), that format and buffer the data to be sent on the data link to the back-end electronics.

The specific details of how the analog signals are processed to yield buffered digital data varies depending on the each detector sub-system, as described in the Chapter 4 for the vertex detector and tracking systems, Chapter 5 for the electromagnetic and hadronic calorimeters, Chapter 7 for the muon systems, and Chapter 9 for the LumiCal. A common set of specifications for the readout electronics parameters are needed to ensure that the detector data from a CEPC collision collected across all sub-systems can be fully assembled into a single event containing all measurements above threshold of all final state particles produced within the detector acceptance.

The most fundamental step in the readout is to provide synchronized data. This is achieved foremost by distributing phase-locked copies of the machine clock from the accelerator to the front-end systems that digitize and buffer the data. The specifications on the clock jitter depend on the level of precision required for timing measurements, where for reference the LHC clock distribution for the HL-LHC upgrade is expected to have an RMS jitter of less than 10 ps. The requirements for the digital transmission and event building are to keep the data aligned on the same clock boundary and depend on the speed of the data transmission, where transfer rates of 25 Gbps have been achieved. The standardization of the clock distribution and data links across the detector sub-systems is advantageous to provide uniform performance and robust synchronization of the data links.

The second parameter common to all readout systems is the maximum latency for receiving a trigger decision to initiate the transfer of data from the front-end buffers to the back-end systems or from the back-end systems to the central DAQ, depending on where the data are buffered. The latency is set by the total transit time for the collision data used by the trigger to provide the data to trigger processors, to process a trigger decision, and to receive the trigger decision by the data buffers. Depending on the complexity of the triggers and internal response times of the detectors providing the data, the latency will be set. With the maximum latency, the required data buffering per sub-detector will depend on the occupancy of the channels served by the same readout segment. The occupancy, channel capacity and amount of data per channel, for channels above threshold, will set the average data volume per DAQ link per trigger. The buffer needs to account for fluctuations with respect to the average to avoid buffer overrun. Control signals to monitor the data buffers and back pressure are used to throttle the trigger, as needed, to avoid data loss. Most notably, the detector data occupancies per readout segment need to model well the beam background contributions in addition to the expected occupancies from collisions.

The off-detector back-end readout systems will provide the data links to the trigger processors and the central DAQ system. Current back-end designs using Advanced Telecommunications Computing Architecture (ATCA) readout platforms are able to provide a common framework for configuring the data management from different front-end

systems [1, 2]. Mezzanine boards are typically implemented to allow customization of the number and types of front-end links to optimize the resources of the back-end readout boards. The ATCA readout crates support high-speed commercial data links that can directly feed commercial network switches in the central event builder.

8.2 Data Acquisition System

The main task of the central DAQ system is to readout data from the front-end electronics with the level-1 trigger decision given by trigger system, then build into a full event with data fragments from different sub-detectors and process data, such as data compression and data quality monitoring. Finally, the data are sent to permanent storage.

8.2.1 Readout Data Rate Estimation

The proposed CEPC detector includes six sub-detectors in the current conceptual design: VTX, silicon tracker, TPC, ECAL, HCAL and dual-readout calorimeter.

Table 8.1 shows the estimated data rate of sub-detectors of CEPC. The event rate reaches ∼32 kHz for Z factory operation from Z boson decays and Bhabha events with the 2 Tesla solenoid option ($\mathcal{L}= 3.2 \times 10^{35}$ cm^2/s). We apply a safety factor and assume a maximum event rate of 100 kHz. With the level-1 trigger operating at 100 kHz, the total raw data rate is 4-8 TBytes/s.

8.2.2 Data Processing Requirements

The purpose of the online event processing will mainly be event classification, data quality monitoring and online filtering to reduce background events. Event building will be performed on the online farm connected to the back-end electronics via a commercial network switch. An event filter will also run on an online farm. Each node of the online farm will process the data of one complete event at a time.

8.3 Conceptual Design Schema

The current LHC experiments have up to 10^8 front-end readout channels and a maximum event building rate of 100 kHz, moving data at speeds of up to 300 GBytes/s (with an average throughput of < 200 GBytes/s required). The HL-LHC Phase-2 Upgrades reach 6000 GBytes/s and average event sizes of 7.4 MBytes [1]. The proposed CEPC DAQ system has the similar requirement in terms of data throughput. Upon the reception of the data, the computing requirements for event processing at the CEPC, in terms of storage and CPU, depend on the reconstruction times and trigger algorithms. As these algorithms are evolving, the current approach is to remain as compatible as possible with the rapidly developing technologies in the computing and network markets.

Figure 8.1 shows the conceptual software architecture design of the CEPC DAQ based on the experience gained from BES III and DayaBay experiments. The DAQ system is connected with the sub-detector back-end electronics in counting rooms through a network switch with the TCP/IP protocol. All other DAQ switches and computers are deployed in a dedicated machine room. The event filter farm is connected to the event builder through additional switches with multiple fibers. The DAQ system will provide

	Total # channels M(10^6)	Occupancy %	Nbit /channel	# Channels readout/evt k(10^3)	Volume /evt MBytes	Data rate @100 kHz GBytes/s
VTX	690	0.3	32	2070	8.3	830
Silicon Tracker						
Barrel	3118	$0.01 \sim 1.6$	32	1508	6.3	630
Endcap	1035	$0.01 \sim 0.8$	32	232	0.8	80
TPC	2	0.1-8	30	1375	5	500
Drift Chamber	0.056	5-10	480	?	3	300
ECAL						
Barrel	17/7.7	0.17	32	28.8/13.1	0.117/0.053	11.7/5.3
Endcap	7.3/3.3	0.31	32	22.4/10.2	0.090/0.041	9.0/4.1
AHCAL						
Barrel	3.6	0.02	32	0.72	0.0029	0.3
Endcap	3.1	0.12	32	3.72	0.015	1.5
DHCAL						
Barrel	32	0.004	2	1.28	0.00032	0.03
Endcap	32	0.01	2	3.2	0.0008	0.08
Dual Readout Calorimeter	22	0.4-1.6	64	88-352	0.704-2.8	70-280

Table 8.1: CEPC DAQ Data Rate Estimation.

other common functions including run control, run monitoring, information sharing, distributed process manager, software configure, Elog, data quality monitoring, remote monitoring and so on.

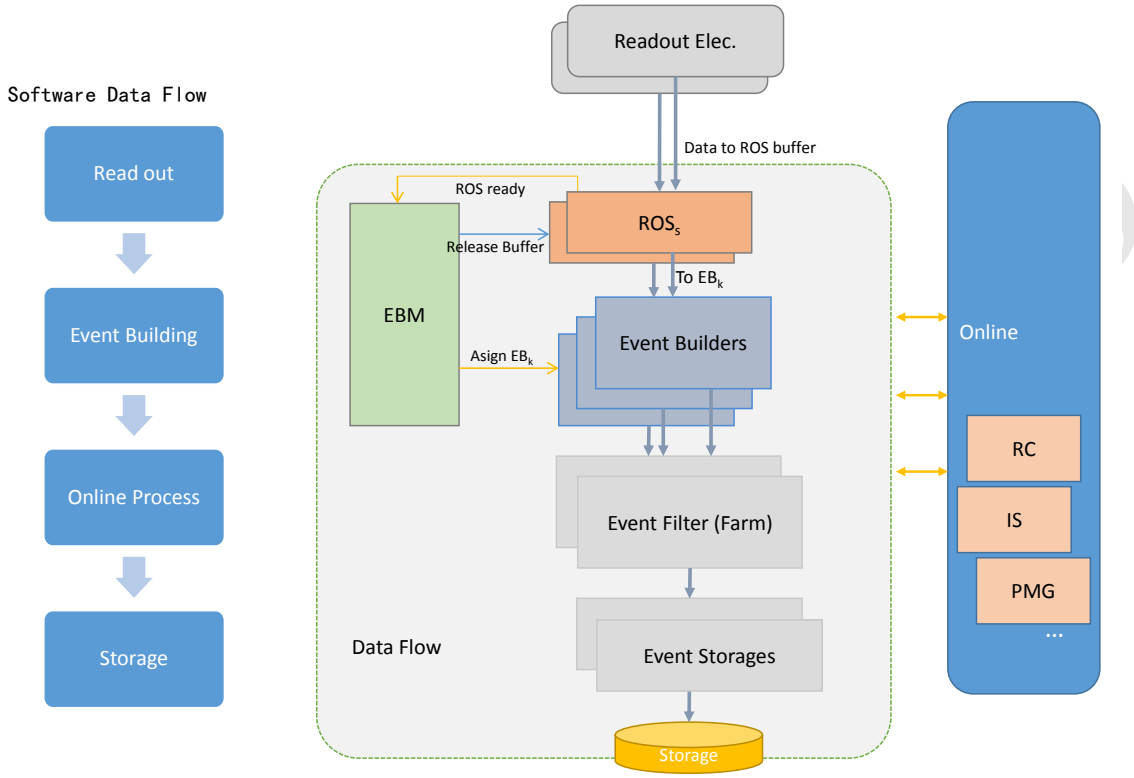

Figure 8.1: DAQ Conceptual Software Architecture Design Diagram.

There are two levels of event building in CEPC DAQ data flow system. The first level is implemented in readout farm which reads out the data from the back-end electronics and builds into a data fragment. The second level implemented in online farm which reads out the data from readout farms and builds into a full event. The two levels of event building could function according to the BES III event building as follows [2]:

1. electronics boards send data to ROS(read out system) through network.
2. ROS receive all data slice of one event and send event ID to EBM(event building manager).
3. EBM assign event ID to a free EB(event builder) node when EBM get all same event ID from all ROSs.
4. EB send data request to each ROSs.
5. ROSs send requested data to EB.
6. EB receive all ROSs data fragments of one event and finish full event building, then send event ID back to EBM.
7. EBM send event ID to ROSs to clear data buffer.

A software trigger can be deployed in the event filter farm. Each event filter node requests a full event from EBs, then sends the event data to process tasks to analyze for software trigger and data quality monitoring, and then in the last step sends triggered event to event storage nodes.

References

[1] J. G. Hegeman, *The CMS Data Acquisition System for the Phase-2 Upgrade*, CERN, CMS-CR-2018-099 (2018) .

[2] M. Liu, J. Lang, S. Yang, T. Perez, W. Kuehn, H. Xu, D. Jin, Q. Wang, L. Li, Z. Liu, et al., *ATCA-based computation platform for data acquisition and triggering in particle physics experiments*, in *Field Programmable Logic and Applications, 2008. FPL 2008. International Conference on*, pp. 287–292, IEEE. 2008.

CHAPTER 9

MACHINE DETECTOR INTERFACE

Suggest to change the title of the Chapter to "Machine detector interfance and luminosity detectorxs.

Machine-Detector Interface (MDI) represents one of the most challenging tasks for the CEPC projects. In general, it will have to address all common issues relevant to both the machine and detector. Topics summarized in this chapter include the interaction region, the final focusing magnets, the detector radiation backgrounds and the luminosity instrumentation. Integration of all the machine and detector components in the interaction region is also briefly discussed. It is critical to achieve comprehensive understanding of MDI issues to assure the optimal performance of the machine and detector.

9.1 Interaction region

The interaction region (IR) is where both electron and positron beams are focused to small spot sizes at the interaction point (IP) to maximize the machine luminosity, and merged but subsequently separated the two beams traveling in separate storage rings. The IR layout, as illustrated in Figure 9.1, has received several necessary updates with respect to the published preliminary CDR [1], to cope with the latest double-ring design and a beam-crossing angle of 33 mrad. The two final focusing magnets, QD0 and QF1, sits inside the detector. The focal length (L^*), defined as the distance from the final focusing magnet (*i.e.* QD0) to the IP, has increased from 1.5 m to 2.2 m. This allows enlarged separation between the two single apertures of the QD0. Compensating magnets are positioned in front of the QD0 and surrounding both the QD0 and QF1 magnets. They are introduced to cancel out the detector solenoid field and minimize the disturbance on the focusing beams. Furthermore, the outer radius of the compensating magnets defines the detector

acceptance to be $|\cos\theta| \leq 0.993$. The luminosity calorimeter (so called "LumiCal"), located right in front of the compensating magnets, is designed to measure the integrated luminosity to a precision of 10^{-3} or better. Tracking disks, labeled as FTD, are designed to measure charged particle trajectories in the forward region.

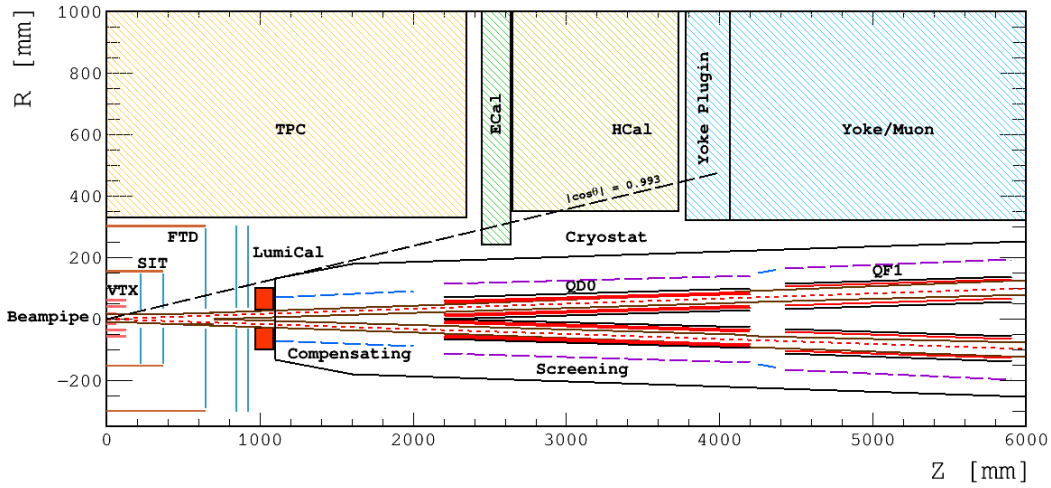

Figure 9.1: Layout of the CEPC interaction region.

9.2 Final focusing magnets

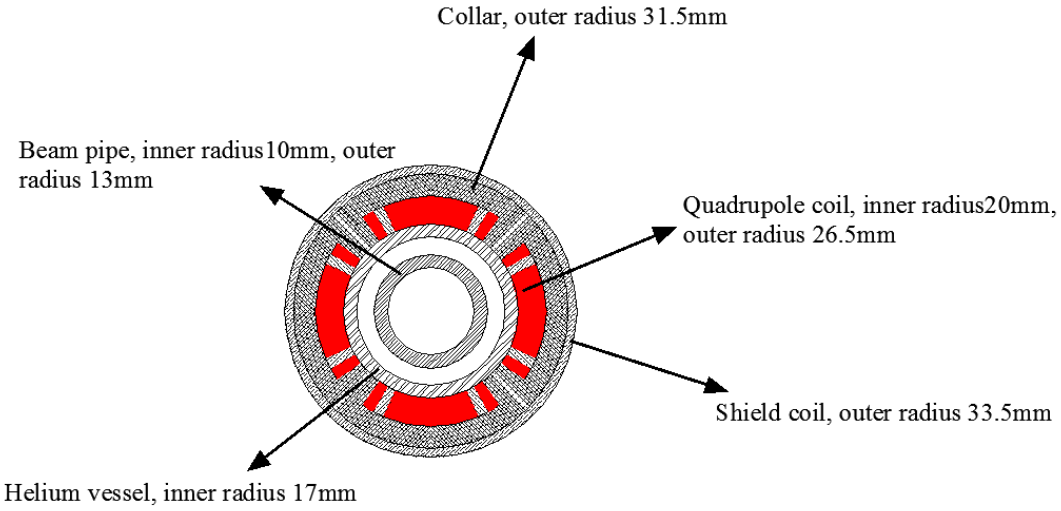

Figure 9.2: Schematic view of the single aperture of the QD0 superconducting magnet.

In the interaction region, compact high gradient quadrupole magnets are designed to focus the electron and positron beams. The two final focusing quadrupoles (QD0 and QF1), are placed inside the CEPC detector and must operate in the background field of the detector solenoid. QD0 is the quadrupole magnet close to the interaction point, with a distance of 2.2 m to the IP. It is designed as a double aperture superconducting magnet and can be realized with two layers of Cos-Theta quadrupole coil using NbTi Rutherford

cables without iron yoke. The cross-sectional view of the single aperture of the QD0 is shown in Figure 9.2. It is designed to deliver a gradient field of 136 T/m and control the field harmonics in the sensitive area to be below 3×10^{-4}. Design parameters are summarized in Table 9.1. The QF1 magnet is similar to the QD0, except that there is an iron yoke around the quadrupole coil for the QF1.

Table 9.1: Main design parameters of QD0 and QF1.

Magnet	QD0	QF1
Field gradient [T/m]	136	110
Magnetic length [m]	2.0	1.48
Coil turns per pole	23	29
Excitation current [A]	2510	2250
Coil layers	2	2
Stored energy [kJ]	25.0	30.5
Inductance [H]	0.008	0.012
Peak field in coil [T]	3.3	3.8
Coil inner diameter [mm]	40	56
Coil outer diameter [mm]	53	69
X direction Lorentz force/octant [kN]	68	110
Y direction Lorentz force/octant [kN]	-140	-120

Additional compensating magnets are introduced to minimize the disturbance from the detector solenoid on the incoming and outgoing beams. The compensating magnets in front of the QD0 is designed to achieve an almost zero integral longitudinal field before entering the QD0. And the compensating magnet right outside the QD0 and QF1 is necessary to screen the detector field. The magnets are based on wound of rectangular NbTi-Cu conductors. To minimize the magnet size, the compensating magnets are segmented into 22 sections with different inner coil diameters. Inside the first section, the central field reaches the peak value of 7.2 Tesla. More detailed design of the final focusing magnets and the compensating magnets can be found in [2].

9.3 Detector backgrounds

Beam and machine induced radiation backgrounds can be the primary concern for the detector design [3–6]. They can cause various radiation damages to the detectors and electronic components, and degrade the detection performance or even kill the detector completely in the extreme case. During data-taking, high rate radiation backgrounds may significantly increase the detector occupancy and impair the data-taking capability of the detector. Therefore it is always desirable to characterize the potential backgrounds at the machine and detector design stage and mitigate their impacts with effective measures. Detailed Monte Carlo simulation, along with lessons and experience learned from other experiments, can serve as the basis for such studies.

The deleterious effects of the radiation backgrounds can be represented with hit density, total ionizing dose (TID), and non-ionizing energy loss (NIEL). The expected hit density can be used to evaluate the detector occupancy. TID is an important quantity for understanding surface damage effects in electronics. NIEL, represented in the 1 MeV neutron equivalent fluence, is important for understanding the bulk damage to silicon devices. The background simulation starts with either generating background particles directly in the IR (e.g. pair production) or propagating them to the region close enough to the IR (e.g. SR photons and off-energy beam particles). Particle interactions with detector components are simulated with GEANT4 [7–9]. The characterization methodology for the ATLAS detector background estimation [10] has been adopted. In the following, main radiation backgrounds originating from synchrotron radiation, beam-beam interactions, and off-energy beam particles, are discussed and their contributions are carefully evaluated. Safety factors of ten are always applied to cope with the uncertainties on the event generation and the detector simulation.

9.3.1 Synchrotron radiation

Synchrotron radiation (SR) photons are prevalent at circular machines. At the CEPC, they are mostly produced in the last bending dipole magnets and in the focusing quadrupoles inside the interaction region. The innermost tracking detectors can be sensitive to photons above 10 keV and vulnerable to high levels of soft photon radiation [1]. In order to reduce the energy and flux of SR photons that enter the straight sections, the field strength of the last bending dipole magnet has been reduced and becomes much weaker than the normal arc dipole fields. This controls the critical energy of SR photons to be below 100 keV and makes the collimation design less difficult.

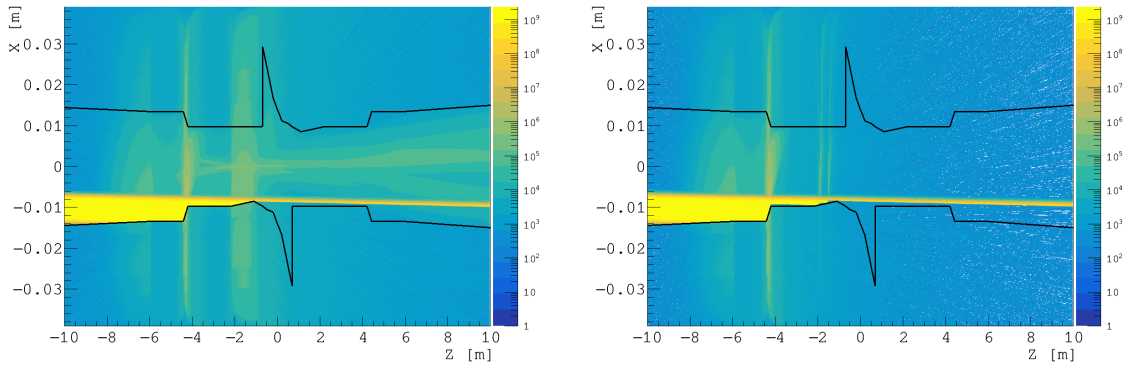

Figure 9.3: Distribution of the synchrotron photon flux formed by the upstream bending magnet on the left side before (a) and after (b) introducing collimators.

The BDSim [11] software based on GEANT4 has been deployed for the detailed studies. It allows generating SR photons from the relevant magnetic elements and transports them to the region of the experimental detectors. Particular care has been taken for

[1] It should be noted that the SR photon energy increases rapidly with the beam energy and additional measures might have to be introduced to allow detector operation at higher operation energies.

a realistic simulation in the tails of the beam density distributions (up to 10 $\sigma_{x/y}$) and for both beam core and halo, as particles form the tails are most effective in producing background particles. SR photons from the last dipole magnet form the light yellow band in Figure 9.3 and can hit the beam pipe in the interaction region. A considerable amount of them are scattered and can hit the central Beryllium beam pipe ($z = \pm 7$ cm) as shown in Figure 9.3(a). Collimators made with high-Z materials (e.g. Tungsten) and particular shapes are designed to block those scattering photons. Three sets of mask tips, located at $|z| = 1.51$, 1.93 and 4.2 m along the beam pipe to the interaction point, are introduced to suppress such SR photons. They can effectively reduce the number of SR photons hitting the central beam pipe from nearly $40,000$ to below 80. This reduction leads to a much lower power deposition in the beam pipe and allows a simplified cooling design for the beam pipe. The resulting photon flux distribution after collimation is shown in Figure 9.3(b). SR photons generated in the final focusing magnets are also carefully evaluated. They are highly forward and do not strike directly the central beam pipe unless the particles are 40 σ_x off the central orbit.

Table 9.2: The input machine parameters to the GUINEA-PIG simulation.

Machine Parameters	**H** (240 GeV)	**W** (160 GeV)	**Z** (91 GeV)
Beam energy [GeV]	120	80	45.5
Particles per bunch [10^{10}]	15	12	8
Transverse size σ_x/σ_y [μm]	20.9/0.068	13.9/0.049	6.0/0.078
Bunch length σ_z [μm]	3260	5900	8500
Emittance $\varepsilon_x/\varepsilon_y$ [nm]	12.1/0.0031	0.54/0.0016	0.18/0.004

9.3.2 Beam-beam interactions

Bremsstrahlung and its subsequent process of pair production are important background at the CEPC. Due to the pinch effect in the beam-beam interaction, the trajectories of beam particles in the bunches are bent, which causes the emission of Bremsstrahlung photons. This process has been studied with the Monte Carlo simulation program GUINEA-PIG [12], which takes into account dynamically changing bunch effects, reduced particle energies and their impacts on the electric and magnetic fields. In addition, the simulation program has been customized to implement the external detector field for the charged particle tracking. This allows improved determination of the positions and momenta of the out-going charged particles before interfacing to the GEANT4 detector simulation. Machine parameters for operation at different energies are listed in Table 9.2, and serve as the input to the GUINEA-PIG simulation. It should be noted that compared to other consequent processes, electron-positron pair production generates most significant detector backgrounds. The processes can be categorized as:

- *Coherent Production*: e^+e^- pairs are produced via the interaction of virtual or real photons (e.g. Bremsstrahlung photons) with the coherent field of the oncoming bunch. Particles can be highly energetic but are dominantly produced with small angle and confined in the beam pipe.

- *Incoherent Production*: e^+e^- pairs are produced through interactions involving two real and/or virtual photons. Most of the particles are confined in the beam pipe by the strong detector solenoid field. However, a small fraction of them are produced with high transverse momentum and large polar angle.

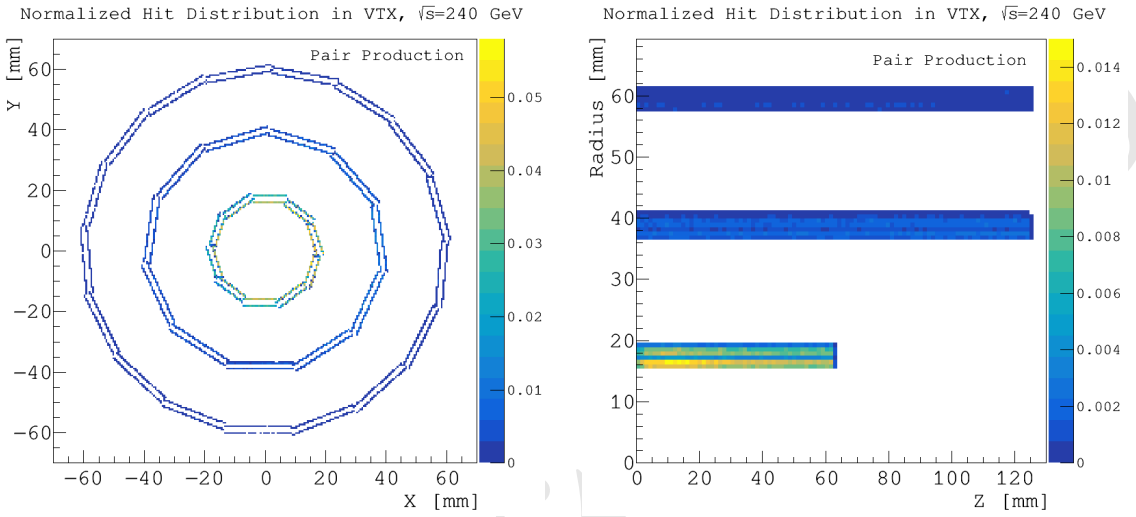

(a) (b)

Figure 9.4: Hit distributions due to the pair production in the $x-y$ and $r-z$ planes of the vertex detector. Figure 9.6 is for radiative Bhabha scattering, it will be good to be clear about the meaning of the pair production here.

As shown in Figure 9.4(a), the resulting hit distribution is nearly uniform in the $\phi-$ direction, even though the beam squeezing is different in the x and y directions. On the other hand, the hit distribution is more dense in the central region as shown in Figure 9.4(b), but decreases rapidly with the increased radius, as shown in Table 9.3.

Table 9.3: Maximum radiation backgrounds originating from the pair production at each vertex detector layer. Which pair production? Coherent or incoherent or both? At what $\sqrt{s}$?

	Hit Density [hits/cm^2·BX]	TID [kRad/year]	NIEL [1 MeV n_{eq}/ cm^2·year]
Layer 1 ($r = 1.6$ cm)	2.2	620	1.2×10^{12}
Layer 2 ($r = 1.8$ cm)	1.5	480	9.1×10^{11}
Layer 3 ($r = 3.7$ cm)	0.18	60	1.2×10^{11}
Layer 4 ($r = 3.9$ cm)	0.15	45	1.0×10^{11}
Layer 5 ($r = 5.8$ cm)	0.03	9.7	3.3×10^{10}
Layer 6 ($r = 6.0$ cm)	0.02	6.8	3.0×10^{10}

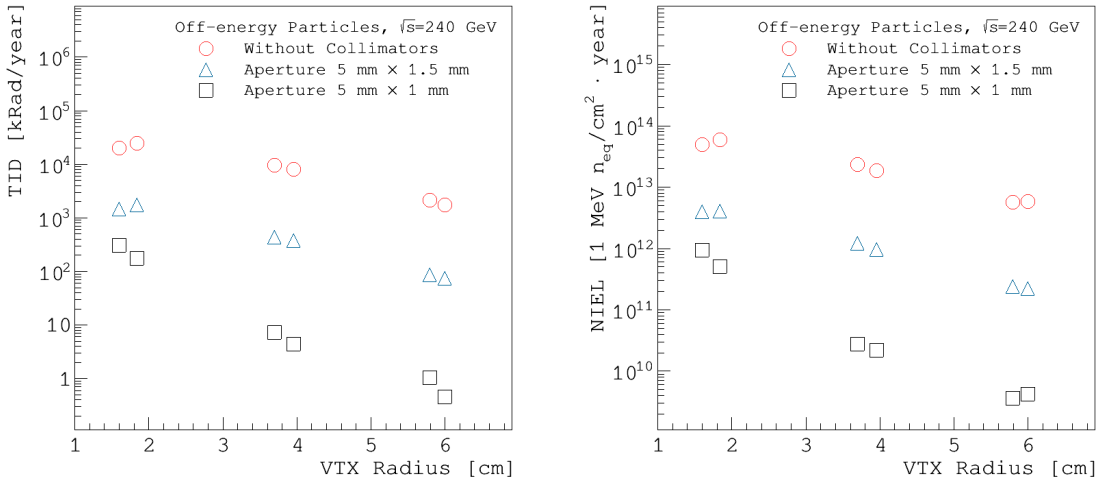

(a) (b)

Figure 9.5: Contributions to TID and NIEL from off-energy beam particles are effectively reduced after introducing the two sets of collimators.

9.3.3 Off-energy beam particles

Circulating beam particles can lose significant amounts of energy in scattering processes. If exceeding 1.5% of the nominal energy (defined as the machine energy acceptance), scattered particles can be kicked off their orbit. A fraction them will get lost close to or in the interaction region. They can interact with machine and/or detector components and contribute to the radiation backgrounds. There are three main scattering processes that are almost entirely responsible for the losses of beam particles, including Bremsstrahlung, radiative Bhabha scattering and beam-gas interaction.

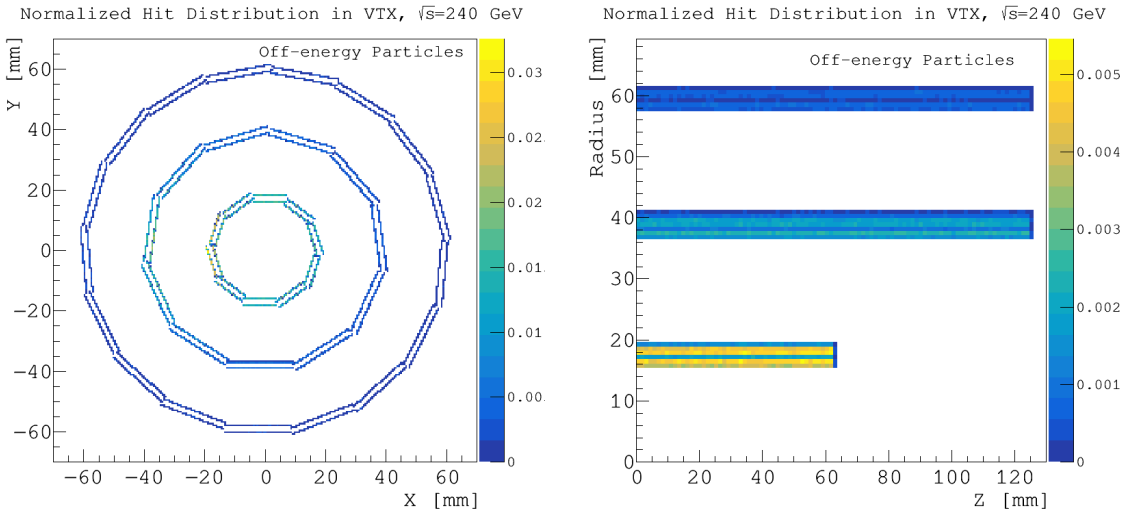

(a) (b)

Figure 9.6: Hit distributions due to the radiative Bhabha scattering process in the $x - y$ and $r - z$ planes of the vertex detector.

While Bremsstrahlung events out of beam-beam interactions are generated with GUINEA-PIG, radiative Bhabha events with small angles are generated with the BBBREM program [13]. Interactions between the beam particles and the residual gas in the beam pipe are simulated with custom code, assuming the gas pressure to be 10^{-7} mbar. The backgrounds originating from the beam-gas interaction is much smaller compared to that from the Radiative Bhabha scattering. Beam particles after interactions are tracked with SAD [14] and transported to the interaction region. Particles lost close to the interaction region, either right after the bunch crossing or after traveling multiple turns, are interfaced to detector simulation.

Backgrounds introduced by off-energy beam particles can be effectively suppressed with proper collimation. The collimator aperture has to be small enough to stop as much as possible the off-energy beam particles, but must be sufficiently large without disturbing the beam. Two sets of collimator pairs, APTX1/Y1 and APTX2/Y2 are placed in the arch region, with aperture size of 5 mm and 1 mm, in the horizontal and vertical planes (it reads as if there are two planes, one horizontal and the other vertical. Suggest to change to "$x-y$ planes" or "transverse planes".), respectively. They are equivalently 14 σ_x and 39 σ_y, which are sufficiently away from the beam clearance region. Fig. 9.5 shows off-energy beam particles entering the IR are reduced significantly after introducing the collimation system. As shown in Fig. 9.6(a), the resulting hit distribution maximizes towards the $-x$ direction due to the nature of the off-energy beam particles that are swept away by the magnets. But along the z direction, the hit distribution is more or less uniform with the additional contribution of the back-scattered particles by the LumiCal in the downstream. For the background estimation, the maximum values in the $-x$ direction are taken. At the first vertex detector layer ($r = 1.6$ cm), the hit density is about 0.22 hits/cm^2 per bunch crossing from the radiative Bhabha scattering. The TID and NIEL are 310 kRad per year and 9.3×10^{11} 1 MeV n_{eq}/cm^2 per year, respectively.

9.3.4 Summary of radiation backgrounds

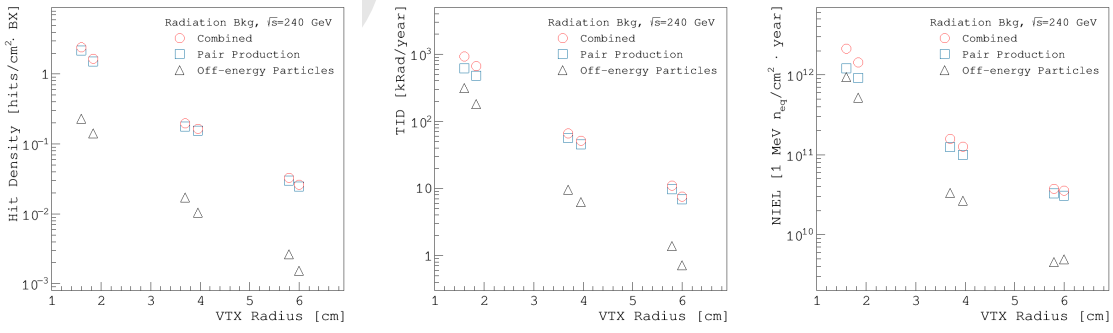

(a) (b) (c)

Figure 9.7: Hit density, TID and NIEL at different vertex detector layers due to the pair production, off-energy beam particles and the two combined. Qualities of these plots are poor.

When operating the machine at the center-of-mass energy of $\sqrt{s} = 240$ GeV, the main detector backgrounds come from the pair-production. The contribution from the off-energy beam particles is nearly an order of magnitude lower. Figure 9.7 shows the

hit density, TID and NIEL at different vertex detector layers, originating from the pair production, off-energy beam particles and the two combined. In addition, TID and NIEL distributions covering the silicon detectors in $r - z$ are shown in Figure 9.8.

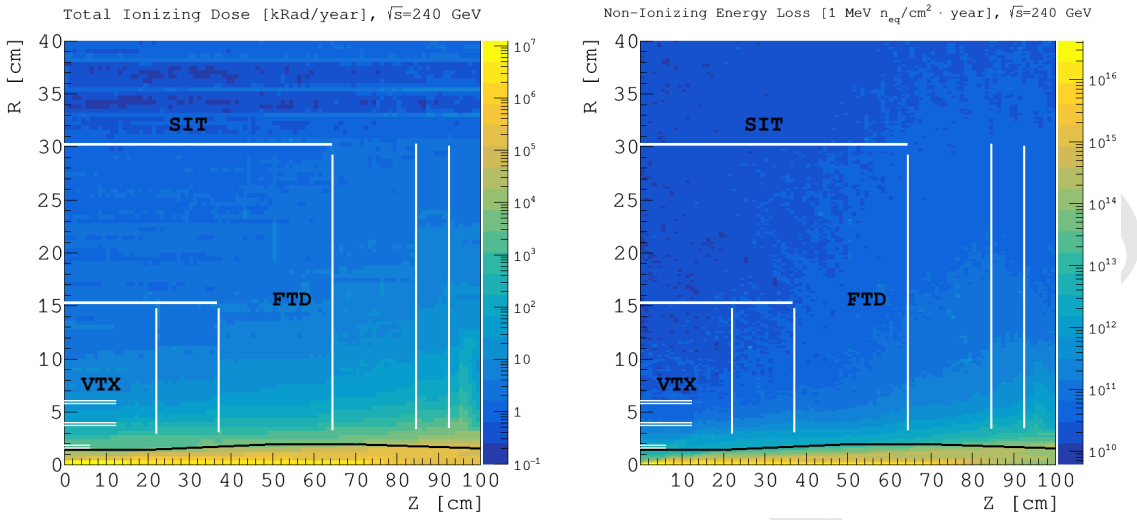

(a) (b)

Figure 9.8: TID and NIEL distribution in $r - z$ for the machine operation at $\sqrt{s} = 240$ GeV.

At lower operation energies, *i.e.* $\sqrt{s} = 160$ GeV for W and $\sqrt{s} = 91$ GeV for Z, the background particles are usually produced with lower energies but with higher rates given the higher machine luminosities. In addition, the pair-production dominates the radiation backgrounds and contributions from other sources become negligible. The resulting radiation backgrounds at the first vertex detector layer at different operation energies are summarized in Table 9.4.

Table 9.4: Summary of the radiation background levels at the first vertex detector layer ($r = 1.6$ cm) at different machine operation energies. How do these numbers relate to those in Table 9.4?

	H (240)	**W** (160)	**Z** (91)
Hit Density [hits/BX]	2.4	2.3	0.25
TID [MRad/year]	0.93	2.9	3.4
NIEL [10^{12} 1 MeV n_{eq}/cm^2·year]	2.1	5.5	6.2

9.4 Luminosity instrumentation

Very forward region at the CEPC will be instrumented with a luminometer (LumiCal), aiming to measure integrated luminosity with a precision of 10^{-3} and 10^{-4} in e^+e^-collisions at the center-of-mass energy of 240 GeV and at the Z pole, respectively. The precision requirements on the integrated luminosity measurement are motivated by the CEPC physics program, intended to test the validity scale of the Standard Model through precision measurements in the Higgs and the electroweak sectors with 10^6 Higgs and 10^{10-12} Z bosons. Many sensitive observables for such measurements critically depend on the uncertainty of the integrated luminosity.

Luminosity at an e^+e^- collider is best measured by counting the Bhabha events of elastic e^+e^- scattering. Its theoretical interpretation is better than 0.05% at the Z pole [15]. The scattered electrons are distributed in the forward direction with a $1/\theta^3$ dependence. The cross section of the BHLUMI [16] simulation is illustrated in Fig. 9.9(a).

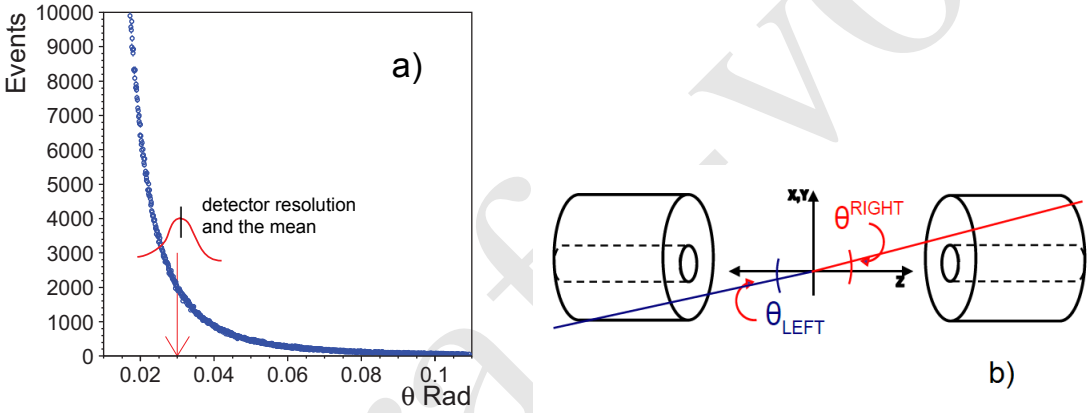

Figure 9.9: a) Distribution of scattered electrons in polar angle of the BHLUMI simulation. The Gaussian curve illustrates the detector resolution to θ measured at a given fiducial edge. The offset of the mean in measurement contributes to the systematic uncertainties. b) Bhabha events is measured preferably in the forward direction of the e^+e^-collision characterized by the back-to-back of elastic scattering and the electromagnetic shower of the electrons.

A Bhabha event is detected with a pair of scattered electrons back-to-back in direction, and the momenta of beam energy. Therefore the luminosity detector is consisted of a pair of forward calorimeters with high precision on detecting electron impact positions. The configuration is sketched in Fig. 9.9(b). Bhabha events are detected in the angular coverage ($\theta_{min} < \theta < \theta_{max}$) of the forward calorimeters. The integrated luminosity (L) of the leading order calculation is

$$\sigma^{vis} = \frac{16\pi\alpha^2}{s}\left(\frac{1}{\theta^2_{min}} - \frac{1}{\theta^2_{max}}\right), \quad \mathcal{L} = \frac{1}{\epsilon}\frac{N_{acc}}{\sigma^{vis}}, \quad \frac{\Delta\mathcal{L}}{\mathcal{L}} \sim \frac{2\Delta\theta}{\theta_{min}}, \tag{9.1}$$

where ϵ is the detection efficiency. The systematic uncertainties are mostly from the precision on θ_{min}, mainly due to mechanical alignment and the detector resolution. The uncertainty propagates to the luminosity calculation is about twice on magnitude.

The dimension of the detector is favorable to have the θ_{min} as low as possible to optimize coverage of the Bhabha cross section. The luminosity detector is planned to be mounted in front of the quadruple magnets at $z = \pm 100$ cm. With the θ_{min} of ~30 mrad,

corresponding to a radius of 30 mm to the beam pipe at $z = 100$ cm, the cross-section, σ^{vis}, after event selection will reach ~ 50 nb. A large detector coverage of σ^{vis} is necessary for statistics required for the Z line-shape study, where the $Z \to q\bar{q}$ cross section is 41 nb. The precision required for 10^{-4} makes a strong demand on the detector resolution. At $\theta = 30$ mrad, it corresponds to an offset of $\Delta\theta \sim 1.5$ μrad, which is equivalent to 1.5 μm in radius at $z = 100$ cm.

Several technological options for LumiCal design are under study, as described in Sec. 9.4.1, with emphases on the precision of polar angle and energy reconstruction of Bhabha particles scattered in the t-channel $V(V = \gamma, Z)$ exchange. The dual beam-pipe configuration with the beam-crossing at 33 mrad results to a boost to particles of e^+e^- collisions. The back-to-back characteristics of Bhabha electrons is shifted by approximately a horizontal offset of 33 mm. The impact to LumiCal design is discussed. The LumiCal together with the quadruple magnet are inserted into the tracking volume that extended to $z = \pm 200$ cm. Shower leakage of electrons off the LumiCal to central tracker is studied by simulation, which is also discussed.

LumiCal at the CEPC is a precision device with challenging requirements on the mechanics and position control. Precision requirements on integral luminosity measurement set the precision of the opening aperture and positioning control of the LumiCal. Various sources of luminosity uncertainty in this respect are reviewed in Sec. 9.4.2. Encouraging estimations on feasibility of the luminosity precision goals are presented. Detailed studies are ongoing, to include the full simulation of physics and machine induced processes and of the detector itself, for various LumiCal positioning and technology choices.

9.4.1 Technological and design options

In the current design of the very forward region at the CEPC, LumiCal is foreseen to cover the polar angle region between 26 mrad and 105 mrad what translates into the detector aperture of 25 mm for the inner radius and 100 mm for the outer, at $z = \pm 100$ cm of the LumiCal front plane from the IP. The detector options shall be considered for

1. precision of the electron impact position to $r \sim 10$ μ m (1 μ m) for the uncertainties on luminosity, corresponding to the systematic uncertainties on luminosity of $\Delta L/L \sim 10^{-3}$ (10^{-4}) in the Higgs (Z-pole) operations;

2. monitoring of the detector alignment and calibration of detector position by tracking of Bhabha electrons with upstream detectors;

3. energy resolution and separation of e/γ for measurements of single photons and radiative Bhabha events;

4. maximum coverage and segmentation of the LumiCal to accommodate the dual beam-pipe and the beam crossing of 33 mrad;

5. minimizing shower leakage into the central tracking volume.

The detector option for the 1 μm precision on electron impact position is very much limited silicon detectors segmented in strips or pixels. Silicon strip detectors of 50 μm readout pitch is commonly reaching a resolution of $\sigma \sim 5$ μm. The uncertainty on the mean ($\bar{\sigma} = \sigma/\sqrt{n}$) would be much smaller. The selection of Bhabha events is set on a fiducial edge of θ_{min}, for example, center in the gap between two silicon strips. The

systematic uncertainty is therefore the number of events being selected with an uncertainty of $\bar{\sigma}$ despite the detector resolution, and would be relatively small, which is indicated by the Gaussian curve in Fig.9.9(a). The alignment of the detector position would be the major systematic requirement for an absolute precision of 1 μm.

A conceptional Luminosity detector is illustrated in Fig. 9.10 for the combination of a silicon detector and a calorimeter around the beam pipe for measurement of the electron impact position energy. The segmentation of the calorimeter is considered for the back-to-back resolution detecting a pair of Bhabha electrons, and for separation of e/γ in case of radiative photon accompanied with the electron or from beam background. The thickness is determined for the energy resolution favorable of $> 20X_0$ for shower containment of a 50 GeV electron. The option on the calorimeter is limited by the space available. The traditional crystal or scintillator-based calorimeter will require more than 20 cm in length for $> 20X_0$. The most compact design would be a sandwiched stack of Silicon samplers with Tungsten in $1X_0$ (3.5 mm thick), to a total of about 10 cm that weights about 400 kg.

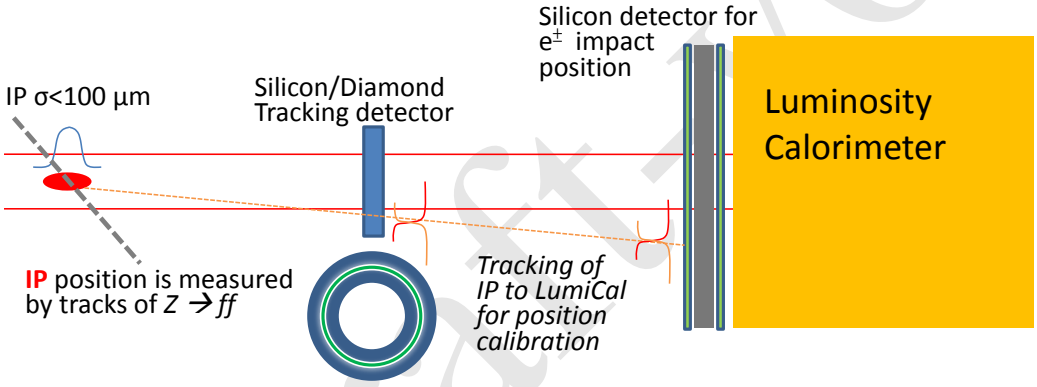

Figure 9.10: A conceptional luminosity detector combination with a upstream silicon/diamond detector for tracking Bhabha electrons to calibrate position of the luminosity detector.

The alignment precision of the front-layer Silicon detector is the most critical issue to reach 1 μm in radius for the luminosity measurement of 10^{-4}. For the precision at the 1 μm level, a monitoring system with laser alignment is required to calibrate the detector position. The θ angle of a detected electron is calculated assuming an IP position measured by the beam steering and the central tracking system. The IP position relative to the luminosity detector could be limited to survey relative to central tracking devices or beam pipe. If feasible, a tracking system on the Bhabha electrons will improve the measurement precision of the electron theta angle. This is illustrated in Fig. 9.10 for the option that a ring of silicon or diamond detector is mounted in front of the Luminosity detector. Such that a electron track is measure from the IP, the ring detector, and the LumiCal impact position. The ring detector offers a second survey, and by extrapolation, to calibrate the LumiCal silicon strip positions.

The front silicon layer of the luminosity detector will measure electron impact positions to a few micron. If this will be a fine-pitch strip detector, the position is measured by strips collecting the ionization charges generated by a traversing electron. In Fig. 9.11, the charge sharing is illustrated for $\eta = Q_r/(Q_r + Q_l)$ with the ionization charges collected by the strips on the right (left) of the impact position. The distribution is collected for a

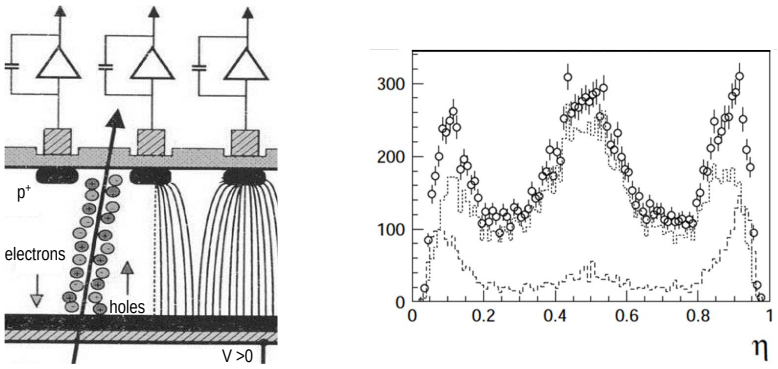

Figure 9.11: Charge collection by silicon strips is illustrated for ionization charges generated by a traversing particle. The $\eta = Q_r/(Q_r + Q_l)$ distributions are made for charge sharing to left and right strips to the impact position, for a test device with strip implementation in 25 μm pitch and the readout of every other strips in 50 μm pitch. The η distributions are also plotted for contents with charges collected by two-strip (dotted) and three-strip (dashed) cases. The middle bump corresponds to the position of the floating strip between two readout strips.

test device having the strips implanted in 25 μm pitch, and the readout in 50 μm pitch by wire bonding to every other strips. The floating strip between two readout strips attracts charges drifting towards it and results to the bump at $\eta \sim 0.5$, in particular for a wide cluster of charges collected by three strips (dotted line). The impact position of a particle is approximated by its center-of-gravity weighted on the charges between two strips. With the η distribution, the non-linear distribution can be corrected to achieve a position resolution of better than ~ 5 μm for the readout pitch of 50 μm. With the strip detectors placed in a magnetic field, the ionization charge in the silicon wafer is drifted toward one side, and therefore the η distribution is tilted un-evenly. Without a proper correction for the η, the true impact position the off-set can be as large as half the readout pitch.

If the luminosity detector will be assembled in a sandwiched silicon-tungsten calorimeter with the type of silicon wafer for the front layer. Wide silicon strips may be chosen in a case like the OPAL LumiCal [17], applying 2.5 mm wide strips in circular span of 11.25°. The resolution on detection of an electron, as well as for e/γ separation is at the 1 mm level. Assuming that the event counting of Bhabha electrons has the fiducial edge, θ_{min}, chosen at the middle between two strips, and the events are evenly divided to left and right strips without charge sharing. The systematic uncertainty to luminosity measurement is by the alignment uncertainty of the strip position of a few microns, and is not by the resolution.

Charge sharing between the gap of two-strips have been studied with prototype wafers[18] shown in Fig. 9.12. The wafer dimension is 65×65 mm^2 implemented with 2 mm wide strips and the gaps from 50 μm to 160 μm. The beam test was conducted with a set of fine-pitched strip detectors as a telescope to provide reference positions of incident electrons scattered across strips and gaps. The charge sharing for electrons in the gaps are compared for η distributions in Fig. 9.12, which are found compatible for the different gap widths. Charge collection shows no loss, and are drifted toward the near strips with the η peaking at the edges. The dispelling charges in the middle of a gap is difficult for deriving the position of an incident electron in the gap. But, it does divide the event fraction cleanly to the near side of the strips.

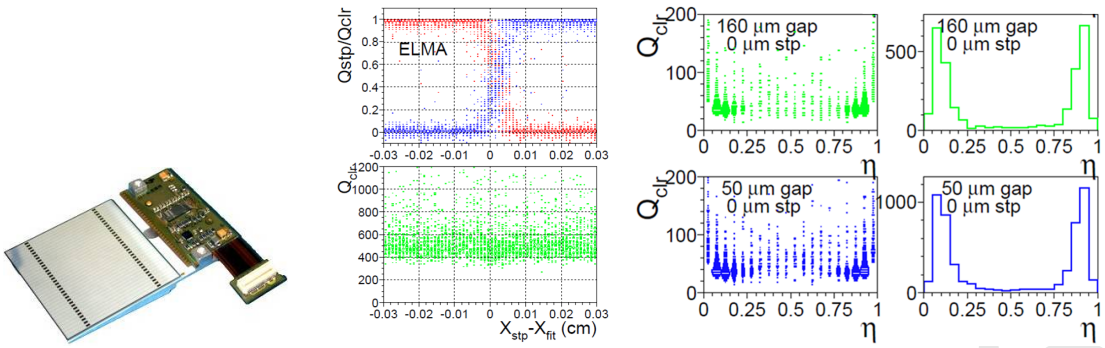

Figure 9.12: Beam tests using prototype silicon wafer of the CMS pre-shower detector (left) were conducted for the collection of ionization charges generated by traversing particles across the gap between strips. The charge sharing by adjacent strips are plotted (middle) to the reference impact position (extrapolation of a upstream telescope). The sum strip charges (middle plots) is compatible to the hits on a strip. The charge sharing in $\eta = Q_r/(Q_r + Q_l)$ peaks near 0 and 1, indicating non-linear response to the randomly distributed beam particles across the gap. Referred to the middle plots twice, but no reference to the right plots. Might also consider to break up this figure into two to make the plots a bit large.

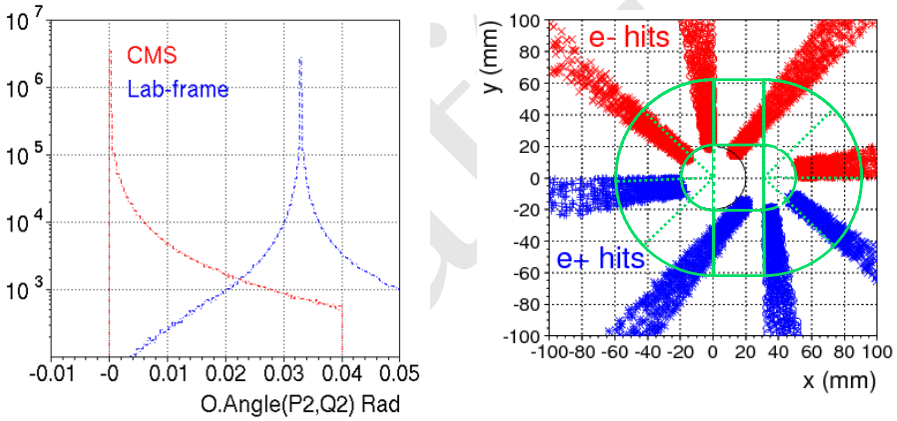

Figure 9.13: Bhabha events of BHLUMI simulation at the Z-pole are plotted for the back-to-back opening angle of scattered electron-position pairs in the Center-of-Mass and the laboratory frames (left). The impact positions on the LumiCal front face are plotted in slides of ϕ angles every 45 degrees (right). The detector coverage is illustrated in green lines indicating a beam-pipe of 20 mm, extended from beam center at $x = \pm 16.5$ mm. Can the label "CMS" in the left plot be changed to "CM frame" to avoid confusion with the CMS experiment? Also, the x-axis title could be a bit more intuitive.

The double ring configuration of the CEPC machine design at the interaction point has a beam crossing angle of 33 mrad. The effect to the electrons of Bhabha interaction is a boost off the accelerator ring center, by maximum 16.5 mrad in horizontal direction. The distribution is simulated with the BHLUMI program. The shift on back-to-back angle is plotted in Fig. 9.13. The boost is toward $+x$ direction of the laboratory frame. The electron impact positions on the LumiCal front-layer at $z = 100$ cm are also plotted in Fig. 9.13, in slices of every 45 degrees to indicate the dependence on p_T direction. The beam-pipe centers are at $x = \pm 16.5$ mm. The green lines indicate the beam-pipe area of 20 mm in radius extending horizontally, and the coverage of the LumiCal in segmentation

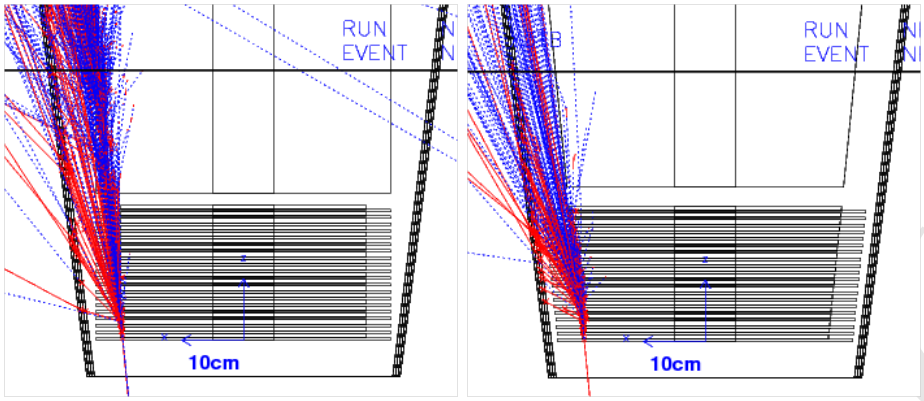

Figure 9.14: Event display of a GEANT simulation for electron shower on the LumiCal configuration stacked with 20 decks of silicon and Tungsten layers in TUBE (left) and CONE (right) shapes.

of circular and rectangular silicon wafers. The electron impact positions are illustrated for >20 mrad to the laboratory frame. Electrons of low scattering angles, in particular for those in $-x$ direction, are lost into beam-pipe. To have both scattered electrons and positrons detected, the corresponding θ_{min} on the horizontal axis is the beam-pipe acceptance plus 16.5 mrad. The loss of events on vertical direction is much less. With a beam pipe as indicated with $\pm y$ dimension equals radius, the horizontal boost does not lead to the loss of electrons with a larger y-position. A large detector coverage for Bhabha events is most favorable. The large opening of beam-pipe position is inevitable. We shall pursue the vertical dimension to be low as possible for a total integrated Bhabha cross section of larger than 50 nb.

The LumiCal mounted in front of the quadruple magnet at $z = \pm 100$ cm is half way in the tracking volume of $z = \pm 200$ cm. Shower leakage of electrons at the edge of LumiCal is investigated with a GEANT simulation with parameters cross-checked with a lateral shower study [19]. The LumiCal is configured assuming a sandwiched Silicon-Tungsten calorimeter stacked in twenty decks of 2 mm air-gap and $1X_0$ tungsten. The air-gap has a layer of silicon wafer of 0.3 mm thick. The front layer of the LumiCal is positioned at $z = \pm 100$ cm. The geometry of the LumiCal is tested in two configurations: a TUBE with uniform inner and outer radii of 25 and 100 mm, respectively; and a CONE shape with the outer edge at a constant angle of $\arctan 0.1$ to the interaction point. The CONE shape is intended for well separated absorption of electron shower in a theta threshold. Illustrated in Fig. 9.14 are the event display of the simulations. Out of the LumiCal, a 5 mm iron cone at $|\cos\theta| = 0.992$ is implemented for absorption of low energy shower secondaries massing into the center tracking volume.

The TUBE configuration leaves a corner of about 5 mrad on the outer edge, where the shower leakage of an incident electron is with energetic shower secondaries. The CONE shape allows the shower fully developed once the electron enters the calorimeter coverage. The shower leakage reaching the Fe-cone is recorded for the particle energies arriving and penetrating through, which are listed in Table 9.5 for 50 GeV and 125 GeV electrons. When the shower is well contained, the leakage is just a few dozens of less than 30 MeV particles. A shower on the edge creates up to 3k secondaries into the tracking

volume mostly of less than 100 MeV. The 5 mm iron layer can filter a large fraction of them, to less than 1k particles traversing through.

9.4.2 Systematic effects

The main measure of luminosity at the CEPC is the count of Bhabha events N_{Bh} detected in coincidence in the two halves of the luminosity calorimeter LumiCal. The luminosity figure is then obtained from the equation of $\mathcal{L} = N_{acc}/(\epsilon\sigma^{vis})$. The visible cross section for the Bhabha process, σ_{vis}, should be integrated over the same phase space as used for the counting of Bhabha events. The limited precision with which the experimental acceptance region is defined gives rise to a number of systematic effects. Further, other processes misidentified as Bhabha and the limited accuracy of the theoretical calculation of σ_{vis} contribute to the overall systematic uncertainty.

A generator-level study was performed to assess the effects related to the precision of the Bhabha acceptance region on Bhabha counting. An underlying assumption of the study is that the LumiCal is centered on the outgoing beam axis. This assumption is essential for data-driven control of the radial offset of LumiCal with respect to the IP, as well as for Bhabha event counting based on the mirrored asymmetric polar-angle acceptance regions on the left and right side of the detector [17] (in further text, *OPAL-style selection*). OPAL-style counting cancels out biases due to left-right asymmetries of the experimental angular acceptance. It is further assumed that for the final state particles hitting the radial region between 50 mm and 75 mm, corresponding to the detector fiducial volume (FV), shower leakage has a negligible effect on the reconstruction of the polar angle and the energy.

Bhabha event samples are generated using the BHLUMI generator [16]. Center-of-mass energy of 240 GeV is assumed, corresponding to approximately the energy of the maximum Higgs boson production cross section. The particles are generated in the range of polar angles including a $\sim$ 7 mrad margin outside the FV to allow non-collinear final state radiation (FSR) to contribute to the events. After event generation, smearing is applied to the final particle vertices and momenta according to the nominal CEPC param-

Table 9.5: Number of particles leaking out of the LumiCal outer radius (N_{enter}) and number of particles passing through the Fe-cone (N_{pass}). Two different detector designs (TUBE and CONE) and two shower energies (50 GeV and 125 GeV) are simulated. Repeat the 100 MeV energy threshold here?

	50 GeV electrons		125 GeV electrons	
	TUBE	CONE	TUBE	CONE
θ (mrad)	$N_{\text{enter}}/N_{\text{pass}}$	$N_{\text{enter}}/N_{\text{pass}}$	$N_{\text{enter}}/N_{\text{pass}}$	$N_{\text{enter}}/N_{\text{pass}}$
40	15.4/5.6	13.6/5.8	38.0/16.0	35.8/14.7
90	392/155	173/76	1028/399	434/19.7
95	501/290	367/152	2389/720	937/382
98	762/216	860/284	1718/473	2176/725
99	553/140	1331/367	1102/273	3306/915

eters. Additional smearing or bias is then applied according to one systematic effect at a time. Four momenta of close-by particles are summed up to account for cluster merging in LumiCal. The selection criteria to count an event consist of the OPAL-style angular selection and the requirement that the energy of both detected showers is above 50% of the nominal beam energy. The relative acceptance bias is determined as the relative difference between the Bhabha count $N_{\mathrm{Bh},i}$ obtained with the inclusion of the considered effect i and N_{Bh} obtained with the nominal set of parameters.

Table 9.6 lists the requirements on beam delivery, MDI and LumiCal installation, needed to limit individual systematic effects in the luminosity measurement to 1×10^{-3}, such as required for the Higgs boson physics program at the CEPC. Parameters influencing the integral luminosity precision are given as follows:

- ΔE_{CM}, uncertainty of the available center-of-mass energy affecting the Bhabha cross-section,
- $E_{e^+} - E_{e^-}$, asymmetry of the incident beam energies resulting in a net longitudinal boost of the event,
- $\frac{\delta\sigma_{E_{beam}}}{\sigma_{E_{beam}}}$, uncertainty of the beam energy spread,
- Δx_{IP} and Δz_{IP}, radial and axial offsets of the IP w.r.t. the LumiCal,
- Beam synchronization, resulting in axial offset of the IP w.r.t. the LumiCal,
- $\sigma_{x_{\mathrm{IP}}}$ and $\sigma_{z_{\mathrm{IP}}}$, radial and axial fluctuations of the scattering position,
- r_{in}, inner radius of the LumiCal acceptance region,
- $\sigma_{r_{\mathrm{shower}}}$, reconstruction precision of the radial shower coordinate,
- Δd_{IP}, uncertainty of the distance between the LumiCal halves.

Most requirements are technically feasible with the present state of the art of accelerator and detector technology. The most important challenge identified is the precision of the inner acceptance radius r_{in} of LumiCal. In order to keep the luminosity precision of 1 per mille, r_{in} must be known to within $10\,\mu\mathrm{m}$. The precision requirement of r_{in} scales linearly with the required luminosity precision, implying a correspondingly stricter requirement for the Z-pole run.

9.4.3 Summary on LumiCal

Instrumentation of the very forward region is very important for the realization of the CEPC physics program. Several technology options are under consideration. Some of them have been successfully applied at LEP or are under study for other future projects. A tracker placed in front of the LumiCal can improve polar angle measurement accuracy, facilitate LumiCal alignment and enable electron-photon separation. LumiCal must be centered on the outgoing beam axis to allow control of the systematic effects at the required level. Precision requirements on beam delivery, MDI and LumiCal installation have been addressed by simulation, and proven to be feasible with the present state-of-the-art of accelerator and detector technology.

Table 9.6: Requirements on beam delivery, MDI and LumiCal installation, needed to limit individual systematic effects to 1×10^{-3}. Should the entry ">1" be "<1" or just "1"?

Parameter	Unit	Limit
ΔE_{CM}	MeV	120
$E_{e^+} - E_{e^-}$	MeV	240
$\frac{\delta\sigma_{E_{beam}}}{\sigma_{E_{beam}}}$		effect canceled
Δx_{IP}	mm	>1
Δz_{IP}	mm	10
Beam synchronization	ps	7
$\sigma_{x_{\text{IP}}}$	mm	1
$\sigma_{z_{\text{IP}}}$	mm	10
r_{in}	mm	10
$\sigma_{r_{\text{shower}}}$	mm	1
Δd_{IP}	μm	500

9.5 Detector integration

Both QD0 and QF1 are located inside the detector, which drastically complicates the support and alignment of the detector and machine components in the interaction region. The two final focus magnets and the LumiCal will possibly be mounted on a dedicated support structure, extended from a pillar outside the detector and suspended from the solenoid cryostat. They might have to been integrated together before being pushed into the interaction region. The amount of material in front of the LumiCal must be minimized so that the high precision of the LumiCal can be maintained. This shall inevitably introduce more complexities to the detector integration. Furthermore, the shaped beam pipe and surrounded silicon detectors will possibly be supported from a structure of carbon fiber reinforced plastic, which can hang at the flanges of the field cage of the Time Projection Chamber (TPC). Significant effort is required to realize a solid mechanical design and to define a reasonable procedure for the detector and machine installation scheme.

References

[1] CEPC-SPPC Study Group, *CEPC-SPPC Preliminary Conceptual Design Report. 1. Physics and Detector*, . IHEP-CEPC-DR-2015-01, IHEP-TH-2015-01, IHEP-EP-2015-01.

[2] CEPC-SPPC Study Group, *CEPC-SPPC Conceptual Design Report. 1 . Accelerator*, . IHEP-CEPC-DR-2018-01, IHEP-AC-2018-01, to be published.

[3] G. von Holtey et al., *Study of beam-induced particle backgrounds at the LEP detectors*, Nucl. Instr. and Meth. **A403** (1998) 205 – 246.

[4] P. M. Lewis et al., *First Measurements of Beam Backgrounds at SuperKEKB*, arXiv:1802.01366 [physics.ins-det].

[5] D. S. Denisov et al., *Machine-Related Backgrounds in the SiD Detector at ILC*, JINST **1** (2006) P12003, arXiv:hep-ex/0608001 [hep-ex].

[6] B. Dalena, J. Esberg, and D. Schulte, *Beam-induced backgrounds in the CLIC 3 TeV CM energy interaction region*, in *International Workshop on Future Linear Colliders (LCWS11) Granada, Spain, September 26-30, 2011*. 2012. arXiv:1202.0563 [physics.acc-ph].

[7] GEANT4 Collaboration, S. Agostinelli et al., *GEANT4: A Simulation toolkit*, Nucl. Instrum. Meth. **A506** (2003) 250–303.

[8] J. Allison et al., *Geant4 developments and applications*, IEEE Trans. Nucl. Sci. **53** (2006) 270.

[9] Geant4 Collaboration, M. Asai et al., *Recent developments in Geant4*, Annals Nucl. Energy **82** (2015) 19–28.

[10] S. Baranov et al., *Estimation of Radiation Background, Impact on Detectors, Activation and Shielding Optimization in ATLAS*, . ATL-GEN-2005-001, ATL-COM-GEN-2005-001, CERN-ATL-GEN-2005-001.

[11] I. Agapov, G. A. Blair, S. Malton, and L. Deacon, *BDSIM: A particle tracking code for accelerator beam-line simulations including particle-matter interactions*, Nucl. Instrum. Meth. **A606** (2009) 708–712.

[12] D. Schulte, *Beam-beam simulation with GUINEA-PIG*, In 5th International Computational Accelerator Physics Conference (1998) . CLIC-NOTE 387.

[13] R. Kleiss and H. Burkhardt, *BBBREM – Monte Carlo simulation of radiative Bhabha scattering in the very forward direction*, Comput. Phys. Commun. **81** (1994) 372 – 380.

[14] K. Oide and H. Koiso, *Anomalous equilibrium emittance due to chromaticity in electron storage rings*, Phys. Rev. **E49** (1994) 4474–4479.

[15] S. Jadach, *Theoretical error of luminosity cross-section at LEP*, in *Electroweak precision data and the Higgs mass. Proceedings, Workshop, Zeuthen, Germany, February 28-March 1, 2003*, pp. 85–95. 2003. arXiv:hep-ph/0306083 [hep-ph].

[16] S. Jadach et al., *Upgrade of the Monte Carlo program BHLUMI for Bhabha scattering at low angles to version 4.04*, Comput. Phys. Commun. **102** (1997) 229–251.

[17] OPAL Collaboration, G. Abbiendi et al., *Precision luminosity for Z0 line shape measurements with a silicon tungsten calorimeter*, Eur. Phys. J. **C14** (2000) 373–425, arXiv:hep-ex/9910066 [hep-ex].

[18] P. Bloch et al., *Performance Study of Non-Irradiated Prototype Silicon Preshower Samplers for CMS*, . CMS-NOTE-2000-042.

[19] Y. Chang et al., *Lateral development of electron showers measured by silicon microstrip detectors*, Nucl. Instr. and Meth. **A388** (1997) 135 – 143.

CHAPTER 10

SIMULATION, RECONSTRUCTION AND PHYSICS OBJECT PERFORMANCE

This Chapter summarizes the expected performances of the CEPC baseline detector concept based on Monte Carlo (MC) simulation studies. Section 10.1 describes software and algorithm tools used, event generation and simulation as well as their reconstruction. Section 10.2 presents the performances for identifying and measuring basic physics objects such as leptons, photons, jets and their flavors that form the building blocks of physics analyses. The results presented represent the first attempt to understand the performance of the CEPC baseline detector. They will likely improve with further studies and optimization.

10.1 Event simulation and reconstruction

The simulations of physics events and detector responses and the reconstruction of the raw detector information are vital for high energy physics experiments. Figure 10.1 shows the flow chart of the event simulation and reconstruction. In this section, the functionalities of key components of the chart are described.

10.1.1 Event simulation

For the studies of the CEPC physics performance, the Whizard [1] package is used as the main event generator to produce physics events. Collaborating with the Whizard team, a dedicated CEPC beam parametrization has been implemented in its official release. The Whizard generator is used to simulate Standard Model processes, including both Higgs boson signal and all its SM background samples. Additionally, Madgraph [2] and Pythia [3] generators are used to produce samples from beyond Standard Model physics.

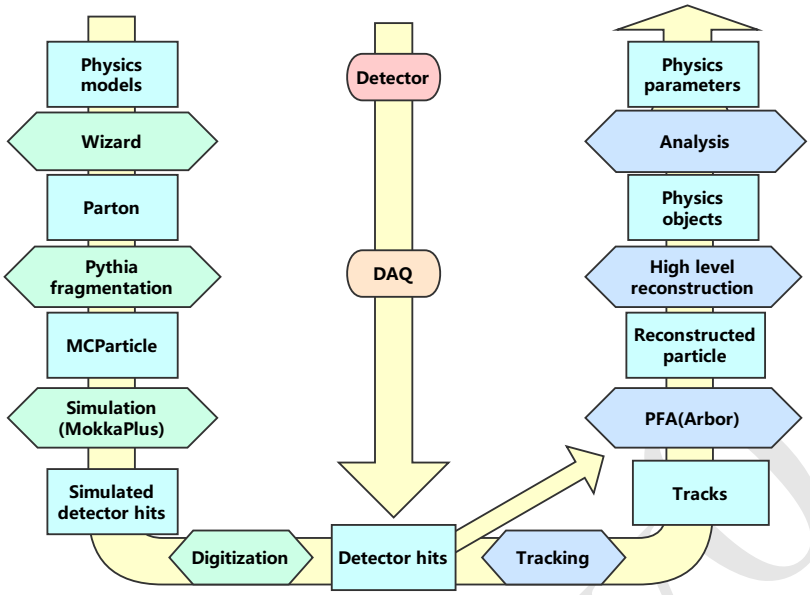

Figure 10.1: The flow chart of the CEPC simulation studies.

A Geant4 based detector simulation framework, MokkaPlus, is used for the CEPC detector simulation. MokkaPlus is a virtual geometry constructor that compiles with the Geant4 libraries [4] and MySQL database [5]. It is an improved version of Mokka [6], a simulation framework used for early linear collider studies. The digitization of simulated energy deposits in the detector are performed using a general algorithm that reproduces the test beam results [7] for the calorimeter and an `ilcsoft` scheme for the tracking detectors. The parameter values of the `ilcsoft` scheme are tuned to match the CEPC detector design. In addition, a fast simulation based on the efficiency and resolution parametrization derived from the full simulation is also developed. The fast simulation is used to produce most of the background samples for studies presented in this report.

10.1.2 Event reconstruction

The event reconstruction chain starts with the track reconstruction, followed by the particle flow interpretation of tracks and calorimeter hits and finally the reconstruction of compound physics objects such as converted photons, K_S's, τ-leptons and jets.

Tracks are reconstructed from hits in the tracking detectors by the tracking module. The module is currently based on the `Clupatra` module [8] of `ilcsoft` which has been shown to have excellent performance. A CEPC-specific tracking module with the flexibility of geometry modification is under development.

A dedicated particle flow reconstruction toolkit, ARBOR [9, 10], has been developed for the CEPC baseline detector concept. ARBOR is composed of a clustering module and a matching module. The clustering module reads the calorimeter hits and forms clusters of hits (also called branches) which are then arranged into a tree topology as illustrated in Figure 10.2 for the 3-prong decay of a τ-lepton. The matching module identifies calorime-

ter clusters with matching tracks and builds reconstructed charged particles. The remaining clusters are reconstructed into photons, neutral hadrons and unassociated fragments. From this unique list of particles, simple particles such as electrons, muons, photons, charged pions and kaons can then be identified.

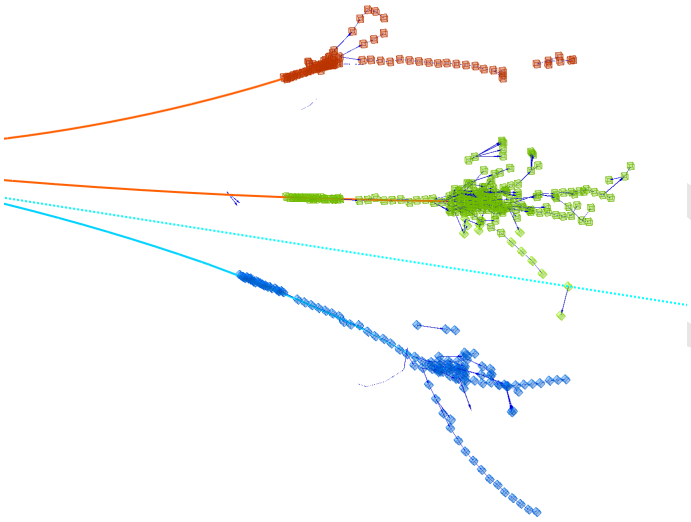

Figure 10.2: An illustration of particle flow reconstruction: the 3-prong decay of a τ-lepton from $Z \to \tau^+\tau^-$ reconstructed by the ARBOR algorithm. Three branches of calorimeter clusters correspond to the three reconstructed charged particles of the τ-lepton decay: a 5.7 GeV π^+ (red), a 27.4 GeV π^+ (green) and a 10.3 GeV π^- (blue). Also shown in cyan dashed line is a 2.2 GeV $\bar{\nu}_\tau$ from Monte Carlo truth information. match track color to with cluster color

The particle flow reconstruction provides a coherent interpretation of an entire physics event and, therefore, is well suited for the reconstruction of compound physics objects such as converted photons, K_S's, τ-leptons and jets. The reconstruction of τ-leptons and jets are described in Section 10.2. CORAL, an algorithm that targets the reconstruction of converted photons, π^0's and K_S's, is being developed.

10.1.2.1 Track reconstruction

The CEPC baseline tracker consists of a silicon tracking system and a barrel TPC. The two subsystems play complementary roles. The silicon system provides high precision spatial point measurements whereas the TPC has more than 200 radial layers which significantly enhances the track finding performance of the detector. In addition, the silicon system includes a forward tracking system that extends the solid angle coverage of the tracker.

The performance of the CEPC tracker is studied using two samples: a single muon particle sample and an $e^+e^- \to Z \to \tau^+\tau^-$ sample at $\sqrt{s} = 91.2$ GeV. The single muon sample is used to characterize the tracking efficiency and momentum resolution for isolated tracks while the $Z \to \tau^+\tau^-$ sample, with the 3-prong decay for one of the two τ-leptons, provides a test for reconstructing closely spaced tracks.

The single muon sample covers a momentum range of 0.1 GeV to 100 GeV and the full angular range. Figure 10.3 shows the extracted efficiency and momentum resolution

as a function of the polar angle for different momentum bins. For muons in the tracking fiducial volume of $|\cos\theta| < 0.985$ and with momentum above 0.5 GeV, the reconstruction efficiency is nearly 100%. The momentum resolution reaches per mille level or better for the momentum range of 10–100 GeV in the barrel region. The resolution is limited by material-induced multiple scatterings at low momentum and by the magnetic field and level-arm at high momentum, consistent with the design goal outlined in Chapter 3. τ-leptons from $Z \to \tau^+\tau^-$ are highly boosted and can lead to three closely spaced charged particles in their 3-prong decays, see Figure 10.2. For this sample, the efficiency for reconstructing all three tracks of the τ decays is found to be close to 100% .

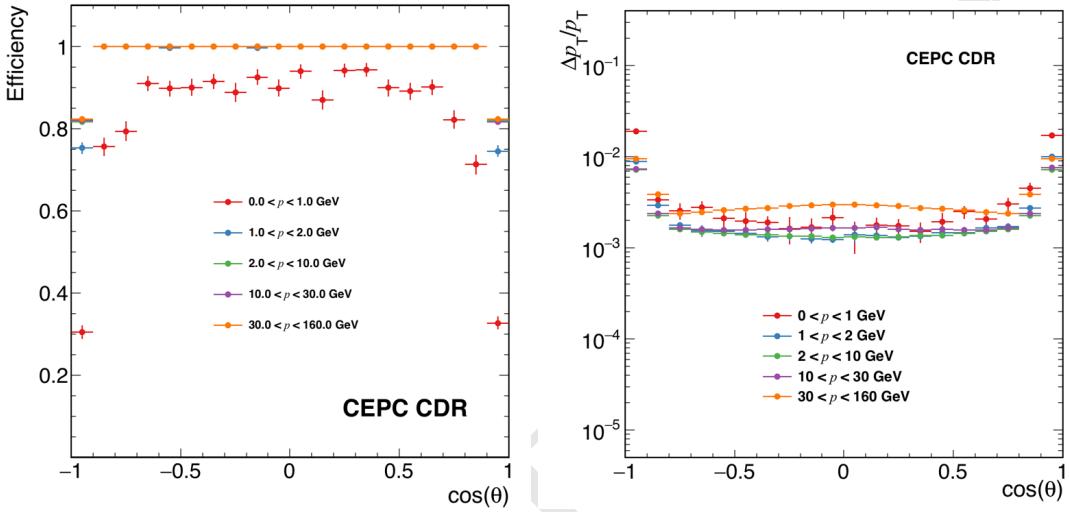

Figure 10.3: Single track reconstruction: (a) efficiency and (b) momentum resolution as a function of the cosine of the polar angle in different momentum bins.

10.1.2.2 Cluster reconstruction

The high-granular calorimeters of the CEPC baseline detector concept are well suited for reconstructing clusters of energy deposits by traversing particles. The fine segmentation allow for the reconstruction of individual particles produced in shower cascades, see Figure 10.2.

Two relevant performance measures of the cluster reconstruction are the energy collection efficiency for single neutral particles and spatial separation capability for two closely spaced neutral particles. For photons with energy above 5 GeV, ARBOR is able to collect more than 99% of the energy deposited in the calorimeter while keeping the mis-clustering rate small. Good cluster spatial separation capability is essential for the reconstruction of compound particle objects such as π^0's and τ-leptons. Figure 10.4(a) is a demonstration of the reconstructed clusters from two closely spaced photons from a π^0 decay. The efficiencies for successfully reconstructing two photon clusters as functions of their separation at the calorimeter entry points are shown in Figure 10.4(b) for three different ECAL cell sizes. The critical distance, defined as the minimum separation at which the efficiency for reconstructing two photon clusters is 50%, is found to be 16 mm for the baseline design of ECAL cell size of 10×10 mm^2. This corresponds to an average

efficiency of 50% for reconstructing two photons as two separate clusters from a 30 GeV π^0 decay.

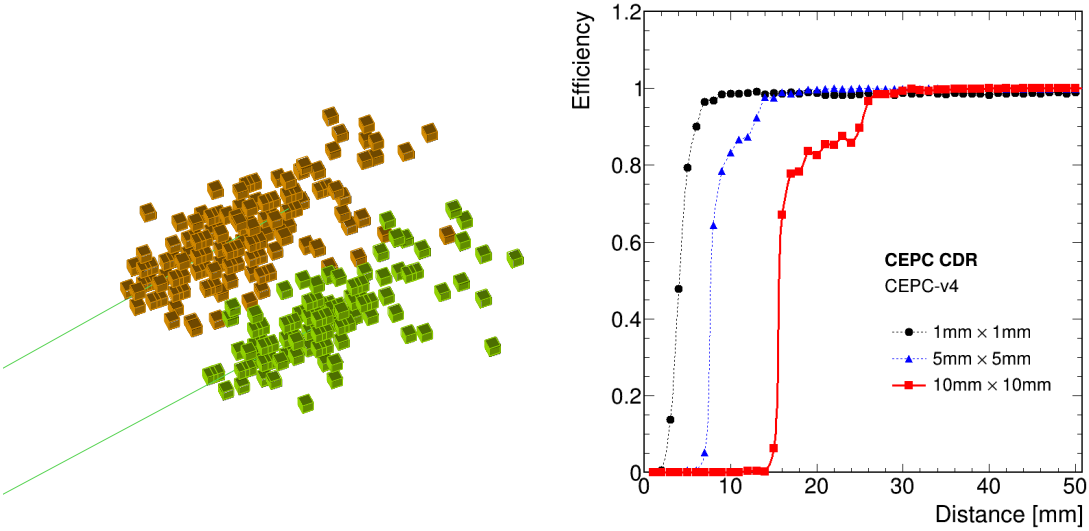

Figure 10.4: (a) Clusters of the two photons of energies of 6.2 GeV and 5.8 GeV from a 10 GeV π^0 decay reconstructed in the Silicon-Tungsten ECAL with a 10×10 mm^2 cell size. (b) Reconstruction efficiencies of two photons as two separate clusters as functions of the distance between their calorimeter impact points for three different ECAL cell sizes. The ECAL cell size of the CEPC baseline detector is chosen to be 10×10 mm^2.

10.2 Object Identifications and Performances

Particle flow reconstruction leads to a unique list of particles from which electrons, muons, photons, τ-leptons, and jets etc., the physics objects as they are customarily called, can be identified or built. These objects serve as building blocks for further physics analyses as presented in Chapter 11. In this section, their general identifications and the expected performances are described. For analyses of specific processes, the identifications and performances can often be improved by utilizing the unique topologies of the events under study.

10.2.1 Leptons

Leptons (ℓ, $\ell = e, \mu$)[1] are bedrocks to the CEPC physics program. $Z \to ee$ and $Z \to \mu\mu$ decays are indispensable for electroweak measurements and for the model-independent identification of the Higgs boson through the recoil mass method. A large fraction of Higgs bosons decay, directly or via cascade, into final states with electrons and muons.

The particle-flow oriented baseline detector, particularly its fine-segmented calorimeter system, provides enormous information for the lepton identification. High energy electrons and hadrons will likely induce thousands of hits whereas muons deposit little energy in the calorimeter. Electrons can be identified from their pencil-like electromagnetic shower development in ECAL matched with tracks in the tracker. Muons exhibit

[1]Unless otherwise noted, leptons refer to electrons, muons or their antiparticles.

themselves as minimum ionizing particles in the calorimeter matched with tracks in the tracker as well as in the muon system. Moreover, the dE/dx measurements in the TPC could provide additional discrimination of electrons from muons and hadrons for energies up to 10 GeV.

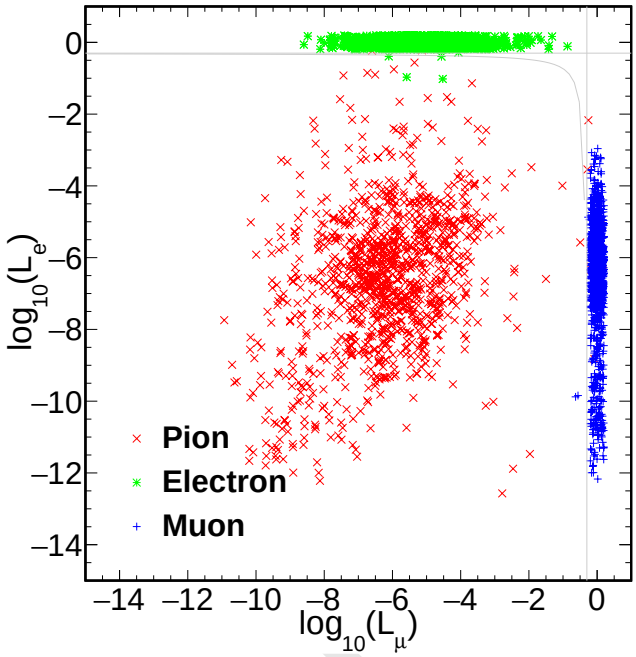

Figure 10.5: Distributions of logarithmics of e-likeliness L_e and μ-likeliness L_μ expected from 40 GeV electrons, muons and charged pions in the barrel calorimeter ($|\cos\theta| < 0.7$).

A lepton identification algorithm, LICH [11], has been developed and implemented in ARBOR. LICH combines more than 20 discriminating variables from the detector to build lepton-likelihoods, e-likeliness (L_e) and μ-likeliness (L_μ), using a multivariate technique. Figure 10.5 comparing two-dimensional distributions of L_e and L_μ expected from single electrons, muons and charged pions, showing clear separations among these particles. For leptons above 2 GeV, an identification efficiency better than 99.5% and a mis-identification rate from hadrons smaller than 1% can be achieved. The main sources of mis-identifications are irreducible backgrounds from the $\pi^\pm \to \mu^\pm$ decays for muons and highly electromagnetic like $\pi^\pm$ clusters (π^0 produced in pion-nucleon interactions) for electrons. The momentum resolution of the tracker (see Section 10.1.2.1) largely determines the resolutions for both electrons and muons. However, small degradations are expected from Bremsstrahlung radiations, particularly for electrons. Recovering the radiation energy losses using the ECAL measurements should improve the resolutions. However, this is not implemented for the current studies.

For complex physics events, lepton identification will be affected by the limited spatial separation capability of the detector. For example, the efficiency for successfully identifying two leptons with opposite charges is found to be 97–98% for the $e^+e^- \to ZH \to \ell\ell H$ events. The small loss of the efficiency can be attributed to overlapping clusters in the calorimeter.

Figure 10.6 shows the reconstructed recoil mass[2] distributions of the $Z \to \mu\mu$ and $Z \to ee$ decays from the $e^+e^- \to ZH$ process and Figure 10.7(a) is the dimuon invariant mass distribution of $H \to \mu^+\mu^-$ again from $e^+e^- \to ZH$. The sharp peaks at the Higgs boson mass are demonstrations of excellent lepton energy/momentum and angular resolutions. The high-mass tails in the recoil mass distributions are due to both initial and final state radiations while the low-mass tail in the dimuon mass distribution is the result of the final-state radiation. The recoil mass distributions are critical for the model-independent identifications of the Higgs boson.

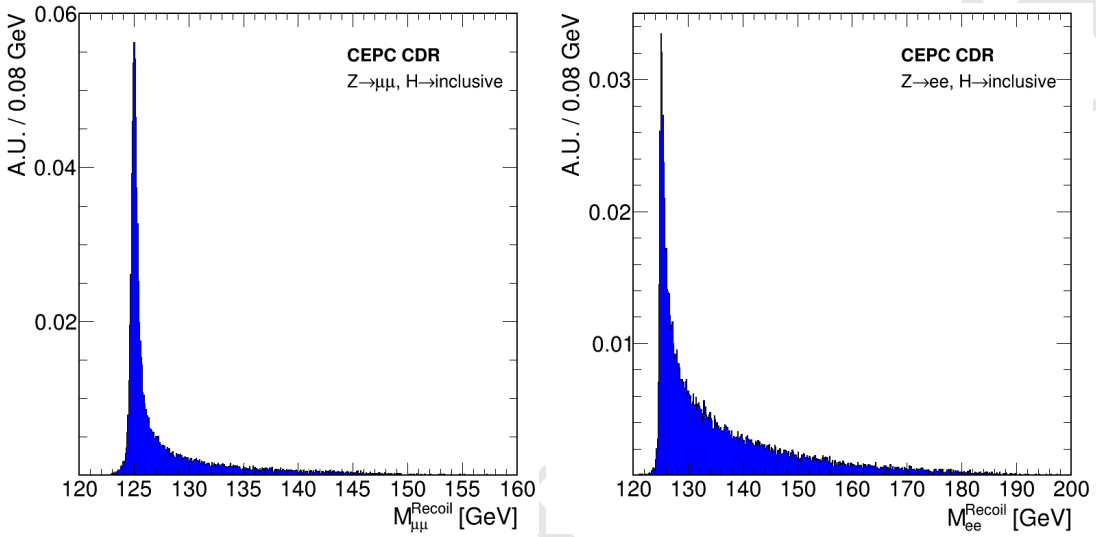

Figure 10.6: The reconstructed recoil mass distributions of $e^+e^- \to ZH$ events with (a) $Z \to \mu\mu$ and (b) $Z \to ee$ decays. As expected, the distributions peak strongly at the Higgs boson mass. The high-mass tails are results of initial- and final-state radiations. Both distributions are normalized to unit area. comment on the resolutions.

10.2.2 Photons

Photons can be produced from either initial and final state radiations or decays of unstable particles. Precise photon measurements are essential, for example, for studying the $H \to \gamma\gamma$ decay and counting neutrino species. Moreover, photons are a large part of secondary particles that form jets and have an important role in the τ-lepton identification, they impact all aspects of the physics at the CEPC.

Photons have similar signatures as electrons in the calorimeter, but in general without matching tracks in the tracker. However, 5–10% of photons converts to e^+e^- pairs through their interaction with the materials in front of the calorimeter. Some of these converted photons will have reconstructed matching tracks. Figure 10.8(a) shows the material in the unit of radiation length and Figure 10.8(b) is the photon conversion rate at different polar angles. For unconverted photons of energies above 5 GeV, the identification efficiency is nearly 100% with more than 99% of their energies reconstructed. For the current studies,

[2]See Section 11.1.2 for the definition.

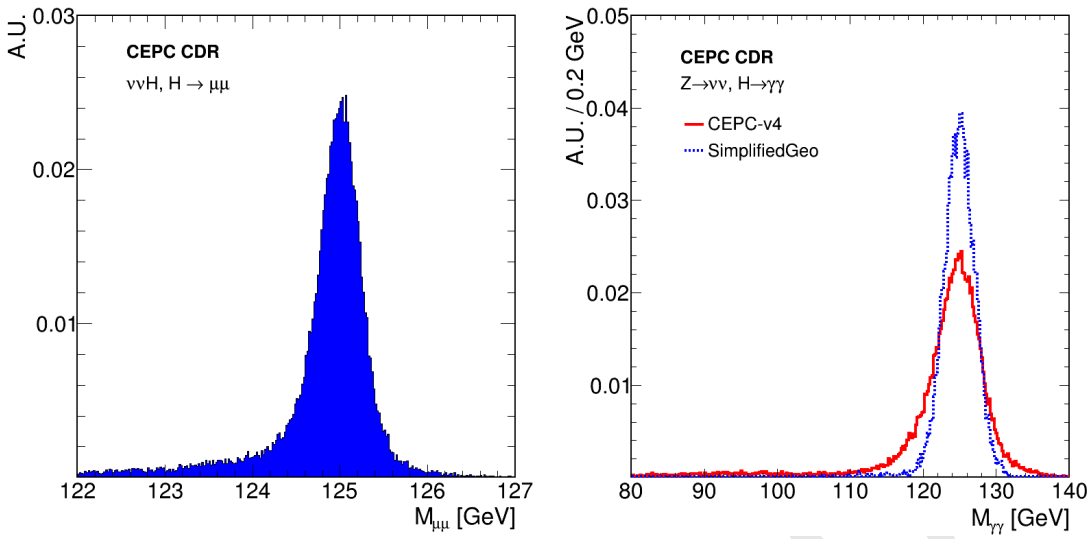

(a) (b)

Figure 10.7: The reconstructed invariant mass distributions of (a) dimuon from the $H \to \mu^+\mu^-$ decay and (b) diphoton from the $H \to \gamma\gamma$ decay produced in the $e^+e^- \to ZH$ process. $H \to \mu^+\mu^-$ has width 0.28 GeV. $H \to \gamma\gamma$ has 2.09 GeV for simplified geometry while CEPC-v4 has 3.48 GeV. Comment on the resolution.

a simplistic algorithm has been used to identify converted photons. Approximately 80% of the converted photons are recovered using this algorithm. The rate of misidentifying a hadronic jet as a photon is found to be negligible.

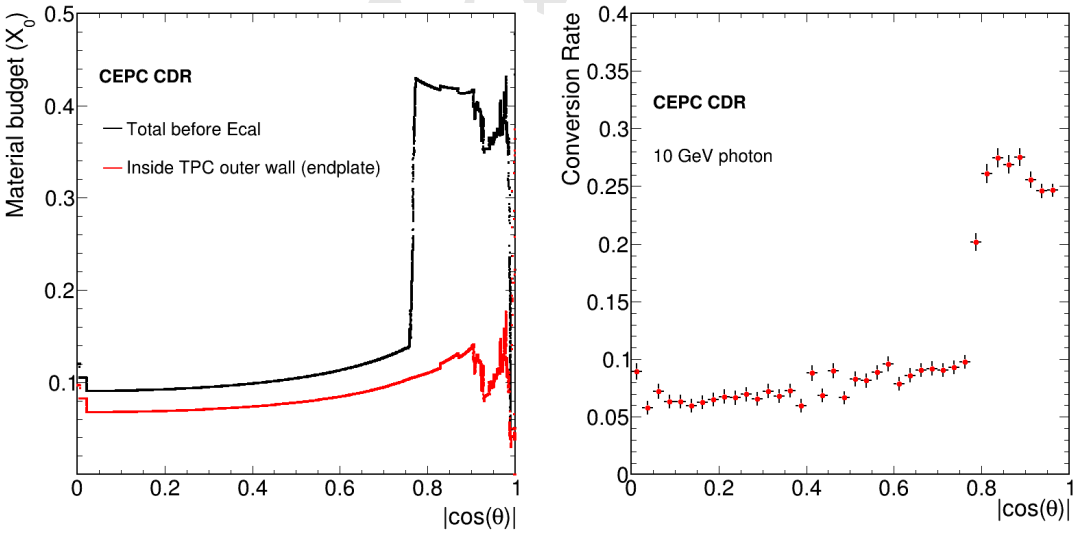

(a) (b)

Figure 10.8: (a) The material in the unit of radiation lengths inside the tracker and (b) the conversion rate of 10 GeV photons for different polar angles.

The photon energy resolution is determined by that of the electromagnetic calorimeter and is demonstrated in Figure 10.9. The resolution is XX% at XX GeV. The dipho-

ton invariant mass distribution of the $H \to \gamma\gamma$ decay serves as a good benchmark for studying the impact of the photon energy resolution. The width of the mass distribution should be dominated by the energy resolution effect because of the narrow intrinsic Higgs boson width. Figure 10.7(b) shows the reconstructed $m_{\gamma\gamma}$ distributions of the $e^+e^- \to ZH \to \nu\bar{\nu}\gamma\gamma$ events. A diphoton mass resolution of approximately 2.7% is expected. Comment on the resolution of the baseline compared with that of CALICE.

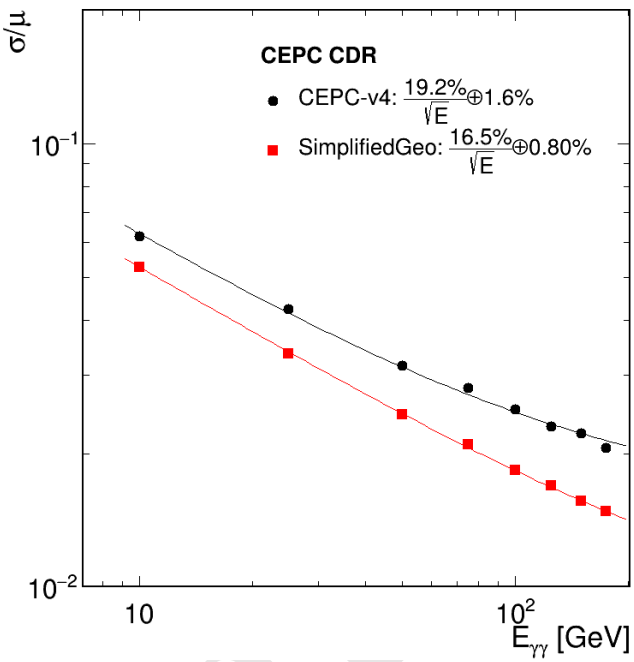

Figure 10.9: Photon energy resolution This looks bad, suggest not to include it. Is it really vs $E_{\gamma\gamma}$, not E_γ?

10.2.3 Tau Leptons

As the heaviest lepton, τ-leptons have a unique role in studying Higgs boson physics. Leptonic decays of τ-leptons, $\tau \to e\nu\nu$ and $\tau \to \mu\nu\nu$, are indistinguishable from electrons or muons. Thus τ-leptons here concern their hadronic decays which appear in the detector as narrow pencil-shaped hadronic jets with low particle multiplicity. A basic τ-lepton identification algorithm has been developed. The algorithm starts with a seed track with its energy above 1.5 GeV and clusters charged and neutral particles in a small cone of radius of 0.15 rad around it to form the τ-lepton candidate. The invariant mass of the all particles in the cone is required to be in the range of 0.2–2 GeV, consistent with the τ-lepton mass. Furthermore, a discriminant variable based on the longitudinal and transverse impact parameters of the leading track is constructed and the variable is required to be consistent with the non-zero lifetime of the τ-lepton. Finally, the total energy in an annular cone or radius between 0.15–0.45 rad is required to be less than 8% of the τ-lepton candidate energy. The main backgrounds are hadronic jets.

Figure 10.10(a) is a graphic representation of the tau identification. The efficiency and the mis-identification rate as functions of the visible energy of the τ-lepton candidate are shown in Fig. 10.10(b). The mis-identification rate is measured from a $Z \to q\bar{q}$ sample of the Z pole run. For energies above 50 GeV, the efficiency is above 80% with less than

1% mis-identification rate. The performance can be further improved by exploiting the details of the shower development and using energy-dependent cone radii.

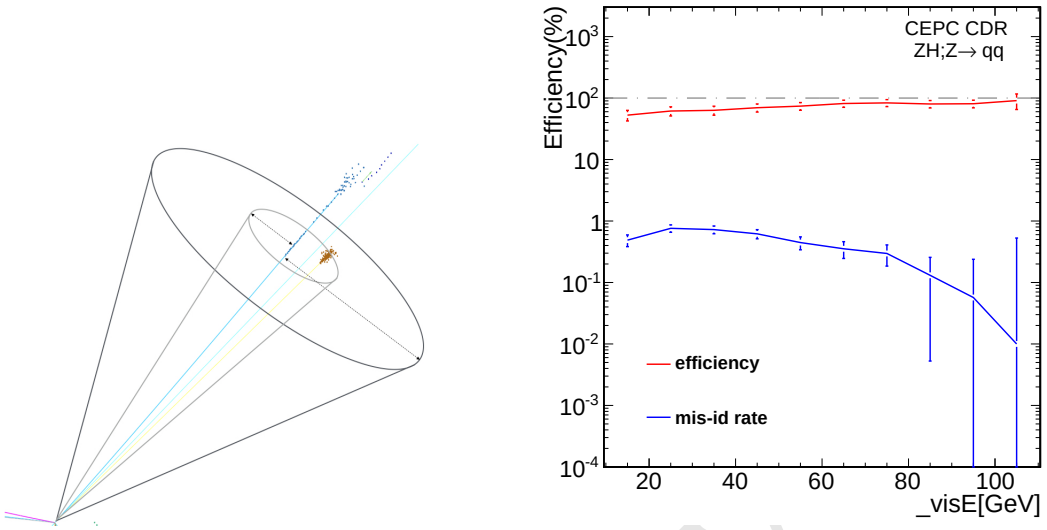

(a) (b)

Figure 10.10: (a) Illustration of τ-lepton identification and (b) the efficiency and mis-identification rate as functions of the visible energy of τ-lepton candidate. What samples are used to measure efficiency and fake rate? The efficiency is a bit low.

10.2.4 Jets

The vast majority of the events produced at the CEPC have hadronic jets in their final states. For example, 70% of the Higgs bosons decays directly to a pair of jets and another 20% decays indirectly to jets through intermediate W or Z bosons. Coincidentally, about 70% of the W or Z bosons each decays to dijets. Thus the impact of jets to the CEPC physics program cannot be overstated.

Jets are formed from particles reconstructed by ARBOR using the Durham clustering algorithm [**?**]. The ambiguity in clustering is the leading source of uncertainty in jet reconstruction and measurements, particularly in events with closely spaced physics objects.

Jet energies are foreseen to be calibrated through a two-step process. First, calibrations are applied to particles identified by ARBOR. While the energies of the charged particles are determined by their track momenta, the energies of neutral particles are currently calibrated using MC simulation and can be calibrated using the test beam or collision data when they are available. Approximately 35% of the jet energy is carried by neutral particles. In the second step, the jet energy are calibrated using physics events. At the CEPC, W and/or Z bosons are copiously produced and can be identified with high efficiency and purity. Thus $W \to q\bar{q}$ and $Z \to q\bar{q}$ decays serve as standard candles for the jet energy calibration. Clean samples of $WW \to \ell\nu q\bar{q}$ (ZH and WW runs), $ZZ \to \nu\bar{\nu}q\bar{q}$ (ZH run) and $Z \to q\bar{q}$ (Z pole run) can be selected. The enormous statistics allows to characterize the jet response in details.

Figure 10.11(a) shows energy ratios between the reconstructed jets and MC particle jets for different polar angles derived using the simulated $ZZ \to \nu\bar{\nu}q\bar{q}$ events. The ratios

are close to unity and thus the corrections are $< 1\%$. The jet energy resolution is shown in Figure 10.11(b) as a function of jet energy. The resolution ranges from 5% for energies below 20 GeV to 3% for energies at 90 GeV. Potential factors that affect the jet energy scale and/or resolution are jet flavor composition, fractions of charged and neutral particles, as well as the stability and uniformity of the detector responses. Given the small jet energy scale correction, a sub-percent level jet energy scale precision should be possible.

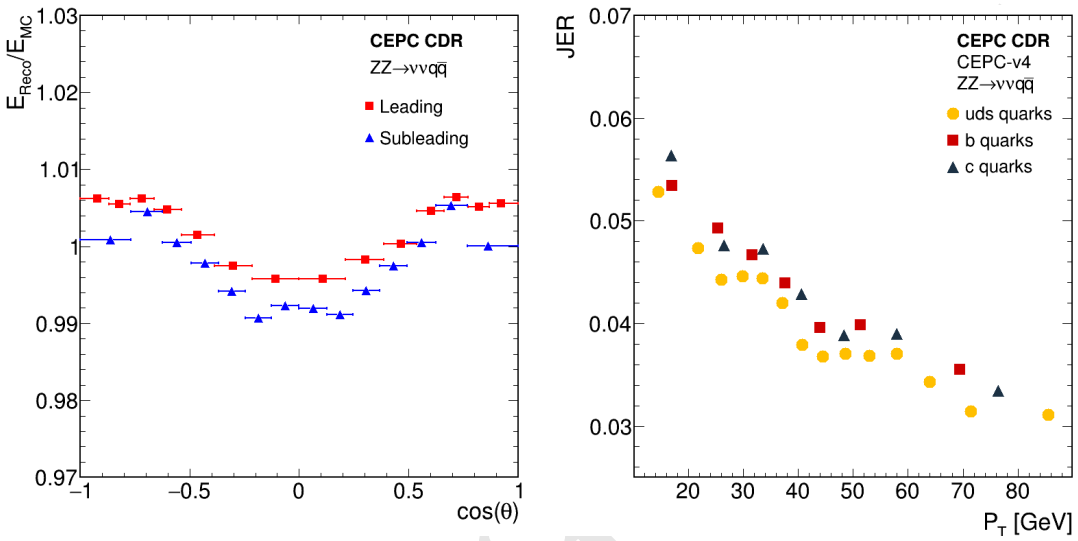

Figure 10.11: (a) The energy ratios between the reconstructed jets and MC particle jets as functions of cosine of their polar angles and (b) jet energy resolution as a function of jet energy. These distributions are derived from the simulated $ZZ \to \nu\bar{\nu}q\bar{q}$ events. The energy ratios are shown for leading and subleading jets separately. I suspect that neutrinos are removed from particle jets? Comment on light and heavy-quark jets.

One key jet performance measure is it's ability to separate hadronic decays of W, Z and Higgs bosons. Figure 10.12(a) compares the reconstructed dijet invariant mass distributions from $W \to q\bar{q}$, $Z \to q\bar{q}$ and $H \to b\bar{b}/c\bar{c}/gg$ decays of $WW \to \ell\nu q\bar{q}$, $ZZ \to \nu\bar{\nu}q\bar{q}$ and $ZH \to \nu\bar{\nu}(b\bar{b}/c\bar{c}/gg)$ processes, respectively. Compared with $W \to q\bar{q}$, the $Z \to q\bar{q}$ and $H \to b\bar{b}/c\bar{c}/gg$ distributions have long low-mass tails. These tails are from the heavy-flavor jets as demonstrated in Figure 10.12(b) where the distributions from $H \to b\bar{b}$, $H \to c\bar{c}$ and $H \to gg$ decays are separately shown and compared. The $H \to gg$ distribution is symmetric and has the best mass resolution at $\sim 4.3\%$, whereas the $H \to b\bar{b}$ decay has a long asymmetric low mass tail and the worst mass resolution at $\sim 7.4\%$ (the core). The degradations in resolution and the distortions in the mass distributions for the $H \to b\bar{b}$ and $H \to c\bar{c}$ decay can be explained by neutrinos produced in semi-leptonic decays of b- and $c-$quarks. The mass resolutions for $W \to q\bar{q}$ and $Z \to q\bar{q}$ are approximately XX GeV, implying that the W and Z boson peaks can be separated by approximately $X\sigma$.

10.2.5 Jet flavor tagging

Identification, i.e tagging, jet flavors is essential for the measurements of the Higgs couplings and the electroweak observables at the CEPC. Heavy-flavor quarks (b and c) from W, Z or Higgs boson decays hadronize quickly to form heavy bottom and charm hadrons

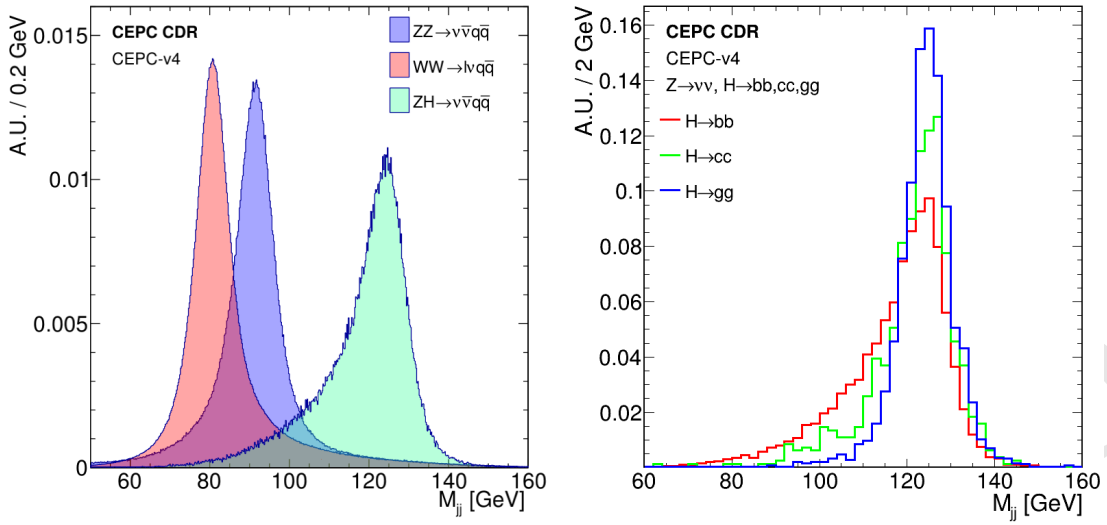

Figure 10.12: Reconstructed dijet mass distributions of (a) the $W \to q\bar{q}$, $Z \to q\bar{q}$ and $H \to b\bar{b}/c\bar{c}/gg$ decays from the $ZZ \to \nu\bar{\nu}q\bar{q}$, $WW \to \ell\nu q\bar{q}$ and $ZH \to \nu\bar{\nu}(b\bar{b}, c\bar{c}, gg)$ processes respectively and (b) the separate $H \to b\bar{b}$, $H \to c\bar{c}$ and $H \to gg$ decays from the $ZH \to \nu\bar{\nu}(b\bar{b}, c\bar{c}, gg)$ process. All distributions are normalized to unit area.

(B^0, $B^\pm$, B_s, D^0, $D^\pm$, ...). Those hadrons are short-lived and have typical decay distances of a few millimeters. Therefore, the reconstruction of their decay vertices, often referred as secondary vertices, is an important tool for tagging jet flavors. Other information such as jet and vertex mass, impact parameters and leptons inside the jets, are also frequently used to differentiate heavy-flavor jets from light-quark and gluon jets.

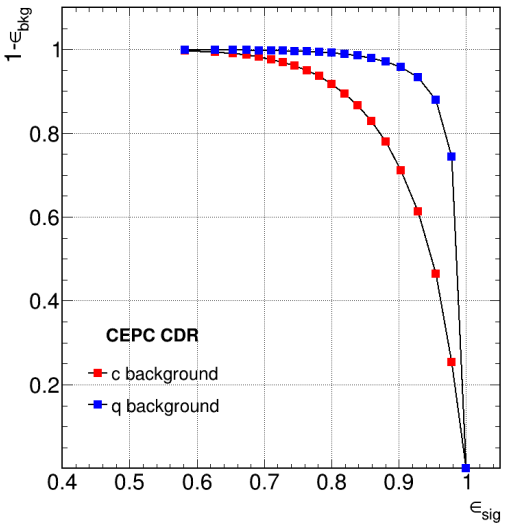

Figure 10.13: Efficiencies for tagging b-jets and vs rejections of background jets, determined from an inclusive $Zq\bar{q}$ sample at the Z pole run.

The jet flavor tagging is performed using LCFIPlus [12], the tagging algorithm used for linear collider studies. LCFIPlus reconstructs secondary vertices from the final-state particles identified by ARBOR. It combines more than 60 discriminant variables to cal-

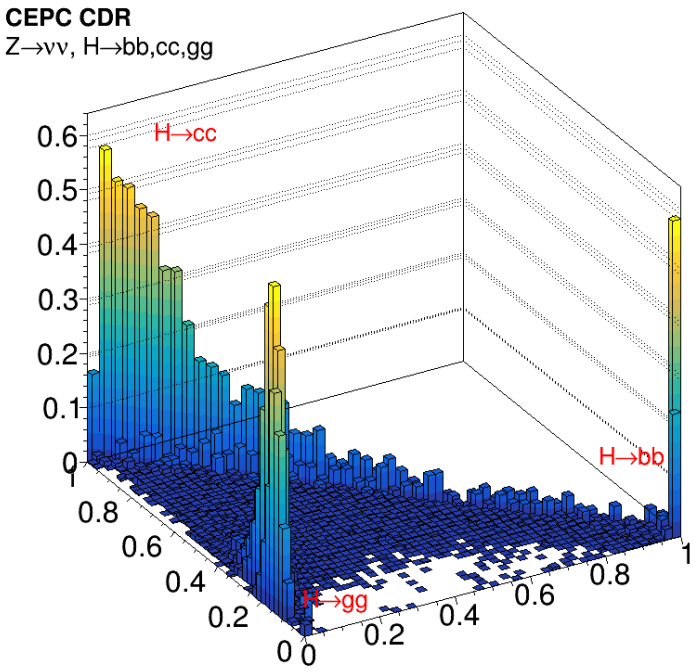

Figure 10.14: The two-dimensional distribution of b-likeliness L_B and c-likeliness L_C of jets from the $H \to b\bar{b}$, $H \to c\bar{c}$ and $H \to gg$ decays, showing clear separations between them. The three decays are plotted with equal weights to demonstrate their differences. Add x- and y-axis titles

culate the b-likeliness (L_B) and c-likeliness (L_C) using a Boosted Decision Tree [13] method. Compared with the b-jet tagging, c-jet tagging is particularly challenging as charm hadrons have shorter lifetimes than bottom hadrons and therefore suffers more from light-quark and gluon jet backgrounds. Benefiting from the high precision vertex system, the CEPC detector provides reasonable separation of c-jets from other flavor jets. Figure 10.13 shows the b-jet tagging efficiencies for different rejections of background jets, measured from a $Z \to q\bar{q}$ sample of the Z pole run. For this sample, b-jets can be tagged with an efficiency of 80% and a purity of 90%. Similarly, an efficiency of 60% and a purity of 60% can be achieved for the c-jet tagging. Purities can be improved by tightening the tagging requirements at the expenses of reduced efficiencies. Figure 10.14 is a demonstration of the b/c-likeliness distributions of the b, c and gluon jets from the $H \to b\bar{b}/c\bar{c}/gg$ decays.

10.2.6 Missing Energies, Momenta and Masses

Neutrinos interact weakly with the detector and for all practical purposes escape detection without traces. The same is true for the hypothesized dark matter particles. However, their existences can be inferred from detectable ("visible") particles. The total energy and momentum of these "missing" particles, missing energy and momentum as they are usually called, can be calculated from the energies and momenta of visible particles through the energy-momentum conservation. Despite of their elusive nature, neutrinos are as important as visible particles for the CEPC physics program. About 20% of the Z bosons and

30% of the W bosons decay directly into final states with neutrinos. Searching for Higgs boson decays to dark matter particles is a key physics goal of the Higgs factory.

The excellent energy and momentum resolutions of the CEPC baseline conceptual detector for the visible particles allow for the determinations of missing energy and momentum with good precision. This is demonstrated using $e^+e^- \to ZH$ events with the $Z \to q\bar{q}$ and $H \to ZZ^* \to \nu\bar{\nu}\nu\bar{\nu}$ decays in Figure 10.15 which shows the missing mass distribution. The missing mass, calculated from the missing energy and momentum, is the invariant mass of the system of all undetected particles. The missing mass distribution peaks at the Higgs boson mass as expected and has a resolution of XX% for the light jets. Add a few sentences once the plots are available.

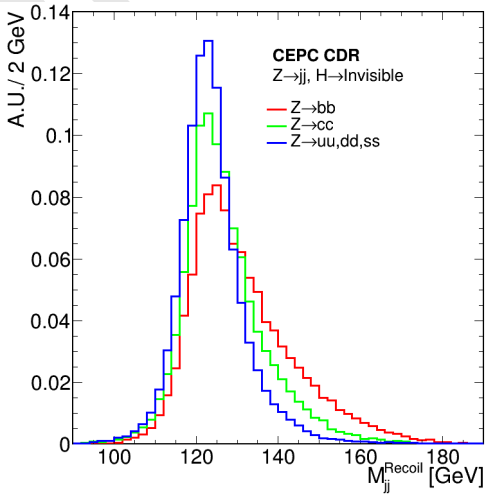

Figure 10.15: The dijet recoil mass (*i.e.*, the missing mass) distributions of $e^+e^- \to ZH$ procexs with the $Z \to q\bar{q}$ and $H \to$ inv decayand (b)

10.2.7 Kaon Identification

Successful identification of charged kaons will greatly benefit the flavor physic program and aid the determinations of jet flavors as well as jet charges. The dE/dx information from the TPC can be used to separate kaons from pions. Assuming a relative dE/dx resolution of 5%, the measurement could lead to 2–4σ separation of π-K for momentum between 2–20 GeV as shown in Figure 10.16.

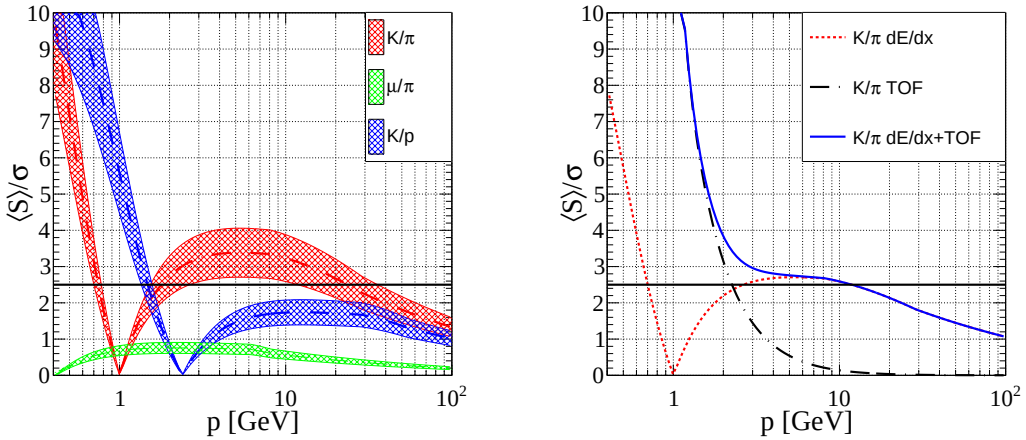

Figure 10.16: Charged particle identifications: (a) K-π, μ-π and K-p separations from the dE/dx measurement in the TPC and (b) the K-π separation from both the dE/dx measurement and the proposed TOF information. The upper boundaries of the bands in (a) are the ideal separations predicted by the Geant4 simulation while the lower boundaries correspond to conservative estimates with a 50% degradation in performance.

The discriminating power of dE/dx vanishes for pions and kaons with their momenta around 1 GeV. Meanwhile, a significant portion of charged particle has energy smaller than 2 GeV at the CEPC. To aid the separation of these low momentum charged particles, it has been proposed to add a Time of Flight (TOF) capability with a 50 ps resolution to the detector design. The ECAL could be instrumented with a few layers of time sensitive readout to provide the TOF information. Using both the TOF and dE/dx information, a separation better than 2σ could be achieved for charged particles with momenta smaller than 20 GeV in the conservative scenario as shown in Figure 10.16(b). For the inclusive $Z \to q\bar{q}$ sample, charged kaons can be identified with an efficiency of 91% and a purity of 94%, integrated over the momentum range of 2–20 GeV.

10.3 Summary

Precise measurements of the Higgs boson properties and the electroweak observables at the CEPC place stringent requirements on the performances of the CEPC detector to identify and measure physics objects such as leptons, photons, τ-leptons, jets and their flavors with high efficiencies and purities as well as high precision. The performances of the CEPC baseline detector have been investigated with full simulation. Benchmark performances are described above and are briefly summarized below:

1 Lepton identification: an efficiency of $> 99.5\%$ with a mis-identification rate of $< 1\%$ for electrons and muons with momenta above 2 GeV, a relative mass resolution of XX% for the $H \to \mu^+\mu^-$ decay;

2 Photon reconstruction: an efficiency of nearly 100% with negligible mis-identification rate from hadronic jets for photons above 5 GeV, relative mass resolution of 2.7% for the $H \to \gamma\gamma$ decay;

3 τ-lepton:

4 A jet energy resolution of 3–5% can be achieved for the energy range relevant at the CEPC, enabling $XX\sigma$ separation of the $W \to q\bar{q}$ and $Z \to q\bar{q}$ decays. The jet energy scale can be measured with an accuracy better than 1%;

5 Jet flavor tagging: efficiency/purity of 80%/90% for b-jets tagging and 60%/60% for c-jets tagging can be achieved for the $Z \to q\bar{q}$ sample of the Z pole run;

6 $K^{\pm}$ identification: kaons can be separated from pions at 2σ for momentum up to 20 GeV, corresponding to efficiency/purity of 95%/95% for identifying kaons in the $Z \to q\bar{q}$ sample integrated over the momentum range of 2–20 GeV.

Though significant progresses have been made in understanding and characterizing the detector performance, the performances can be further enhanced with improved algorithms and better calibrations. Nevertheless, the performances as currently understood are sufficient to fulfill the requirements laid out in Chapter 3 and meet the physics analysis needs as presented in Chapter 11.

References

[1] W. K. et al., *Simulating Multi-Particle Processes at LHC and ILC*, 2011. Eur.Phys.J.C (2011) 1742, arXiv: 0708.4233 [hep-ph].

[2] J. A. et al., *The automated computation of tree-level and next-to-leading order differential cross sections, and their matching to parton shower simulations*, JHEP (2014) 079, arXiv: 1405.0301 [hep-ph].

[3] T. P. Group, *An Introduction to PYTHIA 8.2*, Comput. Phys. Commun. (2015) 159, arXiv:1410.3012 [hep-ph].

[4] S. A. et al., *Geant4 - a simulation toolkit*, Nuclear Instruments and Methods in Physics Research Section A: Accelerators, Spectrometers, Detectors and Associated Equipment (2003) no. 3, .

[5] https://www.mysql.com/.

[6] P. M. de Freitas and H. Videau, *Detector simulation with Mokka/Geant4: Present and future*, .

[7] Y. H. et al., *Software digitizer for high granular gaseous detector*, arXiv: 1405.1286 [physics.ins-det].

[8] F. Gaede, *Track reconstruction at the ILC: the ILD tracking software*, J. Phys. (2014) .

[9] M. Ruan, *Arbor - a new approach of the Particle Flow Algorithm*, arXiv:1403.4784 [physics.ins-det].

[10] M. R. et al., *Reconstruction of physics objects at the Circular Electron Positron Collider*, Eur. Phys. J. C (2018) .

[11] D. et al., *Lepton identification at Particle Flow oriented detector for the future e^+e^- Higgs factories*, Eur. Phys. J. C (2017) , arXiv: 1701.07542 [physics.ins-det].

[12] T. Suehara and T. Tanabe, *LCFIPlus: A Framework for Jet Analysis in Linear Collider Studies*, arXiv: 1506.08371 [physics.ins-det].

[13] J. Therhaag, *TMVA Toolkit for multivariate data analysis in ROOT*, PoS **ICHEP2010** (2010) 510.

CHAPTER 11

BENCHMARK PHYSICS

The historic discovery of a Higgs boson in 2012 by the ATLAS and CMS collaborations [1, 2] and the subsequent studies of the properties of the particle [3–9] indicate the compatibility with the Standard Model (SM) predictions. Although all of the particles in the SM have been discovered, some fundamental questions, e.g. vast difference between the Planck scale and the weak scale, the nature of electroweak phase transition have not been fully understood. The attempt to further address those questions will involve the new physics beyond the SM which could lead a deviation from SM expectations for the precision measurement of the SM. A circular electron positron collider will provide an unique opportunity to have precise measurements of the Higgs, W and Z properties.

The CEPC produces huge statistics of massive SM Bosons. Its physics potential is explored on two different classes of physics benchmarks, the Higgs physics, the precision EW physics. Using the software tools introduced in Section 10.1, the physics potential on Higgs physics is analyzed at full simulation level, see Section 11.1. The accuracies on the EW precision measurements are mainly limited by systematic errors and are estimated in Section 11.2. The synergies of these different physics measurements, the complimentary and comparison to the HL-LHC and other high energy physics programs are discussed in Chapter 12.

11.1 Higgs Boson Physics

The Higgs boson is responsible for the electroweak symmetry breaking. It is the only fundamental scalar particle in the Standard Model observed so far. The discovery of such a particle at the LHC is a major breakthrough on both theoretical and experimental fronts. However, the Standard Model is likely only an effective theory at the electroweak scale.

To explore potential new physics at the electroweak scale and beyond, complementary approaches of direct searches at the energy frontier as well as precision measurements will be needed. The current LHC and the planned HL-LHC have the potential to significantly extend its new physics reach and to measure many of the Higgs boson couplings with precision of a few percents model-dependently.

At the CEPC, in contrast to the LHC, Higgs boson candidate events can be identified through a technique known as the recoil mass method without tagging its decays. Therefore, Higgs boson production can be disentangled from its decay in a model independent way. Moreover, the cleaner environment at a lepton collider allows much better exclusive measurement of Higgs boson decay channels. All of these give the CEPC impressive reach in probing Higgs boson properties. In this section, the results of the current CEPC simulation studies on the precision of the Higgs boson property measurements are summarized. In addition, potential reaches in the CP admixture of the Higgs boson are also estimated. More details can be found in Ref. [10].

11.1.1 Higgs boson production and decay

Production processes for a 125 GeV SM Higgs boson at the CEPC are $e^+e^- \to ZH$ (ZH or Higgsstrahlung), $e^+e^- \to \nu_e\bar{\nu}_e H$ ($\nu\bar{\nu}H$ or W fusion) and $e^+e^- \to e^+e^-H$ (eeH or Z fusion) as illustrated in Figure 11.1. The W and Z fusion processes are collectively referred to as vector-boson fusion (VBF) production.

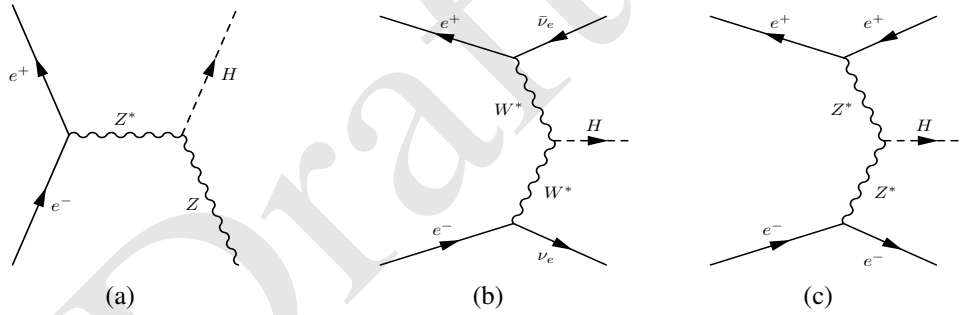

Figure 11.1: Feynman diagrams of the Higgs boson production processes at the CEPC: (a) $e^+e^- \to ZH$, (b) $e^+e^- \to \nu_e\bar{\nu}_e H$ and (c) $e^+e^- \to e^+e^-H$.

The total and individual cross sections for the production of a SM Higgs boson with a mass of 125 GeV as functions of center-of-mass energy are plotted in Figure 11.2 while its decay branching ratios and total width are shown in Table 11.1. As an s-channel process, the cross section of the $e^+e^- \to ZH$ process reaches its maximum at $\sqrt{s} \sim 250$ GeV, and then decreases asymptotically as $1/s$. The VBF production processes are through t-channel exchanges of vector bosons. Their cross sections increase logarithmically as $\ln^2(s/M_V^2)$. Because of the accidental small neutral-current Zee coupling, the VBF cross section is dominated by the W fusion process.

Numerical values of these cross sections at $\sqrt{s} = 240$ GeV are listed in Table 11.2. Because of the interference effects between $e^+e^- \to ZH$ and $e^+e^- \to \nu_e\bar{\nu}_e H$ for the $Z \to \nu_e\bar{\nu}_e$ decay and between $e^+e^- \to ZH$ and $e^+e^- \to e^+e^-H$ for the $Z \to ee$ decay, the cross sections of these processes cannot be separated. The breakdowns in Figure 11.2 and Table 11.2 are for illustration only. The $e^+e^- \to ZH$ cross section shown is from Fig-

ure 11.1(a) only whereas the $e^+e^- \to \nu_e\bar{\nu}_e H$ and $e^+e^- \to e^+e^- H$ cross sections include contributions from their interference with the $e^+e^- \to ZH$ process.

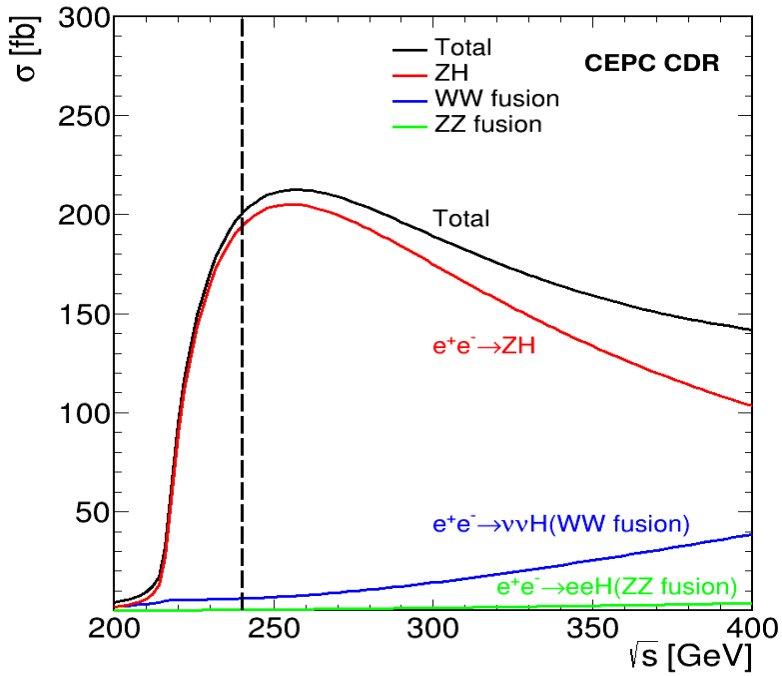

Figure 11.2: Production cross sections of $e^+e^- \to ZH$ and $e^+e^- \to (e^+e^-/\nu\bar{\nu})H$ as functions of $\sqrt{s}$ for a 125 GeV SM Higgs boson. The vertical dashed line indicates $\sqrt{s} = 240$ GeV, the nominal energy of the CEPC Higgs factory.

The CEPC as a Higgs factory is designed to deliver a total of 5.6ab^{-1} integrated luminosity to two detectors in 7 years. Over 10^6 Higgs boson events will be produced during this period. The large statistics, well-defined event kinematics and clean collision environment will enable the CEPC to measure Higgs boson production cross sections as well as its properties (mass, decay width and branching ratios, etc.) with precision far beyond those achievable at the LHC. Compared with hadron collisions, e^+e^- collisions are unaffected by underlying event and pile-up effects. Theoretical calculations are less dependent on higher order QCD radiative corrections. Therefore, more precise tests of theoretical predictions can be performed at the CEPC. The tagging of $e^+e^- \to ZH$ events using the invariant mass of the system recoiling against the Z boson, independent of the Higgs boson decay, is unique to lepton colliders. It provides a powerful tool for the model-independent measurements of the inclusive $e^+e^- \to ZH$ production cross section, $\sigma(ZH)$, and of Higgs boson decay branching ratios. Combinations of these measurements will enable to determine the total Higgs boson decay width and to extract the Higgs boson couplings to fermions and vector bosons, providing sensitive probes to potential new physics beyond the SM.

SM background processes include $e^+e^- \to e^+e^-$ (Bhabha), $e^+e^- \to Z\gamma$ (Z radiative return), $e^+e^- \to WW/ZZ$ (diboson) as well as the single boson production of $e^+e^- \to e^+e^-Z$ and $e^+e^- \to e^+\nu W^-/e^-\bar{\nu}W^+$. Their cross sections and expected numbers of events for an integrated luminosity of 5.6ab^{-1} at $\sqrt{s} = 240$ GeV are shown in Table 11.2 as well. The energy dependence of the cross sections for these and the Higgs boson production processes are shown Figure 3.2. Note that many of these processes can lead to

Table 11.1: Standard model predictions of the decay branching ratios and total width of a 125 GeV Higgs boson. These numbers are obtained from Refs. [11, 12].

Decay mode	Branching ratio	Relative uncertainties
$H \to b\bar{b}$	57.7%	$+3.2\%, -3.3\%$
$H \to c\bar{c}$	2.91%	$+12\%, -12\%$
$H \to \tau^+\tau^-$	6.32%	$+5.7\%, -5.7\%$
$H \to \mu^+\mu^-$	2.19×10^{-4}	$+6.0\%, -5.9\%$
$H \to WW^*$	21.5%	$+4.3\%, -4.2\%$
$H \to ZZ^*$	2.64%	$+4.3\%, -4.2\%$
$H \to \gamma\gamma$	2.28×10^{-3}	$+5.0\%, -4.9\%$
$H \to Z\gamma$	1.53×10^{-3}	$+9.0\%, -8.8\%$
$H \to \gamma\gamma$	8.57%	$+10\%, -10\%$
Γ_H	4.07 MeV	$+4.0\%, -4.0\%$

identical final states and thus can interfere. For example, $e^+e^- \to e^+\nu_e W^- \to e^+\nu_e e^-\bar{\nu}_e$ and $e^+e^- \to e^+e^- Z \to e^+e^-\nu_e\bar{\nu}_e$ have the same final state. Unless otherwise noted, these processes are simulated together to take into account interference effects for the studies presented in this report. Similar to the Higgs boson processes, the breakdowns shown in the table and figure are for illustration only.

11.1.2 Higgs boson tagging

Perhaps the most striking difference between hadron-hadron and e^+e^- collisions is that electron and positron are fundamental particle whereas hadrons are composite particles. Consequently the energy of e^+e^- collisions is known. Therefore through the energy and momentum conservation, the energy and momentum of a Higgs boson can be inferred from other particles in an event without examining the Higgs boson itself. For a Higgsstrahlung event where the Z boson decays to a pair of visible fermions (ff), the mass of the system recoiling against the Z boson, commonly known as the recoil mass, can be calculated assuming the event has a total energy $\sqrt{s}$ and zero total momentum:

$$M^2_{\text{recoil}} = (\sqrt{s} - E_{ff})^2 - p^2_{ff} = s - 2E_{ff}\sqrt{s} + m^2_{ff}. \tag{11.1}$$

Here E_{ff}, p_{ff} and m_{ff} are, respectively, the total energy, momentum and invariant mass of the fermion pair. The M_{recoil} distribution should show a peak at the Higgs boson mass m_H for $e^+e^- \to ZH \to ffH$ and $e^+e^- \to e^+e^-H$ processes, and is expected to be smooth without a resonance structure for background processes in the mass region around 125 GeV. Two important measurements of the Higgs boson can be performed from the M_{recoil} mass spectrum. The Higgs boson mass can be determined from the position of the resonance in the spectrum. The width of the resonance structure is dominated by the beam energy spread (including ISR effects) and energy/momentum resolution of the detector as the natural Higgs boson width is only 4.07 MeV. The best precision of the mass

Table 11.2: Cross sections of Higgs boson production and other SM processes at $\sqrt{s} = 240$ GeV and numbers of events expected in 5.6ab^{-1}. The cross sections are calculated using the Whizard program [13]. Note that there are interferences between the same final states from different processes after the W or Z boson decays. Their treatments are explained in the text.

Process	Cross section	Events in 5.6ab^{-1}
Higgs boson production, cross section in fb		
$e^+e^- \to ZH$	196.2	1.08×10^6
$e^+e^- \to \nu_e\bar{\nu}_e H$	6.19	3.47×10^4
$e^+e^- \to e^+e^- H$	0.28	1.57×10^3
Total	203.7	1.14×10^6
Background processes, cross section in pb		
$e^+e^- \to e^+e^-$ (Bhabha)	24.7	1.4×10^8
$e^+e^- \to q\bar{q}\,(\gamma)$	54.1	2.0×10^8
$e^+e^- \to \mu^+\mu^-\,(\gamma)$ [or $\tau^+\tau^-\,(\gamma)$]	5.3	3.0×10^7
$e^+e^- \to WW$	16.7	9.4×10^7
$e^+e^- \to ZZ$	1.1	6.2×10^6
$e^+e^- \to e^+e^- Z$	4.98	2.8×10^7
$e^+e^- \to e^+\nu W^-/e^-\bar{\nu}W^+$	4.64	2.6×10^7

measurement can be achieved from the leptonic $Z \to \ell\ell\,(\ell = e, \mu)$ decays. The height of the resonance is a measure of the Higgs boson production cross section $\sigma(ZH)$[1]. Through a fit to the M_{recoil} spectrum, the $e^+e^- \to ZH$ event yield, and therefore $\sigma(ZH)$, can be extracted, independent of Higgs boson decays. Higgs boson decay branching ratios can then be determined by measuring the ZH cross sections of individual Higgs boson decay modes. The recoil mass spectrum has been investigated for both leptonic and hadronic Z boson decays as presented below.

The leptonic Z decay is ideal for studying the recoil mass spectrum of the $e^+e^- \to ZX$ events. The decay is easily identifiable and the lepton momenta can be precisely measured. Figure 11.3 shows the reconstructed recoil mass spectra of $e^+e^- \to ZX$ candidates for the $Z \to \mu\mu$ and $Z \to ee$ decay modes. The analyses are based on the full detector simulation for the signal events and on the fast detector simulation for background events. The event selections are entirely based on the information of the two leptons, independent of the final states of Higgs boson decays. This approach is essential for the measurement of the inclusive $e^+e^- \to ZH$ production cross section and the model-independent determination of the Higgs boson branching ratios. SM processes with at least 2 leptons in their final states are considered as backgrounds. As shown in Figure 11.3, the analysis has a good signal-to-background ratio. The long high-mass tail is largely due to the initial-state radiation. Leading background contributions after the selection are from ZZ, WW and $Z\gamma$ events. Compared to the $Z \to \mu\mu$ decay, the analysis of the $Z \to ee$ decay

[1]For the $Z \to ee$ decay, there will be a small contribution from $e^+e^- \to e^+e^- H$ production.

suffers from additional and large background contributions from Bhabha and single boson production.

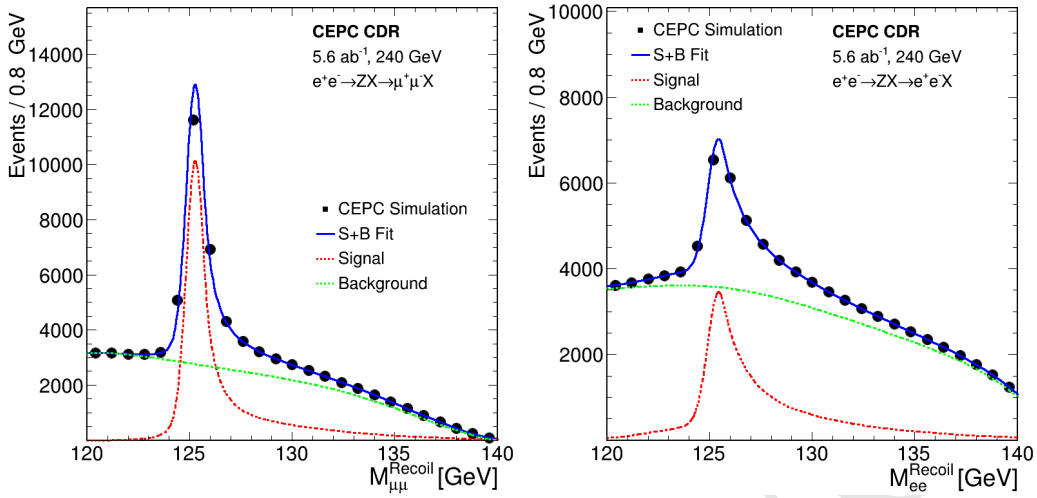

(a) (b)

Figure 11.3: The inclusive recoil mass spectra of $e^+e^- \to ZX$ candidates of (a) $Z \to \mu\mu$ and (b) $Z \to ee$ from an integrated luminosity of 5.6 ab^{-1}. No attempt to identify X is made.

The recoil mass technique can also be applied to the hadronic Z boson decays ($Z \to q\bar{q}$) of the $e^+e^- \to ZX$ candidates. This analysis benefits from a larger $Z \to q\bar{q}$ decay branching ratio, but suffers from worse jet energy resolution compared with the track momentum and electromagnetic energy resolutions. In addition, ambiguity in selecting jets from the $Z \to q\bar{q}$ decay, particularly in events with hadronic decays of the Higgs boson, can degrade the analysis performance and also introduce model dependences. Therefore, the measurement is highly dependent on the detector performance and the jet clustering algorithm. Following the same approach as the ILC study [14], an analysis based on the fast simulation has been performed. After the event selection, main backgrounds arise from $Z\gamma$'s and WW production.

11.1.3 Measurements of $\sigma(ZH)$ and m_H

The inclusive $e^+e^- \to ZH$ production cross section $\sigma(ZH)$ and Higgs boson mass m_H can be extracted from fits to the recoil mass distributions of the $e^+e^- \to ZX \to (\ell^+\ell^-/q\bar{q})X$ candidates. For the leptonic $Z \to \ell\ell$ decays, the recoil mass distribution of the signal process $e^+e^- \to ZH$ (and also $e^+e^- \to e^+e^-H$ in case of the $Z \to ee$ decay) is modeled with a Crystal Ball function [15] whereas the total background is modeled with a polynomial function in the fit. As noted above, the recoil mass distribution is insensitive to the intrinsic Higgs boson width if it were as small as predicted by the SM. The Higgs boson mass can be determined with precision of 6.5 MeV and 14 MeV from the $Z \to \mu\mu$ and $Z \to ee$ decay modes, respectively. In combination, an uncertainty of 5.9 MeV can be achieved. $e^+e^- \to ZX \to q\bar{q}X$ events contribute little to the precision of the m_H measurement due to the poor $Z \to q\bar{q}$ mass resolution, but dominates the precision of the $e^+e^- \to ZH$ cross section measurement benefiting from its large statistics. A relative precision of 0.65% on $\sigma(ZH)$ is predicted from a simple event counting analysis. In com-

parison, the corresponding precision from the $Z \to ee$ and $Z \to \mu\mu$ decays is estimated to be 1.5% and 0.9%, respectively. The combined precision of the three measurements is 0.5%.

For the model-independent measurement of $\sigma(ZH)$, event selections independent of the Higgs boson decays are essential. However, additional selections using the Higgs boson decay information can be applied to improve the Higgs boson mass measurement. This will be particularly effective in suppressing the large backgrounds in the $Z \to ee$ and $Z \to q\bar{q}$ decay modes. This improvement is not implemented in the current study.

11.1.4 Analyses of individual Higgs boson decay modes

Different decay modes of the Higgs boson can be identified through their unique signatures, enabling the measurements of production rates for these decays. Simulation studies of the CEPC baseline conceptual detector have been performed for the Higgs boson decay modes of $H \to b\bar{b}/c\bar{c}/gg$, $H \to WW^*$, $H \to ZZ^*$, $H \to \gamma\gamma$, $H \to Z\gamma$, $H \to \tau^+\tau^-$, $H \to \mu^+\mu^-$ and $H \to \text{inv}$. The large numbers of the decay modes of the H, W and Z boson as well as the τ-lepton lead to a very rich variety of event topologies. This complexity makes it impractical to investigate the full list of final states descending from the Higgs boson decays. Instead, a limited number of final states of individual Higgs boson decay mode has been considered. In most cases, the dominant backgrounds come from SM diboson production and Z production with initial or final state radiations.

The studies are optimized for the dominant ZH process, however the $e^+e^- \to \nu_e\bar{\nu}_e H$ and $e^+e^- \to e^+e^- H$ processes are included whenever applicable. The production cross sections of individual decay mode, $\sigma(ZH) \times \text{BR}$, are extracted. Combined with the inclusive $\sigma(ZH)$ measurement, these measurements will permit the determinations of the Higgs boson decay branching ratios in a model-independent way. Main features of these studies are described below and their results are presented in Section 11.1.5.

For a SM Higgs boson with a mass of 125 GeV, nearly 70% of all Higgs bosons decay into a pair of jets: b-quarks (57.7%), c-quarks (2.9%) and gluons (8.6%). While the $H \to b\bar{b}$ decay has been observed at the LHC, the $H \to c\bar{c}$ and $H \to gg$ decays are difficult, if not impossible, to be conclusively identified even at the HL-LHC due to large backgrounds. In comparison, these three decays can be isolated and studied at the CEPC in detail. This is important as the $H \to c\bar{c}$ decay is likely the only vehicle for investigating the Higgs boson couplings to the second-generation quarks. The study considers all Z boson decay modes except $Z \to \tau^+\tau^-$. The $H \to b\bar{b}/c\bar{c}/gg$ candidates are identified through the dijet invariant mass, or the recoil mass of the visible Z boson decays, or both. Jet flavor tagging is employed to statistically separate $H \to b\bar{b}, c\bar{c}, gg$ contributions. Figure 11.4(a) shows the reconstructed recoil mass distribution of the $Z \to \mu\mu$ decay. Compared with the distribution of inclusive Higgs boson decays shown in Fig. 11.3(a), the background is significantly reduced through the identification of specific Higgs boson decay modes. Figure 11.4(b) is the dijet mass distribution of the $Z \to \nu\bar{\nu}$ decay, showing excellent signal-to-background ratio and good dijet mass resolution.

The W-fusion $e^+e^- \to \nu_e\bar{\nu}_e H$ process has a cross section of 3.2% of that of the ZH process at $\sqrt{s} = 240$ GeV in the SM. This process has been explored with the $H \to b\bar{b}$ decay mode. The analysis suffers from large backgrounds from $ZH \to \nu\bar{\nu}b\bar{b}$ as it has the same signature. However, the $\nu\bar{\nu}H$ and $Z(\nu\bar{\nu})H$ contributions can be separated through the exploration of their kinematic differences. Higgs bosons are produced with different

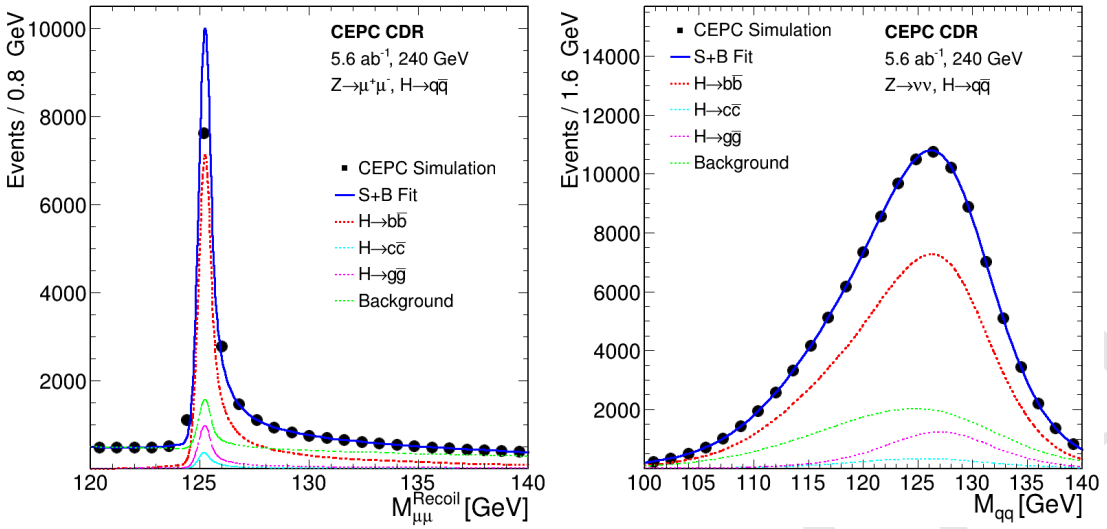

(a) (b)

Figure 11.4: (a) $e^+e^- \to ZH$ production with $H \to b\bar{b}/c\bar{c}/gg$: distributions of (a) the recoil mass of $Z \to \mu\mu$ and (b) the dijet invariant mass distribution for the $Z \to \nu\bar{\nu}$ decay. Contributions from other Higgs boson decays are included in the background.

polar angular distributions. Moreover, the recoil mass distribution of the $b\bar{b}$ system should exhibit a resonance structure at the Z boson mass for $Z(\nu\bar{\nu})H$ and show a continuum spectrum for $e^+e^- \to \nu_e\bar{\nu}_e H$. The $\nu\bar{\nu}H$ contribution is extracted through a fit to the two-dimensional distribution of the cosine of the polar angle and the recoil mass of the $b\bar{b}$ system.

The $H \to WW^*$ and $H \to ZZ^*$ decays are among the first decay modes studied at the LHC and are critical for the discovery of the Higgs boson thanks to the clean leptonic signatures of the W and Z boson decays. However due to their large backgrounds, hadronic final states of the $H \to WW^*$ and $H \to ZZ^*$ decays are out of reach at the LHC despite of their larger branching ratios than leptonic final states. This is not the case at the CEPC. In fact, most of the sensitivities to these two Higgs boson decay modes at the CEPC are expected to be from final states with one or both vector bosons decay hadronically. A number of selected final states have been studied. For $H \to WW^*$, the final states included are $Z \to \ell\ell$, $H \to WW^* \to \ell\nu\ell\nu, \ell\nu q\bar{q}$; $Z \to \nu\bar{\nu}$, $H \to WW^* \to \ell\nu\ell\nu, q\bar{q}q\bar{q}$ and $Z \to q\bar{q}$, $H \to WW^* \to q\bar{q}q\bar{q}$. For $H \to ZZ^*$, they are $Z \to \mu\mu$, $H \to ZZ^* \to \nu\bar{\nu}q\bar{q}$ and $Z \to \nu\bar{\nu}$, $H \to ZZ^* \to \ell\ell q\bar{q}$. A combination of the recoil mass, the invariant mass of the $W \to q\bar{q}$ and $Z \to q\bar{q}$ decay as well as the leptonic decay signatures of W and Z bosons are used to identify ZH events. Some of these analyses suffer from large backgrounds as shown, for example, in Figure 11.5(a), while others are almost background free as illustrated in Figure 11.5(b).

The $H \to \gamma\gamma$ and $H \to Z\gamma$ decays have small branching ratios in the SM as they proceed through W boson and top quark triangular loops. CEPC's sensitivities to these two decay modes have been examined.The $H \to \gamma\gamma$ analysis of ZH production suffers from large $e^+e^- \to (Z/\gamma^*)\gamma\gamma$ background where γ's arise from the initial and final state radiations. All Z boson decay modes other than the $Z \to ee$ decay are considered for the $H \to \gamma\gamma$ studies. The ZH production with $Z \to ee$ has additional large backgrounds

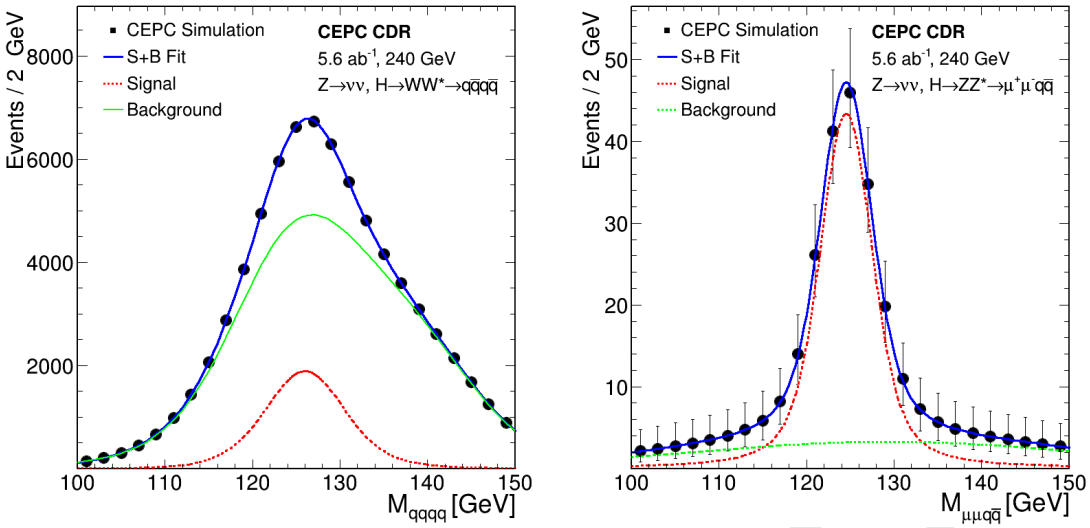

Figure 11.5: (a) $e^+e^- \to ZH$ production with $H \to WW^* \to q\bar{q}q\bar{q}$ and $Z \to \nu\bar{\nu}$: the invariant mass of the 4-jet system. (b) $e^+e^- \to ZH$ production with $H \to ZZ^* \to \mu^+\mu^- q\bar{q}$ and $Z \to \nu\bar{\nu}$: the invariant mass distribution of the dimuon and dijet system. Contributions from other Higgs boson decays are included in the background.

from the Bhabha process. As shown in Figure 11.6(a), the $H \to \gamma\gamma$ signal is expected to appear as a resonance over a smooth background in the diphoton mass distribution. ZH production with $H \to Z\gamma$ decay will lead to events with two on-shell Z bosons and one photon. The $H \to Z\gamma$ study targeted the signal process of $ZH \to ZZ\gamma \to \nu\bar{\nu}q\bar{q}\gamma$. In this final state, the energy and momentum of the $\nu\bar{\nu}$ system can be calculated from the visible energy and momentum of the event. The mass difference between the Higgs boson candidate and the candidate of the associated Z boson can then be calculated. For signal events, this mass difference is expected to be $m_H - m_Z \sim 35$ GeV for correct combinations as shown in Figure 11.7(b). For background events and wrong combinations of signal events, the distribution should be smooth.

Leptonic Higgs boson decays are accessible for $H \to \tau^+\tau^-$ and $H \to \mu^+\mu^-$ at the CEPC. Simulation studies of ZH production with the $H \to \tau^+\tau^-$ decay have been performed for all Z boson decay modes except $Z \to ee$. A boosted decision tree utilizing particle multiplicity and their separations is used to select di-tau candidates from $H \to \tau^+\tau^-$. An impact-parameter based variable of the leading track of the di-tau candidate is used as the final discriminant for the signal extraction. An example distribution of this variable for $Z \to \nu\bar{\nu}$ is shown Figure 11.7(a). Similar to $H \to \gamma\gamma$, the $H \to \mu^+\mu^-$ decay also allows the reconstruction of the Higgs boson with high resolution. The signal is expected to appear as a resonance structure at m_H over the smooth background in the dimuon mass spectrum. Good dimuon mass resolution is essential for the performance. For this study, all Z boson decay modes are considered. Figure 11.7(b) shows the dimuon mass distribution combining all Z boson decay modes.

In the SM, the Higgs boson can decay invisibly via $H \to ZZ^* \to \nu\bar{\nu}\nu\bar{\nu}$ with a branching ratio of 1.06×10^{-3}. In many extensions to the SM, the Higgs boson can decay directly to invisible particles with a significantly higher branching ratio. At the CEPC,

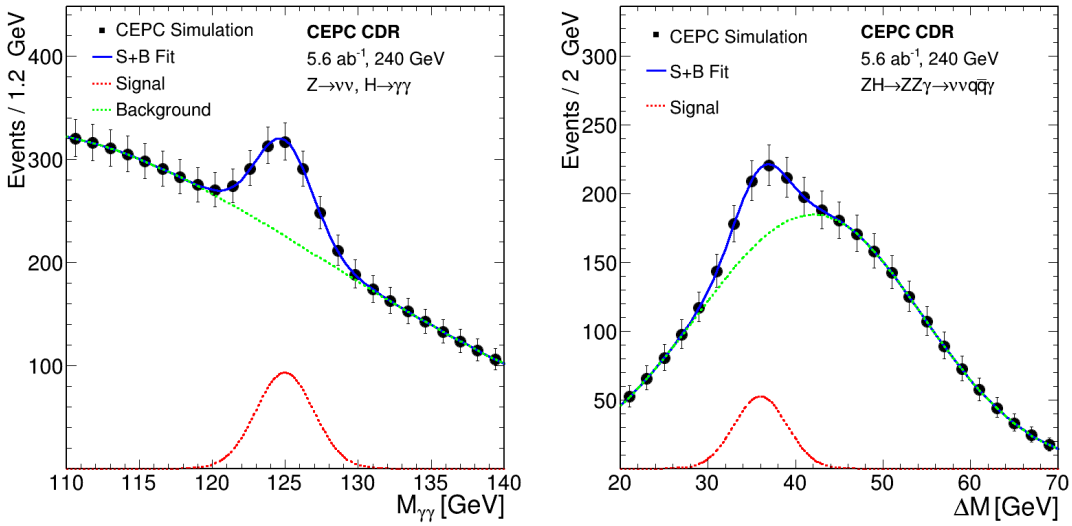

(a) (b)

Figure 11.6: (a) $e^+e^- \to ZH$ production with $H \to \gamma\gamma$: the invariant mass distribution of the selected photon pairs for $Z \to \nu\bar{\nu}$. (b) $e^+e^- \to ZH$ production with $H \to Z\gamma$: the distribution of the mass difference between the reconstructed $Z\gamma$ and Z system.

the $H \to \text{inv}$ decay can be directly identified using the recoil mass information of the Z boson decays. The sensitivity to ZH production with $H \to \text{inv}$ is estimated for $Z \to \ell\ell$ and $Z \to q\bar{q}$ decays. The SM $H \to ZZ^* \to \nu\bar{\nu}\nu\bar{\nu}$ decay is used to model the $H \to \text{inv}$ decay in both the SM and its extension. This is made possible by the fact that the Higgs boson is narrow scalar in the SM so that the production and decay are factorized.

11.1.5 Combination of individual analyses

With the measurements of inclusive cross section $\sigma(ZH)$ and the cross sections of individual Higgs boson decay mode $\sigma(ZH) \times \text{BR}$, the Higgs boson decay branching ratio, BR, can be extracted. Most of the systematic uncertainties associated with the measurement of $\sigma(ZH)$ cancels in this procedure. A maximum likelihood fit is used to estimate the precision on BRs. For a given Higgs boson decay mode, the likelihood has the form:

$$L(\text{BR}, \theta) = \text{Poisson}\left[N^{\text{obs}} \middle| N^{\text{exp}}(\text{BR}, \theta)\right] \cdot G(\theta), \tag{11.2}$$

where BR is the parameter of interest and θ represent nuisance parameters associated with systematic uncertainties. N^{obs} is the number of the observed events, $N^{\text{exp}}(\text{BR}, \theta)$ is the expected number of events, and $G(\theta)$ is a set of constraints on the nuisance parameters within their estimated uncertainties. The number of expected events is the sum of signal and background events. The number of signal events is calculated from the integrated luminosity, the $e^+e^- \to ZH$ cross section $\sigma(ZH)$ measured from the recoil mass method, Higgs boson branching ratio BR, the event selection efficiency ϵ. The number of the expected background events, N^b, is estimated from Monte Carlo samples. Thus

$$N^{\text{exp}}(\text{BR}, \theta) = \text{Lumi}(\theta^{\text{lumi}}) \times \sigma_{ZH}(\theta^{\sigma}) \times \text{BR} \times \epsilon(\theta^{\epsilon}) + N^b(\theta^b), \tag{11.3}$$

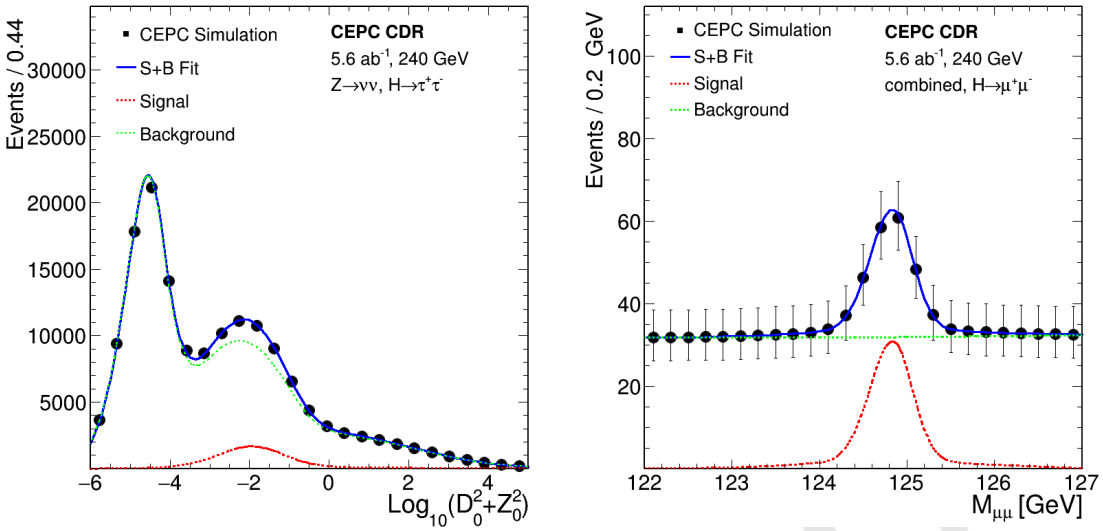

(a) (b)

Figure 11.7: (a) $e^+e^- \to ZH$ production with $H \to \tau^+\tau^-$: the distribution of impact parameter variable of the leading track of the di-tau candidates for the $Z \to \nu\bar{\nu}$ decay mode. Contributions from other Higgs boson decays are included in the background. (b) $e^+e^- \to ZH$ production with $H \to \mu^+\mu^-$: the invariant mass distribution of the selected muon pairs combining all Z boson decay modes.

where θ^X ($X = \text{lumi}, \sigma$, ϵ and b) are the nuisance parameters of their corresponding parameters or measurements. Even with 10^6 Higgs boson events, statistical uncertainties are expected to be dominant and thus systematic uncertainties are not taken into account for the current studies. Thus the nuisance parameters are fixed to their nominal values.

Table 11.3 summarizes the estimated precision of Higgs boson property measurements, combining all studies described above and taking into account cross-feeds between different Higgs boson production processes and decay modes. For the leading Higgs boson decay modes, namely $b\bar{b}$, $c\bar{c}$, gg, WW^*, ZZ^* and $\tau^+\tau^-$, percent level precision are expected. The best achievable statistical uncertainties for 5.6 ab^{-1} are 0.27% for $\sigma(e^+e^- \to ZH) \times \text{BR}(H \to b\bar{b})$ and 0.5% for $\sigma(e^+e^- \to ZH)$. Even for these measurements, statistics is likely the dominant source of uncertainties. Systematic uncertainties from the efficiency/acceptance of the detector, the luminosity and the beam energy determination are expected to be small. The integrated luminosity can be measured with a 0.1% precision, a benchmark already achieved at the LEP [16], and can be potentially improved in the future. The center-of-mass energy will be known better than 1 MeV, resulting negligible uncertainties on the theoretical cross section predictions and experimental recoil mass measurements.

11.1.6 Higgs boson width

The Higgs boson width is of special interest as it is sensitive to BSM physics in Higgs boson decays that are not directly detectable or searched for. However, the 4.07 MeV width predicted by the SM is too small to be measured with a reasonable precision from the distributions of either the invariant mass of the Higgs boson decay products or the recoil mass of the system produced in association with the Higgs boson. Unique to lepton

Table 11.3: Estimated precision of Higgs boson property measurements expected from a CEPC dataset of 5.6 ab^{-1} at $\sqrt{s} = 240$ GeV. All precision are relative except for m_H and $\mathrm{BR}(H \to \mathrm{inv})$ for which Δm_H and 95% CL upper limit on the BSM physics contribution are quoted respectively. The $e^+e^- \to e^+e^-H$ cross section is too small to be measured with a reasonable precision.

Property	Estimated Precision
m_H	5.9 MeV
Γ_H	3.3%
$\sigma(ZH)$	0.5%
$\sigma(\nu\bar{\nu}H)$	3.0%

Decay mode	$\sigma(ZH) \times \mathrm{BR}$	BR
$H \to b\bar{b}$	0.27%	0.56%
$H \to c\bar{c}$	3.26%	3.30%
$H \to gg$	1.27%	1.36%
$H \to WW^*$	0.98%	1.10%
$H \to ZZ^*$	5.09%	5.11%
$H \to \gamma\gamma$	6.84%	6.86%
$H \to Z\gamma$	16%	16%
$H \to \tau^+\tau^-$	0.82%	0.96%
$H \to \mu^+\mu^-$	17%	17%
$H \to \mathrm{inv}$	–	$< 0.32\%$

colliders, the width can be determined from the measurements of Higgs boson production cross sections and its decay branching ratios. This is because the inclusive $e^+e^- \to ZH$ cross section $\sigma(ZH)$ can be measured from the recoil mass distribution, independent of Higgs boson decays.

Measurements of $\sigma(ZH)$ and BR's have been discussed in above. Combining these measurements, the Higgs boson width can be calculated in a model-independent way:

$$\Gamma_H = \frac{\Gamma(H \to ZZ^*)}{\mathrm{BR}(H \to ZZ^*)} \propto \frac{\sigma(ZH)}{\mathrm{BR}(H \to ZZ^*)} \tag{11.4}$$

Here $\Gamma(H \to ZZ^*)$ is the partial width of the $H \to ZZ^*$ decay. Because of the small expected $\mathrm{BR}(H \to ZZ^*)$ value for a 125 GeV Higgs boson (2.64% in the SM), the precision of Γ_H is limited by the $H \to ZZ^*$ statistics. It can be improved using decay final states with expected large BR values, for example the $H \to b\bar{b}$ decay:

$$\Gamma_H = \frac{\Gamma(H \to b\bar{b})}{\mathrm{BR}(H \to b\bar{b})} \tag{11.5}$$

$\Gamma(H \to b\bar{b})$ can be independently extracted from the cross section of the W fusion process:

$$\sigma(\nu\bar{\nu}H \to \nu\bar{\nu}\, b\bar{b}) \propto \Gamma(H \to WW^*) \cdot \mathrm{BR}(H \to b\bar{b}) = \Gamma(H \to b\bar{b}) \cdot \mathrm{BR}(H \to WW^*) \tag{11.6}$$

Thus the Higgs boson total width

$$\Gamma_H = \frac{\Gamma(H \to b\bar{b})}{\mathrm{BR}(H \to b\bar{b})} = \frac{\Gamma(H \to WW^*)}{\mathrm{BR}(H \to WW^*)} \propto \frac{\sigma(\nu\bar{\nu}H)}{\mathrm{BR}(H \to WW^*)} \tag{11.7}$$

Here $\mathrm{BR}(H \to b\bar{b})$ and $\mathrm{BR}(H \to WW^*)$ are measured from the $e^+e^- \to ZH$ process. The limitation of this method is the precision of the $\sigma(e^+e^- \to \nu_e\bar{\nu}_e H)$ measurement.

need to check the numbers. The expected precision on Γ_H is 5.1% from the measurements of $\sigma(ZH)$ and $\mathrm{BR}(H \to ZZ^*)$ and is 3.4% from the measurements of $\sigma(\nu\bar{\nu}H)$ and $\mathrm{BR}(H \to WW^*)$. The former is dominated by the precision of the $\mathrm{BR}(H \to ZZ^*)$ measurement while the latter by the $\sigma(\nu\bar{\nu}H)$ measurement. The combined Γ_H precision of the two measurements is 3.2%, taking into account correlations between the two measurements.

11.1.7 Higgs Boson Coupling Measurements

To understand the implications of the predicted measurement precision shown in Table 11.3 on possible new physics models, one would need to translate them into constraints on the parameters in the Lagrangian. This is frequently referred to as Higgs boson coupling measurement, even though this way of phrasing it can be misleading as discussed in the following.

There are different ways of presenting the constraints. Before going into CEPC results, we briefly comment on the reasons behind choices of schemes in this section. First, the goal of theory interpretation is different from analyzing actual data, where a lot of detailed work will be done to derive the extended sets of observables. Instead, obtaining a broad brushed big picture of the basic capability of the Higgs boson coupling measurement at the CEPC is the goal. Ideally, the presentation would be simple with a intuitive connection with the observables. The presentation would ideally also be free of underlying model assumptions. In addition, it would be convenient if the result presentation can be interfaced directly with higher order computations, RGE evolutions, and so on. However, achieving all of these goals simultaneously is not possible. Two of the most popular and balanced approaches are the so-called κ-framework and the Effective Field Theory (EFT) analysis. As discussed in more detail later, none of these is perfect. At the same time, neither of these is wrong as long as one is careful not to over interpreting the result. Another important aspect of making projections on the physics potential of a future experiment is that they will be compared with other possible future experiments. Hence, CEPC follows the most commonly used approaches to facilitate such comparisons.

Motivated by these arguments, in the following, CEPC presents the projections using both the κ-framework and EFT approach. In the later part of this section, Higgs physics potential beyond coupling determination will be discussed.

11.1.7.1 Coupling fits in the κ-framework

The Standard Model makes specific predictions for the Higgs boson couplings to the SM fermions, $g(Hff;\mathrm{SM})$, and to the SM gauge bosons $g(HVV;\mathrm{SM})$. [2] In the κ-framework, the potential deviations are parameterized by

$$\kappa_f = \frac{g(Hff)}{g(Hff;\mathrm{SM})}, \quad \kappa_V = \frac{g(HVV)}{g(HVV;\mathrm{SM})}, \tag{11.8}$$

with $\kappa_i = 1$ indicating agreement with the SM prediction.

In addition to couplings which are present at tree level, the Standard Model also predicts effective couplings $H\gamma\gamma$ and Hgg, in terms of other SM parameters. Changes in the gluon and photon couplings can be induced by the possible shifts in the Higgs boson couplings described above. In addition, these couplings can also be altered by loop contributions from new physics states. Hence, these couplings will be introduced as two independent couplings, with their ratios to the SM predictions denoted as κ_γ and κ_g.

Furthermore, it is possible that the Higgs boson can decay directly into new physics particles. In this case, two type of new decay channels will be distinguished:

1. Invisible decay. This is a specific channel in which Higgs boson decay into invisible particles. This can be searched for and, if detected, measured.

2. Exotic decay. This includes all the other new physics channels. Whether they can be observed, and, if so, to what precision, depends sensitively on the particular final states. In one extreme, they can be very distinct and can be measured very well. In another extreme, they can be in a form which is completely swamped by the background. Whether postulating a precision for the measurement of the exotic decay or treating it as an independent parameter (essentially assuming it can not be measured directly) is an assumption one has to make. In the latter case, it is common to use the total width Γ_H as an equivalent free parameter.[3]

In general, possible deviations of all Standard Model Higgs boson couplings should be considered. However, in the absence of obvious light new physics states with large couplings to the Higgs boson and other SM particles, a very large deviation ($> \mathcal{O}(1)$) is unlikely. In the case of smaller deviations, the Higgs boson phenomenology will not be sensitive to the deviations [17] κ_e, κ_u, κ_d and κ_s. Therefore, they will not be considered here and set to be their SM values.

The CEPC will not be able to directly measure the Higgs boson coupling to top quarks. A deviation of this coupling from its SM value does enter $H\gamma\gamma$ and Hgg amplitudes. However, this can be viewed as parametrized by κ_γ and κ_g already. Therefore, we will not include κ_t as an independent parameter. Hence, the following set of 10 independent parameters is considered:

$$\kappa_b,\ \kappa_c,\ \kappa_\tau,\ \kappa_\mu,\ \kappa_Z,\ \kappa_W,\ \kappa_\gamma,\ \kappa_g,\ \mathrm{BR}_{\mathrm{inv}},\ \Gamma_H. \tag{11.9}$$

Several assumptions can be made that can lead to a reduced number of parameters (see also [18, 19]). It can be reduced to a 7-parameter set, by assuming lepton universality,

[2] For the discussion of coupling fits and their implications, "H" is used to denoted the 125 GeV Higgs boson.
[3] Total width is a very useful parameter in understanding and deriving parameter precisions in the κ-scheme.

and the absence of exotic and invisible decays (excluding $H \to ZZ^* \to \nu\bar{\nu}\nu\bar{\nu}$) [18, 20]:

$$\kappa_b,\ \kappa_c,\ \kappa_\tau = \kappa_\mu,\ \kappa_Z,\ \kappa_W,\ \kappa_\gamma,\ \kappa_g. \tag{11.10}$$

This is useful for hadron collider studies since it can not measure the Higgs boson total width with precision; it is more useful for models in which this assumption is satisfied.

There are some pros and cons of the κ-framework. κ_is give a simple and intuitive parameterization of potential deviations. It has a direct connection with the observables shown in Table 11.3. It does cover a lot of possible modifications of the coupling. At the same time, κ-framework has its limitations. Strictly speaking, it should not be understood as modifying the SM renormalizable Lagrangian by a multiplicative factor. For instance, individual κ modifications violates gauge invariance. The higher order corrections in the κ framework is not easily defined. κ_is do not summarize all possible effects of new physics neither. For example, in addition to the overall size, potential new physics can also introduce form factors which can change the kinematics of particles connected to a vertex. Manifestations of this effect will be seen in the discussion of the EFT approach. It is useful to pause here and compare with the EFT scheme introduced in detail in the next subsection. The EFT scheme relates κ_Z and κ_W, and further expanse them into three different Lorentz structures. In addition, some of these higher dimensional HVV coupling are also in connection with κ_γ and anomalous trilinear gauge couplings. The current EFT scheme does not include important new degree of freedom $\mathrm{BR}_{\mathrm{inv}}$ and Γ_H as independent parameters. Overall, κ-framework does capture the big picture of the capability of precision Higgs boson measurement at CEPC. It is useful as long as we understand its limitation.

The LHC and especially the HL-LHC will provide valuable and complementary information about the Higgs boson properties. For example, the LHC is capable of directly measure the ttH process [21, 22]. In addition, the LHC could use differential cross sections to differentiate top-loop contributions and other heavy particle-loop contributions to the Higgs boson to gluon coupling [23–26], and similarly to separate contributions from different operators to the Higgs boson to vector boson couplings [27]. For the purpose of the coupling fit in the κ-framework, the LHC with its large statistics, helps improving precision on rare processes such as Higgs to diphoton couplings. Note that a large portion of the systematics intrinsic to a hadron collider would be canceled by taking ratios of measured cross sections. For example, combining the ratio of the rates $pp \to H \to \gamma\gamma$ and $pp \to H \to ZZ^*$ and the measurement of HZZ coupling at the CEPC can significantly improve the measurement of κ_γ. These are the most useful inputs from the LHC to combine with the CEPC. Similar studies of combination with the LHC for the ILC can be found in Refs. [28–32].

The 10-parameter fit and the 7-parameter fit for CEPC with integrate luminosity of $5.6\mathrm{ab}^{-1}$ are shown in Table 11.4. In addition, the combinations with expectations (optimistically assuming no theoretical uncertainties) from the HL-LHC from Ref. [33] are shown in the same tables as well.[4] We assume the HL-LHC will operate at 14 TeV center-of-mass energy and accumulate an integrated luminosity of 3000 fb^{-1}.

The CEPC Higgs boson properties measurements mark a giant step beyond the HL-LHC. First of all, in contrast to the LHC, a lepton collider Higgs factory is capable of

[4]We note here that the LHC and the CEPC have different sources of theoretical uncertainties, for detailed discussion, see Refs. [19, 20, 34–36].

Table 11.4: Coupling measurement precision in percentage from the 7-parameter fit and 10-parameter fit described in the text for the CEPC, and corresponding results after combination with the HL-LHC. All the numbers refer to are relative precision except for $\mathrm{BR}_{\mathrm{inv}}^{\mathrm{bsm}}$ of beyond standard model for which 95% CL upper limit are quoted respectively. Some entries are left vacant for the 7-parameter fit to stress them being dependent parameter under the fitting assumptions of the 7-parameter fit scheme.

	10-parameter fit		7-parameter fit	
	CEPC	+HL-LHC	CEPC	+HL-LHC
Γ_H	3.3	2.6	–	–
κ_b	1.6	1.3	1.6	1.2
κ_c	2.3	2.0	2.3	2.0
κ_g	1.7	1.3	1.7	1.3
κ_W	1.5	1.1	1.4	1.1
κ_τ	1.6	1.2	1.5	1.2
κ_Z	0.25	0.25	0.16	0.15
κ_γ	4.0	1.7	3.9	1.6
κ_μ	8.6	5.0	–	–
$\mathrm{BR}_{\mathrm{inv}}^{\mathrm{bsm}}$	0.33	0.33	–	–

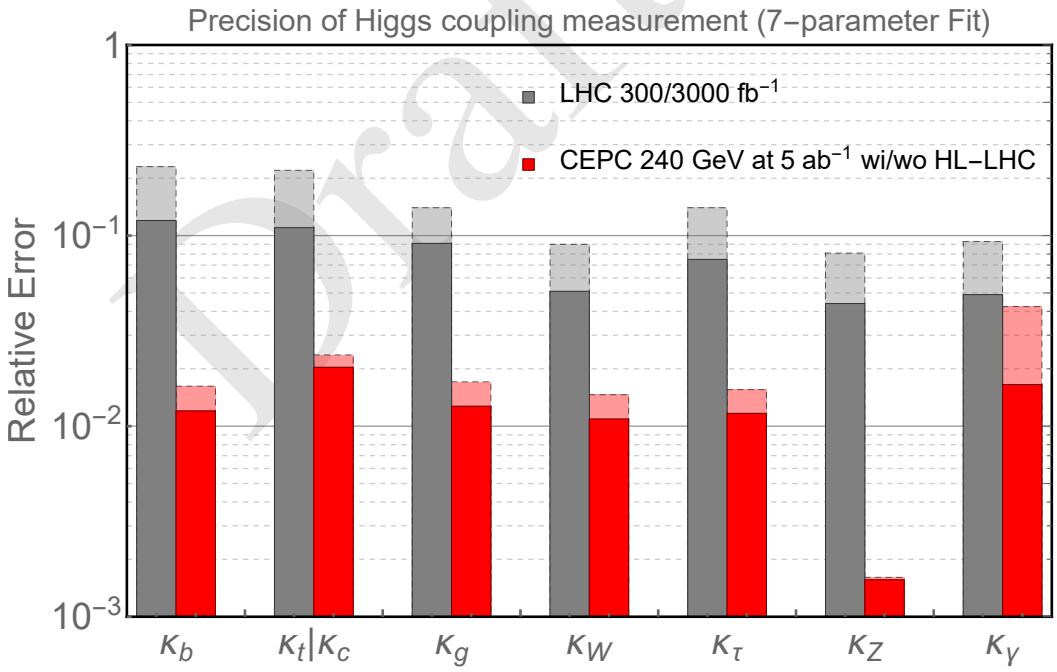

Figure 11.8: The 7 parameter fit result, and comparison with the HL-LHC [33]. The projections for the CEPC at 240 GeV with $5.6\mathrm{ab}^{-1}$ integrated luminosity are shown. The CEPC results without combination with the HL-LHC input are shown with dashed edges. The LHC projections for an integrated luminosity of 300 fb^{-1} are shown in dashed edges.

measuring the absolute width and coupling strengths of the Higgs boson. A comparison with the HL-LHC is only possible with model dependent assumptions. One of such com-

parison is within the framework of a 7-parameter fit, shown in Fig. 11.8. Even with this set of restrictive assumptions, the advantage of the CEPC is still significant. The measurement of κ_Z is more than a factor of 10 better. The CEPC can also improve significantly on a set of channels which suffers from large background at the LHC, such as κ_b, κ_c, and κ_g. Note that this is in comparison with the HL-LHC projection with aggressive assumptions about systematics. Such uncertainties are typically under much better control at lepton colliders. Within this 7-parameter set, the only coupling which the HL-LHC can give a competitive measurement is κ_γ, for which the CEPC's accuracy is limited by statistics. This is also the most valuable input that the HL-LHC can give to the Higgs boson coupling measurement at the CEPC, which underlines the importance of combining the results of these two facilities.

The direct search limit for BSM Higgs boson decay into invisibles $\mathrm{BR}_{\mathrm{inv}}^{\mathrm{bsm}}$ is well motivated, in close connection to dark sectors. The CEPC with $5.6\mathrm{ab}^{-1}$ can measure this to a high accuracy as 95% upper limit 0.31%, as shown in Table 11.4. At the same time, the HL-LHC can only manage a much lower accuracy 6-17% [20] and some improved analysis may reach 2-3.5% [37].

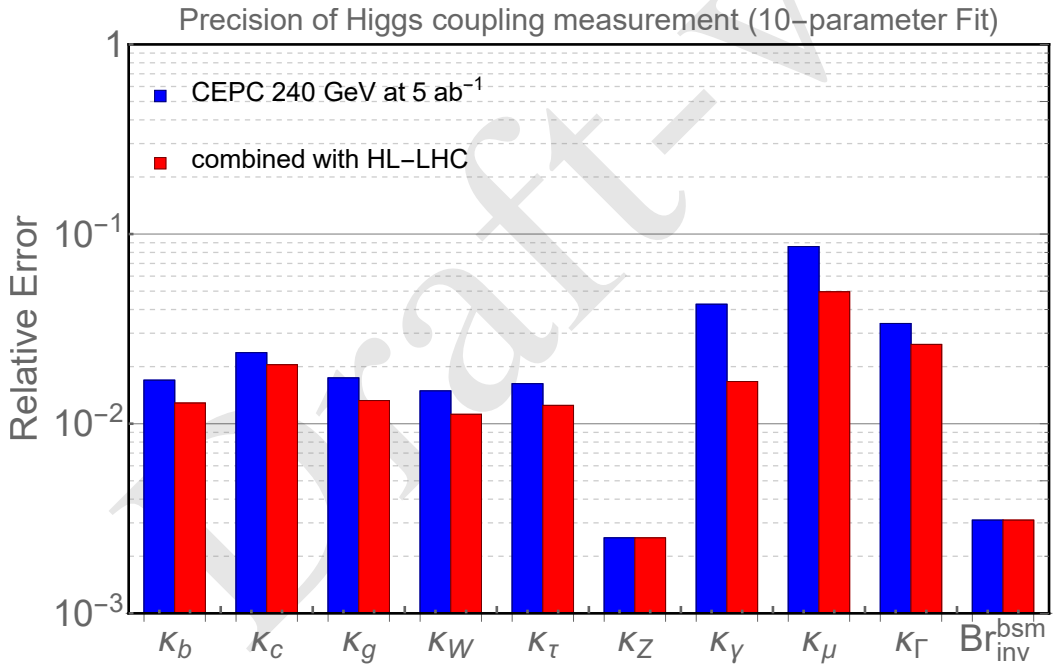

Figure 11.9: The 10 parameter fit result for CEPC at 240 GeV with $5.6\mathrm{ab}^{-1}$ integrated luminosity (blue) and in combination with HL-LHC inputs (red). All the numbers refer to are relative precision except for $\mathrm{BR}_{\mathrm{inv}}^{\mathrm{bsm}}$ for which 95% CL upper limit are quoted respectively.

As discussed above, one of the greatest advantages of lepton collider Higgs boson factory is the capability of determining the Higgs boson coupling *model independently*. The projection of such a determination at the CEPC is shown in Fig. 11.9. The advantage of the higher integrated luminosity at a circular lepton collider is apparent. The CEPC has a clear advantage in the measure of κ_Z. It is also much stronger in κ_μ and $\mathrm{BR}_{\mathrm{inv}}$ measurements.

11.1.7.2 Effective-field-theory analysis

With the assumption that the new physics particles are heavier than the relevant energy of the Higgs factory, their effect can be characterized in the effective-field-theory (EFT) framework, in which higher dimensional operators supplement the Standard Model Lagrangian. Imposing baryon and lepton numbers conservations, all higher dimensional operators are of even dimension:

$$\mathcal{L}_{\rm EFT} = \mathcal{L}_{\rm SM} + \sum_i \frac{c_i^{(6)}}{\Lambda^2}\mathcal{O}_i^{(6)} + \sum_j \frac{c_j^{(8)}}{\Lambda^4}\mathcal{O}_j^{(8)} + \cdots \tag{11.11}$$

The leading effects of new physics at the electroweak scale would be the dimension-six operators. To obtain robust constraints on the Wilson coefficients c_i, a global analysis is required which includes the contributions from all possible dimension-six operators. While a large number of dimension-six operators can be written down, only a subset of them contribute to the Higgs boson processes at leading order. Among these operators, some are much better constrained by other measurements. It is thus reasonable to focus on the operators that primarily contribute to the Higgs boson processes and reduce the parameter space by making appropriate assumptions, as done in many recent studies of EFT global analysis at future lepton colliders [32, 38–43]. Following these studies, the CP-violating operators as well as the ones that induce fermion dipole interactions are discarded in this analysis. At leading order, CP-violating operators do not have linear contributions to the rates of Higgs processes. While they do contribute to the angular observables at the leading order [44, 45], these operators are usually much better constrained by EDM experiments [46–48], though some rooms are still possible for the CP-violating couplings of Higgs boson to the heavy flavor quarks and leptons [49, 50]. The interference between the fermion dipole interactions with SM terms are suppressed by the fermion masses. The corresponding operators also generate dipole moments, which are stringently constrained especially for light fermions. For the operators that modify the Yukawa matrices, only the five diagonal ones that correspond to the top, charm, bottom, tau, and muon Yukawa couplings are considered, which are relevant for the Higgs boson measurements at CEPC.

Before presenting the projections, some brief comments on the EFT framework are in order. In comparison with the κ-framework, a significant advantage of the EFT framework is that it gives physical parameterizations of the new physics effect. EFT operators can be used directly in computations. It also allows natural inclusions of new observables, with possible correlations automatically taken into account. At the same time, the connections with experimental observables are less direct and intuitive. Sometimes, the EFT approach is referred to as model-independent. This is only accurate to a certain extent. At least, it assumes that there are no new light degrees of freedom. In practice, assumptions are often made to simplify the set of EFT operators, as also done here.

The electroweak precision observables are already tightly constrained by the LEP Z-pole and W mass measurements. The CEPC Z-pole run can further improve the constraints set by LEP, thanks to the enormous amount ($\sim 10^{11}$) of Z bosons that can be collected. The W mass can also be constrained within a few MeVs at CEPC even without a dedicated WW threshold run. Given that the expected precisions of the Z-pole observables and the W mass are much higher than the ones of Higgs boson observables, in the Higgs boson analysis, it is assumed that the former ones are perfectly constrained, which significantly simplifies the analysis. In particular, in a convenient basis all the contact

Table 11.5: The estimated constraints on aTGCs from the measurements of the diboson process ($e^+e^- \to WW$) in the semi-leptonic channel at CEPC 240 GeV with $5\,\mathrm{ab}^{-1}$ data and unpolarized beams. All angular distributions are used in the fit. Only the statistical uncertainties of the signal events are considered, assuming a selection efficiency of 80%.

CEPC 240 GeV ($5\,\mathrm{ab}^{-1}$)				
	uncertainty	correlation matrix		
		$\delta g_{1,Z}$	$\delta\kappa_\gamma$	λ_Z
$\delta g_{1,Z}$	1.3×10^{-3}	1	0.08	-0.90
$\delta\kappa_\gamma$	1.0×10^{-3}		1	-0.42
λ_Z	1.4×10^{-3}			1

interaction terms of the form $HVf\bar{f}$ can be discarded since they also modify the fermion gauge couplings. Realistic Z-pole constraints have also been considered in recent studies [32, 41, 43], but certain assumptions (such as flavor-universality) and simplifications are made. Future studies with more general frameworks are desired to fully determine the impact of the Z-pole measurements on the Higgs boson analysis.

The measurements of the triple gauge couplings (TGCs) from the diboson process ($e^+e^- \to WW$) play an important role in the Higgs boson coupling analysis under the EFT framework. Focusing on CP-even dimension-six operators, the modifications to the triple gauge vertices from new physics can be parameterized by three anomalous TGC parameters (aTGCs), conventionally denoted as $\delta g_{1,Z}$, $\delta\kappa_\gamma$ and λ_Z [51, 52]. Among them, $\delta g_{1,Z}$ and $\delta\kappa_\gamma$ are generated by operators that also contribute to the Higgs boson processes. At 240 GeV, the cross section of $e^+e^- \to WW$ is almost two orders of magnitude larger than the one of the Higgsstrahlung process. The measurements of the diboson process thus provide strong constraints on the operators that generate the aTGCs. A dedicated study on the TGC measurements at CEPC is not available at the current moment. A simplified analysis is thus performed to estimate the precision reaches on the aTGCs. The results are shown in Table 11.5. The analysis roughly follows the methods in Refs. [40, 53]. Only the WW events in the semi-leptonic (electron or muon) channel are used, which have good event reconstructions and also a sizable branching fraction ($\approx 29\%$). In particular, the production polar angle, as well as the two decay angles of the leptonic W, can be fully reconstructed, which contain important information on the aTGCs. The two decay angles of the hadronic W can only be reconstructed with a two-fold ambiguity. A χ^2 fit of the three aTGC parameters to the binned distribution of all five angles is performed, from which the one-sigma precisions of the three aTGCs as well as the correlations among them are extracted. A signal selection efficiency of 80% is assumed. The effects of systematics and backgrounds are not considered, assuming they are under control after the selection cuts.

Under the assumptions specified above, the contributions to the Higgs boson and diboson processes from dimension-six operators consist of a total number of twelve degrees of freedom. While all non-redundant basis are equivalent, it is particularly convenient to choose a basis in which the twelve degrees of freedom can be mapped to exactly twelve operators, while the rest are removed by the assumptions. Two such bases are considered in our analysis, one is defined by the set of dimension-six operators in Table 11.6, the other is the so-called "Higgs basis," proposed in Ref. [54]. In the Higgs basis, the

Table 11.6: A complete set of CP-even dimension-six operators that contribute to the Higgs boson and TGC measurements, assuming there is no correction to the Z-pole observables and the W mass, and also no fermion dipole interaction. For $\mathcal{O}_{y_u}$, $\mathcal{O}_{y_d}$ and $\mathcal{O}_{y_e}$, only the contributions to the diagonal elements of the Yukawa matrices that corresponds to the top, charm, bottom, tau, and muon Yukawa couplings are considered.

$\mathcal{O}_H = \frac{1}{2}(\partial_\mu \lvert H^2\rvert)^2$	$\mathcal{O}_{GG} = g_s^2 \lvert H\rvert^2 G^A_{\mu\nu} G^{A,\mu\nu}$
$\mathcal{O}_{WW} = g^2 \lvert H\rvert^2 W^a_{\mu\nu} W^{a,\mu\nu}$	$\mathcal{O}_{y_u} = y_u \lvert H\rvert^2 \bar{Q}_L \tilde{H} u_R \quad (u \to t, c)$
$\mathcal{O}_{BB} = g'^2 \lvert H\rvert^2 B_{\mu\nu} B^{\mu\nu}$	$\mathcal{O}_{y_d} = y_d \lvert H\rvert^2 \bar{Q}_L H d_R \quad (d \to b)$
$\mathcal{O}_{HW} = ig(D^\mu H)^\dagger \sigma^a (D^\nu H) W^a_{\mu\nu}$	$\mathcal{O}_{y_e} = y_e \lvert H\rvert^2 \bar{L}_L H e_R \quad (e \to \tau, \mu)$
$\mathcal{O}_{HB} = ig'(D^\mu H)^\dagger (D^\nu H) B_{\mu\nu}$	$\mathcal{O}_{3W} = \frac{1}{3!} g \epsilon_{abc} W^{a\,\nu}_{\mu} W^b_{\nu\rho} W^{c\,\rho\mu}$

parameters are defined in the broken electroweak phase, and can be directly interpreted as the size of the Higgs boson couplings. Different from the original Higgs basis, this analysis follows Ref. [40], with the parameters associated with the Hgg, $H\gamma\gamma$ and $HZ\gamma$ vertices normalized to the SM one-loop contributions, and denoted as $\bar{c}_{gg}$, $\bar{c}_{\gamma\gamma}$ and $\bar{c}_{Z\gamma}$. The parameter $\bar{c}_{gg}^{\text{eff}}$ is further defined to absorb all contributions to the Hgg vertex. These redefined parameters can be more conveniently interpreted as the precisions of the Higgs couplings analogous to those in the κ framework. The exact definitions of the Higgs basis and the translation to the basis in Table 11.6 can be found in the end of the section.

The estimated precisions of all the Higgs boson rate measurements in Section 11.1.5 (Table 11.3), along with the correlations among them, are included as inputs for the EFT global analysis. In addition, the angular observables of the channel $e^+e^- \to ZH$, $Z \to \ell^+\ell^-$, $H \to b\bar{b}$ are included, following the studies in Refs. [44, 45]. This channel is almost background-free after the selection cuts, with a signal selection efficiency of about 40%. For the TGC measurements, the results in Table 11.5 are used as inputs. The global χ^2 is obtained by summing over the χ^2 of all the measurements. Due to the high precision of the measurements, it is shown that for all observables, keeping only the linear terms of all EFT parameters gives a very good approximation [40]. This greatly simplifies the fitting procedure, as the total χ^2 can be written as

$$\chi^2 = \sum_{ij} (c - c_0)_i \, \sigma_{ij}^{-2} \, (c - c_0)_j \,, \qquad \text{where} \quad \sigma_{ij}^{-2} \equiv (\delta c_i \, \rho_{ij} \, \delta c_j)^{-1} \,, \tag{11.12}$$

where c_i's are the EFT parameters, c_0's are the corresponding central values which are zero by construction, as the measurements are assumed to be SM-like. The one-sigma uncertainties δc_i and the correlation matrix ρ can be obtained from $\sigma_{ij}^{-2} = \partial^2 \chi^2 / \partial c_i \partial c_j$.

For comparison, the reaches of the LHC 14 TeV are also considered, with a total luminosities of $300\,\text{fb}^{-1}$ or $3000\,\text{fb}^{-1}$, which are combined with the diboson ($e^+e^- \to WW$) measurements at LEP as well as the LHC 8 TeV Higgs measurements. For the LHC 14 TeV Higgs boson measurements, the projections by the ATLAS collaboration [33] are used, while the composition of each channel is obtained from Refs. [55–59]. The constraints from the LHC 8 TeV Higgs boson measurements and the diboson measurements at LEP are obtained directly from Ref. [60]. While the LHC diboson measurements could potentially improve the constraints on aTGCs set by LEP [61], they are not included in this analysis due to the potential issues related to the validity of the EFT [62, 63] and the TGC dominance assumption [64].

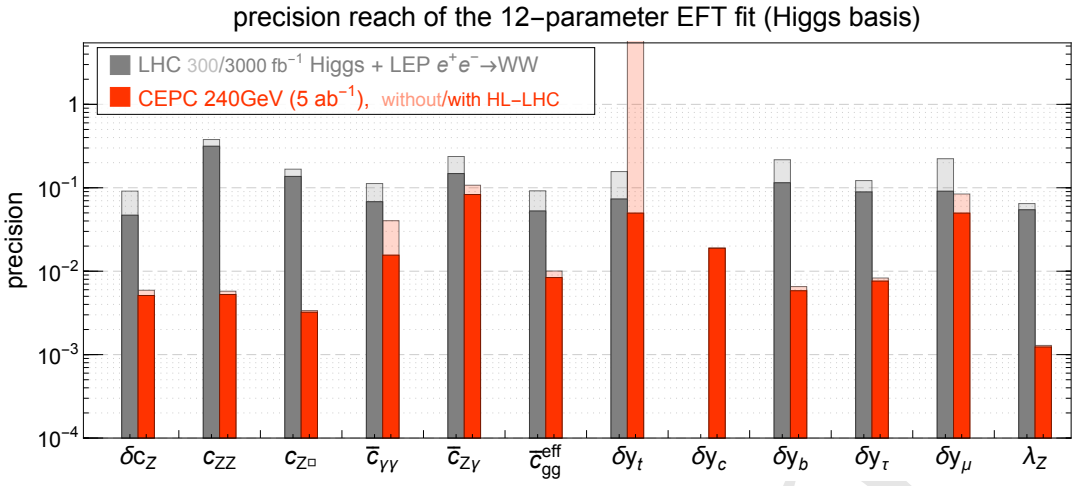

Figure 11.10: One-sigma precision reach of the twelve parameters in the Higgs basis. The first column shows the results from the LHC Higgs boson measurements with $300\,\mathrm{fb}^{-1}$ (light shade) and $3000\,\mathrm{fb}^{-1}$ (solid shade) combined with LEP diboson ($e^+e^- \to WW$) measurement. The second column shows the results from CEPC with $5\,\mathrm{ab}^{-1}$ data collected at 240 GeV with unpolarized beam. The results from CEPC alone are shown in light shades, and the ones from a combination of CEPC and HL-LHC are shown in solid shades. δy_c is fixed to zero for the LHC fits.

The results of the 12-parameter fit at CEPC are shown in Fig. 11.10 for the Higgs basis and Fig. 11.11 for the basis in Table 11.6. The results from LHC Higgs boson measurements (both $300\,\mathrm{fb}^{-1}$ and $3000\,\mathrm{fb}^{-1}$) combined with LEP diboson measurements are shown in comparison. The results of the combination of CEPC with HL-LHC ($3000\,\mathrm{fb}^{-1}$) are also shown in addition to the ones of CEPC alone. In Fig. 11.10, the results are shown in terms of the one-sigma precision of each parameter. The LHC results are shown with gray columns with $300\,\mathrm{fb}^{-1}$ ($3000\,\mathrm{fb}^{-1}$) in light (solid) shades, while the CEPC ones are shown with the red columns, with the CEPC-alone (combination with HL-LHC) results shown in light (solid) shades. In Fig. 11.11, the results are presented in terms of the reaches of $\Lambda/\sqrt{|c_i|}$ at 95% confidence level (CL), where Λ is the scale of new physics and c_i is the corresponding Wilson coefficient for each operator, defined in Eq. 11.11. Four columns are shown separately for LHC $300\,\mathrm{fb}^{-1}$, LHC $3000\,\mathrm{fb}^{-1}$, CEPC alone and CEPC combined with HL-LHC. The results of the global fits are shown with solid shades. The results from individual fits are shown with light shades, which are obtained by switching on one operator at a time with the rest fixed to zero.

It is transparent from Fig. 11.10 that CEPC provides very good reaches on the precisions of Higgs boson couplings, which are of one order of magnitude better than the ones at the LHC. For the parameters $\bar{c}_{\gamma\gamma}$, $\bar{c}_{Z\gamma}$ and δy_μ, the clean signal and small branching ratios of the corresponding channels ($H \to \gamma\gamma/Z\gamma/\mu\mu$) makes the HL-LHC precisions comparable with the CEPC ones. The combination with additional LHC measurements thus provides non-negligible improvements, especially for those parameters. It should be noted that, while δy_t modifies the Hgg vertex via the top loop contribution, CEPC alone could not discriminate it from the Hgg contact interaction obtained from integrating out a heavy new particle in the loop. The parameter $\bar{c}_{gg}^{\mathrm{eff}}$ absorbs both contributions and reflects the overall precision of the Hgg coupling. The combination with the LHC $t\bar{t}H$ measurements could resolve this flat direction. The CEPC measurements, in turn, could improve the constraint on δy_t set by the LHC by providing much better constraints on the other

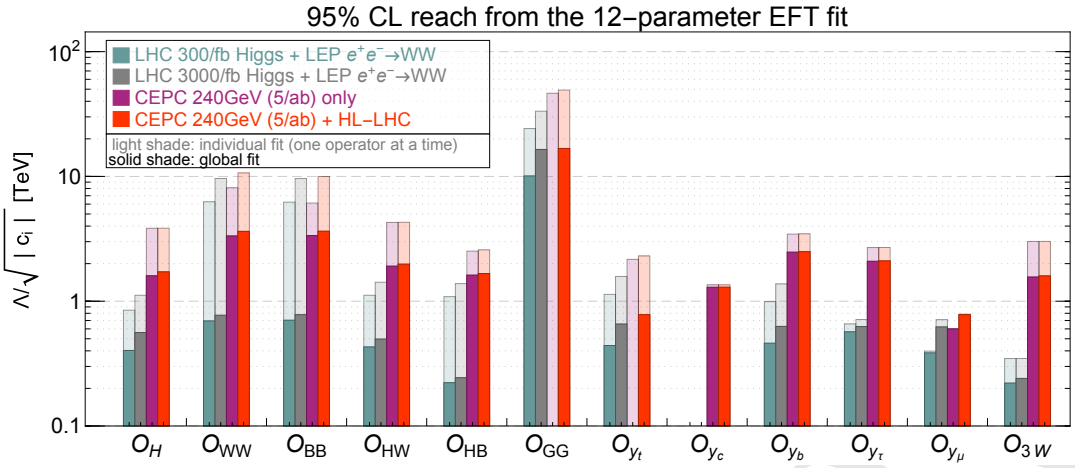

Figure 11.11: The 95% CL reach on $\Lambda/\sqrt{|c_i|}$ for the operators in the basis defined in Table 11.6. The first two columns show the results from LHC Higgs boson measurements with 300 fb^{-1} and 3000 fb^{-1} combined with LEP diboson ($e^+e^- \to WW$) measurement. The last two columns show the results from CEPC alone and the combination of CEPC and HL-LHC (3000 fb^{-1}). The results of the global fits are shown with solid shades. The results from individual fits (by switching on one operator at a time) are shown with light shades. δy_c is fixed to zero for the LHC fits.

parameters that contribute to the $t\bar{t}H$ process. It should also be noted that the measurement of the charm Yukawa coupling is not reported in Ref. [33], while the projection of its constraint has a large variation among different studies and can be much larger than one [65–70]. Therefore, δy_c is fixed to be zero for the LHC-only fits, as treating δy_c as an unconstrained free parameter generates a flat direction in the fit which makes the overall reach much worse. The CEPC, on the other hand, provides excellent measurements of the charm Yukawa and can constrain δy_c to a precision of $\sim 2\%$.

Regarding the reaches of $\Lambda/\sqrt{|c_i|}$ in Fig. 11.11, it is also clear that CEPC has a significantly better performance than the LHC. If the couplings are naïvely assumed to be of order one ($c_i \sim 1$), the Higgs boson measurements at CEPC would be sensitive to new physics scales at multiple TeVs. While the individual reach for some of the operators at the LHC can be comparable to the ones at CEPC (*e.g.*, O_{WW} and O_{BB} from the measurement of $H \to \gamma\gamma$), the reaches of CEPC are much more robust under a global framework thanks to its comprehensive measurements of both the inclusive ZH cross section and the exclusive rates of many Higgs boson decay channels. Operators O_{GG} and O_{y_t} both contribute to the Hgg vertex. While the CEPC could provide strong constraints on either of them if the other is set to zero, they can only be constrained in a global fit if the $t\bar{t}h$ measurements at the LHC are also included. It is also important to note that the validity of EFT could be a potential issue for the LHC measurements [62]. Depending on the size of the couplings, the inferred bounds on the new physics scale Λ could be comparable with or even smaller than the energy scale probed by the LHC. The CEPC has a smaller center of mass energy and much better precisions, which ensures the validity of EFT for most new physics scenarios.

In Table 11.7, the numerical results of the global fit are presented for CEPC in terms of the one-sigma precisions of the 12 parameters and the correlations among them. The results assume an integrated luminosity of 5 ab^{-1} at 240 GeV with unpolarized beams, both without and with the combination of HL-LHC (3000 fb^{-1}) Higgs boson measure-

ments. With both the one-sigma bounds and the correlation matrix, the corresponding *chi-squared* can be reconstructed, which can be used to derive the constraints in any other EFT basis or any particular model that can be matched to the EFT. This offers a convenient way to study the reaches on new physics models, as detailed knowledge of the experimental measurements are not required.

Table 11.7: The one-sigma uncertainties for the 12 parameters from CEPC (240 GeV, $5\,\mathrm{ab}^{-1}$) in the Higgs basis and the basis of dimension-six operators. For both cases, the upper (lower) row correspond to results without (with) the combination of the HL-LHC Higgs boson measurements.. Note that, without the $t\bar{t}h$ measurements, δy_t can not be constrained in a global fit, thus c_{GG} and c_{y_t} can not be resolved.

Higgs basis											
δc_Z	c_{ZZ}	$c_{Z\Box}$	$\bar{c}_{\gamma\gamma}$	$\bar{c}_{Z\gamma}$	$\bar{c}_{gg}^{\mathrm{eff}}$	δy_t	δy_c	δy_b	δy_τ	δy_μ	λ_Z
0.0059	0.0058	0.0034	0.040	0.11	0.010	–	0.019	0.0065	0.0083	0.084	0.0013
0.0051	0.0053	0.0032	0.016	0.083	0.0084	0.050	0.019	0.0058	0.0076	0.050	0.0012
c_i/Λ^2 [TeV^{-2}] of dimension-six operators											
c_H	c_{WW}	c_{BB}	c_{HW}	c_{HB}	c_{GG}	c_{y_t}	c_{y_c}	c_{y_b}	c_{y_τ}	c_{y_μ}	c_{3W}
0.20	0.045	0.044	0.14	0.19	–	–	0.30	0.082	0.11	1.4	0.20
0.17	0.038	0.038	0.13	0.18	0.0018	0.82	0.30	0.080	0.11	0.82	0.20

In the EFT framework, it is explicitly assumed that the Higgs total width is the sum of all the widths of its SM decay channels. This is because the EFT expansion in Eq. 11.11 relies on the assumption that the new physics scale is sufficiently large, while any potential Higgs boson exotic decay necessarily introduces light BSM particles, thus in direct conflict with this assumption. One could nevertheless treat the Higgs boson total width as a free parameter in the EFT global fit and obtain an indirect constraint of it, as done in Ref. [32]. With this treatment, the CEPC could constrain the Higgs boson total width to a precision of 1.8% (1.7% if combined with HL-LHC). This result is significantly better than the one from the 10-parameter coupling fit in Table 11.4 ($3.4\%/2.6\%$). The improvement is mainly because the HWW and HZZ couplings are treated as being independent in the 10-parameter coupling fit, while in the EFT framework they are related to each other under gauge invariance and custodial symmetry. It should also be noted that the Higgs boson width determined using Eq. (11.4) and (11.7) explicitly assumes that the HWW and HZZ couplings are independent of the energy scale. Such an assumption is not valid in the EFT framework with the inclusion of the anomalous couplings.

11.1.7.3 The Higgs boson self-coupling

The Higgs boson self-coupling is a critical parameter governing the dynamics of the electroweak symmetry breaking. In the Standard Model, the Higgs boson trilinear and quadrilinear couplings are fixed once the values of the electroweak VEV and the Higgs boson mass are known. Any deviation from the SM prediction is thus clear evidence of new physics beyond the SM. The Higgs boson trilinear coupling is probed at the LHC with the measurement of the di-Higgs process, $pp \to HH$. Current bounds on the Higgs boson trilinear coupling is at the $\mathcal{O}(10)$ level, while the HL-LHC is expected to improve the precision to the level of $\mathcal{O}(1)$ [71]. The prospects for extracting the Higgs boson quadrilinear coupling are much less promising, even for a 100 TeV hadron collider [72].

To measure the di-Higgs-boson processes at a lepton collider, a sufficiently large center of mass energy ($\gtrsim 400$ GeV) is required, which is likely to be achieved only at a linear collider. The CEPC, instead, can probe the Higgs boson trilinear coupling via its loop contributions to the single Higgs boson processes. This indirect approach neverthe-

less provides competitive reaches since the loop suppression is compensated by the high precision of the Higgs boson measurements at CEPC [73]. With a precision of 0.5% on the inclusive ZH cross section at 240 GeV, the Higgs boson trilinear coupling can be constrained to a precision of 35%, assuming all other Higgs boson couplings that contributes to $e^+e^- \to ZH$ are SM-like. [5] While this indirect bound is comparable to the direct ones at linear colliders, it relies on strong assumptions which are only applicable to some specific models. A more robust approach is to include all possible deviations on the Higgs boson couplings simultaneously and constrain the Higgs boson trilinear coupling in a global fit. The EFT framework presented in Section 11.1.7.2 is ideal for such an analysis. Under this framework, the one-loop contributions of the trilinear Higgs boson coupling to all the relevant Higgs boson production and decay processes are included, following Ref. [42]. The new physics effect is parameterized by the quantity $\delta\kappa_\lambda \equiv \kappa_\lambda - 1$, where κ_λ is the ratio of the Higgs boson trilinear coupling to its SM value,

$$\kappa_\lambda \equiv \frac{\lambda_3}{\lambda_3^{\rm sm}}\,, \qquad \lambda_3^{\rm sm} = \frac{m_H^2}{2v^2}\,. \tag{11.13}$$

The global fit is performed simultaneously with $\delta\kappa_\lambda$ and the 12 EFT parameters in Section 11.1.7.2. The results are presented in Table 11.8. The results for HL-LHC are also shown, which were obtained in Ref. [74] under the same global framework. For CEPC 240 GeV, the one-sigma bound on $\delta\kappa_\lambda$ is around ± 3, significantly worse than the 35% in the $\delta\kappa_\lambda$-only fit. This is a clear indication that it is difficult to resolve the effects of $\delta\kappa_\lambda$ from those of other Higgs boson couplings. For HL-LHC, the reach on $\delta\kappa_\lambda$ is still dominated by the di-Higgs process. However, as a result of the destructive interferences among diagrams, the di-Higgs process at LHC could not constrain $\delta\kappa_\lambda$ very well on its positive side, even with the use of differential observables [75]. The combination of HL-LHC and CEPC 240 GeV thus provides a non-trivial improvement to the HL-LHC result alone, in particular for the two-sigma bound on the positive side, which is improved from $+6.1$ to $+2.8$. This is illustrated in Fig. 11.12, which plots the profiled χ^2 as a function of $\delta\kappa_\lambda$ for the two colliders.

Table 11.8: The $\Delta\chi^2 = 1$ (one-sigma) and $\Delta\chi^2 = 4$ (two-sigma) bounds of $\delta\kappa_\lambda$ for various scenarios, obtained in a global fit by profiling over all other EFT parameters. The results for HL-LHC are obtained from Ref. [74].

bounds on $\delta\kappa_\lambda$	$\Delta\chi^2 = 1$	$\Delta\chi^2 = 4$
CEPC 240 GeV $(5\,\text{ab}^{-1})$	$[-3.2, +3.3]$	$[-6.3, +6.7]$
HL-LHC	$[-0.9, +1.3]$	$[-1.7, +6.1]$
HL-LHC + CEPC 240 GeV	$[-0.8, +1.0]$	$[-1.5, +2.8]$
240 GeV $(5\,\text{ab}^{-1})$ + 350 GeV $(1.5\,\text{ab}^{-1})$	$[-0.48, +0.48]$	$[-0.96, +0.96]$

It is also important to note that the reach on $\delta\kappa_\lambda$ in the global framework is significantly improved if an additional run at a higher energy, such as 350 GeV, is available. The global constraint on $\delta\kappa_\lambda$ is improved by almost one order of magnitude with $1.5\,\text{ab}^{-1}$ data

[5] A better precision can be obtained by also using the exclusive channels, such as $\sigma(ZH) \times \text{BR}(H \to b\bar{b})$, but would require an even stronger assumption that all Higgs boson couplings contributing to the branching ratios are also SM-like except the Higgs boson trilinear coupling.

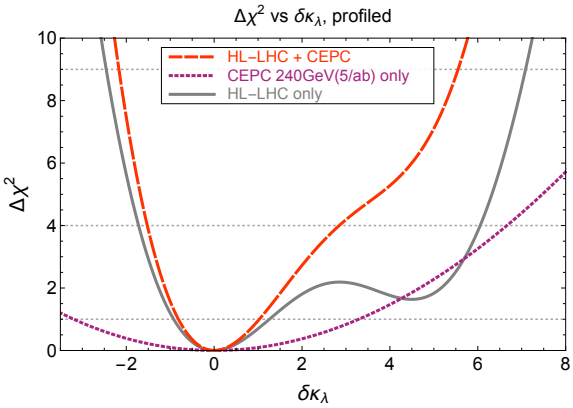

Figure 11.12: Chi-square as a function of $\delta\kappa_\lambda$ after profiling over all other EFT parameters for HL-LHC, CEPC and their combination.

collected at the 350 GeV on top of the $5\,\mathrm{ab}^{-1}$ at 240 GeV. The usefulness of the 350 GeV run in discriminating different EFT parameters is thoroughly discussed in Ref. [40]. In addition, it was pointed out in Refs. [42, 73] that the sensitivity of $\sigma(ZH)$ to $\delta\kappa_\lambda$ is maximized near the ZH threshold and decreases as the center of mass energy increases – a feature not exhibited by the other EFT parameters. Measuring $e^+e^- \to ZH$ at two different energies is thus particularly helpful in discriminating $\delta\kappa_\lambda$ with other EFT parameters.

11.1.7.4 Higgs and top couplings

Interactions of the Higgs boson with the top quark are widely viewed as a window to new physics beyond the Standard Model. Parameterizing effects of new physics in terms of dimension-six gauge-invariant operators modifying the Higgs-top interactions [76, 77], the Higgs-top couplings physics potential at CEPC can be evaluated [78–81]. This EFT basis enlarges the Higgs EFT considered above. Moreover, the CP violation effects in the third generation Yukawas can be reflected as the complexity of the Wilson coefficients of operator $\mathcal{O}_{y_t}$ and $\mathcal{O}_{y_b}$,

$$\Delta y_t = y_t^{\mathrm{SM}} \left(\Re[C_{y_t}] \frac{v^3}{2m_t\Lambda^2} + i\Im[C_{y_t}] \frac{v^3}{2m_t\Lambda^2} \right) \tag{11.14}$$

$$\Delta y_b = y_t^{\mathrm{SM}} \left(\Re[C_{y_b}] \frac{v^3}{2m_b\Lambda^2} + i\Im[C_{y_b}] \frac{v^3}{2m_b\Lambda^2} \right). \tag{11.15}$$

In this section, the effect of introducing CP phases in the Yukawa operators in Higgs boson physics are discussed. For more detailed discussion on a complete set of Higgs and Top operators, see Ref. [78]. The dominant sources of constraints are from $H \to \gamma\gamma$ and $H \to gg$ for $\mathcal{O}_{y_t}$, and $H \to gg$ and $H \to b\bar{b}$ for $\mathcal{O}_{y_b}$. Given that $H \to gg$ measurements are sensitive to both operators, a joint analysis of $\mathcal{O}_{y_t}$ and $\mathcal{O}_{y_b}$ will yield a significantly different result comparing to individual operator analysis. A joint analysis for these two operators in terms of Yukawa coupling strengths and the associated CP phases is performed at CEPC. The important physics cases for such considerations are highlighted.

In Fig. 11.13 constraints on the top and bottom Yukawa coupling strengths and their CP phases are presented in the left panel and right panel, respectively. The 68% and 95% exclusion bands are shown in solid and dashed lines. The limits for CEPC are shown in *bright* black and magenta lines for individual operator analysis and the *bright* green and

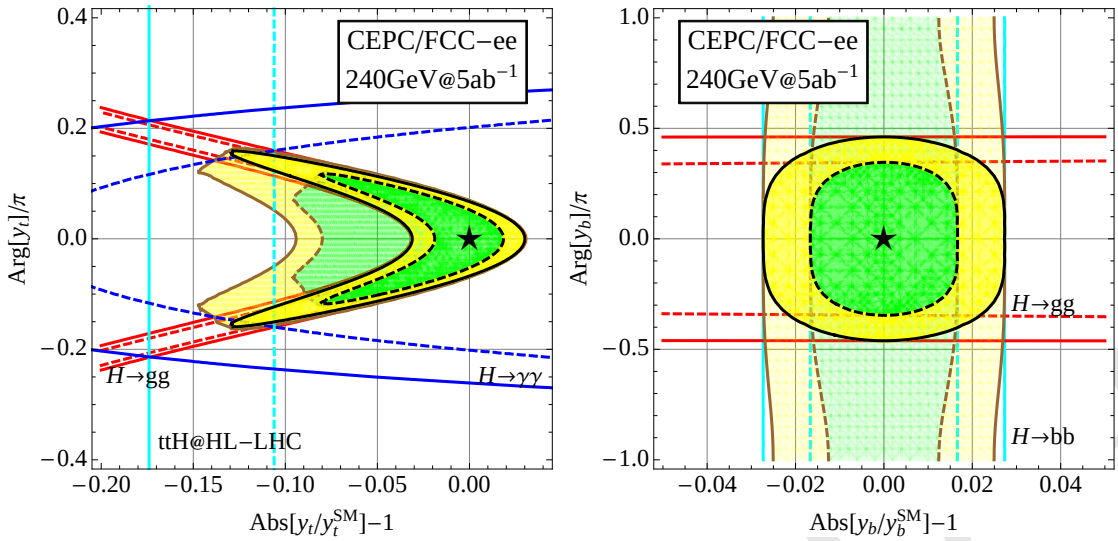

Figure 11.13: Results for analysis on C_{y_t} and C_{y_b} in the projected allowed regions for modification to top and bottom Yukawa couplings in magnitude and CP phase at 68% and 95% confidence level. The combined results for CEPC are shown in black curves. The source of individual constraints for the single operator analysis are labeled correspondingly. For a joint analysis of simultaneous appearance of both $\mathcal{O}_{y_t}$ and $\mathcal{O}_{y_b}$ operators, the results for CEPC are shown in the enlarged yellow (95%) and green regions (68%) with thick brown boundary lines.

yellow shaded regions representing the 68% and 95% allowed parameter space, respectively. The *dimmed* thick black curves represent the results after turning on both operators $\mathcal{O}_{tH}$ and $\mathcal{O}_{bH}$ at the same time, using a profile-likelihood method profiling over other parameters. Furthermore, in the left panel the cyan band represents constraints from HL-LHC $t\bar{t}H$ measurements, red bands are constraints from CEPC $H \to gg$ measurements and blue bands are constraints from CEPC $H \to \gamma\gamma$ measurements. Similarly in the right panel, the cyan bands are constraints from $H \to b\bar{b}$ and the red bands are constraints from $H \to gg$ at CEPC.

The left panel of Fig. 11.13 shows that the expected sensitivity on the modification in the magnitude of top Yukawa is at around $\pm 3\%$ for the single operator analysis, which is relaxed to $[-9.5\%, +3\%]$ for the joint analysis allowing the bottom Yukawa and the associated CP phase to vary freely, in the case of zero CP phase in the top Yukawa. The phase of the top Yukawa could be constrained to be $\pm 0.16\pi$. The constraints on the phase of the top Yukawa is driven by the $H \to \gamma\gamma$ measurements, where a sizable phase shift will enlarge the Higgs boson to diphoton rate via reducing the interference with SM W-loop. The constraints on the magnitude of the top Yukawa modification is driven by the $H \to gg$ measurements due to the dominant contribution to $H \to gg$ being from top-loop. Note that constraints from $H \to gg$ measurement is not entirely vertical, this is a result of the different sizes of the top-loop contribution to Hgg through scalar and pseudoscalar couplings. Similarly, as shown in the right panel of Fig. 11.13 for the bottom Yukawa magnitude modification, the constraint is $\pm 2.5\%$ and, for the bottom Yukawa CP phase, the constraints changes from $\pm 0.47\pi$ to no constraint for simultaneous modification to top Yukawa.

11.1.8 Tests of Higgs boson spin/CP

The CP parity of a Higgs boson, and more generally its anomalous couplings to gauge bosons in the presence of BSM physics, can be measured at the CEPC based on the $e^+e^- \to Z^* \to ZH \to \mu^+\mu^- b\bar{b}$ process. It is convenient to express the anomalous coupling measurements in terms of physical quantities of effective fractions of events of the anomalous contribution relative to the SM predictions as detailed in Refs. [82–84], which are invariant under independent re-scalings of all couplings.

Two of the anomalous HZZ coupling measurements are of particular interest at the CEPC: the fraction of the high-order CP-even contribution due to either SM contribution or new physics, f_{a2}, and the fraction of a CP-odd contribution due to new physics, f_{a3}. The following two types of observables can be used to measure these anomalous couplings of the Higgs bosons.

1. The dependence of the $e^+e^- \to Z^* \to ZH$ cross section on $\sqrt{s}$ is different for different CP property of the Higgs boson [84]. Therefore, measurements of the cross section at several different energies will yield useful information about anomalous HZZ couplings. However this has non-trivial implications to the accelerator design and is not included in this study as a single value of $\sqrt{s}$ is assumed for the CEPC operating as a Higgs boson factory.

2. Angular distributions, $\cos\theta_1$ or $\cos\theta_2$ and Φ as defined in Figure 11.14. These angles are also sensitive to interference between CP-even and CP-odd couplings. In particular forward-backward asymmetry with respect to $\cos\theta_1$ or $\cos\theta_2$ and non-trivial phase in the Φ distributions can lead to an unambiguous interpretation of CP violation.

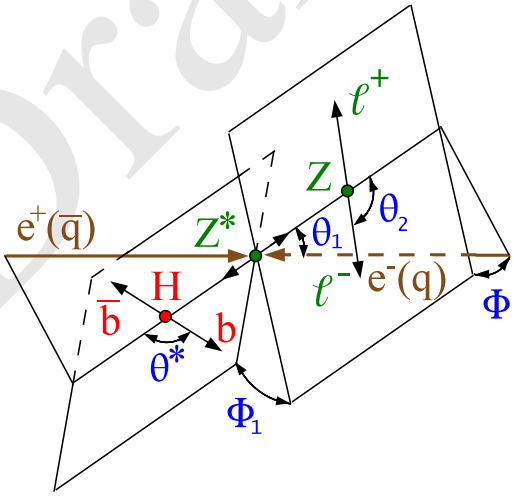

Figure 11.14: Higgs boson production and decay angles of the $e^+e^- \to Z^* \to ZH \to \mu^+\mu^- b\bar{b}$ process.

To estimate the sensitivities on the anomalous couplings, a maximum likelihood fit [84] is performed to match observed three-dimensional angular distributions to theory predictions including signal and background processes. In this likelihood fit, the signal probability density functions are from analytical predictions that are validated using a dedicated MC program, the JHU generator [82, 83], which incorporates all the anomalous couplings, spin correlations, interference of all contributing amplitudes. The background

probability density function is modeled from simulation based on $e^+e^- \to ZZ \to \ell^+\ell^- b\bar{b}$ process in Madgraph [85].

Several thousand statistically-independent experiments are generated and fitted to estimate the sensitivity to f_{a2} and f_{a3}, defined as the smallest values that can be measured with 3σ away from 0. All other parameters in the fit, including the number of expected signal and background events, are fixed. Figure 11.15 shows precision on f_{a2} and f_{a3} obtained with generated experiments. The expected sensitivity on f_{a2} and f_{a3} are 0.018 and 0.007 respectively.

The sensitivities of f_{a2} and f_{a3} are then converted to the equivalent parameters defined for the on-shell $H \to ZZ^*$ decays, $f_{a2}^{\rm dec}$ and $f_{a3}^{\rm dec}$, in order to compare with the sensitivities from the LHC experiments as described in Ref. [84]. The corresponding sensitivities of $f_{a2}^{\rm dec}$ and $f_{a3}^{\rm dec}$ are 2×10^{-4} and 1.3×10^{-4} respectively. The much smaller values in the $f_{a2,a3}^{\rm dec}$ are due to the much smaller $m^2_{Z^*}$ in the $H \to ZZ^*$ decay compared to the value in the $Z^* \to ZH$ production. A simultaneous fit of f_{a2} and f_{a3} can also performed with the 68% and 95% confidence level contours shown in Figure 11.15.

Compared to the ultimate sensitivity of HL-LHC as shown in Ref. [84], the sensitivities in the f_{a2} and f_{a3} at the CEPC are a factor of 300 and 3 better. Further improvements can be achieved by exploring kinematics in the $H \to b\bar{b}$ decays, including other Z decay final states, and combining with the overall cross-section dependence of the signal with a threshold scan in $\sqrt{s}$.

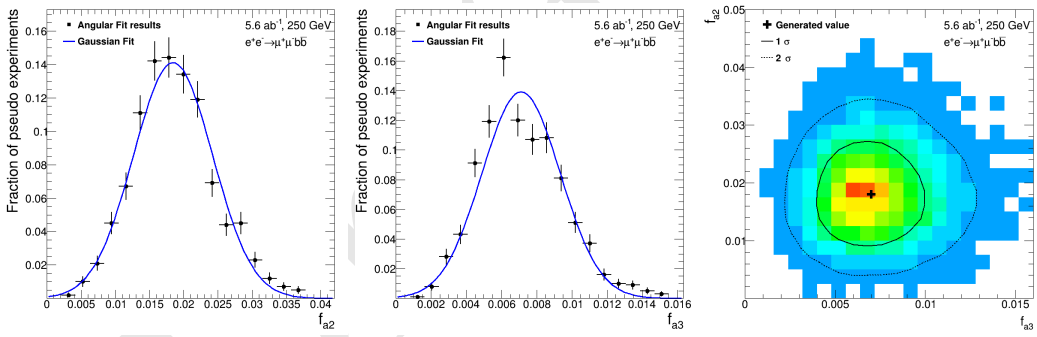

Figure 11.15: Distribution of fitted values of f_{a2} and f_{a3} in a large number of generated experiments. In the left and middle plots, only the parameter shown is floated. Other parameters are fixed to SM expectations. Right plot: simultaneous fit of non-zero f_{a2} and f_{a3}, with 68% and 95% confidence level contours shown.

11.1.9 Summary

Many new physics models predict Higgs boson coupling deviations at the sub-percent level, beyond those achievable at the LHC. The CEPC complements the LHC and will be able to study the properties of the Higgs boson in great details with unprecedented precision. At the CEPC, most of Higgs boson couplings can be measured with precision at a percent level or better, in particular the coupling to the Z boson can be determined with a precision of 0.25%. More importantly, the CEPC will able to measure many of the key Higgs boson properties such as the total width and decay branching ratios model independently, greatly enhancing the coverage of new physics searches. Furthermore, the clean event environment of the CEPC will allow the detailed study of known decay modes

and the identification of potential unknown decay modes that are impractical to test at the LHC.

This section provides a snapshot of the current studies, many of them are ongoing and more analyses are needed to fully understand the physics potential of the CEPC. Nevertheless, the results presented here have already built a strong case for the CEPC as a Higgs factory. The CEPC has the potential to "undress" the Higgs boson as what the LEP has done to the Z boson, and potentially shed light on new physics.

11.2 W and Z Boson Physics

With high production cross sections and large integrated luminosity, the CEPC will reach a new level of precision for the measurements of the properties of the W and Z bosons. Precise measurements of the W and Z boson masses, widths, and couplings are critical to test the consistency of the SM [86]. In addition, many BSM models predict new couplings of the W and Z bosons to other elementary particles. Precise electroweak measurements performed at the CEPC could discover deviations from the SM predictions and reveal the existence of new particles that are beyond the reaches of direct searches at the current experiments.

Significant improvements are expected from the CEPC measurements. Table 11.9 lists the expected precision from CEPC compared to achieved precisions from the LEP experiments for various measurements. Details about the estimation of these uncertainties are described in this section.

Table 11.9: The expected precision in a selected set of EW precision measurements in CEPC and the comparison with the precision from LEP experiments. The CEPC accelerator running mode and total integrated luminosity expected for each measurement are also listed. Depending on detector solenoid field during Z pole operation, the integrated luminosity varied from 8 ab^{-1} to 16 ab^{-1}.

Observable	LEP precision	CEPC precision	CEPC runs	$\int \mathcal{L}$ needed in CEPC
m_Z	2 MeV	0.5 MeV	Z threshold scan	8–16 ab^{-1}
$A_{FB}^{0,b}$	1.7%	0.1%	Z threshold scan	8–16 ab^{-1}
$A_{FB}^{0,\mu}$	7.7%	0.3%	Z threshold scan	8–16 ab^{-1}
$A_{FB}^{0,e}$	17%	0.5%	Z threshold scan	8–16 ab^{-1}
$\sin^2\theta_W^{\mathrm{eff}}$	0.07%	0.001%	Z threshold scan	8–16 ab^{-1}
R_b	0.3%	0.02%	Z pole	8–16 ab^{-1}
R_μ	0.2%	0.01%	Z pole	8–16 ab^{-1}
N_ν	1.7%	0.05%	ZH runs	5.6 ab^{-1}
m_W	33 MeV	2-3 MeV	ZH runs	5.6 ab^{-1}
m_W	33 MeV	1 MeV	WW threshold	2.6 ab^{-1}

11.2.1 Z pole measurements

The CEPC offers the possibility of dedicated low-energy runs at the Z pole for at least two years with a high instantaneous luminosity ($1.6 - 3.2 \times 10^{35}\mathrm{cm}^{-2}\mathrm{s}{-}1$). The expected integrated luminosity for CEPC Z pole runs is more than 8 ab^{-1}, and it is expected to produce about 10^{12} Z bosons (Tera-Z).

These runs allow high precision electroweak measurements of the Z boson decay partial widths, e.g. the parameters $R_b = \Gamma_{Z\to b\bar{b}}/\Gamma_{\mathrm{had}}$ and $R_\ell = \Gamma_{\mathrm{had}}/\Gamma_{Z\to \ell\bar{\ell}}$[6]. It would also perform high precision measurements of the forward-backward charge asymmetry (A_{FB}), the effective weak mixing angle ($\sin^2\theta_W^{\mathrm{eff}}$), number of light neutrino species (N_ν), and the mass of the Z boson (M_Z). It is also possible to perform some measurements with the Z boson without these dedicated low-energy runs near or at the Z pole. For example, the direct measurement of the number of light neutrino species can be performed in ZH runs at 240 GeV.

11.2.1.1 R_b

The partial width of the Z boson to its individual decay channel is proportional to the square of the fundamental Z-fermion couplings. The ratio of the partial widths R_b is sensitive to electroweak radiative corrections from new particles. For example, the existence of the scalar top quarks or charginos in supersymmetry could lead to a visible change of R_b from the SM prediction.

Precise measurements of R_b have been made by LEP collaborations [87–91] and by the SLD collaboration [92] using hadronic Z events.

Decays of b-hadrons were tagged using tracks with large impact parameters and/or reconstructed secondary vertices, complemented by event shape variables. The combination of LEP and SLD measurements yields a value of 0.21629 ± 0.00066 for R_b. The relative statistical uncertainty of R_b is above 0.2%, and systematic uncertainty is about 0.2%.

A relative precision of 0.02% can be achieved for the measurement of R_b at the CEPC, and it will improve the current precision in experimental measurement by one order of magnitude. The main systematic uncertainty is due to hemisphere tag correlations in $Z \to b\bar{b}$ events (0.02%).The uncertainty due to hemisphere tag correlations can be reduced to a level of 0.02% from the expected improvement in the b-tagging performance of the CEPC detector. The improvement of b-tagging efficiency is the key to reduce this uncertainty, and this uncertainty becomes irrelevant in the limit of 100% b-tagging efficiency. Due to that fact that a next-generation vertex detector will be used in the CEPC detector, the b-tagging efficiency is expected to be around 70% with a b-jet purity of 95% as shown in Figure 10.13, which is about 15%-20% higher than the efficiency achieved in previous experiments. The uncertainty due to hemisphere tag correlations can be reduce to 0.02% level, which is a factor of ten lower than previous measurements.

11.2.1.2 The partial decay width of $Z \to \mu^+\mu^-$

The $\mu^+\mu^-$ channel provides the cleanest leptonic final state. Combining the measurements from all four LEP experiments [93–96], the overall uncertainty of R_μ is 0.2%. The statistical uncertainty of R_μ is 0.15%.

[6]Here R_ℓ is defined as the ratio to any *one* charged lepton flavor, assuming lepton universality, not the ratio to the sum of all lepton flavors.

A precision of 0.01% can be achieved at the CEPC. The main systematic is the uncertainty of photon energy scale in the $Z \to \mu^+\mu^-\gamma$ process. About 2% of the $Z \to \mu^+\mu^-$ sample are classified as $Z \to \mu^+\mu^-\gamma$ events with a photon detected in ECAL. For this class of events, the most critical cut is that on the difference between the expected and measured photon energy ($|E_\gamma^{expected} - E_\gamma^{expected}| < 5\sigma_\gamma$), which is very efficient in removing the $Z \to \tau\tau$ background.

Therefore, the uncertainty due to photon energy scale and resolution in $Z \to \mu^+\mu^-\gamma$ process can be reduced to 0.01%. The main challenge in this measurement is to reduce the systematics due to QED ISR events. More detailed studies of radiative events in Z threshold scan runs are expected. Benefitting from high statistics in Z threshold scan runs, the source of uncertainty can be reduced to a level of 0.03%.

11.2.1.3 The forward-backward asymmetry A_{FB}^b at the Z pole

The measurement of the forward-backward asymmetry in $e^+e^- \to b\bar{b}$ events at the Z pole, $A_{FB}^{b,0}$, gives an important test of the Standard Model. $A_{FB}^{b,0}$ offers the most precise determination of the weak mixing angle. The measurements have been made at SLD and LEP experiments [97–101].

$Z \to b\bar{b}$ events were identified by tagging two b jets. Each event was divided into forward and backward categories by the plane perpendicular to the thrust axis which contains the interaction point. The combination of the LEP and SLD measurements gives a measured value of $A_{FB}^{b,0} = 0.1000 \pm 0.0017$. The statistical uncertainty is 1.2% and the main systematic uncertainties come from hemisphere tag correlations for b events (1.2%), tracking resolution and vertex detector alignment (0.8%), charm physics modeling (0.5%), and QCD and thrust axis correction (0.7%).

A precision of 10^{-4} can be achieved for the measurement of $A_{FB}^{b,0}$ at the CEPC, improving the current precision by more than a factor of 10. The expected statistical uncertainty is at a level of 0.01%. The uncertainty due to hemisphere tag correlations for b events can be reduced to 0.1% due to high b-tagging efficiency. The expected tracking momentum resolution in the CEPC detector is $\sigma/p_T = 2 \times 10^{-4} \times p_T + 0.005$, which is 10 times better than the resolutions of the LEP detectors. The uncertainty due to QCD and thrust axis correction can be reduced to 0.1% due to at least 10 times better granularity in the CEPC calorimeters. Overall, the expected systematics at CEPC measurement can be reduced to a level of 0.15%.

11.2.1.4 The prospects for the effective weak mixing angle measurement

The weak mixing angle $\sin^2\theta_W^{\text{eff}}$ is a very important parameter in the electroweak theory of the SM. It is the only free parameter that fixes the relative couplings of all fermions to the Z. It describes the rotation of the original W^0 and B^0 vector boson states into the observed γ and Z bosons as a result of spontaneous symmetry breaking. The weak mixing angle is very sensitive to electroweak radiative corrections, and it can be used perform a precise test of the SM theory. Furthermore, if there is any new heavy gauge boson Z', the weak mixing angle is expected to deviate from the SM prediction due to the contribution from physics in loop corrections. Therefore $\sin^2\theta_W^{\text{eff}}$ is very sensitive to new physics as well.

The centre-of-mass energy dependence of the forward-backward asymmetry arises from the interference of the Z boson with the virtual photon and thus depends on $\sin^2\theta_W^{\text{eff}}$.

In other words, the effective weak mixing angle can be extracted by studying the $\sqrt{s}$ dependence of the forward-backward asymmetry.

The effective weak mixing angle measurement has been performed in LEP using $Z \to b\bar{b}$ events and $Z \to \ell^+\ell^-$ events. The forward-backward asymmetry A_{FB} in one Z-pole dataset and two off Z-pole datasets ($\sqrt{s}$ = 89.4 GeV , $\sqrt{s}$ = 93.0 GeV) are used to extract $\sin^2\theta_W^{\rm eff}$. The current experimental result is $\sin^2\theta_W^{\rm eff} = 0.23153 \pm 0.00016$. $Z \to b\bar{b}$ events were identified by tagging two b jets. The main uncertainty includes uncertainty on the A_{FB}^b measurement as described in Section 11.2.1.3. and the statistical uncertainty in off Z-pole datasets.

Both Z-pole and off Z-pole runs are needed to perform the effective weak mixing angle measurement at the CEPC. The Z off-peak runs are expensive, therefore we need to optimize the integrated luminosity for off-peak runs. In order to improve the precision of $\sin^2\theta_W^{\rm eff}$ by a factor of 3, the required CEPC integrated luminosity for Z-pole runs are $8-16$ ab^{-1} and at least $2-4$ ab^{-1} integrated luminosity is needed for off Z-pole runs.The expected precision of effective weak mixing angle measurement in CEPC using $Z \to b\bar{b}$ events is expected to be 0.02%.

11.2.1.5 Z mass measurement

The mass m_Z is a fundamental parameter in the SM and was determined with an overall uncertainty of 2 MeV by four LEP experiments. The mass scan around the Z peak was performed from 87 GeV to 94 GeV. The Z mass was measured by a combined fit to the hadronic and leptonic cross sections in the on-peak and off-peak datasets. Most of the m_Z information is extracted from the off-peak runs. Taking the OPAL measurement as one example, six off-peak datasets were used to complete the m_Z scan. The main uncertainty of m_Z includes the statistical uncertainty (1 MeV/c^2), and the LEP beam energy (about 1 MeV/c^2).

A precision of 0.5 MeV can be achieved in CEPC measurement. The mass scan around the Z peak is the key for improving m_Z measurements.

The LEP measurement was limited by the statistics in their off-peak runs, therefore the luminosity in Z off-peak runs plays an important role in the m_Z measurement. We propose six off-peak runs and one on-peak run in CEPC Z mass scan, as listed in Table **??**. The expected m_Z uncertainty in CEPC due to statistics is about 0.1 MeV.

Another important systematic is beam momentum scale uncertainty. The beam momentum uncertainty in the CEPC accelerator is expected to be accurate to the 10 ppm level, which is about five times better than LEP. The uncertainty on m_Z due to the uncertainty on the beam energy can be reduced to less than 0.5 MeV.

Hadronic decay channels of the Z events are also expected to be used to measure m_Z since the leptonic decay channels suffer from low statistics. The uncertainty due to jet energy scale and resolution results in about 0.1 MeV in the m_Z measurement.

11.2.1.6 Neutrino species counting

Two different methods have been used to determine the number of light neutrino species (N_ν) at LEP. The first one is the indirect method using the analysis of the Z lineshape, and it uses the data collected by the Z threshold scan runs. The Z peak scan at CEPC can improve the LEP determination of N_ν by a factor of three. The second method is a direct measurement, which is based on the measurement of the cross section for the radiative

process $e^+e^- \to \nu\nu\gamma$. The second method at CEPC is supposed to use the ZH runs and improve the LEP direct determination by a factor of ten.

The systematic uncertainties of theoretical origin associated with the two methods are completely different: the indirect one relies on the precision calculation of the Z partial decay widths, while the direct one needs the calculation of higher order radiative corrections for the process $e^+e^- \to \nu\bar{\nu}\gamma$. Moreover the two methods use completely different datasets, therefore they are independent and complementary. The sensitivity to new physics will be different for these two methods. In the direct method, one can measure N_ν as a function of $\sqrt{s}$. A deviation of N_ν from an integer value would signal the presence of new physics. Possible contributions include WIMP dark matter particles, and other weakly coupled particles such as exotic neutrinos, gravitinos, or KK gravitons in theories with large extra dimensions. Thus, when we refer to the number of neutrino species, we actually include any number of possible invisible particles other than neutrinos. The subprocess $e^+e^- \to \nu_e\bar{\nu}_e\gamma$ is particularly important because it will allow to investigate possible deviations with respect to the SM in the vertex γW^+W^-, in a complementary way with respect to the W^+W^- production cross section, where both γW^+W^- and ZW^+W^- vertices appear in the matrix element.

Indirect method from Z line shape The indirect method assumes all contributions from invisible channels are coming from the $Z \to \nu\bar{\nu}$ decay, assuming that the total Z width does not receive additional contribution with respect to the SM ones. This method used the analysis of Z lineshape, subtracting the visible partial widths of the hadrons ($\Gamma_{\rm had}$), and the partial widths of the leptons (Γ_ℓ) from the total width Γ_Z. The invisible width $\Gamma_{\rm inv}$ can be written as:

$$\Gamma_{\rm inv} = N_\nu \Gamma_\nu = \Gamma_Z - \Gamma_{\rm had} - 3\Gamma_\ell. \tag{11.16}$$

We take as our definition of the number of neutrinos $N_\nu = \Gamma_{\rm inv}/\Gamma_\nu$, i.e. the ratio of the invisible width to the Standard Model expectation for the partial width to a single neutrino species.

Using the input from SM model, we can rewrite equation 11.16 as follows:

$$N_\nu = \frac{\Gamma_\ell}{\Gamma_\nu}\left(\sqrt{\frac{12\pi R_\ell}{M_Z^2\sigma^0_{\rm had}}} - R_\ell - 3\right). \tag{11.17}$$

The final LEP1 result was $N_\nu = 2.9840 \pm 0.0082$ [102]. As shown in equation 11.17, the precision of N_ν depends on the the lepton partial width R_ℓ measurement, the Z mass measurement, and the hadronic cross section of the Z boson on its mass peak ($\sigma^0_{\rm had}$). The decomposition of the error on N_ν is given by [102]

$$\delta N_\nu \simeq 10.5\frac{\delta n_{\rm had}}{n_{\rm had}} \oplus 3.0\frac{\delta n_{\rm lept}}{n_{\rm lept}} \oplus 7.5\frac{\delta\mathcal{L}}{\mathcal{L}}, \tag{11.18}$$

where $\delta n_{\rm had}/n_{\rm had}$, $\delta n_{\rm lep}/n_{\rm lep}$ and $\delta\mathcal{L}/\mathcal{L}$ represent the total errors on the number of selected hadronic and leptonic events and on the luminosity determination. The symbol $\oplus$ denotes the sum in quadrature. The final theoretical uncertainty of 0.061% [103]-(0.054% [104, 105]), available at the end of LEP operation [102] for the small angle Bhabha process, reflects in a systematic uncertainty of 0.15%, i.e. $\sim$ 50% of the total uncertainty of 0.27%, on N_ν.

The precision of 0.1% in N_ν measurement with the indirect method can be achieved in CEPC measurement, which improves the current precision by a factor of three. Benefitting from the recent development of luminosity detector technology, the uncertainty due to luminosity can be reduced to 0.05%. The theoretical uncertainty of predictions for the small angle Bhabha process can be reduced, conservatively, to 0.05% or below, mainly due to the recent progress in the evaluation of the hadronic contribution to the photon vacuum polarization [106–108]. This uncertainy can be pushed down even further, close to the 0.01% scale, once the NNLO QED predictions are matched to higher order soft/collinear contributions.

Direct method using $e^+e^- \to \nu\bar{\nu}\gamma$ events The direct method is based on the process $e^+e^- \to \nu\bar{\nu}\gamma$, whose cross section is proportional to N_ν, with the typical signature in the detector of only one photon with energy $E_\gamma = (s - M_Z^2)/(2\sqrt{s})$. The most precise direct N_ν measurements at LEP were carried out by the L3 collaboration and Delphi collaboration. By combining the direct measurements at LEP, the current experimental result is $N_\nu = 2.92 \pm 0.05$ (Fulvio: I remember an error of the form $\pm 0.05 \pm 0.04$ but I am not sure). The statistical uncertainty of N_ν in the previous measurement is 1.7%. The main systematic uncertainty from the L3 measurement includes the uncertainty in single photon trigger efficiency (0.6%), and photon identification efficiency (0.3%), and the uncertainty in identifying the converted photons (0.5%). The systematic uncertainty of theoretical origin is due to the knowledge of higher order radiative corrections to the process $e^+e^- \to \nu\bar{\nu}\gamma$, within the SM. At LEP an uncertainty at the % level was achieved through complete tree-level matrix elements for $e^+e^- \to \nu\bar{\nu}\gamma$ and $e^+e^- \to \nu\bar{\nu}\gamma\gamma$, properly combined with higher orders initial state multiphoton radiation [109]. The bulk of the electroweak corrections were accounted for through running couplings on top of the tree-level matrix elements or through $\mathcal{O}(\alpha)$ corrections to $Z\gamma$ production [109–114]. A first calculation including one-loop electroweak corrections appeared in Ref. [115], with an estimated uncertainty of the order of 1%

An overall precision of 0.2% can be achieved for the direct measurement of N_ν at CEPC, and it will improve the current precision by a factor of 10. Due to the excellent performance of the CEPC inner tracker, the uncertainty due to converted photons' selection efficiency is expected to be negligible. The granularity of the CEPC EM calorimeter is expected to be 10 to 100 times better than the detectors at LEP. Therefore photons can be identified with high purity with loose EM shower shape based selection. The uncertainty of photon efficiency can be reduced to less than 0.05%. On the theoretical side, the control of electroweak corrections should be moved to the two-loop level, in addition to the matching to higher order QED corrections. Given the recent progress in the calculation of NNLO corrections for $2 \to 3$ processes at the LHC, the program looks feasible. It would be also worth to investigate the ratio $\sigma(e^+e^- \to \nu\bar{\nu}\gamma)/\sigma(e^+e^- \to \mu^+\mu^-\gamma)$, where (large) part of the ISR radiative corrections are expected to cancel, provided the luminosity allows enough statistics for the process $e^+e^- \to \mu^+\mu^-\gamma$.

11.2.2 Measurement of the W boson mass

In e^+e^- collisions, W bosons are mainly produced in pairs, through the reaction $e^+e^- \to W^+W^-$. At threshold, $\sqrt{s} \sim 2m_W$, the cross section of this process is very sensitive to m_W, providing a natural method for the measurement of this parameter. At centre-of-

mass energies above the W^+W^- production threshold, m_W can be determined from the peak of the invariant mass distribution of its decay products. Both methods are very complementary : while the former requires an accurate theoretical prediction of the W^+W^- production cross section as a function of m_W and a precise determination of the collider luminosity, the latter mostly relies on a good resolution in the reconstruction of the hadronic invariant mass, and a precise control of the detector calibration.

Both methods have been used at LEP. With only about 40 pb^{-1} collected by the four LEP experiments at $\sqrt{s} \sim 161.3$ GeV and given the low cross section at threshold, the former is limited by a significant statistical uncertainty of about 200 MeV. The final state reconstruction method exploited the full LEP2 dataset, about 2.6 fb^{-1} collected between $\sqrt{s} \sim 161.3$ GeV and 206 GeV, and achieved a total uncertainty of 33 MeV. While this measurement used both the $W^+W^- \to \ell\nu qq$ and $W^+W^- \to qqqq$ channels, the fully hadronic channel is limited by uncertainties in the modeling of hadronization and interactions between the decaying W bosons, and the semi-leptonic final state dominates the precision of the final result.

Accounting for results from the CDF and D0 experiments at the TeVatron, and from ATLAS at the LHC, the present world-average value of m_W has an uncertainty estimated between 12 and 13 MeV. The uncertainty is expected to fall below 10 MeV when including final LHC measurement results. A natural goal for CEPC is thus to reach a precision well below 5 MeV, making optimal use of W^+W^- cross section data around $\sqrt{s} \sim 161$ GeV, and of the final state invariant mass distributions at $\sqrt{s} \sim 240$ GeV. The achievable precision of both methods is described below.

Determination of m_W and Γ_W from the W^+W^- production cross section

In this section, the possibility of extracting the W boson mass and width from the production cross section is explored. The study assumes a total integrated luminosity of $L = 3.2$ ab^{-1}, which can be collected in one year, assuming an instantaneous luminosity of 2.5ab^{-1}. For this study, the GENTLE program version 2.0 [] is used to calculate $\sigma_{W^+W^-}$ as a function of the centre-of-mass energy, m_W and Γ_W. The behaviour of the cross section as a function of the centre-of-mass energy, $E_{\rm c.m.}$, is illustrated in Figure 11.16.

The statistical sensitivity of the measurement is optimized in the following way:

- the total integrated luminosity is shared between one, two or three values of $E_{\rm c.m.}$;
- in the two-point scenario, a three-dimensional optimization is performed, scanning both values $E_{\rm c.m.}$ in steps of 100 MeV, and the fraction of integrated luminosity spent at each point in steps of 5%;
- in the three point scenario, a corresponding five-dimensional optimization is performed.

Sources of systematic uncertainties can be categorized as correlated or uncorrelated between measurements at different values of $E_{\rm c.m.}$. The following sources are considered:

- Uncorrelated sources: this category includes the uncertainties associated with the beam energy calibration, and the beam energy spread. For the former, an uncertainty of 0.5 MeV is assumed, and the latter can be controlled to 1%, at each value of $E_{\rm c.m.}$;;
- Correlated sources: this category includes the uncertainties from the integrated luminosity, the detection efficiency, the purity, and the theoretical W-pair cross section. It

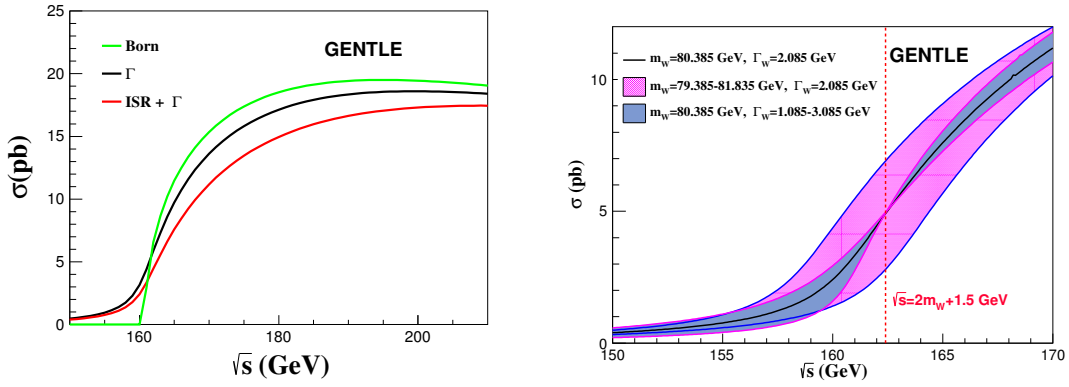

(a) (b)

Figure 11.16: W^+W^- production as a function of $E_{\mathrm{c.m.}}$, (a) at Born level, including finite width effects, and including initial state radiation corrections; and (b) for a range of values of m_W and Γ_W.

is assumed that these sources sum up to a total relative uncertainty of 2×10^{-4} on the ratio between measured and predicted cross sections.

The result of the statistical optimization leads to a three-point scenario, with most of the data collected at energies of 157.5 and 162.5 GeV. A summary of given in Table 11.10. The final measurement uncertainties, assuming this optimal scenario and systematic uncertainties are describea above, are collected in Table 11.11. We conclude that an uncertainty of about 1 MeV can be achieved for m_W, and 3 MeV for Γ_W. While the former is still dominated by statistical uncertainties, the latter is significantly affected by the beam energy spread.

Table 11.10: The proposed 3 $e^+e^- \to W^+W^-$ threshold scan runs and their integrated luminosity, for a total integrated luminosity of 3.2 ab^{-1}.

Beam Energy (GeV)	Luminosity (ab^{-1})
157.5	1.0
161.5	0.2
162.5	2.0

Determination of m_W by kinematic reconstruction

According to LEP experience, the fully hadronic final state is limited by systematic uncertainties that are difficult to control using data. The present section therefore concentrates on the semi-leptonic final states, where one W boson decays to an electron or a muon, while the other decays hadronically. An estimate of the m_W measurement potential is presented based on $WW \to \ell\nu qq$ events ($\ell = e, \mu$), and the potential of hadronic Z boson decays to calibrate the measurement of the hadronic invariant mass is evaluated.

The W^+W^- cross section at $\sqrt{s} = 240$ GeV is about 17 pb. For an integrated luminosity of 5.6 ab^{-1}, this corresponds to a sample of about 95×10^6 W boson pairs,

Table 11.11: Dominant systematic uncertainties in the measurement of m_W and Γ_w, using the production cross section at threshold at CEPC. All numbers are given in MeV.

Observable	m_W	Γ_W
Sources or uncertainty (MeV)		
Statistics	0.8	1.1
Beam energy	0.4	0.5
Beam spread	–	0.9
Corr. syst.	0.5	0.1
Total	1.0	2.9

Table 11.12: Efficiency of the event selection criteria in the $WW \to \mu\nu qq$ channel.

Selection	Efficiency (%)	Nb. of events
$E_\mu > 10$ GeV, $\lvert\cos(\theta_\mu)\rvert < 0.995$	85.4	11.9×10^6
$p_{\mathrm{T}}^{\mathrm{miss}} > 10$ GeV	82.0	11.5×10^6
$m_{\mathrm{vis}} > 0.5 \times \sqrt{s}$	75.6	10.6×10^6
b-tag score < 0.5	71.3	10.0×10^6

and 28×10^6 $WW \to \ell\nu qq$ events. For ZZ production, the cross section is about 1 pb, yielding about 5.6×10^6 Z boson pairs, and 1.6×10^6 $ZZ \to \nu\nu qq$ events. While the Z boson mass is more precisely known than m_W and the $Z \to qq$ resonance provides a useful check of the detector calibration, the sample is small compared to the $W \to qq$ one, and the presence of heavy quarks in Z boson decays has to be accounted for when deriving constraints on the hadronic response in W events.

W^+W^- event selection criteria will require the presence of one reconstructed electron or muon with energy greater than 10 GeV, and missing transverse momentum greater than 10 GeV. The invariant mass of all reconstructed final state particles should exceed 50% of the centre-of-mass energy; the hadronic system, $i.e.$ the set of all particles excluding the selected lepton, is clustered into two jets and its invariant mass distribution is used to probe the W boson mass. A b-tag veto can be applied to enrich the selected samples in light-quark decays, and reduce the systematic differences between the W and Z boson samples. In the $\mu\nu qq$ channel, the efficiency of these criteria is 71.3%, as shown in Table 11.12. Corresponding selection efficiciencies for $ZZ \to \nu\nu qq$ events are shown in Table 11.13. The corresponding hadronic invariant mass distributions are shown in Figure 11.17. After these selections, backgrounds are expected to be small and play a negligible role in the measurement.

Given the large expected statistics, the availability of the $e\nu qq$ channel and the good resolution in the invariant mass distribution, the statistical sensitivity of the m_W measurement is better than 1 MeV. Using the $ZZ \to \nu\nu qq$ sample alone, the detector calibration

Table 11.13: Efficiency of the event selection criteria in the $ZZ \to \nu\nu qq$ channel.

Selection	Efficiency (%)	Nb. of events
Missing Energy > 35 GeV	69.9%	1.12×10^6
$m_{\text{vis}} > 0.2 \times \sqrt{s}$	66.4%	1.06×10^6
b-tag score < 0.5	50.1%	0.80×10^6

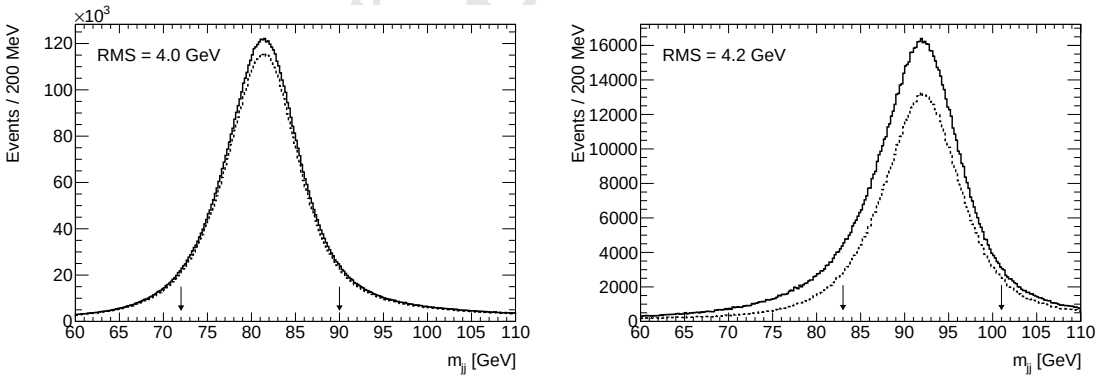

(a) (b)

Figure 11.17: Dijet invariant mass distributions for (a) $WW \to \mu\nu qq$ events, without and with a b-jet veto cut, and correspondingly for (b) $ZZ \to \nu\nu qq$ events. The RMS of the distributions are quoted for the interval indicated by the arrows.

can be checked to about 6 MeV. Further calibration samples can be extracted from radiative return events ($e^+e^- \to Z\gamma$). In addition, runs at $\sqrt{s} = 91.2$ GeV will be required for general detector alignment, monitoring and calibrations; these runs will provide copious samples of hadronic Z boson decays that will further constrain the hadronic calibration. Combining all information, the statistical precision of the calibration samples will match that of the W boson decays.

The statistical sensitivity can be further enhanced using kinematics fits, constraining the reconstructed lepton and jet momenta to match the known center of mass energy ($\Sigma_i E_i = \sqrt{s}$) and total event momentum ($\Sigma_i \vec{p}_i = \vec{0}$). This method was routinely used at LEP, gaining a factor of about 3 in the statistical precision, at the expense of an explicit dependence of the measurement on the beam energy. Given the expected statistical precision at CEPC, this refinement seems unnecessary here. In these conditions, the beam energy calibration, and initial state radiation are expected to contribute less than 1 MeV to the measurement uncertainty. Further significant sources of systematic uncertainty include the lepton momentum scale, which can be reduced using Z boson decays as discussed above, and the modelling of hadronization. The latter can be strongly reduced using measurements of rates and distributions of identified particles, in both Z and W boson decays.

The primary sources of uncertainty are summarized in Table 11.14, comparing LEP and CEPC. A total uncertainty at the level of 3 MeV seems reachable.

Table 11.14: Dominant systematic uncertainties in the measurement of m_W using direct reconstruction, as achieved at LEP, and expected at CEPC.

Collider	LEP	CEPC
$\sqrt{s}$ (GeV)	180–203	240
$\int \mathcal{L}$	2.6 fb^{-1}	5.6 ab^{-1}
Channels	$\ell\nu qq, qqqq$	$\ell\nu qq$
Sources or uncertainty (MeV)		
Statistics	25	1.0
Beam energy	9	1.0
Hadronization	13	1.5
Radiative corrections	8	1.0
Detector effects	10	1.5
Total	33	3.0

11.2.3 Oblique Parameter

Using the estimated experimental capabilities of CEPC, we carry out a fit to determine the sensitivity of CEPC to the oblique electroweak parameters S and T [116, 117]. We omit the parameter U that is often included in fits as it arises from a dimension-8 operator in theories with a weakly coupled Higgs boson [118], and so is expected to be much smaller

Obs.	Value	Exp. Uncertainty	Th. Uncertainty
$\alpha_s(M_Z^2)$	0.1185	1.0×10^{-4} [36]	1.5×10^{-4}
$\Delta\alpha^{(5)}_{\rm had}(m_Z^2)$	276.5×10^{-4}	4.7×10^{-5} [120]	–
m_Z [GeV]	91.1875	**0.0005**	–
m_t [GeV] (pole)	173.34	0.6 [121]	0.25 [122]
m_h [GeV]	125.14	0.1 [120]	–
m_W [GeV]	80.358617 [123]	**0.001**	1.4×10^{-3}
$A_{\rm FB}^{0,b}$	0.102971 [124, 125]	$\mathbf{1.0 \times 10^{-4}}$	8.3×10^{-5}
$A_{\rm FB}^{0,\mu}$	0.016181 [124]	$\mathbf{4.9 \times 10^{-5}}$	2.6×10^{-5}
$A_{\rm FB}^{0,e}$	0.016181 [124]	$\mathbf{8.1 \times 10^{-5}}$	2.6×10^{-5}
Γ_Z [GeV]	2.494682 [126]	**0.0005**	2×10^{-4}
$R_b \equiv \Gamma_b/\Gamma_{\rm had}$	0.2158459 [126]	$\mathbf{4.3 \times 10^{-5}}$	7×10^{-5}
$R_\ell \equiv \Gamma_{\rm had}/\Gamma_\ell$	20.751285 [126]	$\mathbf{2.1 \times 10^{-3}}$	1.5×10^{-3}
$\Gamma_{Z\to\rm inv}$ [GeV]	0.167177 [126]	$\mathbf{8.4 \times 10^{-5}}$	–

Table 11.15: Inputs to the CEPC fit. Numbers in bold are expected experimental uncertainties from CEPC measurements. Other entries reflect anticipated uncertainties at the time of CEPC operation. The numbers in the "Value" column for the first five parameters are current measurements; those below the horizontal line give the Standard Model calculated value as a function of the five parameters. Theory uncertainties are future projections assuming complete 3-loop calculations, based on estimates in Refs. [123, 124, 127, 128].

than S and T which arise at dimension 6. In the electroweak fit we treat the following five well-measured observables as parameters, from which the Standard Model prediction for all of the other observables may be computed:

$$\alpha_s(m_Z^2), \Delta\alpha^{(5)}_{\rm had}(m_Z^2), m_Z, m_t, m_h. \tag{11.19}$$

Of these parameters, CEPC is expected to significantly improve our knowledge of m_Z. The primary power of CEPC is in improving the precision of measurements of other observables, including m_W and $\sin^2\theta^\ell_{\rm eff}$, which may be derived from these parameters. Readers interested in more background information may find a thorough and up-to-date review of the status of electroweak precision in Ref. [119].

The inputs to the fit are listed in Table 11.15. Notice that we have performed the fit directly using forward-backward asymmetry parameters $A_{\rm FB}^{0,f}$ as inputs, rather than the derived quantities $\sin^2\theta^f_{\rm eff}$ that were used in earlier work [129, 130]. The forward-backward asymmetries more directly reflect the experimental measurements; on the other hand, theoretical predictions are often expressed in terms of the effective weak mixing angles [124, 125]. They are related through the asymmetry parameters A_f:

$$A_f = \frac{1 - 4|Q_f|\sin^2\theta^f_{\rm eff}}{1 - 4|Q_f|\sin^2\theta^f_{\rm eff} + 8|Q_f|^2\sin^4\theta^f_{\rm eff}}, \tag{11.20}$$

$$A_{\rm FB}^{0,f} = \frac{3}{4}A_e A_f. \tag{11.21}$$

There is an extensive literature on the computation of the S and T dependence of observables (e.g. [116, 117, 131]); a convenient tabulation of the results may be found in Appendix A of [132]. Assembling these results, we obtain a prediction of the observables in terms of the five input parameters, S, and T. In the fit we compute a profile likelihood, floating the five parameters to obtain the maximum likelihood for given S and T.

The fit is performed following [129] (which in turn relied on [133–135]): in constructing a likelihood we treat experimental uncertainties as Gaussian but theory uncertainties as a flat prior, leading to an effective χ^2 function

$$\chi^2_{\rm mod} = \sum_j \left[-2\log\left(\mathrm{erf}\left(\frac{M_j - O_j + \delta_j}{\sqrt{2}\sigma_j} \right) - \mathrm{erf}\left(\frac{M_j - O_j - \delta_j}{\sqrt{2}\sigma_j} \right) \right) - 2\log\left(\sqrt{2\pi}\sigma_j \right) \right], \tag{11.22}$$

with M_j the measured value, O_j the prediction for the observable, σ_j the experimental uncertainty, and δ_j the theory uncertainty.

Our estimates of theory uncertainties assume that full three-loop computations of the parametric dependence of observables in the Standard Model will be completed. The remaining uncertainties are estimated based on [123, 124, 127, 128]. In the case of the W mass measurement, an uncertainty of 1 MeV from the computation of the near-threshold WW cross section is added in quadrature with the estimated four-loop theory uncertainty in the observable itself.

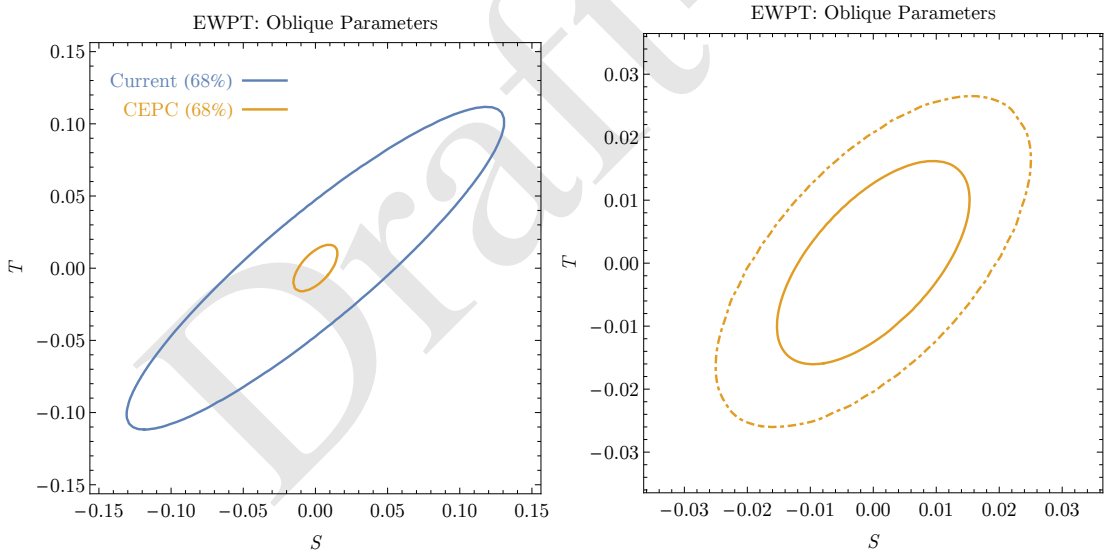

Figure 11.18: CEPC constraints on the oblique parameters S and T. Left panel: comparison of CEPC projection (orange) to current constraints (blue). Contours are 68% confidence level. Right panel: a closer look at the CEPC fit, showing 68% confidence level (solid) and 95% confidence level (dashed).

The results of the fit are depicted in Fig. 11.18. Solid contours are 68% confidence level curves, meaning $\Delta\chi^2_{\rm mod} = 2.30$; the dashed contour is 98% C.L. ($\Delta\chi^2_{\rm mod} = 6.18$). For clarity we have assumed that the measured central values will precisely agree with Standard Model predictions. In particular, the contour depicting current constraints is artificially displaced to be centered at the origin, though it accurately reflects the size of the uncertainties in current data. From the figure, we see that the results of CEPC will significantly shrink the error bars on the S and T parameters relative to currently available data.

By fixing $T = 0$ or $S = 0$, we can also obtain the projected one-parameter 68% C.L. bounds on S and T. As one-parameter fits these correspond to $\Delta\chi^2_{\rm mod} = 1.0$. We obtain:

$$|S| < 3.6 \times 10^{-2}\ \text{(current)}, \quad 7.9 \times 10^{-3}\ \text{(CEPC projection)}, \tag{11.23}$$

$$|T| < 3.1 \times 10^{-2}\ \text{(current)}, \quad 8.4 \times 10^{-3}\ \text{(CEPC projection)}. \tag{11.24}$$

Thus CEPC will achieve about a factor of 4 additional precision on both of the electroweak oblique parameters.

References

[1] ATLAS Collaboration Collaboration, *Observation of a new particle in the search for the Standard Model Higgs boson with the ATLAS detector at the LHC*, Phys. Lett. B **716** (2012) 1, arXiv:1207.7214 [hep-ex].

[2] CMS Collaboration Collaboration, *Observation of a new boson at a mass of 125 GeV with the CMS experiment at the LHC*, Phys. Lett. **B716** (2012) 30, arXiv:1207.7235 [hep-ex].

[3] ATLAS Collaboration, G. Aad et al., *Measurements of Higgs boson production and couplings in diboson final states with the ATLAS detector at the LHC*, Phys. Lett. **B726** (2013) 88–119, arXiv:1307.1427 [hep-ex]. [Erratum: Phys. Lett.B734,406(2014)].

[4] ATLAS Collaboration, G. Aad et al., *Evidence for the spin-0 nature of the Higgs boson using ATLAS data*, Phys. Lett. **B726** (2013) 120–144, arXiv:1307.1432 [hep-ex].

[5] CMS Collaboration Collaboration, S. Chatrchyan et al., *Observation of a new boson with mass near 125 GeV in pp collisions at $\sqrt{s}$ = 7 and 8 TeV*, JHEP **1306** (2013) 081, arXiv:1303.4571 [hep-ex].

[6] CMS Collaboration Collaboration, *Evidence for the direct decay of the 125 GeV Higgs boson to fermions*, Nature Phys. **10** (2014) , arXiv:1401.6527 [hep-ex].

[7] CMS Collaboration, V. Khachatryan et al., *Constraints on the spin-parity and anomalous HVV couplings of the Higgs boson in proton collisions at 7 and 8 TeV*, Phys. Rev. **D92** (2015) no. 1, 012004, arXiv:1411.3441 [hep-ex].

[8] ATLAS, CMS Collaboration, G. Aad et al., *Combined Measurement of the Higgs Boson Mass in pp Collisions at $\sqrt{s} = 7$ and 8 TeV with the ATLAS and CMS Experiments*, Phys. Rev. Lett. **114** (2015) 191803, arXiv:1503.07589 [hep-ex].

[9] ATLAS, CMS Collaboration, G. Aad et al., *Measurements of the Higgs boson production and decay rates and constraints on its couplings from a combined ATLAS and CMS analysis of the LHC pp collision data at $\sqrt{s} = 7$ and 8 TeV*, JHEP **08** (2016) 045, arXiv:1606.02266 [hep-ex].

[10] F. An, Y. Bai, C. Chen, X. Chen, Z. Chen, J. Guimaraes da Costa, and Z. Cui, *Precision Higgs Boson Physics at the CEPC*, TBD (2018) , arXiv:nnnn.nnnn.

[11] LHC Higgs Cross Section Working Group, S. Dittmaier, C. Mariotti, G. Passarino and R. Tanaka (Eds.), *Handbook of LHC Higgs Cross Sections: 1. Inclusive Observables*, arXiv:1101.0593 [hep-ph].

[12] LHC Higgs Cross Section Working Group, *Handbook of LHC Higgs Cross Sections: 2. Differential Distributions*, arXiv:1201.3084 [hep-ph].

[13] W. Kilian, T. Ohl, and J. Reuter, *WHIZARD: Simulating Multi-Particle Processes at LHC and ILC*, Eur. Phys. J. **C71** (2011) 1742, arXiv:0708.4233 [hep-ph].

[14] Y. Haddad, *Feasibility of a minimum bias analysis of $e^+e^- \to ZH \to q\bar{q} + X$ at a 250 GeV ILC*, arXiv:1404.3164 [hep-ph].

[15] M. Oreglia, *A Study of the Reactions $\psi' \to \gamma\gamma\psi$*, SLAC-R-0236 (1980) . http://www.slac.stanford.edu/cgi-wrap/getdoc/slac-r-23\6.pdf.

[16] ALEPH, DELPHI, L3, OPAL, LEP Electroweak Collaboration, S. Schael et al., *Electroweak Measurements in Electron-Positron Collisions at W-Boson-Pair Energies at LEP*, Phys. Rept. **532** (2013) 119, arXiv:1302.3415 [hep-ex].

[17] J. Gao, *Probing light-quark Yukawa couplings via hadronic event shapes at lepton colliders*, JHEP **01** (2018) 038, arXiv:1608.01746 [hep-ph].

[18] LHC Higgs Cross Section Working Group Collaboration, A. David et al., *LHC HXSWG interim recommendations to explore the coupling structure of a Higgs-like particle*, arXiv:1209.0040 [hep-ph].

[19] LHC Higgs Cross Section Working Group Collaboration, J. R. Andersen et al., *Handbook of LHC Higgs Cross Sections: 3. Higgs Properties*, arXiv:1307.1347 [hep-ph].

[20] S. Dawson, A. Gritsan, H. Logan, J. Qian, C. Tully, et al., *Working Group Report: Higgs Boson*, arXiv:1310.8361 [hep-ex].

[21] CMS Collaboration Collaboration, *Search for the associated production of the Higgs boson with a top-quark pair*, JHEP **1409** (2014) 087, arXiv:1408.1682 [hep-ex].

[22] ATLAS Collaboration Collaboration, *Search for $H \to \gamma\gamma$ produced in association with top quarks and constraints on the Yukawa coupling between the top quark and the Higgs boson using data taken at 7 TeV and 8 TeV with the ATLAS detector*, Phys. Lett. **B740** (2015) 222, arXiv:1409.3122 [hep-ex].

[23] A. Banfi, A. Martin, and V. Sanz, *Probing top-partners in Higgs+jets*, JHEP **1408** (2014) 053, arXiv:1308.4771 [hep-ph].

[24] A. Azatov and A. Paul, *Probing Higgs couplings with high p_T Higgs production*, JHEP **1401** (2014) 014, arXiv:1309.5273 [hep-ph].

[25] C. Grojean, E. Salvioni, M. Schlaffer, and A. Weiler, *Very boosted Higgs in gluon fusion*, JHEP **1405** (2014) 022, arXiv:1312.3317 [hep-ph].

[26] M. Buschmann, C. Englert, D. Goncalves, T. Plehn, and M. Spannowsky, *Resolving the Higgs-Gluon Coupling with Jets*, Phys. Rev. **D90** (2014) 013010, arXiv:1405.7651 [hep-ph].

[27] J. Ellis, V. Sanz, and T. You, *Complete Higgs Sector Constraints on Dimension-6 Operators*, JHEP **1407** (2014) 036, arXiv:1404.3667 [hep-ph].

[28] T. Han, Z. Liu, and J. Sayre, *Potential Precision on Higgs Couplings and Total Width at the ILC*, Phys. Rev. **D89** (2014) 113006, arXiv:1311.7155 [hep-ph].

[29] M. Klute, R. Lafaye, T. Plehn, M. Rauch, and D. Zerwas, *Measuring Higgs Couplings at a Linear Collider*, Europhys. Lett. **101** (2013) 51001, arXiv:1301.1322 [hep-ph].

[30] M. E. Peskin, *Estimation of LHC and ILC Capabilities for Precision Higgs Boson Coupling Measurements*, arXiv:1312.4974 [hep-ph].

[31] K. Fujii et al., *Physics Case for the 250 GeV Stage of the International Linear Collider*, arXiv:1710.07621 [hep-ex].

[32] T. Barklow, K. Fujii, S. Jung, R. Karl, J. List, T. Ogawa, M. E. Peskin, and J. Tian, *Improved Formalism for Precision Higgs Coupling Fits*, arXiv:1708.08912 [hep-ph].

[33] ATLAS Collaboration, *Projections for measurements of Higgs boson signal strengths and coupling parameters with the ATLAS detector at a HL-LHC*, ATL-PHYS-PUB-2014-016 (2014) . http://cds.cern.ch/record/1956710.

[34] A. Denner, S. Heinemeyer, I. Puljak, D. Rebuzzi, and M. Spira, *Standard Model Higgs-Boson Branching Ratios with Uncertainties*, Eur. Phys. J. **C71** (2011) 1753, arXiv:1107.5909 [hep-ph].

[35] L. G. Almeida, S. J. Lee, S. Pokorski, and J. D. Wells, *Study of the standard model Higgs boson partial widths and branching fractions*, Phys. Rev. **D89** (2014) 033006, arXiv:1311.6721 [hep-ph].

[36] G. P. Lepage, P. B. Mackenzie, and M. E. Peskin, *Expected Precision of Higgs Boson Partial Widths within the Standard Model*, arXiv:1404.0319 [hep-ph].

[37] C. Bernaciak, T. Plehn, P. Schichtel, and J. Tattersall, *Spying an invisible Higgs boson*, Phys. Rev. **D91** (2015) 035024, arXiv:1411.7699 [hep-ph].

[38] J. Ellis and T. You, *Sensitivities of Prospective Future e+e- Colliders to Decoupled New Physics*, JHEP **03** (2016) 089, arXiv:1510.04561 [hep-ph].

[39] J. Ellis, P. Roloff, V. Sanz, and T. You, *Dimension-6 Operator Analysis of the CLIC Sensitivity to New Physics*, arXiv:1701.04804 [hep-ph].

[40] G. Durieux, C. Grojean, J. Gu, and K. Wang, *The leptonic future of the Higgs*, JHEP **09** (2017) 014, arXiv:1704.02333 [hep-ph].

[41] T. Barklow, K. Fujii, S. Jung, M. E. Peskin, and J. Tian, *Model-Independent Determination of the Triple Higgs Coupling at e+e- Colliders*, arXiv:1708.09079 [hep-ph].

[42] S. Di Vita, G. Durieux, C. Grojean, J. Gu, Z. Liu, G. Panico, M. Riembau, and T. Vantalon, *A global view on the Higgs self-coupling at lepton colliders*, arXiv:1711.03978 [hep-ph].

[43] W. H. Chiu, S. C. Leung, T. Liu, K.-F. Lyu, and L.-T. Wang, *Probing 6D Operators at Future e^-e^+ Colliders*, arXiv:1711.04046 [hep-ph].

[44] M. Beneke, D. Boito, and Y.-M. Wang, *Anomalous Higgs couplings in angular asymmetries of $H \to Z\ell^+\ell^-$ and $e^+ e^- \to HZ$*, JHEP **11** (2014) 028, arXiv:1406.1361 [hep-ph].

[45] N. Craig, J. Gu, Z. Liu, and K. Wang, *Beyond Higgs Couplings: Probing the Higgs with Angular Observables at Future $e^+ e^-$ Colliders*, JHEP **03** (2016) 050, arXiv:1512.06877 [hep-ph].

[46] S. M. Barr and A. Zee, *Electric Dipole Moment of the Electron and of the Neutron*, Phys. Rev. Lett. **65** (1990) 21–24. [Erratum: Phys. Rev. Lett.65,2920(1990)].

[47] J. Fan and M. Reece, *Probing Charged Matter Through Higgs Diphoton Decay, Gamma Ray Lines, and EDMs*, JHEP **06** (2013) 004, arXiv:1301.2597 [hep-ph].

[48] ACME Collaboration, J. Baron et al., *Order of Magnitude Smaller Limit on the Electric Dipole Moment of the Electron*, Science **343** (2014) 269–272, arXiv:1310.7534 [physics.atom-ph].

[49] Y. T. Chien, V. Cirigliano, W. Dekens, J. de Vries, and E. Mereghetti, *Direct and indirect constraints on CP-violating Higgs-quark and Higgs-gluon interactions*, JHEP **02** (2016) 011, arXiv:1510.00725 [hep-ph]. [JHEP02,011(2016)].

[50] R. Harnik, A. Martin, T. Okui, R. Primulando, and F. Yu, *Measuring CP violation in $h \to \tau^+\tau^-$ at colliders*, Phys. Rev. **D88** (2013) no. 7, 076009, arXiv:1308.1094 [hep-ph].

[51] K. Hagiwara, S. Ishihara, R. Szalapski, and D. Zeppenfeld, *Low-energy effects of new interactions in the electroweak boson sector*, Phys. Rev. **D48** (1993) 2182–2203.

[52] G. Gounaris et al., *Triple gauge boson couplings*, in *AGS / RHIC Users Annual Meeting Upton, New York, June 15-16, 1995*, pp. 525–576. 1996. arXiv:hep-ph/9601233 [hep-ph]. http://alice.cern.ch/format/showfull?sysnb=0215385. [,525(1996)].

[53] L. Bian, J. Shu, and Y. Zhang, *Prospects for Triple Gauge Coupling Measurements at Future Lepton Colliders and the 14 TeV LHC*, JHEP **09** (2015) 206, arXiv:1507.02238 [hep-ph].

[54] A. Falkowski, *Higgs Basis: Proposal for an EFT basis choice for LHC HXSWG*, LHCHXSWG-INT-2015-001 (March, 2015) . https://cds.cern.ch/record/2001958.

[55] *Projections for measurements of Higgs boson cross sections, branching ratios and coupling parameters with the ATLAS detector at a HL-LHC*, ATL-PHYS-PUB-2013-014 (Oct, 2013) . https://cds.cern.ch/record/1611186.

[56] *HL-LHC projections for signal and background yield measurements of the $H \to \gamma\gamma$ when the Higgs boson is produced in association with t quarks, W or Z bosons*, ATL-PHYS-PUB-2014-012 (Jul, 2014) . https://cds.cern.ch/record/1741011.

[57] *Update of the prospects for the $H \to Z\gamma$ search at the High-Luminosity LHC*, ATL-PHYS-PUB-2014-006 (May, 2014) . https://cds.cern.ch/record/1703276.

[58] *Prospects for the study of the Higgs boson in the VH(bb) channel at HL-LHC*, ATL-PHYS-PUB-2014-011 (Jul, 2014) . https://cds.cern.ch/record/1740962.

[59] *Studies of the VBF $H \to \tau_l\tau_{had}$ analysis at High Luminosity LHC conditions*, ATL-PHYS-PUB-2014-018 (Oct, 2014) . https://cds.cern.ch/record/1956732.

[60] A. Falkowski, M. Gonzalez-Alonso, A. Greljo, and D. Marzocca, *Global constraints on anomalous triple gauge couplings in effective field theory approach*, Phys. Rev. Lett. **116** (2016) no. 1, 011801, arXiv:1508.00581 [hep-ph].

[61] A. Butter, O. J. P. Éboli, J. Gonzalez-Fraile, M. C. Gonzalez-Garcia, T. Plehn, and M. Rauch, *The Gauge-Higgs Legacy of the LHC Run I*, JHEP **07** (2016) 152, arXiv:1604.03105 [hep-ph].

[62] R. Contino, A. Falkowski, F. Goertz, C. Grojean, and F. Riva, *On the Validity of the Effective Field Theory Approach to SM Precision Tests*, JHEP **07** (2016) 144, arXiv:1604.06444 [hep-ph].

[63] A. Falkowski, M. Gonzalez-Alonso, A. Greljo, D. Marzocca, and M. Son, *Anomalous Triple Gauge Couplings in the Effective Field Theory Approach at the LHC*, JHEP **02** (2017) 115, arXiv:1609.06312 [hep-ph].

[64] Z. Zhang, *Time to Go Beyond Triple-Gauge-Boson-Coupling Interpretation of W Pair Production*, Phys. Rev. Lett. **118** (2017) no. 1, 011803, arXiv:1610.01618 [hep-ph].

[65] ATLAS Collaboration, *Search for the Standard Model Higgs and Z Boson decays to $J/\psi\,\gamma$: HL-LHC projections*, ATL-PHYS-PUB-2015-043 (Sep, 2015) . http://cds.cern.ch/record/2054550.

[66] G. T. Bodwin, F. Petriello, S. Stoynev, and M. Velasco, *Higgs boson decays to quarkonia and the $H\bar{c}c$ coupling*, Phys. Rev. **D88** (2013) no. 5, 053003, arXiv:1306.5770 [hep-ph].

[67] G. Perez, Y. Soreq, E. Stamou, and K. Tobioka, *Constraining the charm Yukawa and Higgs-quark coupling universality*, Phys. Rev. **D92** (2015) no. 3, 033016, arXiv:1503.00290 [hep-ph].

[68] I. Brivio, F. Goertz, and G. Isidori, *Probing the Charm Quark Yukawa Coupling in Higgs+Charm Production*, Phys. Rev. Lett. **115** (2015) no. 21, 211801, arXiv:1507.02916 [hep-ph].

[69] F. Bishara, U. Haisch, P. F. Monni, and E. Re, *Constraining Light-Quark Yukawa Couplings from Higgs Distributions*, arXiv:1606.09253 [hep-ph].

[70] L. M. Carpenter, T. Han, K. Hendricks, Z. Qian, and N. Zhou, *Higgs Boson Decay to Light Jets at the LHC*, Phys. Rev. **D95** (2017) no. 5, 053003, arXiv:1611.05463 [hep-ph].

[71] ATLAS Collaboration Collaboration, *Study of the double Higgs production channel $H(\to b\bar{b})H(\to \gamma\gamma)$ with the ATLAS experiment at the HL-LHC*, ATL-PHYS-PUB-2017-001, CERN, Geneva, Jan, 2017. https://cds.cern.ch/record/2243387.

[72] R. Contino et al., *Physics at a 100 TeV pp collider: Higgs and EW symmetry breaking studies*, CERN Yellow Report (2017) no. 3, 255–440, arXiv:1606.09408 [hep-ph].

[73] M. McCullough, *An Indirect Model-Dependent Probe of the Higgs Self-Coupling*, Phys. Rev. **D90** (2014) 015001, arXiv:1312.3322 [hep-ph].

[74] S. Di Vita, C. Grojean, G. Panico, M. Riembau, and T. Vantalon, *A global view on the Higgs self-coupling*, JHEP **09** (2017) 069, arXiv:1704.01953 [hep-ph].

[75] A. Azatov, R. Contino, G. Panico, and M. Son, *Effective field theory analysis of double Higgs boson production via gluon fusion*, Phys. Rev. **D92** (2015) no. 3, 035001, arXiv:1502.00539 [hep-ph].

[76] J. A. Aguilar-Saavedra, *A Minimal set of top anomalous couplings*, Nucl. Phys. **B812** (2009) 181–204, arXiv:0811.3842 [hep-ph].

[77] J. A. Aguilar-Saavedra, *A Minimal set of top-Higgs anomalous couplings*, Nucl. Phys. **B821** (2009) 215–227, arXiv:0904.2387 [hep-ph].

[78] Z. Liu, I. Low, and L.-T. Wang, *Higgs-Top Interactions at Future Circular e^+e^- Colliders*, arXiv:2018.nnnn.

[79] G. Li, H.-R. Wang, and S.-h. Zhu, *Probing CP-violating $h\bar{t}t$ coupling in $e^+e^- \to h\gamma$*, arXiv:1506.06453 [hep-ph].

[80] E. Vryonidou and C. Zhang, *Dimension-six electroweak top-loop effects in Higgs production and decay*, arXiv:1804.09766 [hep-ph].

[81] G. Durieux, *Precision constraints on the top-quark effective field theory at future lepton colliders*, PoS **DIS2017** (2018) 088, arXiv:1708.09849 [hep-ph].

[82] Y. Gao, A. V. Gritsan, Z. Guo, K. Melnikov, M. Schulze, and N. V. Tran, *Spin determination of single-produced resonances at hadron colliders*, Phys. Rev. **D81** (2010) 075022, arXiv:1001.3396 [hep-ph].

[83] S. Bolognesi, Y. Gao, A. V. Gritsan, K. Melnikov, M. Schulze, N. V. Tran, and A. Whitbeck, *On the spin and parity of a single-produced resonance at the LHC*, Phys. Rev. **D86** (2012) 095031, arXiv:1208.4018 [hep-ph].

[84] I. Anderson et al., *Constraining anomalous HVV interactions at proton and lepton colliders*, Phys. Rev. **D89** (2014) no. 3, 035007, arXiv:1309.4819 [hep-ph].

[85] J. Alwall, P. Demin, S. de Visscher, R. Frederix, M. Herquet, F. Maltoni, T. Plehn, D. L. Rainwater, and T. Stelzer, *MadGraph/MadEvent v4: The New Web Generation*, JHEP **09** (2007) 028, arXiv:0706.2334 [hep-ph].

[86] J. Erler, S. Heinemeyer, W. Hollik, G. Weiglein, and P. Zerwas, *Physics impact of GigaZ*, Phys.Lett. **B486** (2000) 125–133, arXiv:hep-ph/0005024 [hep-ph].

[87] ALEPH Collaboration, DELPHI Collaboration, L3 Collaboration, OPAL Collaboration, LEP Electroweak Working Group Collaboration, J. Alcaraz et al., *A Combination of preliminary electroweak measurements and constraints on the standard model*, arXiv:hep-ex/0612034 [hep-ex].

[88] L3 Collaboration, M. Acciarri et al., *Measurement of R(b) and Br($b \to$ lepton neutrino X) at LEP using double tag methods*, Eur. Phys. J. **C13** (2000) 47–61, arXiv:hep-ex/9909045 [hep-ex].

[89] OPAL Collaboration, G. Abbiendi et al., *A Measurement of R(b) using a double tagging method*, Eur. Phys. J. **C8** (1999) 217–239, arXiv:hep-ex/9810002 [hep-ex].

[90] DELPHI Collaboration Collaboration, P. Abreu et al., *A Precise measurement of the partial decay width ratio* $R_b^0 = \Gamma(b\bar{b})/\Gamma(\mathrm{had})$, Eur.Phys.J. **C10** (1999) 415–442.

[91] ALEPH Collaboration, R. Barate et al., *A Measurement of R(b) using mutually exclusive tags*, Phys. Lett. **B401** (1997) 163–175.

[92] SLD Collaboration Collaboration, K. Abe et al., *Measurement of the branching ratio of the Z0 into heavy quarks*, Phys.Rev. **D71** (2005) 112004, arXiv:hep-ex/0503005 [hep-ex].

[93] OPAL Collaboration, G. Abbiendi et al., *Precise determination of the Z resonance parameters at LEP: 'Zedometry'*, Eur. Phys. J. **C19** (2001) 587–651, arXiv:hep-ex/0012018 [hep-ex].

[94] DELPHI Collaboration, P. Abreu et al., *Cross-sections and leptonic forward backward asymmetries from the Z0 running of LEP*, Eur. Phys. J. **C16** (2000) 371–405.

[95] L3 Collaboration, M. Acciarri et al., *Measurements of cross-sections and forward backward asymmetries at the Z resonance and determination of electroweak parameters*, Eur. Phys. J. **C16** (2000) 1–40, arXiv:hep-ex/0002046 [hep-ex].

[96] ALEPH Collaboration, R. Barate et al., *Measurement of the Z resonance parameters at LEP*, Eur. Phys. J. **C14** (2000) 1–50.

[97] SLD Collaboration, K. Abe et al., *Direct measurements of A(b) and A(c) using vertex/kaon charge tags at SLD*, Phys. Rev. Lett. **94** (2005) 091801, arXiv:hep-ex/0410042 [hep-ex].

[98] ALEPH Collaboration Collaboration, A. Heister et al., *Measurement of A^b(FB) using inclusive b hadron decays*, Eur.Phys.J. **C22** (2001) 201–215, arXiv:hep-ex/0107033 [hep-ex].

[99] OPAL Collaboration Collaboration, G. Abbiendi et al., *Measurement of the b quark forward backward asymmetry around the Z0 peak using an inclusive tag*, Phys.Lett. **B546** (2002) 29–47, arXiv:hep-ex/0209076 [hep-ex].

[100] DELPHI Collaboration Collaboration, J. Abdallah et al., *Determination of A^b(FB) at the Z pole using inclusive charge reconstruction and lifetime tagging*, Eur.Phys.J. **C40** (2005) 1–25, arXiv:hep-ex/0412004 [hep-ex].

[101] L3 Collaboration Collaboration, M. Acciarri et al., *Measurement of the $e^+e^- \to Z \to b\bar{b}$ forward–backward asymmetry and the B0 anti-B0 mixing parameter using prompt leptons*, Phys.Lett. **B448** (1999) 152–162.

[102] ALEPH Collaboration, DELPHI Collaboration, L3 Collaboration, OPAL Collaboration, SLD Collaboration, LEP Electroweak Working Group, SLD Electroweak Group, SLD Heavy Flavour Group Collaboration, S. Schael et al., *Precision electroweak measurements on the Z resonance*, Phys.Rept. **427** (2006) 257–454, arXiv:hep-ex/0509008 [hep-ex].

[103] B. F. L. Ward, S. Jadach, M. Melles, and S. A. Yost, *New results on the theoretical precision of the LEP / SLC luminosity*, Phys. Lett. **B450** (1999) 262–266, arXiv:hep-ph/9811245 [hep-ph].

[104] G. Montagna, M. Moretti, O. Nicrosini, A. Pallavicini, and F. Piccinini, *Light pair corrections to small angle Bhabha scattering in a realistic set up at LEP*, Phys. Lett. **B459** (1999) 649–652, arXiv:hep-ph/9905235 [hep-ph].

[105] G. Montagna, M. Moretti, O. Nicrosini, A. Pallavicini, and F. Piccinini, *Light pair correction to Bhabha scattering at small angle*, Nucl. Phys. **B547** (1999) 39–59, arXiv:hep-ph/9811436 [hep-ph].

[106] F. Jegerlehner, *Variations on Photon Vacuum Polarization*, arXiv:1711.06089 [hep-ph].

[107] C. M. Carloni Calame, *Selected topics in electroweak physics at future e^+e^- colliders*, . CEPC Workshop, Wuhan, China.

[108] S. Jadach, *QED calculations for Bhabha luminometer*, . FCAL Workshop at INP-PAN, Cracow, Poland.

[109] G. Montagna, M. Moretti, O. Nicrosini, and F. Piccinini, *Single photon and multiphoton final states with missing energy at e^+e^- colliders*, Nucl. Phys. **B541** (1999) 31–49, arXiv:hep-ph/9807465 [hep-ph].

[110] Y. Kurihara, J. Fujimoto, T. Ishikawa, Y. Shimizu, and T. Munehisa, *(grc neutrino neutrino gamma) Event generator for the single photon and double photon emission associated with neutrino pair production*, Comput. Phys. Commun. **136** (2001) 250–268, arXiv:hep-ph/9908422 [hep-ph].

[111] A. Jacholkowska, J. Kalinowski, and Z. Was, *Higher order QED corrections to $e^+e^- \to \nu\bar{\nu}\gamma$ at LEP-2*, Eur. Phys. J. **C6** (1999) 485–491, arXiv:hep-ph/9803375 [hep-ph].

[112] S. Jadach, B. F. L. Ward, and Z. Was, *The Monte Carlo program KORALZ, for the lepton or quark pair production at LEP / SLC energies: From version 4.0 to version 4.04*, Comput. Phys. Commun. **124** (2000) 233–237, arXiv:hep-ph/9905205 [hep-ph].

[113] S. Jadach, B. F. L. Ward, and Z. Was, *The Monte Carlo program KORALZ, version 4.0, for the lepton or quark pair production at LEP / SLC energies*, Comput. Phys. Commun. **79** (1994) 503–522.

[114] S. Jadach, B. F. L. Ward, and Z. Was, *The Monte Carlo program KORALZ, version 3.8, for the lepton or quark pair production at LEP / SLC energies*, Comput. Phys. Commun. **66** (1991) 276–292.

[115] D. Bardin, S. Jadach, T. Riemann, and Z. Was, *Predictions for anti-nu nu gamma production at LEP*, Eur. Phys. J. **C24** (2002) 373–383, arXiv:hep-ph/0110371 [hep-ph].

[116] M. E. Peskin and T. Takeuchi, *A New constraint on a strongly interacting Higgs sector*, Phys.Rev.Lett. **65** (1990) 964–967.

[117] M. E. Peskin and T. Takeuchi, *Estimation of oblique electroweak corrections*, Phys.Rev. **D46** (1992) 381–409.

[118] J. Wudka, *Effective Lagrangians (for electroweak physics)*, in *4th Mexican Workshop on Particles and Fields Yucatan, Mexico, October 25-29, 1993*, pp. 61–106. 1994. arXiv:hep-ph/9405206 [hep-ph].

[119] J. Erler and F. Ayres, *Electroweak Model and Constraints on New Physics*, Particle Data Group review . http://pdg.lbl.gov/2014/reviews/rpp2014-rev-standard-model.pdf.

[120] M. Baak, J. Cuth, J. Haller, A. Hoecker, R. Kogler, et al., *The global electroweak fit at NNLO and prospects for the LHC and ILC*, arXiv:1407.3792 [hep-ph].

[121] CMS Collaboration, *Projected improvement of the accuracy of top-quark mass measurements at the upgraded LHC*, CMS-PAS-FTR-13-017, CERN, Geneva, 2013. https://cds.cern.ch/record/1605627.

[122] J. Erler, *Status of Precision Extractions of α_s and Heavy Quark Masses*, AIP Conf. Proc. **1701** (2016) 020009, arXiv:1412.4435 [hep-ph].

[123] M. Awramik, M. Czakon, A. Freitas, and G. Weiglein, *Precise prediction for the W boson mass in the standard model*, Phys.Rev. **D69** (2004) 053006, arXiv:hep-ph/0311148 [hep-ph].

[124] M. Awramik, M. Czakon, and A. Freitas, *Electroweak two-loop corrections to the effective weak mixing angle*, JHEP **0611** (2006) 048, arXiv:hep-ph/0608099 [hep-ph].

[125] I. Dubovyk, A. Freitas, J. Gluza, T. Riemann, and J. Usovitsch, *The two-loop electroweak bosonic corrections to $\sin^2\theta^{\rm b}_{\rm eff}$*, Phys. Lett. **B762** (2016) 184–189, arXiv:1607.08375 [hep-ph].

[126] I. Dubovyk, A. Freitas, J. Gluza, T. Riemann, and J. Usovitsch, *Complete electroweak two-loop corrections to Z boson production and decay*, arXiv:1804.10236 [hep-ph].

[127] A. Freitas, K. Hagiwara, S. Heinemeyer, P. Langacker, K. Moenig, M. Tanabashi, and G. W. Wilson, *Exploring Quantum Physics at the ILC*, in *Proceedings, 2013 Community Summer Study on the Future of U.S. Particle Physics: Snowmass on the Mississippi (CSS2013): Minneapolis, MN, USA, July 29-August 6, 2013*. 2013. arXiv:1307.3962 [hep-ph]. https://inspirehep.net/record/1242667/files/arXiv:1307.3962.pdf.

[128] A. Freitas, *Higher-order electroweak corrections to the partial widths and branching ratios of the Z boson*, JHEP **04** (2014) 070, arXiv:1401.2447 [hep-ph].

[129] J. Fan, M. Reece, and L.-T. Wang, *Possible Futures of Electroweak Precision: ILC, FCC-ee, and CEPC*, JHEP **09** (2015) 196, arXiv:1411.1054 [hep-ph].

[130] CEPC-SPPC Study Group, CEPC-SPPC Preliminary Conceptual Design Report. 1. Physics and Detector (2015) . http://cepc.ihep.ac.cn/preCDR/volume.html.

[131] C. Burgess, S. Godfrey, H. Konig, D. London, and I. Maksymyk, *Model independent global constraints on new physics*, Phys.Rev. **D49** (1994) 6115–6147, arXiv:hep-ph/9312291 [hep-ph].

[132] M. Ciuchini, E. Franco, S. Mishima, and L. Silvestrini, *Electroweak Precision Observables, New Physics and the Nature of a 126 GeV Higgs Boson*, JHEP **08** (2013) 106, arXiv:1306.4644 [hep-ph].

[133] A. Hocker, H. Lacker, S. Laplace, and F. Le Diberder, *A New approach to a global fit of the CKM matrix*, Eur.Phys.J. **C21** (2001) 225–259, arXiv:hep-ph/0104062 [hep-ph].

[134] H. Flacher, M. Goebel, J. Haller, A. Hocker, K. Monig, et al., *Revisiting the Global Electroweak Fit of the Standard Model and Beyond with Gfitter*, Eur.Phys.J. **C60** (2009) 543–583, arXiv:0811.0009 [hep-ph].

[135] R. Lafaye, T. Plehn, M. Rauch, D. Zerwas, and M. Duhrssen, *Measuring the Higgs Sector*, JHEP **0908** (2009) 009, arXiv:0904.3866 [hep-ph].

CHAPTER 12

FUTURE PLANS AND R&D PROSPECTS

Since the release of the pre-CDR, the main effort of the CDR has been focusing on exploring different concepts of the detector design. In addition to a baseline detector optimized from ILD with 3T magnetic filed, two alternative detectors are also proposed. One with a full-silicon tracker and another one with a drift chamber under 2T magnetic field. The baseline concept detector is used to evaluate the physics potential of the 240 GeV CEPC accelerator.

For the next TDR phase more in-depth studies will be carried out. (ADD SUMMARY OF THE REST SECTIONS...)

12.1 Tracking

12.1.1 Vertex

As the inner most layers, the vertex detector has to fulfill the most demanding requirements imposed by the physics program. To meet these requirements of single-point resolution, low material budget, fast readout, low power consumption and radiation tolerance, coherent R&D activities have to be pursued:

- Enhancement of density, radiation hardness and ultra-light module assembling.
- Explore smaller production line for TowerJazz and LAPIS in conjunction with the NpD (Nano-particle deposition) technique.
- Improve te charge collection efficiency of the TowerJazz process by N-type implant
- Improve the radiation hardness and low power design for SOI process.

- Sensor thinning for CMOS and SOI.
- Detailed designs for mechanical supports to enable cooling, cabling and power conservation.

12.1.2 Silicon tracker

Placed outside the vertex detector and after the TPC, the silicon tracker forms the complete tracking system of CEPC. The silicon tracker is designed to have low material budget and high tracking efficiency. With preliminary studies, several critical R&D items are identified for the next TDR phase:

- Alternative pixelated strip sensors with CMOS technologies;
- p^+-on-n silicon microstrip sensors with slim-edge structure;
- Front-end electronics with low power consumption and low noise, fabricated with CMOS technologies of small feature size;
- Efficient powering with low material budget and CO_2 cooling techniques;
- Lightweight but robust support structure and related mechanics;
- Detector layout optimization, in particular in the forward region.

12.1.3 TPC

Time Projection Chambers is considered as the baseline central tracker for the CEPC tracking system. Modularized design with gas amplification and readout pad optimization have been investigated. The low power consumption electronics and ion backflow (IBF) are also considered. The future R&D consists:

- Hybrid structure TPC detector module,
- Laser calibration and alignment system.

12.1.4 Full-silicon tracker

To demonstrate a viable option for CEPC under the same detector boundary conditions of the baseline design, the TPC is replaced with a full-silicon tracker (CEPC-FST) layout. A second approach is used to fulfill the CEPC tracking volume with the ILC-SID tracker to achieve better momentum resolution. To explore the full potential of the all silicon tracker, possible improvements are:

- Optimize the layout for better performance and lower cost based on satisfy mechanics.
- Study physical performance and find out which physics processes are suitable for evaluation.

12.1.5 Drift Chamber tracker

The drift chamber tracker is another option to provide good tracking, high precision momentum measurement and excellent particle identification by cluster counting.

- Final layout optimization of the full tracking system, which, besides the drift chamber, includes the vertex detector and the silicon micro-strip detector layers (the silicon wrapper, as indicated in Figure 3.12).
- Studies for a non-flammable gas mixture alternative to He/Isobutane 90/10.
- Particle identification performance with cluster counting, to be assessed in beam tests of realistic drift chamber prototypes.
- Full length ($>$ 4 m) prototypes to establish limits of the wires electrostatic stability.

12.2 Calorimetry

Electromagnetic calorimeter (ECAL) and hadron calorimeter (HCAL) makes the calorimeters of the CEPC detector which is use for precise energy measurements of electron, photon, tau and hadronic jets. The basic requirements for ECAL and HCAL resolution are $16\%/\sqrt{E}$ and $50\%/\sqrt{E}$ with the Particle Flow Algorithm (PFA). The main development areas are:

12.2.1 HCAL

The future plans of HCAL should include prototype design and construction based on MOST funds support.

- DDHCAL based on RPC, Test beams and performance study
- MRPC with better time resolution (about 50ps)
- AHCAL based on scintillator + SiPM, prototype design and construction, performance study

12.2.2 Dual-readout calorimeter

Concerning the dual-readout calorimeter, a 3-year R&D programme is being pursued in order to address and clarify the following issues:

- absorber material choice, current candidates are lead, brass and iron;
- machining and assembly procedure for modules of $\sim 10 \times 10\ cm^2$ cross section;
- development of a modular, projective solution for a 4π calorimeter concerning both the construction of single modules and the design and construction of a full detector;
- identification of adequate solid-state photo-sensors in order to independently optimise both Čerenkov and scintillation light detection (with respect to PDE, linearity, dynamic range and cross-talk performance);
- readout granularity (i.e. identify the optimal fibre grouping into a single readout channel);
- identification of a tailored front-end electronics, likely composed by an ASIC and an FPGA chip, in order to extract in real time both charge and time information (in

principle, a time resolution of 100 ps should allow to identify the shower starting point inside the calorimeter with a precision of about 6 cm);

- particle ID performance with Particle Flow Algorithms, with and without a longitudinal segmentation;
- development and validation of full and fast simulations of both testbeam modules and an integrated 4π detector;
- assessment of the performance for the most relevant physics channels (such as W, Z, H decays).

12.3 Magnet

A detector superconducting solenoid with 3.0T central field is chosen for this CDR for feasibility reasons. It makes full cancelation to avoid disturbance to the beam with technologies in coming years. For the TDR phase, the following R&D work will be conducted:

- Further development of longer and higher Ic Aluminum based NbTi superconductor, the length longer than 100m, and Ic will larger than 15kA at 4 T background magnetic field. (For the reference, we have developed 10m long Aluminum based NbTi superconductor, the Ic 5kA at 4 T background magnetic field up to now.)
- Build a prototype to study large coil winding process and cooling method by liquid helium thermal siphon.
- Study of candidate option by using large HTS magnet and the related cooling method at 20K.

12.4 Muon system

Located within the solenoid flux return yoke, the muon system is required to identify muons with very high efficiency. Both Resitive Plate Chamber (RPC) and Micro Pattern Gas detector (MPGD) are considered in CDR. Future R&D requires detailed studies of different technologies and further optimization of baseline design parameters. Several critical R&D items have been identified, including:

- Long-lived particles optimization: Explore new physics scenario of long-lived particles and exotic decays. Optimize detector parameters and technologies.
- Layout and geometry optimization: Detailed studies on the structure of the segments and modules need to be carried out to minimise the dead area and to optimise the interface for routing, support and assembly.
- Detector optimization: Study aging effects, improve long-term reliability and stability, readout technologies.
- Detector industrialization: Improve massive and large area production procedures for all technologies.

12.5 DAQ

New technologies will emerge before the CEPC DAQ system has to be built. Attention will be made to follow and explore the ongoing improvement of the data communication and processing technologies. In particular the following areas will be addressed:

- The high speed and low latency communication technology should be the key point for data readout.
- A high efficient data flow distribution schema is another key point for data dispatching on a huge computing farm. There the data are concentrated, re-formatted, possibly zero-suppressed, assembled full event and filtered.
- Online software trigger and data compression algorithm should be study and provided by physics. But the implementation of the data processing inside online farm is DAQ scope.

12.6 Machine detector interface

Machine-Detector Interface (MDI) represents one of the most challenging topics in which both the accelerator and detector will be covered. The interaction region (IR) has to focus both electron and positron beams to small spot sizes to maximize the machine luminosity. The following R&D will be carried out during the next TDR phase:

- Interaction region layout re-design/optimization
- Background models validation with experimental data, e.g. SuperKEKB/Belle II
- Beampipe design together with SR photon protection, HOM absorber and cooling if needed
- Installation scheme that involves both LumiCal and final focusing magnets
- Prototyping R&D on LumiCal, and demonstration of alignment of desired precision with laser and optical devices.

12.7 Physics objects performance

The physics objects performance is determined by the detector geometry and reconstruction algorithms, including tracking, particle flow, and particle identification algorithms. For the TDR phase, the following items should be addressed:

- Theory/Pheno: The control of theoretical uncertainty
- Data analysis: Calibration Methods, In-situ Calibration
- Development and validation of sub-detector digitization algorithms.
- Advanced reconstruction algorithm and pattern recognition studies.

References

[1] CEPC project website. http://cepc.ihep.ac.cn.

[2] The CEPC-SPPC Study Group, *CEPC-SPPC Preliminary Conceptual Design Report, Volume II - Accelerator*, 2015. IHEP-CEPC-DR-2015-01, IHEP-AC-2015-01.

[3] The ATLAS Collaboration, G. Aad et al., *Observation of a new particle in the search for the Standard Model Higgs boson with the ATLAS detector at the LHC*, Phys. Lett. B **716** (2012) 1–29, arXiv:1207.7214 [hep-ex].

[4] The CMS Collaboration, S. Chatrchyan et al., *Observation of a new boson at a mass of 125 GeV with the CMS experiment at the LHC*, Phys. Lett. **B716** (2012) 30–61, arXiv:1207.7235 [hep-ex].